

UNCLASSIFIED

AD 273 805

*Reproduced
by the*

**ARMED SERVICES TECHNICAL INFORMATION AGENCY
ARLINGTON HALL STATION
ARLINGTON 12, VIRGINIA**



UNCLASSIFIED

**Best
Available
Copy**

NOTICE: When government or other drawings, specifications or other data are used for any purpose other than in connection with a definitely related government procurement operation, the U. S. Government thereby incurs no responsibility, nor any obligation whatsoever; and the fact that the Government may have formulated, furnished, or in any way supplied the said drawings, specifications, or other data is not to be regarded by implication or otherwise as in any manner licensing the holder or any other person or corporation, or conveying any rights or permission to manufacture, use or sell any patented invention that may in any way be related thereto.

273805
CATALOGED BY ASTIA
AS AD No. - 273805

RADC-TDR-61-303

School of Electrical Engineering
CORNELL UNIVERSITY
Ithaca, New York

RESEARCH REPORT EE 516

**THEORETICAL AND EXPERIMENTAL INVESTIGATION
OF LINEAR BEAM MICROWAVE TUBES**

Final Report, Parts II C and III

1 April 1957 to 31 August 1961

Approved by

G. Conrad Dalman
Lester F. Eastman
Paul R. McIsaac

NOX

Published under Contract No. AF30(602)-1696
Rome Air Development Center, Griffiss Air Force Base, N. Y.

ASTIA

RADC-TDR-61-303

School of Electrical Engineering
CORNELL UNIVERSITY
Ithaca, New York

RESEARCH REPORT EE 516

THEORETICAL AND EXPERIMENTAL INVESTIGATION
OF LINEAR-BEAM MICROWAVE TUBES

Final Report, Parts IIC and III

1 April 1957 to 31 August 1961

Approved by

G. Conrad Dalman
Lester F. Eastman
Paul R. McIsaac

Published under Contract No. AF 30(602)-1696
Rome Air Development Center, Griffiss Air Force Base, New York

CONTENTS OF FINAL REPORT

| | Page |
|---------------------------------------|------|
| FOREWORD | vii |
| PART I | |
| GENERAL | |
| ABSTRACT | 1 |
| INTRODUCTION | 4 |
| DISCUSSION | 6 |
| A Beam-Circuit Interaction Studies | 6 |
| B. Circuit Studies | 17 |
| C Beam Analyzer Studies | 21 |
| D. Cathode Studies | 22 |
| CONCLUSIONS | 28 |

PART II

BEAM-CIRCUIT INTERACTION

THE VELOCITY DISTRIBUTION IN A VELOCITY-MODULATED
ELECTRON BEAM FROM A SHIELDED PIERCE GUN
A. S. Gilmour, Jr.

NONLINEAR SPACE-CHARGE-WAVE ANALYSIS P. R. McIsaac

ON THE NONLINEAR THEORY OF THE PLANE
KLYSTRON TUBE S. Olving

NONLINEAR SPACE-CHARGE-WAVE THEORY OF THE
RADIALLY FINITE ELECTRON BEAM

S. Olving

HARMONIC ANALYSIS OF ELECTRON BEAMS IN
KLYSTRONS

W. E. Blair

NONLINEAR ANALYSIS OF KLYSTRON BEAMS

J. E. Romaine

ON THE DYNAMICS OF MAGNETICALLY FOCUSED
ELECTRON BEAMS

P. S. Bottorff

THE KINETIC A-C POWER FLOW IN NONHOMOGENEOUS
RELATIVISTIC ELECTRON BEAMS

S. Olving

AN INTRODUCTORY RELATIVISTIC STUDY OF THE
LLEWELLYN ELECTRONIC GAP

S. Olving

BALLISTIC ANALYSIS OF AN ELECTRON BEAM IN
A KLYSTRON

I. Turkekul

LARGE-SIGNAL THEORY OF GRIDDED KLYSTRON
GAP

W. M. Sackinger

PART III
CIRCUIT STUDIES

KLYSTRON CAVITIES FOR MINIMUM SPURIOUS
OUTPUT POWER

L. A. MacKenzie

NOTE ON THE PRELIMINARY RESULTS OF SPURIOUS
OUTPUT POWER MEASUREMENTS

A. Ray Howland, Jr.

PERTURBATION TECHNIQUE

W. E. Blair

PART IV
BEAM ANALYZER

A BEAM TESTER FOR STUDYING THE CHARACTERISTICS
OF D-C AND VELOCITY-MODULATED ELECTRON BEAMS

A. S. Gilmour, Jr.

PART V
CATHODE STUDIES

SOME EFFECTS OF ION BOMBARDMENT ON THE EMITTING
PROPERTIES OF OXIDE-COATED CATHODES H. Hollister

STUDIES OF CONTINUOUSLY OPERATED CATHODES N. Erdibil

LONG-PULSE DIODE STUDY H. Hollister

FINAL REPORT

PART II C:
BEAM-CIRCUIT INTERACTION

BALLISTIC ANALYSIS OF AN ELECTRON BEAM IN A KLYSTRON

I. Turkekul

School of Electrical Engineering
CORNELL UNIVERSITY
Ithaca, New York

RESEARCH REPORT EE 508

BALLISTIC ANALYSIS OF AN ELECTRON BEAM IN A KLYSTRON

I. Turkekul

LINEAR BEAM MICROWAVE TUBES

Technical Report No. 16

30 August 1961

Published under Contract No. AF30(602)-1696
Rome Air Development Center, Griffiss Air Force Base, New York

TABLE OF CONTENTS

| | Page |
|---|-----------|
| ABSTRACT | v |
| I. INTRODUCTION | 1 |
| II. ANALYSIS OF THE FIRST GAP | 2 |
| A. GRAPHIC ANALYSIS | 2 |
| B. FIRST-ORDER ANALYSIS | 6 |
| 1. Velocity Modulation | 6 |
| 2. Density Modulation | 8 |
| C. SECOND-ORDER ANALYSIS | 11 |
| 1. Velocity Modulation | 11 |
| 2. Density Modulation | 16 |
| III. ANALYSIS OF THE DRIFT SPACE | 21 |
| A. DENSITY | 22 |
| B. VELOCITY | 24 |
| CONCLUSIONS AND RECOMMENDATIONS | 32 |
| A. FIRST GAP | 32 |
| B. DRIFT SPACE | 33 |
| C. RECOMMENDATION | 33 |
| REFERENCES | 34 |

ABSTRACT

The behavior of an electron beam in a buncher gap is investigated using a graphic analysis based on the results given by a Burroughs Datatron 220 digital computer. The velocity and current distribution emerging from this gap are found. The graphic results are approached by successively approximating the transit time correction factor.

The results obtained by successive approximation are then used as initial conditions in analyzing the behavior of the electron beam in the drift space.

I. INTRODUCTION

The ballistic approach of analyzing an electron beam in a velocity-modulated tube was first introduced by Webster.¹ Although this theory lacks validity at or after crossover because of space-charge forces and does not apply to electron beams of finite radius because of fringing of the space-charge fields, it has two advantages: (1) It is simple and provides an insight into the physical phenomena, and thus serves as a guide for more complicated theories. (2) It is fairly accurate at large-signal levels for low-perveance beams.

The current tendency to demand higher power levels from klystrons increases the importance of ballistic theory. In an experiment, Mihran² showed that for large signals, the electron beam shows ballistic behavior; i.e., at large signal levels, the debunching effect of the space-charge forces becomes less important. At the same time, in finite beams, the space-charge forces act to enhance bunching at large signals by debunching inner and outer electrons differently.

The purpose of this study is to analyze the electron beam, both in the first gap and in the drift space, using a ballistic approach, and to express the functional relationships among the various parameters in analytic form. To simplify this analysis, the following assumptions are made: (1) beam of infinite cross section, (2) negligible space charge, (3) gridded finite gaps, (4) nonrelativistic velocities.

II. ANALYSIS OF THE FIRST GAP

The first or buncher gap modulates the velocity of an electron beam. This, in turn, causes density modulation in the drift space. In a finite gap, however, density modulation also takes place. This factor has been neglected in previous analyses, and including it extends Webster's analysis.

Analytical expressions of functional relationships will be based on an exact graphic method with the assumptions mentioned. Thus, in this chapter, a graphic analysis is first made and then analytical formulas are obtained by successive approximations.

A. GRAPHIC ANALYSIS (Computer Problem)³

The equation of motion of electrons in the buncher gap, with a sinusoidal input voltage and no space charge, is a simple second-order differential equation,

$$\ddot{z} = \frac{eV_1}{md} \sin \omega t . \quad (2.1)$$

Using the notation of Figure 1, integrating Equation (2.1) twice, and substituting boundary conditions at $t = t_a$ and at $t = t_b$, one obtains

$$\dot{z} = v_o + \frac{eV_1}{m\omega d} (\cos \omega t_a - \cos \omega t_b) , \quad (2.2)$$

$$d = \left(v_o + \frac{eV_1}{m\omega d} \cos \omega t_a \right) (t_b - t_a) + \frac{eV_1}{m\omega d} (\sin \omega t_a - \sin \omega t_b) . \quad (2.3)$$

Defining the d-c transit angle and depth of modulation gives

$$\theta_g = \frac{\omega d}{v_o} , \quad (2.4)$$

$$a = \frac{V_1}{V_o} ; \quad (2.5)$$

and normalizing with respect to d-c velocity gives

$$Z = \frac{z}{v_o} = 1 + \frac{a}{2\theta_g} (\cos \omega t_a - \cos \omega t_b) , \quad (2.6)$$

$$\theta_g = 1 + \frac{a}{2\theta_g} \cos \omega t_a (\omega t_b - \omega t_a) + \frac{a}{2\theta_g} (\sin \omega t_a - \sin \omega t_b) . \quad (2.7)$$

Equations (2.6) and (2.7) completely define the motion of electrons during

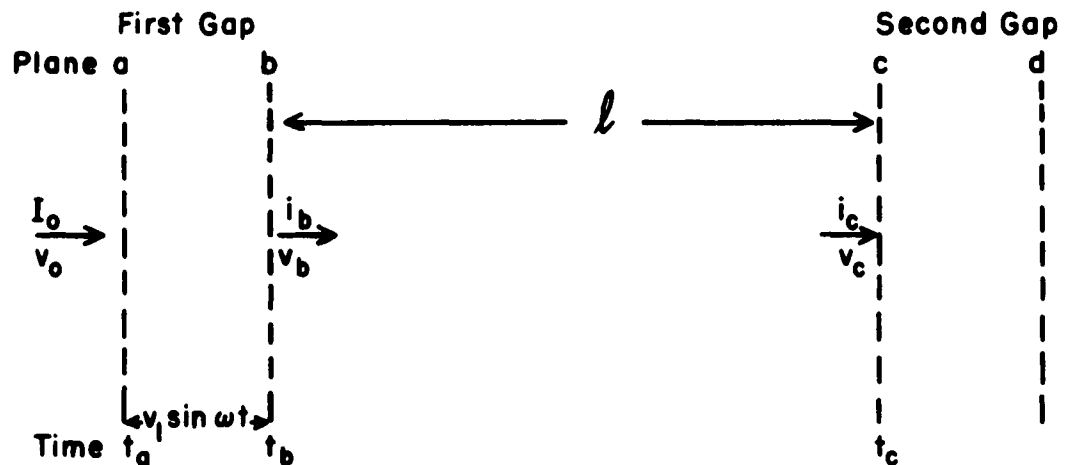


Figure 1. Schematic Diagram of Two-Cavity Klystron with Parallel Gridded Gaps.

the passage through the gap and give the implicit relation between entrance time and exit time with gap transit angle and depth of modulation as parameters.

The numerical computations of Equations (2.6) and (2.7) have been carried out by a Burroughs Datatron 220 digital computer, and are presented in a series of graphs of normalized exit velocity, v_b/v_o , versus exit time, ωt_b ; normalized exit current, i_b/I_o , versus exit time, ωt_b ; and the transit time correction factor, $\omega t_b - \omega t_a - \theta_g$, versus entrance time, ωt_a .

Exit current is obtained by applying the principle of conservation of charge through the gap; it can be determined from

$$\frac{i_b}{I_o} = \left| \frac{d\omega t_a}{d\omega t_b} \right| . \quad (2.8)$$

Numerical values of the normalized current are found by measuring the slope of the curves of the transit time correction factor versus entrance time at each point. Figures 2a, b, c show the results of this method for three different gap transit angles with depth of modulation as a parameter. Additional results will be presented in later sections.

It can be seen from Figures 2a, b, and c that the normalized exit current gradually becomes peaked as the d-c gap transit angle (θ_g) is increased, and that there is a phase difference between the normalized exit current and the normalized exit velocity. Since deceleration and acceleration of electrons during the corresponding half cycles of the input voltage counteract each other, there is a limit to this peaking of the exit current as the d-c gap transit angle is further increased; $\theta_g = \pi$

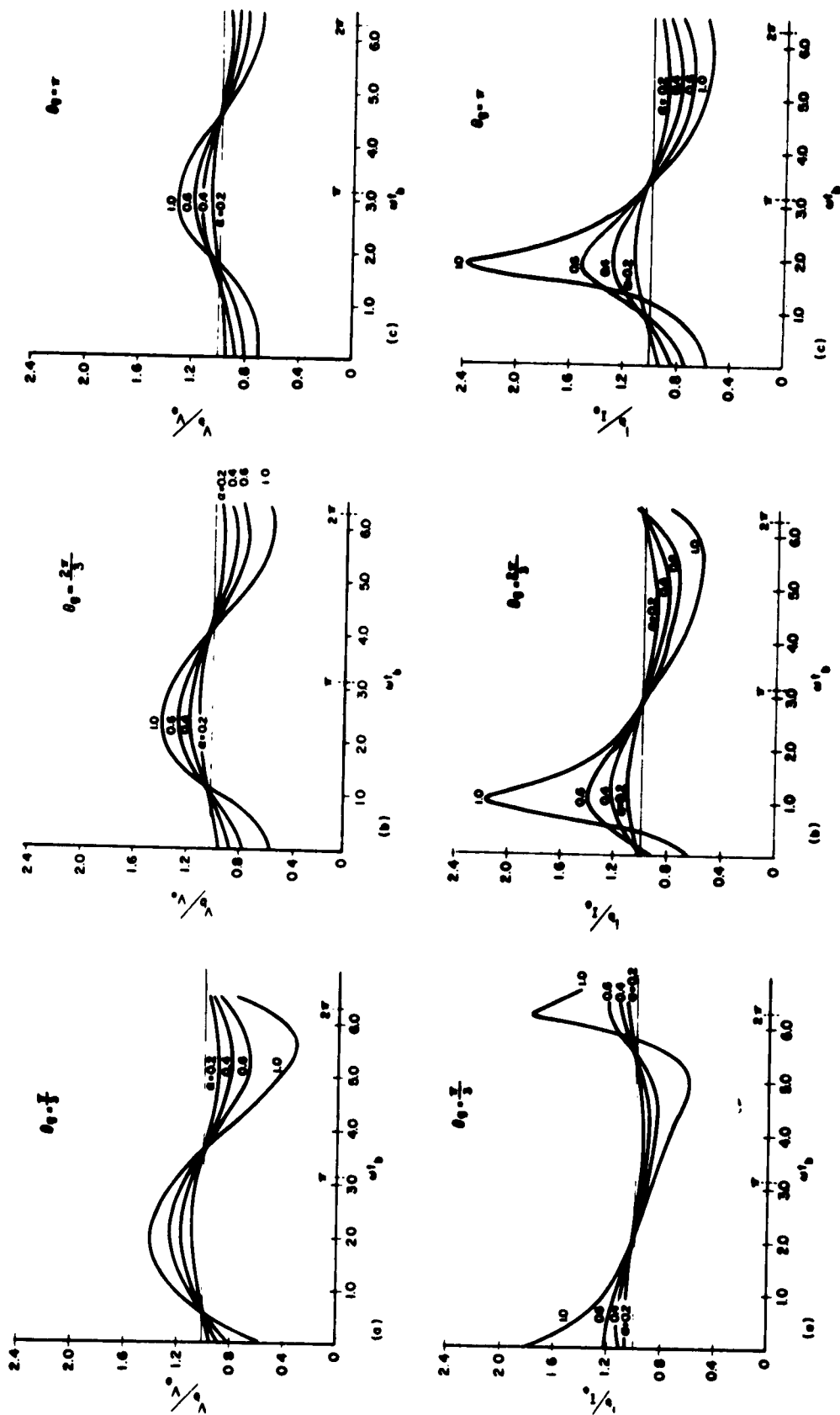


Figure 2. Normalized Exit Velocity v_b/v_o versus Exit Time ωt_b , and Normalized Exit Current i_b/I_o versus Exit Time ωt_b , for Different D-C Gap Transit Angles, Obtained by Graphic Analysis.

is a practical gap transit angle and it is used in the computations throughout the rest of this study.

The wave forms of the exit velocity and the exit current show that harmonics are present in both and that transit-time effects are nonlinear in the buncher gap.

B. FIRST-ORDER ANALYSIS

When the results of graphic analysis are known, one can proceed with the analytical study by making approximations in the derivations, and comparing the results thus obtained with those of the exact graphic method. The discrepancies will show the validity and the range of the analytical forms.

1. Velocity Modulation

One must approximate the transit time, since it plays an important role in the physical phenomena within the buncher gap. Assuming a correction term,

$$\omega t_b = \omega t_a + \theta , \quad (2.9)$$

where

$$\theta \equiv \theta_g (1 + \delta) \quad \theta_g \delta = \omega t_b - \omega t_a - \theta_g , \quad (2.10)$$

and substituting Equation (2.9) into Equation (2.2), one obtains for $t = t_b$,

$$\begin{aligned} v_b &= v_o + \frac{e}{m} \frac{V_1}{\omega d} 2 \sin \frac{\theta}{2} \sin \left(\omega t_b - \frac{\theta}{2} \right) \\ &= v_o + \frac{1}{2} v_o a \frac{\sin \frac{\theta}{2}}{\theta_g} \sin \left(\omega t_b - \frac{\theta}{2} \right) . \end{aligned} \quad (2.11)$$

Expanding $\sin(\omega t_b - \theta/2)$ by trigonometrical identities and neglecting δ terms of higher order than the linear term, one can write Equation (2.11) as

$$\frac{v_b}{v_o} = 1 + \frac{1}{2} \mu a \sin\left(\omega t_b - \frac{\theta g}{2}\right) + \frac{1}{2} a \delta \cos \frac{\theta g}{2} \sin\left(\omega t_b - \frac{\theta g}{2}\right) - \frac{1}{4} \mu a \theta g \cos\left(\omega t_b - \frac{\theta g}{2}\right), \quad (2.12)$$

where

$$\mu \equiv \frac{\sin \frac{\theta g}{2}}{\frac{\theta g}{2}}. \quad (2.13)$$

Integrating Equation (2.2) and substituting in it the boundary conditions at $t = t_a$ and at $t = t_b$, and Equation (2.9), one obtains

$$d = \frac{v_o \theta}{\omega} + \frac{a \theta v_o}{2 \omega \theta g} \cos(\omega t_b - \theta) + \frac{a v_o}{2 \omega \theta g} [\sin(\omega t_b - \theta) - \sin \omega t_b]. \quad (2.14)$$

Assuming

$$\cos[\omega t_b - \theta g (1 + \delta)] \approx \cos(\omega t_b - \theta g),$$

$$\sin[\omega t_b - \theta g (1 + \delta)] \approx \sin(\omega t_b - \theta g),$$

$$\sin[\omega t_b - \theta g \delta] \approx \sin \omega t_b,$$

and neglecting the $a \delta$ term gives

$$\delta = \frac{a}{2 \theta g} [A \sin \omega t_b + B \cos \omega t_b], \quad (2.15)$$

where

$$A \equiv 1 - \cos \theta_g - \theta_g \sin \theta_g , \quad (2.16a)$$

$$B \equiv \sin \theta_g - \theta_g \cos \theta_g . \quad (2.16b)$$

Substitution of Equation (2.15) into Equation (2.12) leads to

$$\frac{v_b}{v_o} = 1 + \Delta + \frac{1}{2} \mu a \sin \left(\omega t_b - \frac{\theta_g}{2} \right) + M \sin 2(\omega t_b + \varphi) , \quad (2.17)$$

where

$$\Delta \equiv \frac{1}{2} \left(\frac{a}{2\theta_g} \right)^2 (\cos \theta_g - 1) , \quad (2.18a)$$

$$M \equiv \sqrt{P^2 + Q^2} , \quad (2.18b)$$

$$P \equiv \frac{1}{2} \left(\frac{a}{2\theta_g} \right)^2 (\sin 2\theta_g - \sin \theta_g - \theta_g + 2\theta_g \sin^2 \theta_g) , \quad (2.18c)$$

$$Q \equiv -\frac{1}{2} \left(\frac{a}{2\theta_g} \right)^2 (1 + \cos \theta_g - 2 \cos^2 \theta_g - \theta_g \sin 2\theta_g) , \quad (2.18d)$$

$$2\varphi \equiv \tan^{-1} \frac{Q}{P} . \quad (2.18e)$$

Equation (2.15) is plotted in Figure 3 for $\theta_g = \pi$. It can be seen that while Equation (2.15) approximates well the graphic method for small signals, it is a less satisfactory approximation for large signals.

2. Density Modulation

Substituting Equation (2.15) into Equation (2.10) and rewriting it, one obtains

$$\omega t_a = \omega t_b - \theta_g - \frac{a}{2\theta_g} [A \sin \omega t_b + B \cos \omega t_b] . \quad (2.19)$$

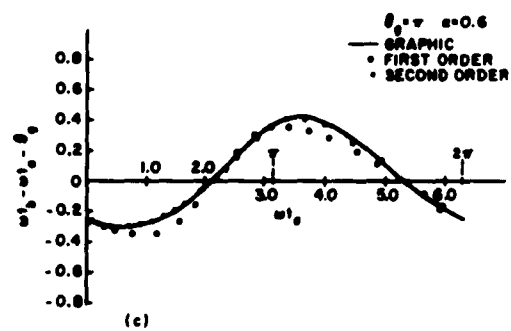
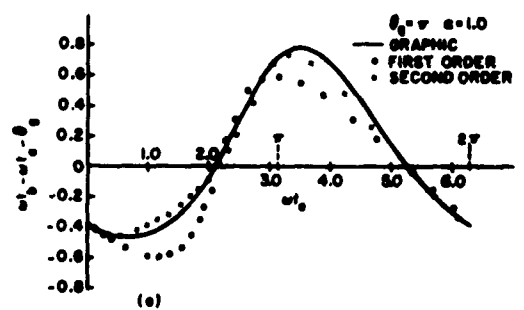
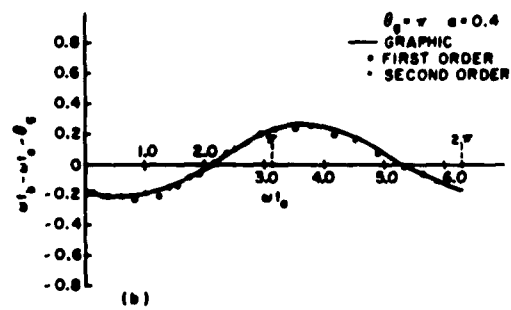
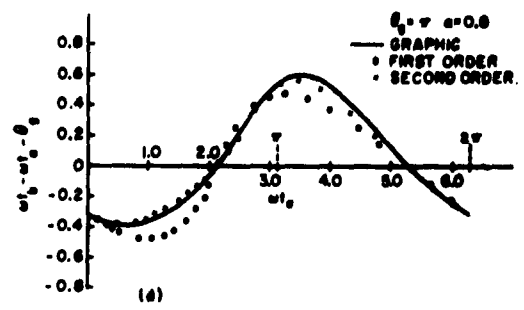
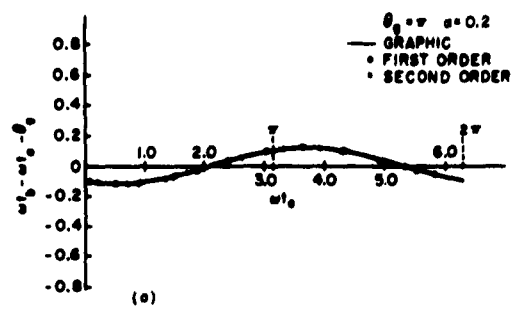


Figure 3. Transit-Time Correction Factor $(\omega_{t_b} - \omega_{t_a} - \theta_g)$ versus Entrance Time ω_{t_a} Comparing Graphic and Analytical Methods.

As in the graphic method, by using Equation (2.8), one can express the normalized exit current as

$$\frac{i_b}{I_o} = 1 + \frac{a}{2\theta g} (B \sin \omega t_b - A \cos \omega t_b) \quad . \quad (2.20)$$

Equation (2.20) can also be written as

$$\frac{i_b}{I_o} = 1 + N \sin(\omega t_b + \psi) \quad , \quad (2.21)$$

where

$$N \equiv \frac{ac}{2\theta g} \quad , \quad (2.22a)$$

$$C \equiv \sqrt{A^2 + B^2} \quad , \quad (2.22b)$$

$$\tan \psi \equiv \frac{-A}{B} \quad . \quad (2.22c)$$

From Figure 3 one can anticipate that Equation (2.21) will approach the results of the graphic method for small signals, but the discrepancy will be considerable for large signals.

It should be observed that the first-order analysis introduces a second harmonic term into the velocity expression, while only the fundamental is involved in the current expression. One can conclude that the first-order analysis results in analytic forms which approximate those of the graphic method for the small-signal case, and that the method of approximation for the transit-time correction factor appears promising for the large-signal case. In the following analysis, therefore, this approach will be followed.

C. SECOND-ORDER ANALYSIS

Extending the transit-time correction-factor approximation one step further, assume that

$$\theta \equiv \theta_g (1 + \delta_1 + \delta_2) , \quad (2.23)$$

where δ_1 is given by Equation (2.15). Substituting Equation (2.23) into Equation (2.14), assuming

$$\cos(\omega t_b - \theta) \approx \cos(\omega t_b - \theta_g - \theta_g \delta_1) + \theta_g \delta_2 \sin(\omega t_b - \theta_g - \theta_g \delta_1) ,$$

$$\sin(\omega t_b - \theta) \approx \sin(\omega t_b - \theta_g - \theta_g \delta_1) - \theta_g \delta_2 \cos(\omega t_b - \theta_g - \theta_g \delta_1) ,$$

and neglecting $\alpha \delta_2$ and δ_2^2 terms, one obtains

$$\delta_2 = -\delta_1 + \frac{a}{2\theta_g^2} [\sin \omega t_b - \sin(\omega t_b - \theta_g - \theta_g \delta_1) - \theta_g (1 + \delta_1) \cos(\omega t_b - \theta_g - \theta_g \delta_1)] , \quad (2.24a)$$

and

$$\omega t_b - \omega t_a - \theta_g = \frac{a}{2\theta_g} [\sin \omega t_b - \sin(\omega t_b - \theta_g - \theta_g \delta_1) - \theta_g (1 + \delta_1) \cos(\omega t_b - \theta_g - \theta_g \delta_1)] . \quad (2.24b)$$

Equation (2.24b) is plotted in Figure 3 for $\theta_g = \pi$. It can be seen from this figure that Equation (2.24b) gives a fair approximation to the graphic results for larger signal values.

1. Velocity Modulation

Substitution of Equation (2.24a) into Equation (2.13) leads, after some rearrangement, to

$$\begin{aligned}
\frac{v_b}{v_o} = & 1 + \frac{1}{2} \left(\frac{a}{2\theta g} \right)^2 (\cos \theta g - 1) - \frac{1}{4} \left(\frac{a}{2\theta g} \right)^4 \left[A^2 + B^2 - AB \sin 2\theta g - \frac{B^2 - A^2}{2} \cos 2\theta g \right] \\
& + \left(\frac{a}{2\theta g} \right) \left[\sin \theta g - \frac{\theta g}{4} \left(\frac{a}{2\theta g} \right)^2 (2A + A \cos 2\theta g - B \sin 2\theta g) \right] \sin \omega t_b \\
& - \left(\frac{a}{2\theta g} \right) \left[1 - \cos \theta g + \frac{\theta g}{4} \left(\frac{a}{2\theta g} \right)^2 (2B - A \sin 2\theta g - B \cos 2\theta g) \right] \cos \omega t_b \\
& + \frac{1}{2} \left(\frac{a}{2\theta g} \right)^2 B \left\{ \cos \theta g - A \sin \theta g + \frac{1}{2} \left(\frac{a}{2\theta g} \right)^2 [(A^2 + B^2) \sin 2\theta g - 2AB] \right\} \sin 2\omega t_b \\
& - \frac{1}{2} \left(\frac{a}{2\theta g} \right)^2 \left\{ A \cos \theta g + B \sin \theta g - \frac{1}{2} \left(\frac{a}{2\theta g} \right)^2 [(A^2 + B^2) \cos 2\theta g + A^2 - B^2] \right\} \cos 2\omega t_b \\
& + \frac{\theta g}{4} \left(\frac{a}{2\theta g} \right)^3 (A \cos 2\theta g + B \sin 2\theta g) \sin 3\omega t_b \\
& - \frac{\theta g}{4} \left(\frac{a}{2\theta g} \right)^3 (A \sin 2\theta g - B \cos 2\theta g) \cos 3\omega t_b + \frac{1}{8} \left(\frac{a}{2\theta g} \right)^4 [(B^2 - A^2) \sin 2\theta g \\
& + 2AB \cos 2\theta g] \sin 4\omega t_b + \frac{1}{8} \left(\frac{a}{2\theta g} \right)^4 [(B^2 - A^2) \cos 2\theta g - 2AB \sin 2\theta g] \cos 4\omega t_b
\end{aligned}$$

(2.25)

Equation (2.25) is plotted in Figure 4 for $\theta_g = \pi$ for comparison with the graphic method and in Figures 5 and 6 with the d-c gap transit angle as a parameter. It can be seen from Figure 4 that Equation (2.25) approximates the graphic method fairly well up to large signals. Figures 5 and 6 show the effect of the d-c gap transit angle on the velocity modulation. It can be seen that, as expected, the modulation effect decreases,

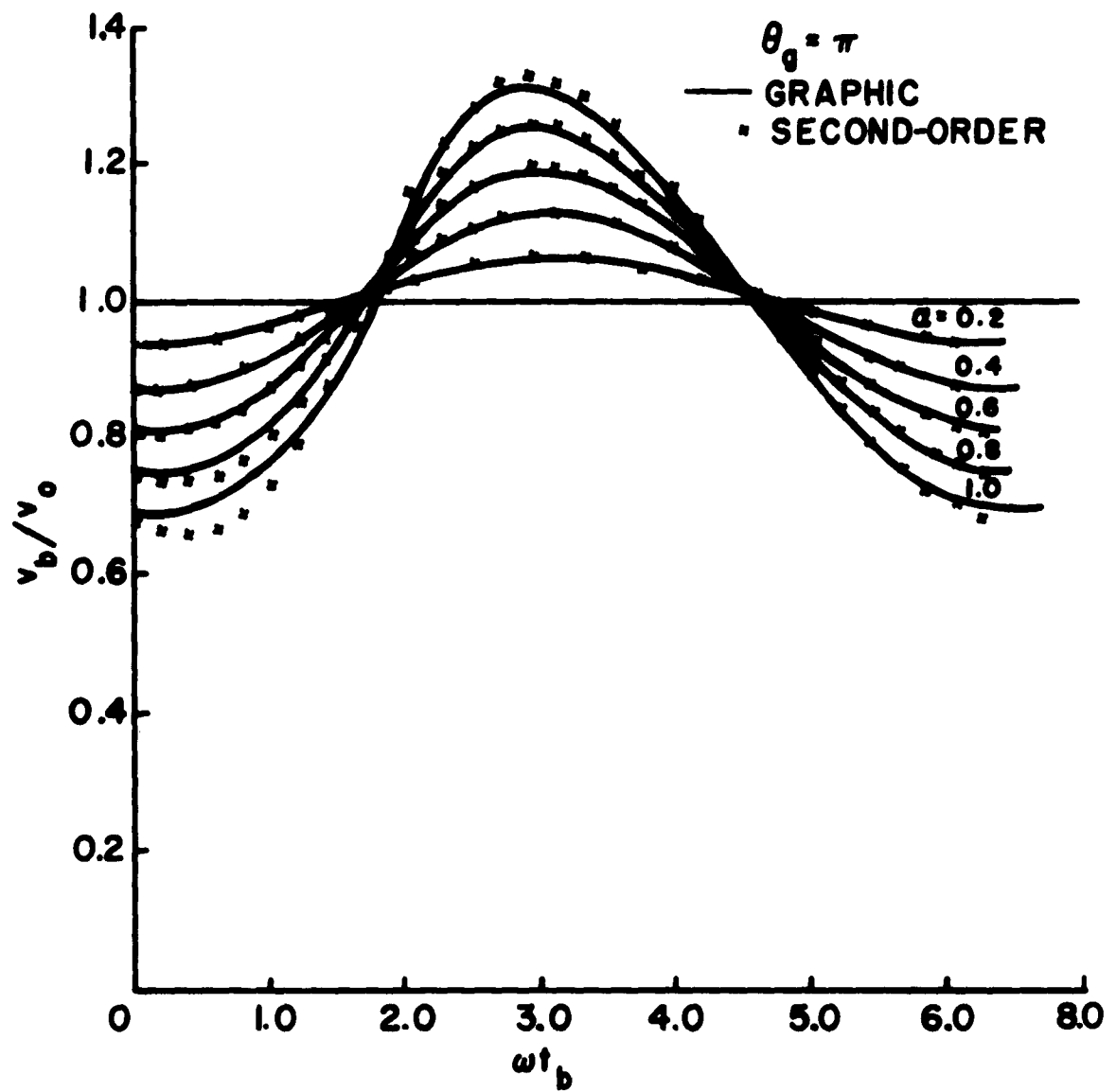


Figure 4. Normalized Exit Velocity v_b/v_0 versus Exit Time ωt_b , Comparing Graphic and Second-Order Methods.

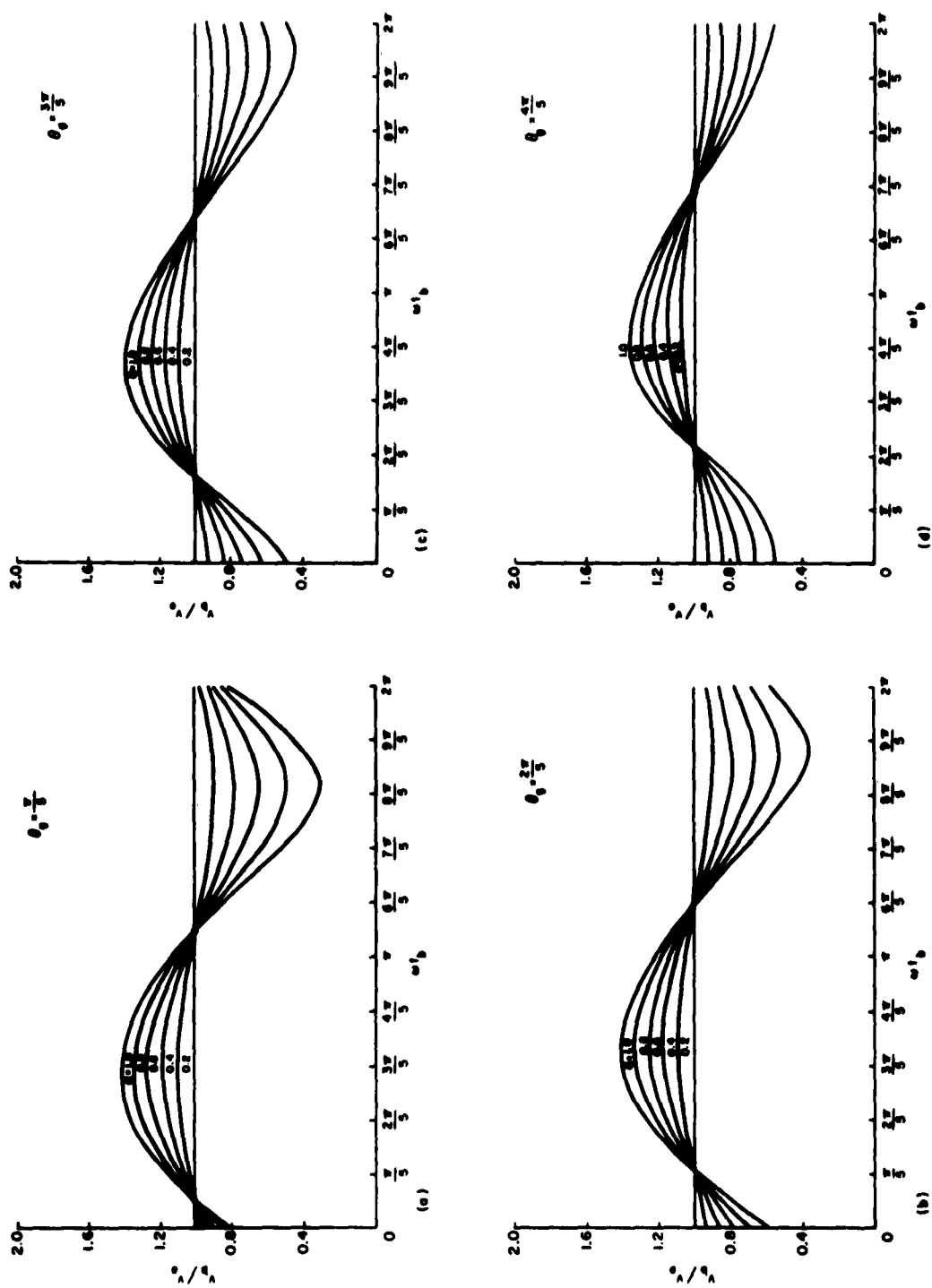


Figure 5. Normalized Exit Velocity v_b/v_0 versus Exit Time ωt_b for Different D-C Gap Transit Angles and Depths of Modulation.

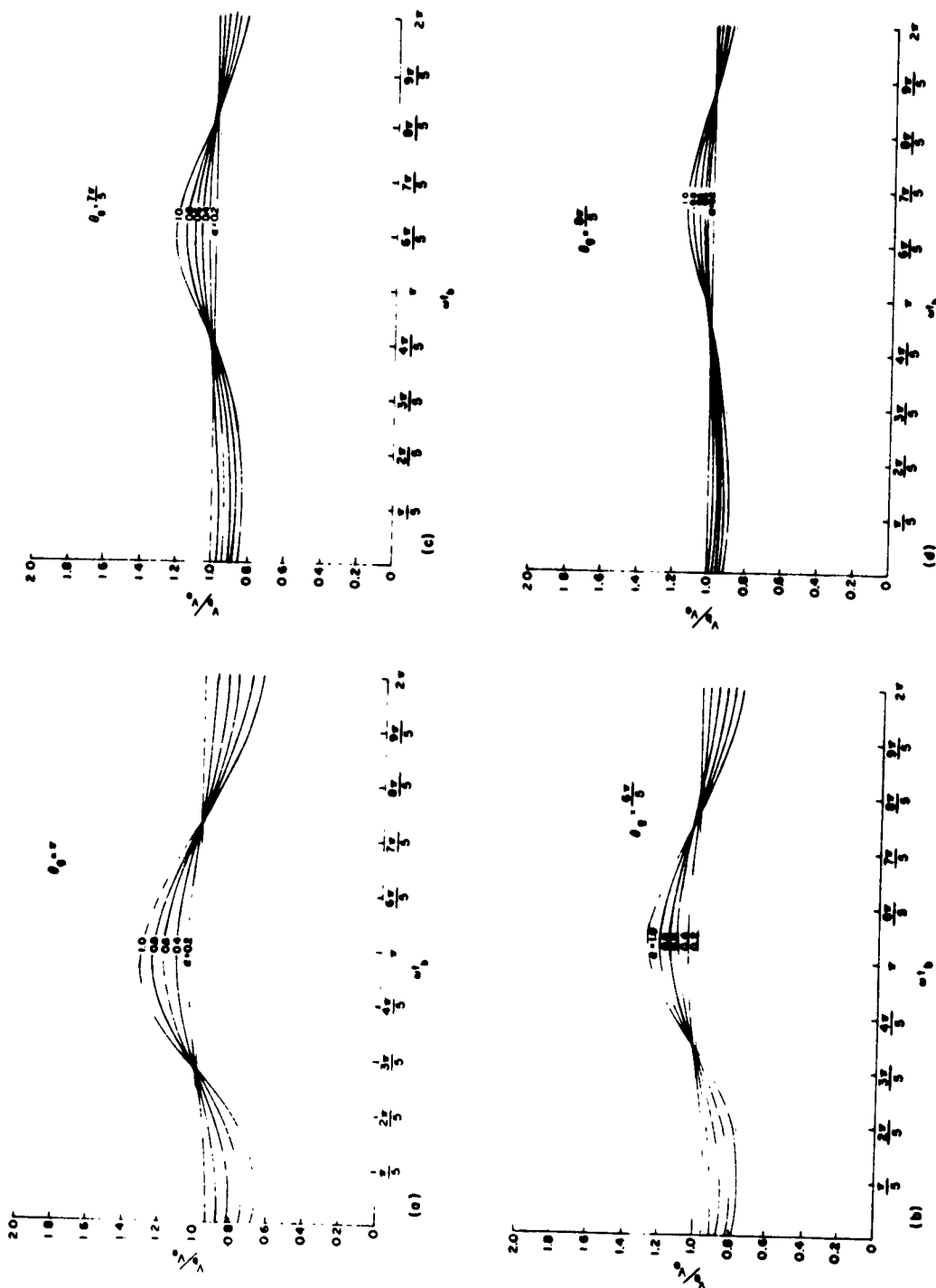


Figure 6. Normalized Exit Velocity v_b/v_o versus Exit Time ωt_b for Different D-C Gap Transit Angles and Depths of Modulation.

because of partial cancellation, as the d-c gap transit angle is increased.

2. Density Modulation

Differentiating Equation (2.24b) and neglecting third-order terms, one obtains

$$\frac{i_b}{I_o} = \frac{d\omega t_a}{d\omega t_b} = 1 - \frac{a}{2\theta g} \left[\cos \omega t_b - \cos(\omega t_b - \theta g) + \theta g \left(1 - \theta g \frac{d\delta_1}{d\omega t_b} \right. \right. \\ \left. \left. - \theta g \delta_1 \frac{d\delta_1}{d\omega t_b} \right) \sin(\omega t_b - \theta g) - \theta g^2 \left(\delta_1 + \delta_1^2 - \theta g \delta_1 \frac{d\delta_1}{d\omega t_b} \right) \cos(\omega t_b - \theta g) \right] . \quad (2.26)$$

Substituting Equation (2.15) and its derivative with respect to ωt_b and rearranging terms gives

$$\frac{i_b}{I_o} = 1 + \left(\frac{a}{2\theta g} \right) \left\{ B + \frac{1}{2} \left(\frac{a}{2\theta g} \right)^2 \left[(A^2 + B^2 + \theta g AB) \sin \theta g - \frac{(A^2 - B^2) \theta g}{2} \cos \theta g \right] \right\} \sin \omega t_b \\ - \left(\frac{a}{2\theta g} \right) \left\{ A - \frac{1}{2} \left(\frac{a}{2\theta g} \right)^2 \left[(A^2 + B^2 - \theta g AB) \cos \theta g - \frac{(A^2 - B^2)}{2} \theta g \sin \theta g \right] \right\} \cos \omega t_b \\ + \left(\frac{a}{2\theta g} \right)^2 \theta g (A \cos \theta g + B \sin \theta g) \sin 2\omega t_b - \left(\frac{a}{2\theta g} \right)^2 \theta g (A \sin \theta g - B \cos \theta g) \cos 2\omega t_b \\ + \left(\frac{a}{2\theta g} \right)^3 \left[AB \cos \theta g - \frac{(A^2 - B^2)}{4} \theta g \cos \theta g + \frac{(B^2 - A^2 - \theta g AB)}{2} \sin \theta g \right] \sin 3\omega t_b \\ - \left(\frac{a}{2\theta g} \right)^3 \left[AB \sin \theta g - \frac{(A^2 - B^2)}{4} \theta g \sin \theta g - \frac{(B^2 - A^2 - \theta g AB)}{2} \cos \theta g \right] \cos 3\omega t_b . \quad (2.27)$$

Equation (2.27) is plotted in Figure 7 for $\theta_g = \pi$ for comparison with the graphic method and in Figures 8 and 9 with the d-c gap transit angle as a parameter. Again it can be seen from Figure 7 that Equation (2.27) approximates the graphic method fairly well up to large signals. Figures 8 and 9 show the effect of the d-c gap transit angle on density modulation. It can be seen that as in the graphic method, density modulation first increases with the d-c gap transit angle and then decreases.

It should be observed that the second-order analysis introduces harmonics up to the third harmonic in the current expression, and up to the fourth harmonic in the velocity expression, and that it extends the approximation to larger signals.

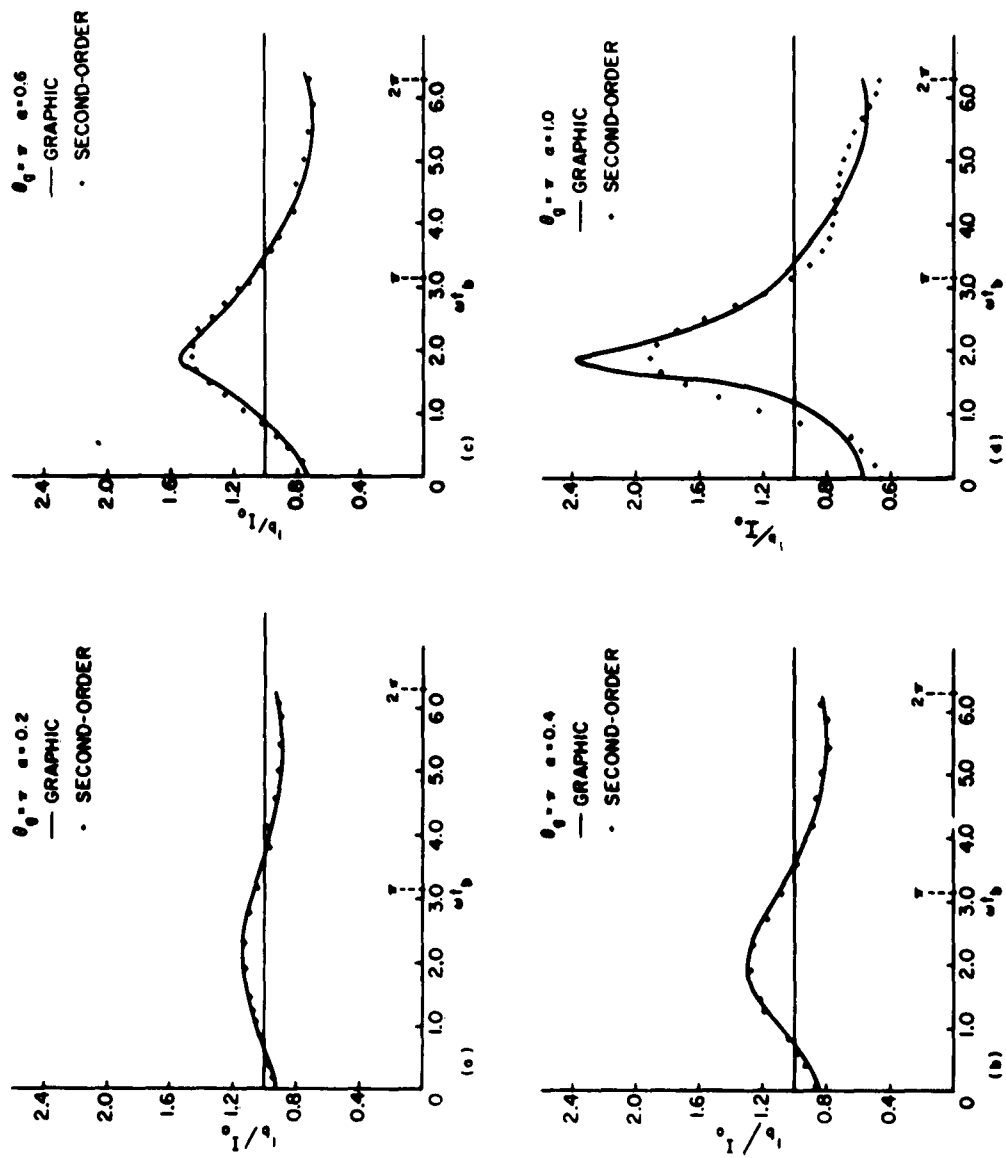


Figure 7. Normalized Exit Current i_b/I_o versus Exit Time ωt_b Comparing Graphic and Second-Order Methods.

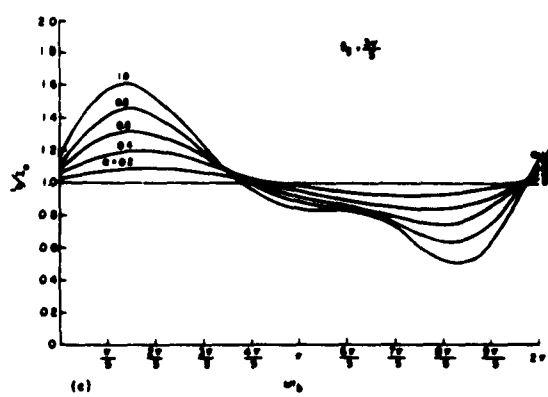
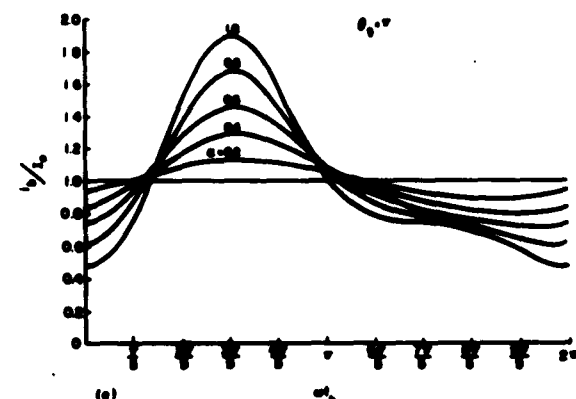
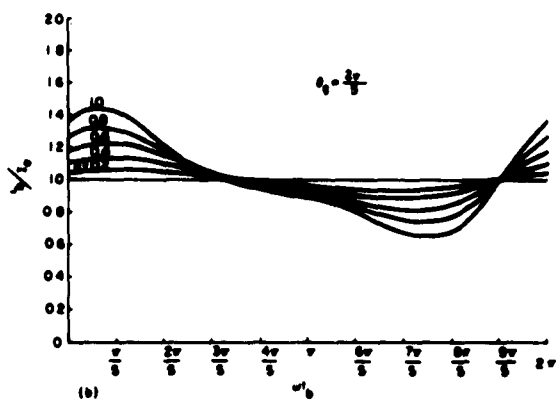
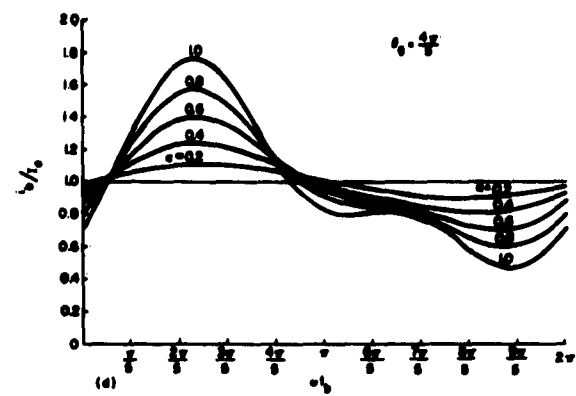
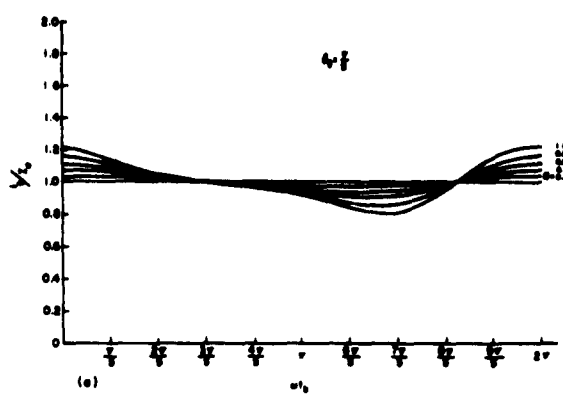


Figure 8. Normalized Exit Current i_b/I_o versus Exit Time ωt_b for Different D-C Gap Transit Angles and Depths of Modulation.

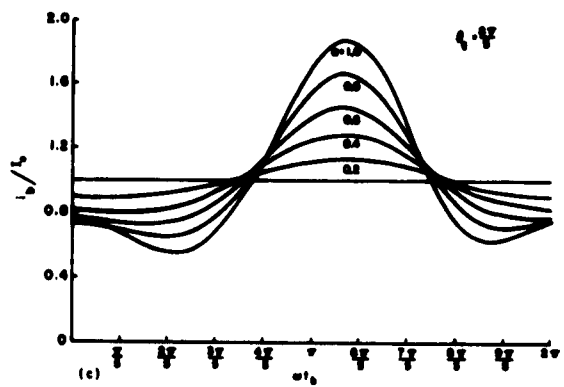
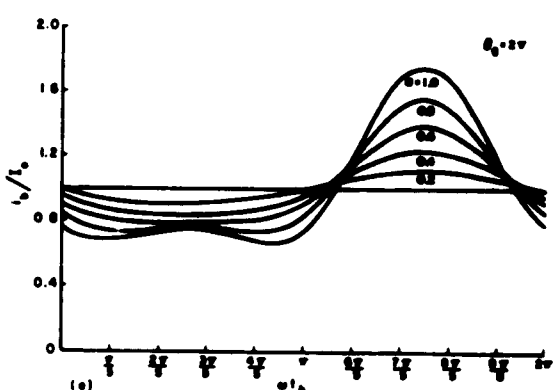
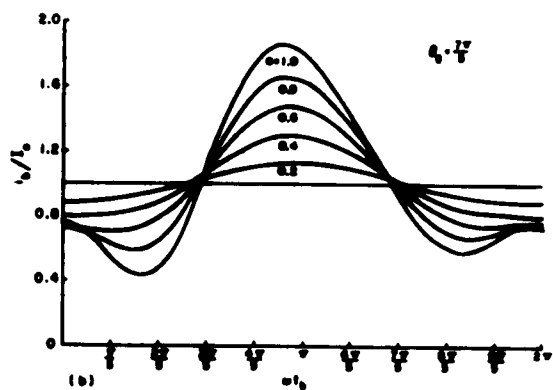
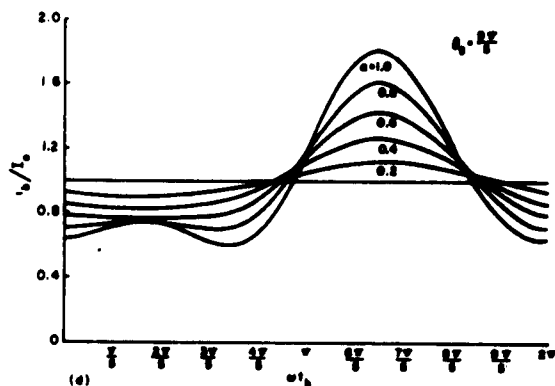
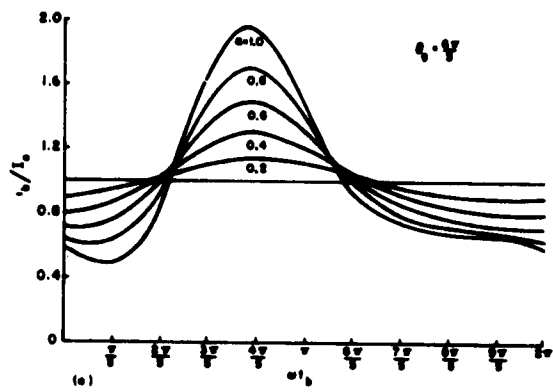


Figure 9. Normalized Exit Current
 i_b/I_o **versus Exit Time**
 wt_b **for Different D-C Gap**
Transit Angles and Depths
of Modulation.

III. ANALYSIS OF THE DRIFT SPACE

The electron beam enters the drift space with both velocity modulation and density modulation, and it drifts in a field-free space. This drift action produces further bunching of electrons, thereby increasing the harmonic content of the beam current. In his analysis, Webster neglects the density modulation produced in the gap, since his analysis deals with small signals. It was shown in the previous chapter that the density modulation in the first gap was considerable for large signals. The present analysis will consider the density modulation in the gap. It will include only first-order terms and will not consider space-charge debunching. Although the present analysis is not valid after crossover, it will be extended beyond crossover; for qualitatively, it anticipates important trends.

The time at plane c (see Figure 1) can be expressed as

$$\omega t_c = \omega t_b + \frac{\omega l}{v_b} . \quad (3.1)$$

Shifting the reference of time,

$$\omega t_b' = \omega t_b - \frac{\theta}{2} . \quad (3.2)$$

Dropping the prime, and neglecting the second-harmonic term in Equation (2.17), one obtains from Equation (3.1),

$$\omega t_c - \phi = \omega t_b - X \sin \omega t_b , \quad (3.3)$$

where

$$\phi \equiv \theta_0 (1 - \Delta) + \frac{\theta g}{2} , \quad (3.4a)$$

$$\theta_0 \equiv \frac{\omega_1}{v_0} , \quad (3.4b)$$

$$X \equiv \frac{1}{2} \mu a \theta_0 . \quad (3.4c)$$

Equation (3.3) shows the functional relationship between the entrance and exit times of the drift space.

A. DENSITY

The principle of conservation of charge for the drift space states that

$$i_b d\omega t_b = i_c d\omega t_c . \quad (3.5)$$

One can express the current at plane c as a Fourier series given by

$$i_c = A_0 + \sum_{n=1}^{\infty} A_n \cos n(\omega t_c - \phi) + B_n \sin n(\omega t_c - \phi) , \quad (3.6)$$

where

$$A_0 = I_0 , \quad (3.7a)$$

$$A_n = \frac{1}{\pi} \int_0^{2\pi} i_c \cos n(\omega t_c - \phi) d\omega t_c , \quad (3.7b)$$

$$B_n = \frac{1}{\pi} \int_0^{2\pi} i_c \sin n(\omega t_c - \phi) d\omega t_c . \quad (3.7c)$$

If one uses Equations (2.20), (3.2), (3.3) and (3.5), then Equations (3.7b and c) become

$$A_n = \frac{I_o}{\pi} \int_0^{2\pi} \left[1 + N \sin \left(\omega t_b + \psi + \frac{\theta g}{2} \right) \right] \cos n [\omega t_b - X \sin \omega t_b] d\omega t_b , \quad (3.8a)$$

$$B_n = \frac{I_o}{\pi} \int_0^{2\pi} \left[1 + N \sin \left(\omega t_b + \psi + \frac{\theta g}{2} \right) \right] \sin n [\omega t_b - X \sin \omega t_b] d\omega t_b . \quad (3.8b)$$

Using Bessel function expressions⁴ for trigonometric functions, integrating, and using recursion formulas for Bessel functions, one obtains

$$\begin{aligned} \frac{i_c}{I_o} = & 1 + 2 \left[1 + \frac{N}{X} \sin \left(\psi + \frac{\theta g}{2} \right) \right] \sum_{n=1}^{\infty} J_n(nX) \cos n (\omega t_c - \phi) , \\ & + 2N \cos \left(\psi + \frac{\theta g}{2} \right) \sum_{n=1}^{\infty} \frac{J'_n(nX)}{n} \sin n (\omega t_c - \phi) . \end{aligned} \quad (3.9)$$

It can be seen from Equation (3.9) that the beam current at plane c is rich in harmonics and that each harmonic can be calculated for any specified condition from the equation. Equation (3.9) reduces to that of Webster for small signals. It should also be noted that an additional phase angle, β_n , is introduced by the two independent components of each harmonic, given by

$$\tan^{-1} \beta_n = \frac{N \cos \left(\psi + \frac{\theta g}{2} \right) n J_n(nX)}{\left[1 + \frac{N}{X} \sin \left(\psi + \frac{\theta g}{2} \right) \right] J'_n(nX)} \quad (3.10)$$

Figures 10a, 11a, and 12a show the first three harmonics and Figures 10b, 11b, and 12b show the phase angles of these harmonics as a function of the bunching parameter (X), with the depth of modulation as a parameter, for $\theta_g = \pi$. The maximum amplitudes of the fundamental current for different depths of modulation (see Figure 10a) are seen to be greater than the usual value of 1.16, which was also predicted in a ballistic analysis by Webber⁵ that included space-charge effects.

The first three harmonics are also plotted in Figure 13 as functions of the drift angle θ_o for $\theta_g = \pi$. Qualitatively Figure 13a resembles the experimental curves of Mihran; he observes a saturation of the maxima of the fundamental current, although he did not explain the reason for this.

Although space-charge effects were neglected in this study, the results obtained parallel those of others within the range of validity. A comparison with Solymar's⁶ results is shown in Figure 14, where it was assumed that

$$\beta_p Z = \frac{\theta_o}{k} . \quad (3.11)$$

B. VELOCITY

The transit time through the drift space can be assumed to be

$$\omega t_b - (\omega t_c - \phi) = \sum_{l=1}^{\infty} b_l \sin l (\omega t_c - \phi) , \quad (3.12)$$

where

$$b_l = \frac{1}{\pi} \int_{-\pi}^{\pi} [\omega t_b - (\omega t_c - \phi)] \sin l (\omega t_c - \phi) d(\omega t_c - \phi) . \quad (3.13)$$

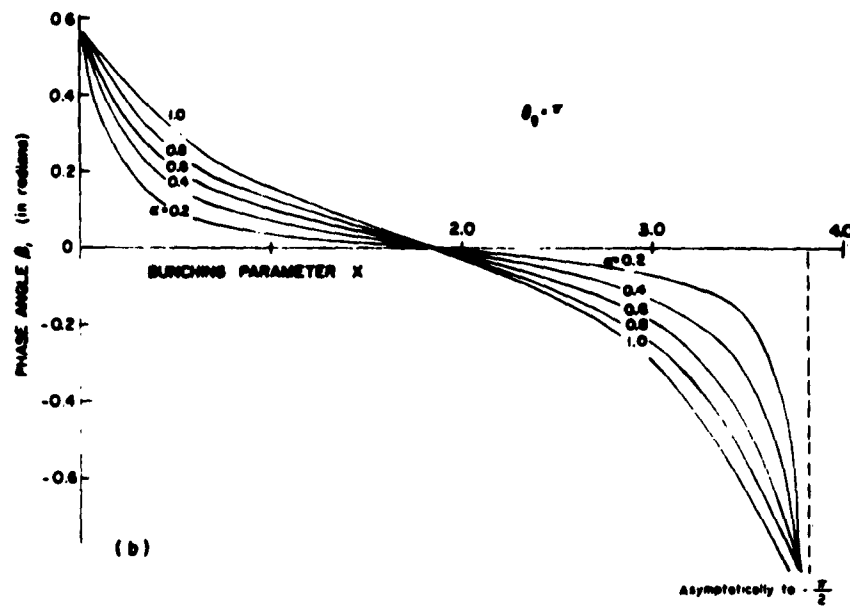
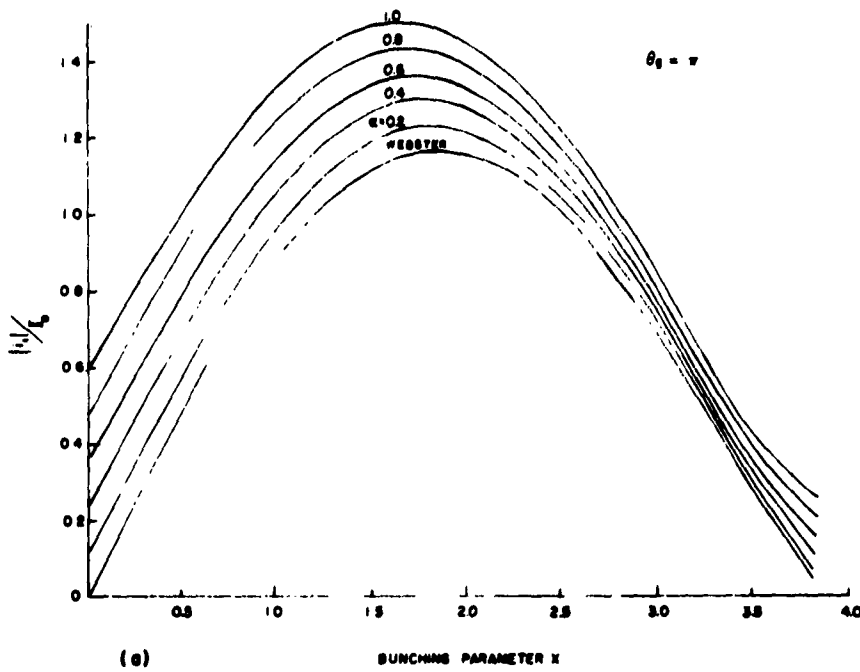


Figure 10. (a) Absolute Value of Normalized Fundamental Current $|i_1|/I_0$ versus Bunching Parameter X , (b) Phase Angle, β , versus Bunching Parameter X .

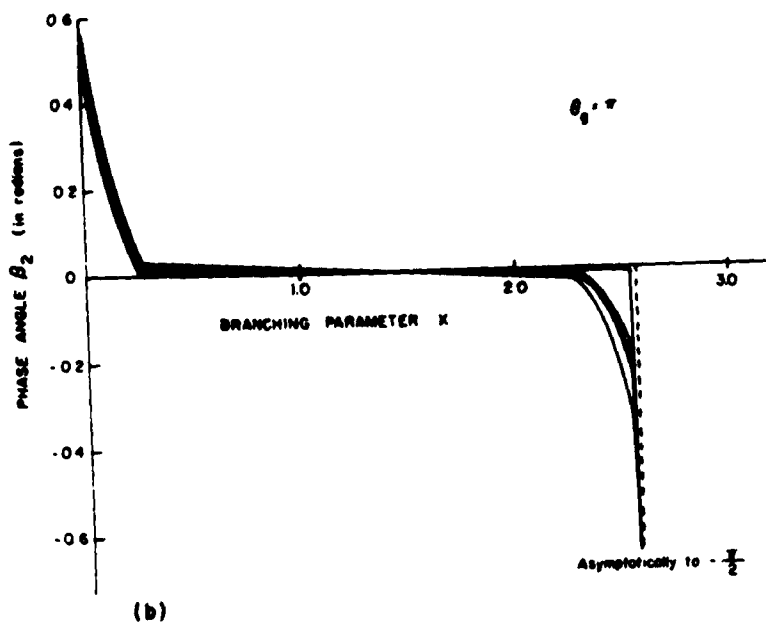
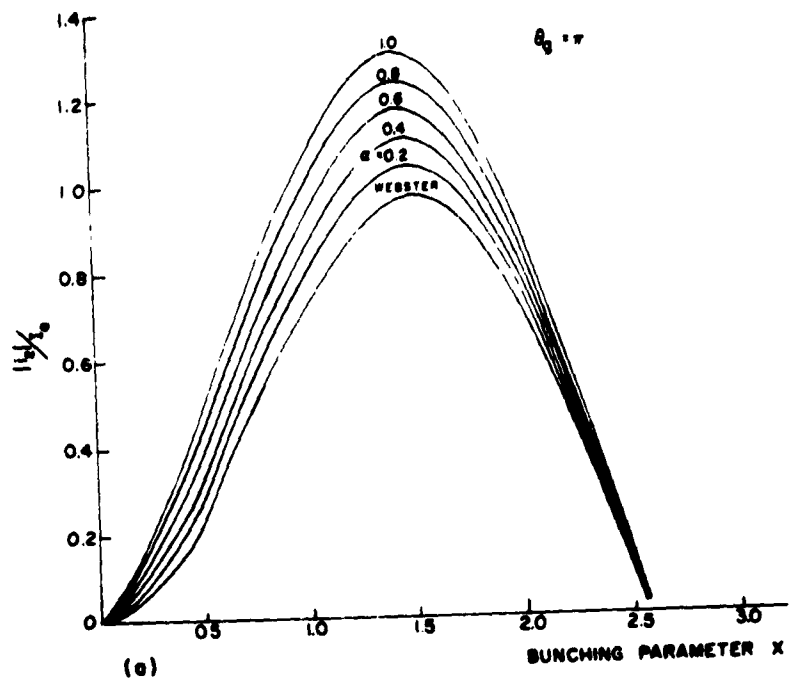


Figure 11. (a) Absolute Value of Normalized Second-Harmonic Current $|i_2|/I_0$ versus Bunching Parameter X , (b) Phase Angle β_2 versus Bunching Parameter X , in Drift Space.

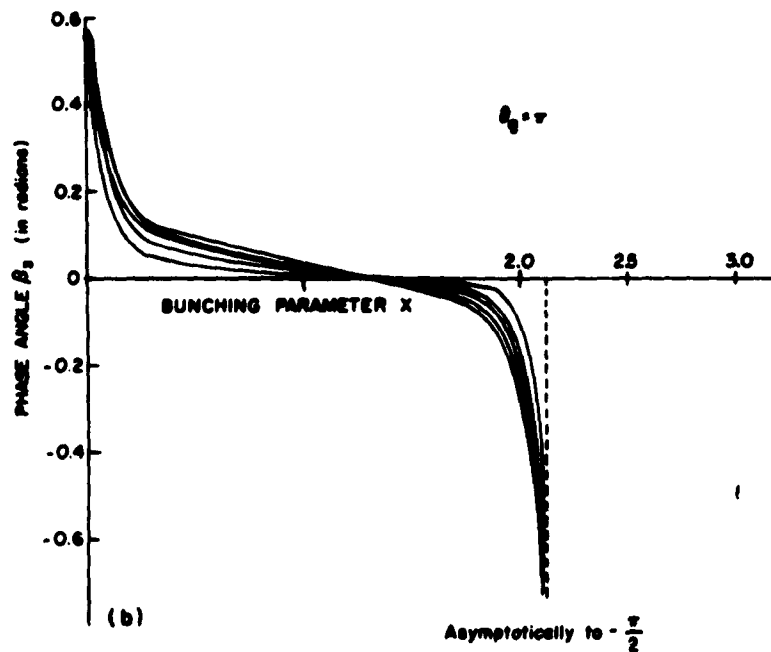
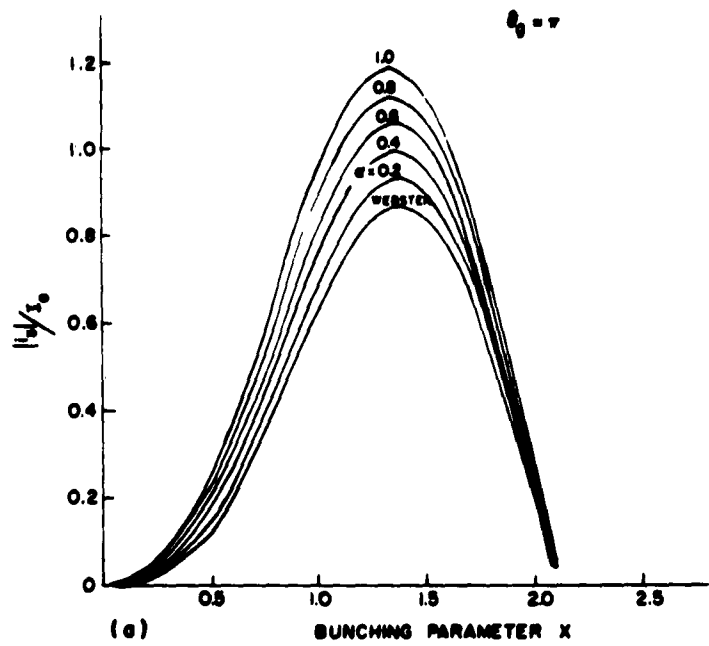


Figure 12. (a) Absolute Value of Normalized Third-Harmonic Current $|i_3|/I_0$ versus Bunching Parameter X , (b) Phase Angle β_3 versus Bunching Parameter X in the Drift Space.

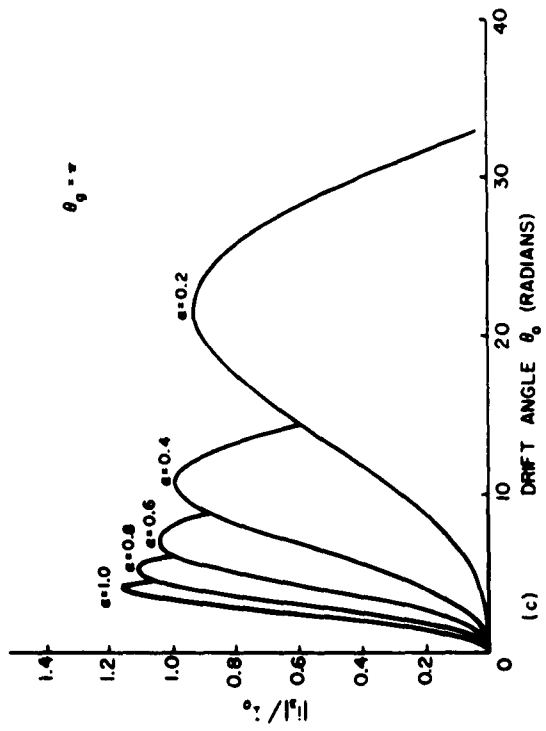
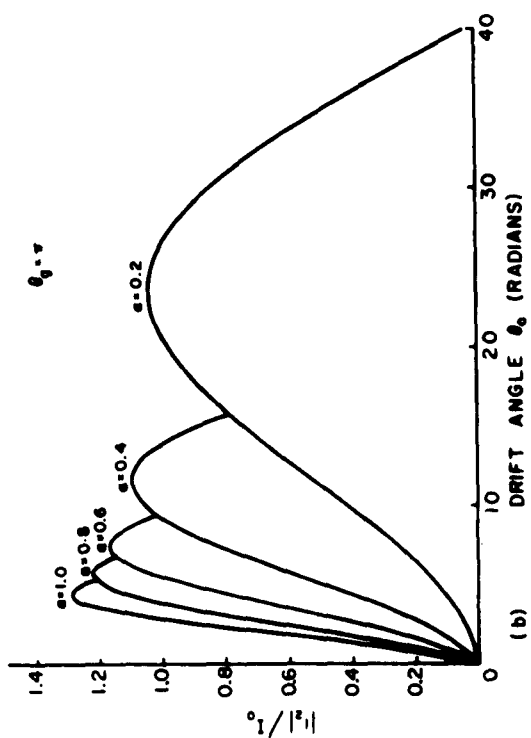
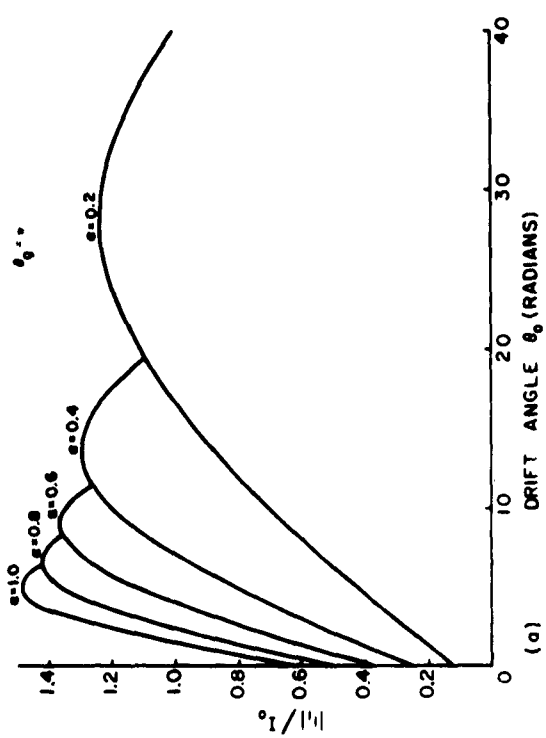


Figure 13. Absolute Value of Normalized Components of Current versus Drift Angle for Different Depths of Modulation.

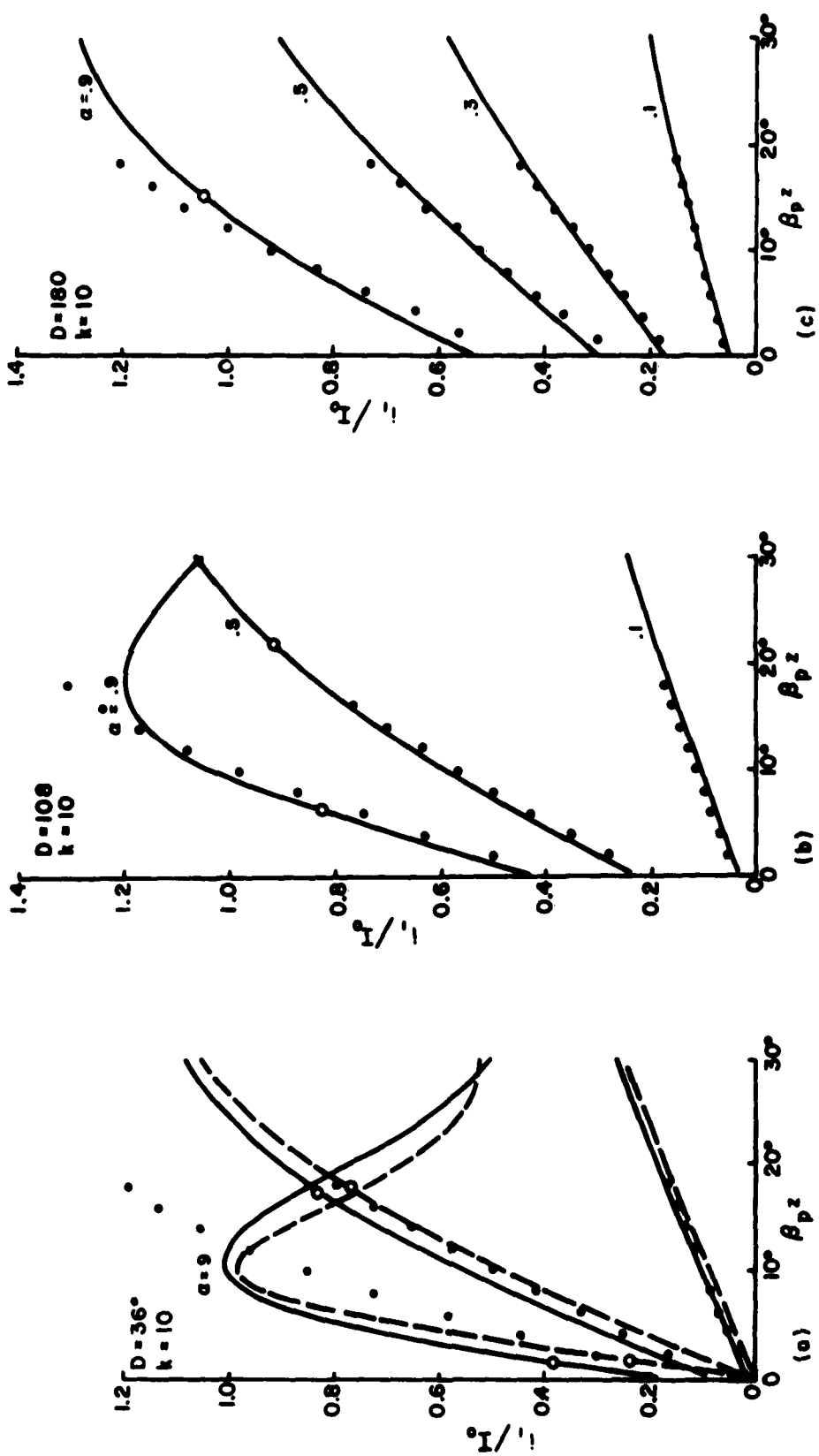


Figure 14. Normalized Fundamental Current i_1/I_0 versus Normalized Drift Distance $\beta_p z$ for Different D-C Gap Transit Angles. (The curves shown are those calculated by Solymar. The solid dots are the points calculated from Equation (3.9) of this study.)

Integrating Equation (3.13) by parts and substituting Equation (3.3), one obtains

$$\omega t_b = \omega t_c - \phi + \sum_{l=1}^{\infty} \frac{2}{l} J_l(1X) \sin l(\omega t_c - \phi) . \quad (3.14)$$

Equation (3.14) shows the functional relationship between the entrance time and the exit time of the drift space. Figure 15 shows a comparison of Equation (3.3) and (3.14), where only the first three harmonics are included in Equation (3.14).

Since the drift space is assumed to be field-free, the equation of motion becomes

$$\ddot{z} = 0 . \quad (3.15)$$

Integrating Equation (3.15) and applying the boundary conditions at $t = t_b$, substituting Equation (2.17) with second harmonic terms neglected and Equations (3.2) and (3.14), one obtains

$$\frac{v_c}{v_o} = 1 + \Delta + \frac{1}{2} \mu a \sin \left[(\omega t_c - \phi) + \sum_{l=1}^{\infty} \frac{2 J_l(1X)}{l} \sin l(\omega t_c - \phi) \right] . \quad (3.16)$$

Equation (3.16) is plotted in Figure 16 with depth of modulation as a parameter for $\theta_g = \pi$ and $\theta_o = \pi/2$.

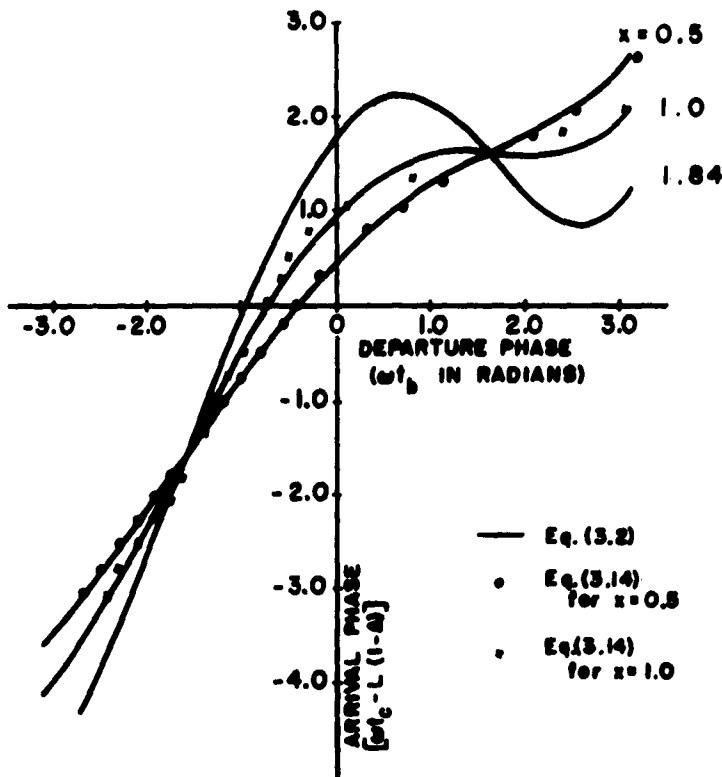


Figure 15. Arrival Phase, $\omega t_c - L(1 - \Delta)$, versus Departure Phase ωt_b for the Drift Space for Different Bunching Parameters.

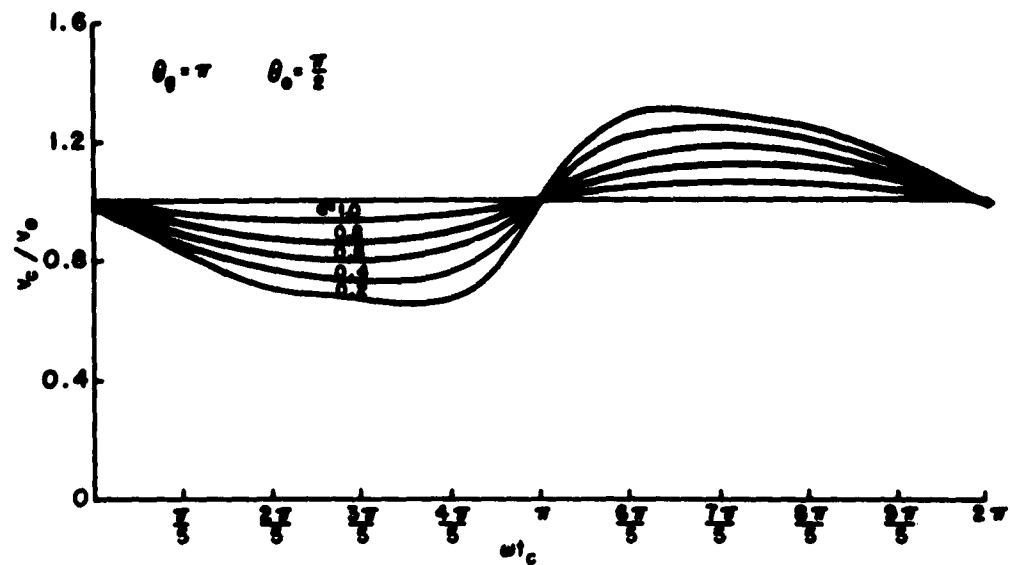


Figure 16. Normalized Exit Velocity v_c/v_o versus Exit Time ωt_c at End of Drift Space for Different Depths of Modulation.

CONCLUSIONS AND RECOMMENDATIONS

Although this study was based on a very simple model, many interesting and important results were obtained that may serve as guides for future investigations.

Exact graphic analysis reveals the physical relationship in the first gap and in the drift space, but it is tedious and time consuming and does not give the functional relationships among various parameters. Approximating the graphic method analytically, on the other hand, is demonstrated to be valid; the second-order method both approximates the large-signal cases well and also gives analytical formulas which reveal information about the harmonics.

The conclusions from this ballistic analysis can be grouped under the first gap and the drift space.

A. FIRST GAP

1. Both velocity and current modulations are produced during the passage of the beam through the gap, and the transit time plays an important role in these phenomena.
2. The velocity modulation is proportional to the depth of modulation, but is inversely proportional to the d-c gap transit angle.
3. The difference between the minimum velocity and the d-c velocity is greater than the corresponding difference between the maximum velocity and the d-c velocity.
4. The current modulation, on the other hand, is also proportional to the depth of modulation; but, first it increases and then it decreases as

the d-c gap transit angle is increased continuously.

5. Both velocity and current expressions contain harmonics at the exit of the first gap, but this effect is more pronounced in the current expression.

B. DRIFT SPACE

1. In a field-free space, density modulation is produced in a velocity-modulated beam through drift action. The beam current develops harmonics, and the amplitudes of harmonics are proportional to the depth of modulation.

2. The maximum value of the fundamental current is seen to be greater than the value of 1.16 predicted by Webster.⁵ The point in the drift space at which the maximum value of a harmonic occurs is inversely proportional to the depth of modulation. These results have been shown, at least qualitatively, in the work of others.

3. An additional phase angle β_n is introduced into the current by the two independent components of each harmonic.

4. The velocity becomes more nonlinear at the end of the drift space; the extreme values do not change considerably.

C. RECOMMENDATION

This report has dealt with the simplest case. Investigation of the second gap and inclusion of the effects of space charge and of gridless gaps for finite beams would be a logical continuation of this study.

REFERENCES

1. D. L. Webster, "Cathode Ray Bunching," Jour. Appl. Phys., 10 (July 1939), pp. 501-508.
2. T. G. Mihran, "The Effect of Space Charge on Bunching in a Two-Cavity Klystron," I. R. E. Trans., Ed-6 (January 1959).
3. G. C. Dalman, unpublished work.
4. H. B. Dwight, Tables of Integrals and Other Mathematical Data, New York: MacMillan (1953), pp. 174-191.
5. S. E. Webber, "Ballistic Analysis of a Two-Cavity Finite Beam Klystron," I. R. E. Trans., Ed-5 (April 1958), pp. 98-108.
6. L. Solymar, "Exact Solutions of the One-Dimensional Bunching Problem," Jour. Elect. Control, 10 (March 1961).

LARGE-SIGNAL THEORY OF GRIDDED KLYSTRON GAP

W. M. Sackinger

School of Electrical Engineering
CORNELL UNIVERSITY
Ithaca, New York

RESEARCH REPORT EE 483

LARGE-SIGNAL THEORY OF GRIDDED KLYSTRON GAP

W. M. Sackinger

LINEAR BEAM MICROWAVE TUBES

Technical Report No. 8

15 November 1961

Published under Contract No. AF30(602)-1696
Rome Air Development Center, Griffiss Air Force Base, New York

ACKNOWLEDGMENTS

It is a pleasure to thank Professor P. R. McIsaac for stimulating discussions and guidance during the course of this research, Professor G. C. Dalman for suggesting the topic, Visiting Professor S. Olving for pointing out the generality of these results, Professor H. S. Sack for guidance in choosing a course of study, and Professor Walter Johnson of the University of Notre Dame for providing the background upon which this thesis is based.

Grateful thanks are due to Mrs. Ruth Jones, the staff of Research Publications of the School of Electrical Engineering, and everyone else who assisted in preparing this for publication. This research was conducted under the Air Force Contract No. AF30(602)-1696, without whose support it would have been impossible.

Finally, I wish to thank Patricia Sackinger for her continued patience and encouragement.

CONTENTS

| | Page |
|--|------|
| ABSTRACT | |
| I. INTRODUCTION | 1 |
| II. LARGE SIGNAL BALLISTIC THEORY OF GRIDDED GAPS WITH ARBITRARY INPUT VELOCITY | 4 |
| A. SYMBOLS USED IN THIS SECTION | 4 |
| B. THE ANALYTICAL PROBLEM | 6 |
| C. MATHEMATICAL SOLUTION OF THE TRAJECTORY | 7 |
| D. REDUCTION TO SMALL SIGNALS | 17 |
| E. EXIT CURRENT AND KINETIC POWER | 19 |
| III. DISCUSSION | |
| A. VARIATION OF ENTRANCE TIME | 24 |
| B. EXPRESSING FUNCTIONS IN TERMS OF EXIT TIME | 26 |
| C. MEANING OF A VARIATION IN ENTRANCE VELOCITY | 32 |
| IV. APPLICATION TO X-RAY SUPPRESSION | |
| A. INFORMATION REQUIRED FOR X-RAY SUPPRESSION | 35 |
| B. LARGE SIGNAL SPACE-CHARGE WAVE THEORY IN DRIFT REGION | 36 |
| C. LARGE-SIGNAL BALLISTIC THEORY IN THE OUT- PUT GAP REGION | 41 |
| D. CALCULATION PROCEDURE | 43 |
| E. RESULTS | 32 |
| V. CONCLUSIONS AND RECOMMENDATIONS | 61 |

| | Page |
|--|-------------|
| APPENDIX | |
| A. DERIVATION OF POWER SERIES INVERSION | 63 |
| B. CONVERGENCE OF POWER SERIES INVERSION | 65 |
| REFERENCES | 69 |

ABSTRACT

A general theoretical expression is derived for an electron trajectory in an oscillating electric field. The limits upon the validity of the analysis are found, and application is made to the ballistic theory of gridded klystron gaps. In the case of the input gap, exact results for exit current and exit velocity are obtained for large signals, the only restriction being that the normalized modulation voltage magnitude be less than the normalized gap length. Large-signal analytical expressions for exit current and exit velocity are obtained for an output gap, and results of numerical calculations are presented graphically for several arbitrary cases. It appears from these results that an r-f structure placed beyond the output gap could be used to reduce the velocities of high-velocity electrons in the beam, and help reduce production of X-rays at the collector.

I. INTRODUCTION

With the invention of the klystron by the Varian brothers in 1939 came the first theoretical analysis of the device by Webster.¹ His analysis used ballistic theory, but he limited his treatment with a restriction to small input signals. Many papers have recently been written about klystron operation, but theoretical analyses have been almost invariably limited by this same assumption. The space-charge wave theory, proposed by Hahn² and also Ramo,³ was also limited by the small-signal assumptions, but since it included the effects of space charge in the drift region, it was presumably more accurate and has recently enjoyed much popularity.

Both of these approaches dealt primarily with the behavior of the beam in the drift region, and relatively little was said about the behavior of the beam in the two gap regions. Usually, the gap was assumed to be gridded, with a very short length, and it was assumed that no power was added to the beam by the input gap. The input gap was supposed to produce pure velocity modulation with no current modulation, and these conditions were used as boundary conditions on the treatments of the drift space. Early treatments of the input gap region were similar to the method given here, in that they considered the electron passing through a time-varying electric field that was constant in the Z direction, the direction of beam flow. The velocity was calculated at the end of this gridded gap. The more recent approach has been to use kinetic energy, and assume that the gap is so short that the difference between entrance and exit time is negligible. Thus the electric field would be essentially a constant in time for each electron. If the gap angle $\phi_0 = \omega d / \dot{Z}_0$ is not

small, this procedure is incorrect, because the kinetic energy is based upon a time integral of Newton's second law where the force is not a function of time. This will be illustrated more clearly in the exact ballistic treatment in Section II.

Modern klystron designers are responding to the demand for higher and higher power outputs, and several theoretical analyses have treated this problem, for in high power operation, the small-signal assumptions of previous theories are invalid. Perhaps the most fruitful approach, although a tedious one, is that of Paschke.^{4,5,6} Paschke writes the general nonlinear space-charge wave equation for the drift space, and solves it by successive approximation; that is, he solves for a linear solution similar to that given by Hahn² and Ramo³ and substitutes this into the nonlinear equation to get a second-order solution. This process is repeated to get a third-order solution. His results have been verified by experimental work of Mihran.^{7,8} Paschke, however, uses the traditional small-signal assumption at the input gap, where he applies the boundary condition of pure velocity modulation to his drift-space analysis.

A clear exposition of the problem faced in ballistic gap theory is given by Beck.⁹ Beck extends the analysis of the gridded gap to the case of a gap length ϕ_0 which is nonzero, but small. His first approximation involves the assumption that the transit angle of the electron going across the gap is the d-c transit angle ϕ_0 , and subsequently he allows the actual transit angle to deviate from this by a small amount δ . By several approximations, a fairly simple expression for δ is derived. This expression is useful, but no limits upon its validity have been established, and whether it is valid for extremely large signals is not known. A

similar approach to this problem has been given by Blair,¹⁰ except that Blair extends these approximation methods to higher orders. The simplest large-signal gap theory has undoubtedly been that presented by Warnecke and Guénard.¹¹ Their graphic methods are applicable to very large signals and give rather rapid results. There seems to be no limit to the applicability of graphic techniques, but they have the disadvantage of only moderate accuracy and must be repeated for every choice of parameters. The problem has been very well formulated by Warnecke and Guénard, however, and has been clearly restated by Kleen.¹² The methods they give are definitely the best available to date for the extremely large signal treatment of the gap region.

All of the methods of analysis mentioned above with the exception of the graphic method share the same problem of small-signal limitation. It would be useful to obtain an analytic expression that is valid for large signal levels. Almost as important as obtaining the expression is finding the limit upon its validity; this requirement has been almost universally neglected.

Such an analytic expression, when found, could be used to establish rigorous boundary conditions on the large-signal treatments of the drift region. Furthermore, the gap theory coupled with the drift-space theory can give a fairly complete theoretical description of the operation of modern, high-power klystrons. This would include answers to such problems as (1) analyzing the beam current for harmonic content that may produce spurious outputs and (2) finding the velocity and current distribution of the electrons in the beam after passing through the output gap to give information about the production of dangerous high-intensity

X-rays at the collector. In this treatment, application of the theory is made to the second problem. Finally, it would be possible ultimately to apply the theory for the 2-cavity klystron to the multicavity klystron, which is becoming so useful in high-power applications.

II. LARGE SIGNAL BALLISTIC THEORY OF GRIDDED GAPS WITH ARBITRARY INPUT VELOCITY

A. SYMBOLS USED IN THIS SECTION

$$a = \frac{\text{magnitude of applied voltage}}{\text{d-c beam voltage}} = \frac{V}{V_0}$$

Δ = small increment of any quantity following.

ϵ = eccentricity, defined in Equations (13), (32).

ζ = mean anomaly, defined in Equations (14), (33).

θ = phase of applied voltage relative to time $t = 0$.

ν = summation index, equal to 0, 1, 2, 3, 4 . . .

ρ_a = total charge density at entrance plane a.

ρ_b = total charge density at exit plane b.

ϕ_0 = normalized length of the gap, equal to $\frac{\omega d}{Z_0}$.

ω = angular frequency of applied voltage.

A = unit cross-sectional area of a beam.

b_l = coefficient in Fourier series expansion.

d = length of the gridded gap.

e = electronic charge.

E = electric field in the gridded gap.

g = normalized time-varying part of the entrance velocity, defined in Equation (30).

I_a = total conduction current at entrance plane a.

I_b = total conduction current at exit plane b.
 I_o = d-c beam current before any gap modulation.
 I_z = total conduction current at any arbitrary plane Z within the gap.
 J_a = total conduction current density at entrance plane a.
 J_z = total conduction current density at any arbitrary plane Z within the gap.
 J_l = Bessel function of the first kind of the l^{th} order.
 J_v = Bessel function of the first kind of the v^{th} order.
 l = summation index, equal to 1, 2, 3, 4, . . .
 m = electronic mass.
 m = arbitrary term index in the series, Equation (41) only.
 n = number of particles per unit volume at an arbitrary plane Z in the gap.
 n_a = number of particles per unit volume at the entrance plane a of the gap.
 q_a = total charge at plane a.
 q_b = total charge at plane b.
 t = time that an electron arrives at an arbitrary plane Z within the gap.
 t_a = time that an electron passes entrance plane a.
 t_b = time that an electron passes exit plane b.
 u = eccentric anomaly, defined in Equation (12).
 V = magnitude of applied voltage.
 V_o = magnitude of d-c beam voltage.
 $v(t)$ = total velocity of an electron at arbitrary time t within the gridded gap.
 $v(t_a)$ = total velocity of an electron at entrance plane a, at time t_a .
 $v_{\text{out}}(t_a)$ = total velocity of an electron at exit plane b.
 Z = arbitrary position co-ordinate of an electron within the gap.

\dot{Z} = total velocity of an electron at an arbitrary plane within the gap. Dot indicates time derivative.

\dot{Z}_0 = d-c beam velocity, defined in Equation (29).

\ddot{Z} = acceleration of an electron at an arbitrary plane in the gap.

B. THE ANALYTICAL PROBLEM

The ballistic theory developed for electron beams neglects any forces on an electron resulting from the presence of other electrons. Furthermore it usually assumes that all quantities vary in the Z direction only; i. e., in the direction of beam flow. We are adopting these assumptions. This is tantamount to assuming that the time-varying part of the space-charge density function is negligibly small and that we are considering only confined flow. That is, the electrons are constrained to move in the Z direction only, as if the beam were of infinite cross section and immersed in an infinitely strong magnetic focusing field. These assumptions will be discussed in more detail in Section IV, when we apply the theory to a specific problem.

Furthermore, we assume the region of electron flow to be gridded, and consider the electric field between these grids to be constant in Z and to be a sinusoidal function of time. The electric field is assumed to be due only to the voltage across the grids. The amplitude and phase of the gap voltage is always assumed to be known, whether supplied externally or induced by a bunched beam. This will be discussed further in Section IV.

As has been pointed out by Kleen¹² and others,^{10,11} the successive integration of Newton's law to get velocity and displacement involves no special difficulty. The difficulty arises in carrying through the method

of quadratures, which requires the inversion of the distance as a function of time to get the time as a function of distance. This is then substituted into the velocity function of time to yield finally the velocity as a function of distance, i. e., the path of the particle. This reduction of the problem to quadratures is of frequent use in classical mechanics, but can be applied successfully elsewhere whenever the inversion can be carried out.

In this case, the inversion process requires the solution of a transcendental equation, and all previous theories using this approach approximated the inversion of the transcendental equation in various ways. Because of its very special form, however, this equation can be readily inverted so that a complete, exact solution can be obtained.

C. MATHEMATICAL SOLUTION OF THE TRAJECTORY

Following our previous treatment,¹³ we consider a single electron incident from the left into the gridded gap as shown in Figure 1.

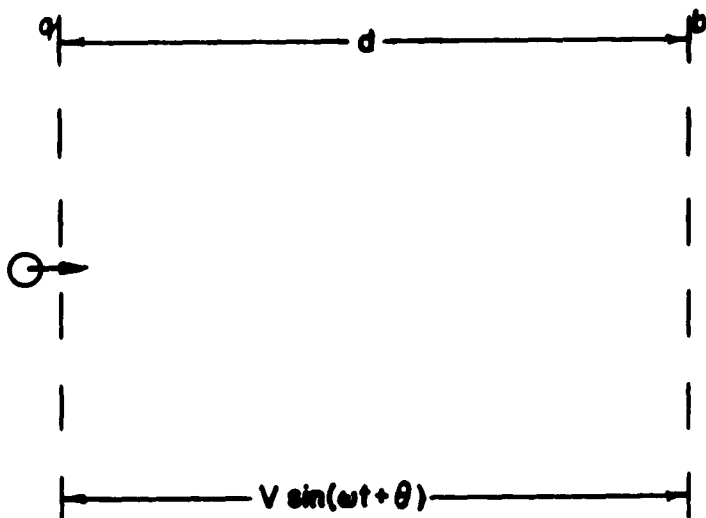


Figure 1. Diagram of Ideal Gridded Gap.

For a field distribution in the Z direction of

$$E = \frac{V}{d} \sin(\omega t + \theta) , \quad (1)$$

we have, for Newton's second law,

$$m\ddot{Z} = \frac{eV}{d} \sin(\omega t + \theta) , \quad (2)$$

or

$$\ddot{Z} = \frac{eV}{md} \sin(\omega t + \theta) . \quad (3)$$

This second-order differential equation, together with its boundary conditions, completely describes the path of the particle in the gap. The voltage is allowed to have any magnitude V and any arbitrary phase θ with respect to the time $t = 0$.

Integrating once gives us the velocity equation:

$$\int_{v(t_a)}^{v(t)} d\dot{Z} = \int_{t_a}^t \frac{eV}{md} \sin(\omega t + \theta) dt , \quad (4)$$

$$v(t) = v(t_a) - \frac{eV}{md\omega} [\cos(\omega t + \theta) - \cos(\omega t_a + \theta)] . \quad (5)$$

In carrying out this integration, we have chosen as lower limits the initial conditions on the electron as it entered the gap, and as upper limits any arbitrary time, with its corresponding velocity, that the electron is in the gap. For the input gap of a klystron, the initial velocity $v(t_a)$ would be merely the d-c velocity \dot{Z}_0 . For the moment, however, we wish to keep the theory as general as possible, and later specialize it in its applications.

Integrating Equation (5) again gives us the distance equation:

$$\int_0^{Z(t)} dZ = \int_{t_a}^t \left\{ v(t_a) - \frac{eV}{md\omega} [\cos(\omega t + \theta) - \cos(\omega t_a + \theta)] \right\} dt , \quad (6)$$

$$Z(t) = \left[v(t_a) + \frac{eV}{md\omega} \cos(\omega t_a + \theta) \right] (t - t_a) - \frac{eV}{md\omega^2} [\sin(\omega t + \theta) - \sin(\omega t_a + \theta)] . \quad (7)$$

In this integration we have chosen the entrance time t_a and the entrance position $Z(t_a) = 0$ as lower limits with arbitrary upper limits. In this notation, $Z(t_a)$ means the position at a particular entrance time t_a for the particular electron.

Knowing the position and velocity as a function of time for this electron, we can now invert the distance relation, substitute into the velocity relation, and find the velocity as a function of distance. Rearranging Equation (7), we have

$$Z(t) + \left[v(t_a) + \frac{eV}{md\omega} \cos(\omega t_a + \theta) \right] t_a - \frac{eV}{md\omega^2} \sin(\omega t_a + \theta) = \left[v(t_a) + \frac{eV}{md\omega} \cos(\omega t_a + \theta) \right] t - \frac{eV}{md\omega^2} \sin(\omega t + \theta) . \quad (8)$$

Assuming that

$$v(t_a) + \frac{eV}{md\omega} \cos(\omega t_a + \theta) > 0 , \quad (9)$$

we divide both sides of Equation (8) by this quantity. We investigate this

assumption later. We then have

$$\begin{aligned}
 t_a + \frac{Z(t)}{\left[v(t_a) + \frac{eV}{md\omega} \cos(\omega t_a + \theta) \right]} - \frac{eV \sin(\omega t_a + \theta)}{md\omega^2 \left[v(t_a) + \frac{eV}{md\omega} \cos(\omega t_a + \theta) \right]} \\
 = t - \frac{\frac{eV}{md\omega^2} \left[v(t_a) + \frac{eV}{md\omega} \cos(\omega t_a + \theta) \right]}{\left[v(t_a) + \frac{eV}{md\omega} \cos(\omega t_a + \theta) \right]} \sin(\omega t + \theta) . \quad (10)
 \end{aligned}$$

Before this equation is amenable to inversion, we must perform some algebraic manipulation. Multiply both sides of the equation by ω , and add θ to both sides. Since we now are used to the convention of writing the distance Z at some arbitrary time t as $Z(t)$, we drop the t and merely call it Z , although retaining exactly the same meaning. Equation (10) then becomes

$$\begin{aligned}
 (\omega t_a + \theta) + \frac{\omega Z}{\left[v(t_a) + \frac{eV}{md\omega} \cos(\omega t_a + \theta) \right]} - \frac{eV \sin(\omega t_a + \theta)}{md\omega \left[v(t_a) + \frac{eV}{md\omega} \cos(\omega t_a + \theta) \right]} \\
 = (\omega t + \theta) - \frac{\frac{eV}{md\omega} \left[v(t_a) + \frac{eV}{md\omega} \cos(\omega t_a + \theta) \right]}{\left[v(t_a) + \frac{eV}{md\omega} \cos(\omega t_a + \theta) \right]} \sin(\omega t + \theta) . \quad (11)
 \end{aligned}$$

Define the following symbols:

$$u = (\omega t + \theta) , \quad (12)$$

$$\epsilon = \frac{eV}{md\omega \left[v(t_a) + \frac{eV}{md\omega} \cos(\omega t_a + \theta) \right]} \quad (13)$$

$$\begin{aligned}
 \zeta = & (\omega t_a + \theta) + \frac{\omega Z}{\left[v(t_a) + \frac{eV}{md\omega} \cos(\omega t_a + \theta) \right]} \\
 & - \frac{eV \sin(\omega t_a + \theta)}{md\omega \left[v(t_a) + \frac{eV}{md\omega} \cos(\omega t_a + \theta) \right]} . \quad (14)
 \end{aligned}$$

Then, Equation (11) may be written in the compact form

$$\zeta = u - \epsilon \sin u . \quad (15)$$

In this equation, the only term containing t is u , and the only term containing Z is ζ . Thus, if we can solve this transcendental equation for u in terms of ζ and ϵ , we will have, by a short algebraic step, the quantity t as a function of Z and the various initial conditions.

Several methods of approximation¹⁰⁻¹² have been used to invert Equation (15). Here we shall develop an exact inversion. Equation (15) is Kepler's equation from celestial mechanics. It occurs often in the classical astronomical literature. Its inversion is usually attributed to Bessel, but was originally developed by Lagrange.¹⁴ The classical treatise on the subject of celestial mechanics is that of Tisserand,¹⁵ who treats this equation in considerable detail. A more popular alternate derivation is given by Whittaker,¹⁶ but we derive the identical result in a manner slightly different from the classical authors.

From inspection, one can see that the quantity $u - \zeta$ is a periodic function of ζ with period 2π . Expanding in a Fourier series gives

$$u - \zeta = \sum_{l=1}^{\infty} b_l \sin l \zeta , \quad (16)$$

where

$$b_l = \frac{1}{\pi} \int_{-\pi}^{\pi} (u - \zeta) \sin l \zeta \, d\zeta \quad . \quad (17)$$

Integrating by parts gives

$$b_l = \frac{1}{\pi} \left[-\frac{\cos l \zeta}{l} (u - \zeta) \right]_{-\pi}^{\pi} + \frac{1}{\pi l} \int_{-\pi}^{\pi} \cos l \zeta \, d(u - \zeta) \quad , \quad (18)$$

but the first term drops out when evaluated, so we have

$$b_l = \frac{1}{l\pi} \int_{-\pi}^{\pi} \cos l \zeta \, du - \frac{1}{l\pi} \int_{-\pi}^{\pi} \cos l \zeta \, d\zeta \quad . \quad (19)$$

The last term in Equation (19) drops out also, so that in the final form

$$b_l = \frac{1}{l\pi} \int_{-\pi}^{\pi} \cos l \zeta \, du \quad , \quad (20)$$

or

$$b_l = \frac{1}{l\pi} \int_{-\pi}^{\pi} \cos [u - \epsilon \sin u] \, du \quad . \quad (21)$$

Now, recall that the Bessel function of the first kind is defined by

$$J_n(x) = \frac{1}{2\pi} \int_{-\pi}^{\pi} \cos (n\theta - x \sin \theta) \, d\theta \quad , \quad (22)$$

so that in this case

$$b_l = \frac{2}{l} J_l(l\epsilon) \quad , \quad (23)$$

and the inversion series is

$$u = \zeta + \sum_{l=1}^{\infty} \frac{2}{l} J_l(l\epsilon) \sin l\zeta \quad . \quad (24)$$

From the definition of u in Equation (12), we have the final result for the inversion:

$$t = \frac{1}{\omega} \left[-\theta + \zeta + \sum_{l=1}^{\infty} \frac{2}{l} J_l(l\epsilon) \sin l\zeta \right] \quad . \quad (25)$$

Note that Equation (24) can be substituted directly into the velocity Equation (5) to give the velocity as a function of distance:

$$v(z) = v(t_a) - \frac{eV}{md\omega} \left\{ \cos \left[\zeta + \sum_{l=1}^{\infty} \frac{2}{l} J_l(l\epsilon) \sin l\zeta \right] - \cos(\omega t_a + \theta) \right\} \quad . \quad (26)$$

In order to investigate assumption (9), we shall define ζ and ϵ in a more conventional way. Let

$$a = \frac{\text{signal voltage magnitude}}{\text{beam voltage magnitude}} = \frac{V}{V_o} \quad , \quad (27)$$

$$\phi_o = \frac{\omega d}{Z_o} = \text{d-c transit angle} \quad , \quad (28)$$

$$\dot{Z}_o = \sqrt{\frac{2eV_o}{m}} \quad , \quad (29)$$

$$\frac{v(t_a)}{Z_o} = 1 + g(t_a) \quad . \quad (30)$$

Thus we have the relation that

$$\frac{eV}{md\omega} = \frac{a \dot{Z}_o}{Z \phi_o} \quad . \quad (31)$$

This relation enables us to introduce convenient, normalized quantities into our relationships, in terms of easily measurable parameters. Substituting Equations (30) and (31) into definitions (13) and (14), we have

$$\epsilon = \frac{a}{2\phi_o [1 + g(t_a) + \frac{a}{2\phi_o} \cos(\omega t_a + \theta)]} \quad , \quad (32)$$

$$\zeta = \omega t_a + \theta + \frac{\omega Z}{\dot{Z}_o [1 + g(t_a) + \frac{a}{2\phi_o} \cos(\omega t_a + \theta)]} \quad .$$

$$- \frac{a \sin(\omega t_a + \theta)}{2\phi_o [1 + g(t_a) + \frac{a}{2\phi_o} \cos(\omega t_a + \theta)]} \quad . \quad (33)$$

In terms of these normalized parameters, the assumption (9) is

$$\dot{Z}_o [1 + g(t_a) + \frac{a}{2\phi_o} \cos(\omega t_a + \theta)] > 0 \quad . \quad (34)$$

Since $\dot{Z}_o > 0$, we can divide by \dot{Z}_o without changing the inequality, and

$$1 + g(t_a) + \frac{a}{2\phi_o} \cos(\omega t_a + \theta) > 0 \quad . \quad (35)$$

This is the first restriction on the validity of the analysis. Actually, we will see shortly that a more stringent requirement than this exists for convergence of the series in Equations (24)-(26), but at least this is a definite upper bound on the analysis. If inequality (35) is violated, then it would be possible to have the time t at the point Z be infinite, meaning that the electron velocity would become negative and the electron would never reach that point. When such a condition is reached in a practical device, inefficiency of operation would radically increase because of electron interaction within the gap itself. Signal levels large enough to violate Equation (35), then, are of no interest at this point.

The special case of the input gap simplifies Equation (35), for then

$$v(t_a) = \dot{Z}_0 ; \quad g(t_a) = 0 , \quad (36)$$

and Equation (35) reduces to

$$\frac{a}{Z\phi_0} < 1 . \quad (37)$$

When actually evaluating the series expressions in Equations (24)-(26), it is found that the terms have different signs - some positive, others negative. According to Tisserand¹⁵ (p. 262), the series remains convergent for ϵ between zero and one, whatever the values of ζ may be. That is, the criterion for convergence is

$$0 < \epsilon < 1 . \quad (38)$$

In the special case of the input gap, where Equation (36) holds, inequality (38) reduces to the condition,

$$a < \phi_0 . \quad (39)$$

In general, however, if relation (38) is satisfied, the convergence holds, and

$$0 < \frac{a}{2\phi_0 \left[1 + g(t_a) + \frac{a}{2\phi_0} \cos(\omega t_a + \theta) \right]} < 1 \quad . \quad (40)$$

In the astronomical literature, the quantity ϵ is called the eccentricity, and ζ is called the mean anomaly. Much work has been done in this field, some of which is directly applicable to our problem. The inversion problem, as done here, gives the series with the greatest applicability. For small values of ϵ , however, the development of u as a power series in ϵ is possible. This series has been given first by Lagrange,¹⁴ also by Laplace,¹⁷ and follows:

$$\begin{aligned} u = & \zeta + \epsilon \sin \zeta + \frac{\epsilon^2}{2} \sin 2\zeta \\ & + \frac{\epsilon^3}{3 \cdot 2 \cdot 2^2} (3^2 \sin 3\zeta - 3 \sin \zeta) \\ & + \frac{\epsilon^4}{4 \cdot 3 \cdot 2 \cdot 1 \cdot 2^3} (4^3 \sin 4\zeta - 4 \cdot 2^3 \sin 2\zeta) \\ & + \frac{\epsilon^5}{5 \cdot 4 \cdot 3 \cdot 2 \cdot 1 \cdot 2^4} (5^4 \sin 5\zeta - 5 \cdot 3^4 \sin 3\zeta + \frac{5 \cdot 4}{1 \cdot 2} \sin \zeta) \\ & + \frac{\epsilon^6}{6 \cdot 5 \cdot 4 \cdot 3 \cdot 2 \cdot 1 \cdot 2^5} (6^5 \sin 6\zeta - 6 \cdot 4^5 \sin 4\zeta + \frac{6 \cdot 5}{1 \cdot 2} 2^5 \sin 2\zeta) \\ & + \dots \\ & + \frac{\epsilon^m}{2^{m-1} m!} \left[m^{m-1} \sin m\zeta - \frac{m}{1} (m-2)^{m-1} \sin (m-2)\zeta \right] \end{aligned}$$

$$+ \frac{m(m-1)}{1 \cdot 2} (m-4)^{m-1} \sin(m-4)\zeta - \dots \Big] , \\ + \dots . \quad (41)$$

The derivation of this series, as given by Tisserand¹⁵ (pp. 262-269), is found in the Appendix.

As would be expected, this series is useful only for relatively small values of ϵ . Indeed, Laplace¹⁸ was the first to show that this series converges only if

$$\epsilon < 0.6627\dots \quad (42)$$

A simplified proof of this limit of convergence is also given in the Appendix. Since the application of this theory will undoubtedly be to large-signal cases, the expression (41) will be of limited value in computations. However, it may provide an easier adaptation to the boundary conditions on a drift region analysis, and for that reason it is included.

D. REDUCTION TO SMALL SIGNALS

The expression (25) can be easily reduced, in the limit of small a , to the small-signal expression. Writing out Equation (25) in full, gives

$$\begin{aligned} \omega t = \omega t_a + & \frac{\omega Z}{Z_0 \left[1 + g(t_a) + \frac{a}{2\phi_0} \cos(\omega t_a + \theta) \right]} \\ - & \frac{a \sin(\omega t_a + \theta)}{2\phi_0 \left[1 + g(t_a) + \frac{a}{2\phi_0} \cos(\omega t_a + \theta) \right]} \end{aligned}$$

$$\begin{aligned}
& + \sum_{l=1}^{\infty} \frac{2}{T} J_l \left\{ \frac{l \epsilon}{2\phi_0 [1 + g(t_a) + \frac{a}{2\phi_0} \cos(\omega t_a + \theta)]} \right\} \\
& \cdot \sin l \left\{ \omega t_a + \theta + \frac{\omega Z}{\dot{Z}_0 [1 + g(t_a) + \frac{a}{2\phi_0} \cos(\omega t_a + \theta)]} \right. \\
& \left. - \frac{a \sin(\omega t_a + \theta)}{2\phi_0 [1 + g(t_a) + \frac{a}{2\phi_0} \cos(\omega t_a + \theta)]} \right\} . \quad (43)
\end{aligned}$$

To simplify this expression, we choose the following assumptions:

$$\theta = 0 , \quad (44)$$

$$g(t_a) = 0 , \quad (45)$$

$$\left[1 + \frac{a}{2\phi_0} \cos(\omega t_a) \right]^{-1} \approx 1 - \frac{a}{2\phi_0} \cos(\omega t_a) , \quad (46)$$

$$J_l(l\epsilon) \approx \frac{(l\epsilon)^l}{2^l l!} . \quad (47)$$

Then, setting $Z = d$ and $t = t_b$, for the arrival time at the exit plane of the input gap, we have, neglecting order a^2 ,

$$\begin{aligned}
\omega t_b - \omega t_a &= \phi_0 - \frac{a}{2\phi_0} \sin \omega t_a + \frac{a}{2\phi_0} \sin(\omega t_a + \phi_0) \\
& - \frac{a}{2} \cos \omega t_a + O(a^2) . \quad (48)
\end{aligned}$$

Therefore, the exit velocity given from Equation (5) is

$$V_{out}(t_a) \approx \dot{Z}_0 \left[1 - \frac{a}{2\phi_0} (\cos(\omega t_a + \phi_0) - \cos(\omega t_a)) \right] . \quad (49)$$

This is essentially the small-signal result obtained by Beck⁹ (p. 353). The assumptions made in Equations (44)-(47) are very radical; some of them can be justified under all conditions, and some can be justified only under small-signal conditions. A complete discussion of all these points is given in Section III.

E. EXIT CURRENT AND KINETIC POWER

When using ballistic theory and considering only current carried by the motion of electrons, it is common to use the law of conservation of charge to compute current. In order to justify this, we recall that the current crossing a surface S in space is defined as the rate that charge flows across S . We will use this definition in the following derivation.

Consider two planes, 1 and 2, as shown in Figure 2. Now consider some small finite area on planes 1 and 2, called ΔA . For electrons incident from the left, the charge that passes plane 1 in some

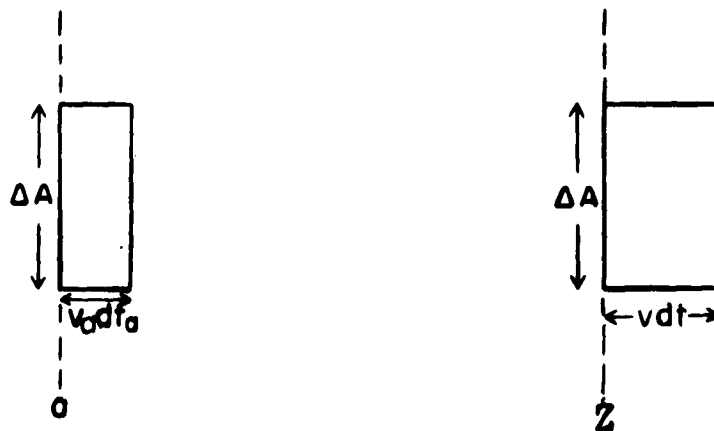


Figure 2. Illustration of Charge Conservation.

small time interval dt_a is merely the number of particles which pass plane a , multiplied by the charge of each particle. But the number which pass plane a in the infinitesimal time dt_a is equal to the number contained in the small volume

$$dV_a = v_a dt_a \Delta A \quad . \quad (50)$$

This is given by $n_a dV_a$, and the charge is

$$\Delta q_a = n_a e v_a \Delta A \quad , \quad (51)$$

where n_a is the number of particles per unit volume at time t_a , and v_a is the average velocity of the particles at time t_a . The interval dt_a is assumed to be so short that n_a and v_a are constant during the interval.

Following the same particles to the plane Z , we can say in a similar way that the charge crossing plane Z in a short time interval dt is the electronic charge multiplied by the number of electrons in the small volume dV , that is

$$\Delta q = n e v dt \Delta A \quad . \quad (52)$$

Here, n is the number of particles per unit volume at plane Z , and v is their velocity. These are assumed constant during the interval dt , and are in general different from n_a and v_a .

From conservation of charge, these two charge increments are the same; therefore

$$n_a e v_a dt_a \Delta A = n e v dt \Delta A \quad . \quad (53)$$

But current density J_z is defined as nev , so Equation (53) may be

written as

$$J_a \Delta A dt_a = J_z \Delta A dt \quad . \quad (54)$$

Integrating over a beam cross section, we have the total current. If the current density is assumed not to vary with transverse dimensions, then

$$I_a dt_a = I_z dt \quad , \quad (55)$$

that is,

$$I_z = I_a \left[1 / \frac{dt}{dt_a} \right] \quad , \quad (56)$$

wherever the derivatives in Equation (56) are defined. A full discussion of expression (56) is given in Section III. These expressions for current implicitly assume an electron stream composed of many electrons with different entrance times t_a , so that actually t_a becomes a time variable instead of a constant for a single electron. The Equation (56) can be written out in full for the current at any plane Z as a function of entrance time t_a :

$$\begin{aligned} \frac{I_z}{I_o} = & \frac{I_a}{I_o} \left[1 + g(t_a) + \frac{a}{2\phi_o} \cos(\omega t_a + \theta) \right]^2 \\ & \left[1 + 2g(t_a) + g^2(t_a) + \frac{a}{2\phi_o} \cos(\omega t_a + \theta) + \frac{a}{2\phi_o} g(t_a) \cos(\omega t_a + \theta) \right. \\ & \left. + \left(\frac{\omega Z}{Z_o} \right) \frac{a}{2\phi_o} \sin(\omega t_a + \theta) - \left(\frac{\omega Z}{Z_o} \right) \left[\frac{dg(t_a)}{dt_a} \right] \frac{1}{\omega} - \left(\frac{a}{2\phi_o} \right)^2 \sin^2(\omega t_a + \theta) \right. \\ & \left. + \left(\frac{a}{2\phi_o} \right) \left[\frac{dg(t_a)}{dt_a} \right] \frac{1}{\omega} \sin(\omega t_a + \theta) + \sum_{n=0}^{\infty} \left[\left(\frac{a}{2\phi_o} \right)^2 \sin(\omega t_a + \theta) - \left(\frac{a}{2\phi_o} \right) \frac{dg(t_a)}{dt_a} \frac{1}{\omega} \right] \right] . \end{aligned}$$

$$\begin{aligned}
& \cdot \left\{ J_v \left\{ \frac{(v+1)a}{2\phi_0 [1 + g(t_a) + \frac{a}{2\phi_0} \cos(\omega t_a + \theta)]} \right\} \right. \\
& \cdot \left. - J_v + 2 \left\{ \frac{(v+1)a}{2\phi_0 [1 + g(t_a) + \frac{a}{2\phi_0} \cos(\omega t_a + \theta)]} \right\} \right\} \\
& \cdot \sin(v+1)\omega \left\{ t_a + \frac{Z}{Z_0} \frac{1}{[1 + g(t_a) + \frac{a}{2\phi_0} \cos(\omega t_a + \theta)]} \right. \\
& \left. + \frac{\theta}{\omega} - \frac{a \sin(\omega t_a + \theta)}{2\phi_0 \omega [1 + g(t_a) + \frac{a}{2\phi_0} \cos(\omega t_a + \theta)]} \right\} \\
& + 2 \left\{ 1 + 2g(t_a) + g^2(t_a) + \frac{a}{2\phi_0} \cos(\omega t_a + \theta) \right. \\
& \left. + \frac{a}{2\phi_0} g(t_a) \cos(\omega t_a + \theta) + \left(\frac{\omega Z}{Z_0}\right) \frac{a}{2\phi_0} \sin(\omega t_a + \theta) \right. \\
& \left. - \left(\frac{\omega Z}{Z_0}\right) \left[\frac{dg(t_a)}{dt_a} \right] \frac{1}{\omega} - \left(\frac{a}{2\phi_0}\right)^2 \sin^2(\omega t_a + \theta) \right. \\
& \left. + \frac{a}{2\phi_0} \left[\frac{dg(t_a)}{dt_a} \right] \frac{1}{\omega} \sin(\omega t_a + \theta) \right\} \\
& \cdot J_v + 1 \left\{ \frac{(v+1)a}{2\phi_0 [1 + g(t_a) + \frac{a}{2\phi_0} \cos(\omega t_a + \theta)]} \right\} \\
& \cdot \cos(v+1) \left\{ \omega t_a + \left(\frac{\omega Z}{Z_0}\right) \frac{1}{[1 + g(t_a) + \frac{a}{2\phi_0} \cos(\omega t_a + \theta)]} \right. \\
& \left. + \theta - \frac{a \sin(\omega t_a + \theta)}{2\phi_0 [1 + g(t_a) + \frac{a}{2\phi_0} \cos(\omega t_a + \theta)]} \right\}^{-1} \tag{57}
\end{aligned}$$

This Equation (57) is the most general ballistic expression for the current at any point Z in a gridded gap. The derivation arises merely from taking the derivative of the expression (25) with respect to t_a .

At plane a , we have the number of particles $n_a v_a dt_a \Delta A$, each with kinetic energy $\frac{mv_a^2}{2}$. We have the same number of particles at plane Z , but here each has a kinetic energy of $\frac{mv^2}{2}$. Thus the gain in kinetic energy for these particles is

$$\Delta E = (n_a v_a dt_a \Delta A) \frac{m}{2} (v^2 - v_a^2) \quad . \quad (58)$$

Inserting the definition of current density and integrating over a beam cross section, we have the total kinetic energy change of the beam in a small interval of time, dt_a :

$$\begin{aligned} dE &= \int_{\text{beam}} J_a dA dt_a \frac{m}{2e} (v^2 - v_a^2) \\ &= I_a dt_a \frac{m}{2e} (v^2 - v_a^2) \quad . \quad (59) \end{aligned}$$

Since power is rate of change of energy, we have for the kinetic power

$$P_a = \frac{dE}{dt_a} = I_a \frac{m}{2e} (v^2 - v_a^2) \quad . \quad (60)$$

This expression will be useful in Section IV, when we wish compute the average kinetic power gained or lost by the beam over a period. This is found by integrating this instantaneous power function over a whole period and dividing by 2π .

In the two sections following, we show the meaning of this functional form, discuss the effect of varying some of its parameters, and

specialize Equations (26) and (57) to the input and output gaps of a two-cavity klystron.

III. DISCUSSION

A. VARIATION OF ENTRANCE TIME

In the expression that has been derived for the current, we have assumed implicitly that more than one electron is crossing the gap. It is entirely reasonable to assume this, since, in the klystron, electrons are continually being emitted from the cathode and are focused into a uniform beam.

Let us first assume that the electrons enter the gap with a constant velocity, the d-c beam velocity \dot{Z}_0 , thus assuming that $g(t_a) = 0$. This assumption is valid for the input gap. The velocity and current expressions are simplified by this assumption and become

$$\begin{aligned}
 \frac{v(Z)}{\dot{Z}_0} = & 1 - \frac{a}{2\phi_0} \left[\cos \left(\omega t_a + \theta + \frac{\omega Z}{\dot{Z}_0 \left[1 + \frac{a}{2\phi_0} \cos(\omega t_a + \theta) \right]} \right) \right. \\
 & - \frac{a \sin(\omega t_a + \theta)}{2\phi_0 \left[1 + \frac{a}{2\phi_0} \cos(\omega t_a + \theta) \right]} + \sum_{l=1}^{\infty} \frac{2}{T} J_l \left\{ \frac{l a}{2\phi_0 \left[1 + \frac{a}{2\phi_0} \cos(\omega t_a + \theta) \right]} \right\} \\
 & \cdot \sin l \left\{ \omega t_a + \theta + \frac{\omega Z}{\dot{Z}_0 \left[1 + \frac{a}{2\phi_0} \cos(\omega t_a + \theta) \right]} - \frac{a \sin(\omega t_a + \theta)}{2\phi_0 \left[1 + \frac{a}{2\phi_0} \cos(\omega t_a + \theta) \right]} \right\} \\
 & \left. - \cos(\omega t_a + \theta) \right] . \tag{61}
 \end{aligned}$$

and

$$\begin{aligned}
 \frac{I_z}{I_0} = & \left[1 + \frac{a}{2\phi_0} \cos(\omega t_a + \theta) \right]^2 \left[1 + \frac{a}{2\phi_0} \cos(\omega t_a + \theta) + \left(\frac{\omega Z}{Z_0} \right) \frac{a}{2\phi_0} \sin(\omega t_a + \theta) \right. \\
 & \left. - \left(\frac{a}{2\phi_0} \right)^2 \sin^2(\omega t_a + \theta) + \sum_{v=0}^{\infty} \left[\left(\frac{a}{2\phi_0} \right)^2 \sin(\omega t_a + \theta) \right] \right] \\
 & \cdot \left(J_v \left\{ \frac{(v+1)a}{2\phi_0 \left[1 + \frac{a}{2\phi_0} \cos(\omega t_a + \theta) \right]} \right\} - J_{v+2} \left\{ \frac{(v+1)a}{2\phi_0 \left[1 + \frac{a}{2\phi_0} \cos(\omega t_a + \theta) \right]} \right\} \right) \\
 & \cdot \sin(v+1) \left\{ \omega t_a + \frac{\omega Z}{Z_0 \left[1 + \frac{a}{2\phi_0} \cos(\omega t_a + \theta) \right]} + \theta - \frac{a \sin(\omega t_a + \theta)}{2\phi_0 \left[1 + \frac{a}{2\phi_0} \cos(\omega t_a + \theta) \right]} \right\} \\
 & + 2 \left[1 + \frac{a}{2\phi_0} \cos(\omega t_a + \theta) + \left(\frac{\omega Z}{Z_0} \right) \frac{a}{2\phi_0} \sin(\omega t_a + \theta) - \left(\frac{a}{2\phi_0} \right)^2 \sin^2(\omega t_a + \theta) \right] \\
 & \cdot J_{v+1} \left\{ \frac{(v+1)a}{2\phi_0 \left[1 + \frac{a}{2\phi_0} \cos(\omega t_a + \theta) \right]} \right\} \cdot \cos(v+1) \left\{ \omega t_a + \theta + \frac{\omega Z}{Z_0 \left[1 + \frac{a}{2\phi_0} \cos(\omega t_a + \theta) \right]} \right. \\
 & \left. - \frac{a \sin(\omega t_a + \theta)}{2\phi_0 \left[1 + \frac{a}{2\phi_0} \cos(\omega t_a + \theta) \right]} \right\}^{-1} \quad (62)
 \end{aligned}$$

It may be assumed without loss of generality, that for the input gap, the phase θ is zero. This assumption is based upon the fact that there are a uniform number of electrons passing plane a per unit time t_a . That is, it makes no difference whether the input gap voltage is zero or any other value at $t = 0$, insofar as the periodic behavior of the output

velocity and current is concerned. This further simplifies expressions (61), (62).

With more than one electron to consider, we naturally have more than one entrance time t_a . First of all, for a particular choice of t_a , we may see a large number N of electrons at the plane a . Now, at some time an instant later, we shall have another group of N electrons at plane a , with a different number for their initial time t_a . As we continue to increase real time, the entrance time t_a likewise increases, as long as we consider the different electrons, each group of which has its own entrance time t_a . In this way, we can use the time of entrance of the electron t_a as our real time variable. There are an equal number of electrons passing plane a per unit time, for the constant current and constant velocity input. Thus, we have established the meaning of using the entrance time t_a as a variable, and expressing functions and derivatives of functions in terms of this variable.

B. EXPRESSING FUNCTIONS IN TERMS OF EXIT TIME

In a manner similar to that indicated in Section A, the velocity and current functions may also be expressed in terms of exit time t_b . We have derived a functional relationship between the exit time and the entrance time of an electron. If one wishes to express the velocity and current as functions of exit time, it is only necessary to solve Equation (11) for t_a as a function of t . This is extremely difficult, and perhaps impossible for a transcendental equation as complex as this. Fortunately, it is not necessary to express the current and velocity in terms of the exit time t_b , as the entrance time t_a is entirely adequate for our purposes. It should be noted, however, that if the exit time is desired,

it can be easily calculated numerically for several values of the entrance time from expression (25) with $Z = d$. The expression of current and velocity as functions of exit time is thus quite possible in graphic or numerical form. For a choice of t_a , the corresponding t_b can be found, and then the current and velocity can also be found for that particular t_a . Then a plot can be readily made of current and velocity versus t_b .

There may be an apparent anomalous relationship between t_a and t_b that makes it difficult to express current and velocity in terms of t_b . This difficulty is that for very large signals it would seem that crossover could occur within the gap to some extent, so that for a given exit time there could be several corresponding entrance times. That is, several groups of electrons that entered the gap at different times could conceivably leave the gap at the same time. This would involve, then, the entrance time being a multivalued function of the exit time, so that for a given exit time, there would be several values for the entrance time and no unique entrance time.

When this difficulty occurs, as it undoubtedly does at some modulation level, the rigorous current relationships derived in Equations (50)-(57) are no longer true. One cannot simply take a derivative of a multivalued function, or invert these derivatives. Instead, the computation of the current corresponding to the exit time t_b must be carried out through a summation process, adding up all the incremental charges that had different entrance times t_a but that have the same exit time t_b .

Fortunately, we do not need to concern ourselves with such large signal levels here. We can have a large degree of velocity change and of

current bunching within the gap without the crossover actually taking place. Indeed, one might expect the point of the divergence of the series in Equation (25) to be the point of crossover. To investigate this point, we use a graphic technique.

Consider the Kepler equation

$$\zeta = u - \epsilon \sin u . \quad (63)$$

For the case where $\epsilon = 1$, the series diverges. In this case, we have the behavior illustrated in Figure 3. Now we can see that the slope zero is indeed the reason for the divergence, for when the equation is inverted, as in Figure 4, an infinite slope results. If the case proceeded for larger values of ϵ , then upon inversion there would be no unique value for u for a given ζ . Indeed, there could be three values of u for the properly chosen value of ζ .

To illustrate that this point of series divergence is not necessarily the point of maximum bunching, let us make a rough graph of the derivative of u with respect to ζ . This is given in Figure 5.

This derivative goes to infinity at $\zeta = 0, 2\pi, 4\pi$, etc. Note that for values of $\epsilon < 1$, the derivative does not go to infinity at these points but remains finite and positive for all ζ . For values of $\epsilon > 1$, the slope of the curve u versus ζ becomes negative for $\zeta = 0$, indicating that the derivative function in Figure 5 would become negative. The behavior of this derivative is important, because it is related to the current. Letting $u = \omega t_b$ and $\theta = 0$ for an input gap, we have

$$\frac{dt_b}{dt_a} = \frac{d(\omega t_b)}{d(\omega t_a)} = \frac{du}{d\zeta} \frac{d\zeta}{d(\omega t_a)} . \quad (64)$$

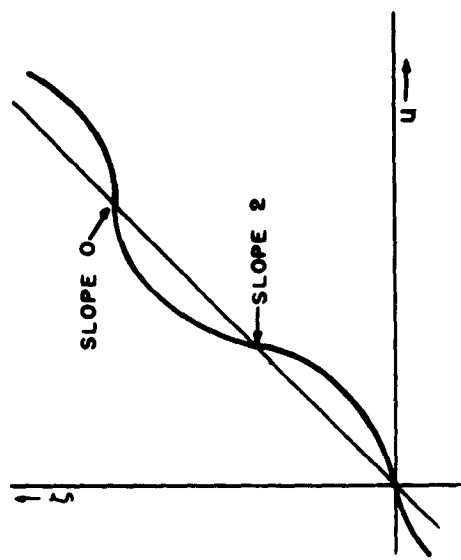


Figure 3. ξ versus u for $\epsilon = 1$.

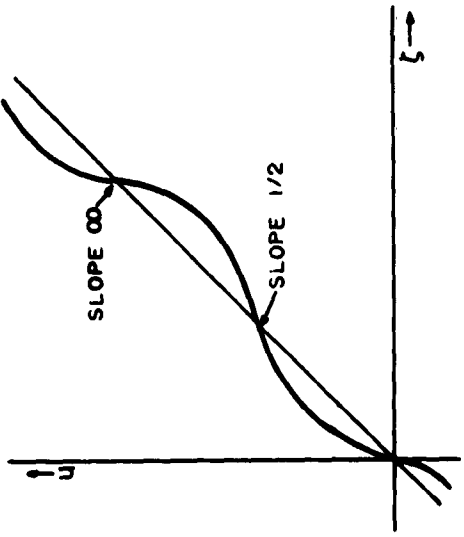


Figure 4. u versus ξ for $\epsilon = 1$.

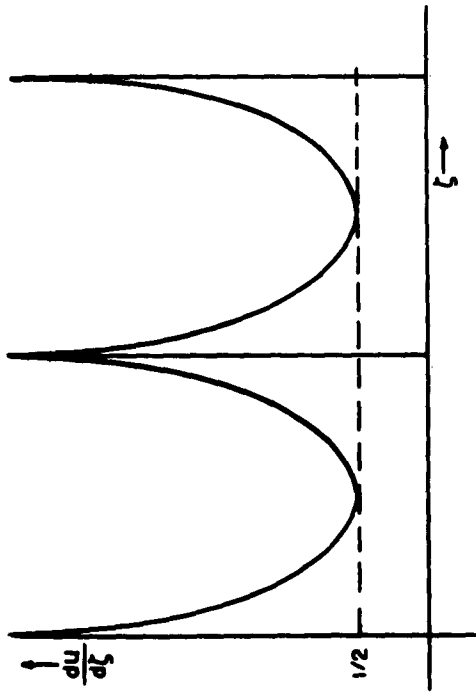


Figure 5. $\frac{du}{d\xi}$ versus ξ for $\epsilon = 1$.

The current as derived in Equation (56) is merely the inverse of Equation (64). In order to know where zeros and infinite peaks occur in the current, one need only know the behavior of the two derivatives $du/d\xi$ and $d\xi/d(\omega t_a)$.

Examining the expression for ϵ in Equation (32), we see that ϵ approaches one most rapidly with increasing a if the time value ωt_a is equal to π . For $\epsilon = 1$ and $\omega t_a = \pi$, the restriction in Equation (39) can be derived. We would therefore like to examine the current at this first point of series divergence. Knowing the approximate behavior of $du/d\xi$, we calculate $d\xi/d(\omega t_a)$ by differentiating Equation (33):

$$\frac{d\xi}{d(\omega t_a)} = \frac{1}{(1 + \frac{a}{2\phi_0} \cos \omega t_a)^2} \left[1 + \frac{a}{2\phi_0} \cos \omega t_a + \frac{a}{2} \sin \omega t_a - \left(\frac{a}{2\phi_0} \right)^2 \sin^2 \omega t_a \right]. \quad (65)$$

From Equation (32), we can deduce that if $\epsilon = 1$ and ωt_a is set equal to π , then this determines that $a/2\phi_0 = 1/2$. Using this relation in Equation (65) together with $\omega t_a = \pi$ we find

$$\left. \frac{d\xi}{d(\omega t_a)} \right|_{\omega t_a = \pi} = 2. \quad (66)$$

Therefore, $d\xi/d(\omega t_a)$ is finite and not zero for these values. We know that $du/d\xi$ is positive for all values of ξ when $\epsilon = 1$, and therefore we find the product $(du/d\xi) [d\xi/d(\omega t_a)]$ is nonzero for these values. Thus there is no crossover at $\epsilon = 1$, $\omega t_a = \pi$, even though the series diverges. We can see from the graph of $du/d\xi$ that nothing unusual happens to this derivative as ϵ increases from 0 to 1. It is always positive and finite. Therefore, we expect any erratic behavior

of the current to be due to the zeros of $d\zeta/d(\omega t_a)$.

This erratic behavior is well illustrated if one makes $\phi_0 \sim 10^3$, $a \sim 10$. Then, in Equation (65), terms containing the ratio $a/2\phi_0$ will be negligible, and the equation can be written

$$\frac{d\zeta}{d(\omega t_a)} \approx 1 + \frac{a}{2} \sin \omega t_a . \quad (67)$$

Here, $\epsilon \ll 1$ for all time so that $du/d\zeta$ is positive. If $a \geq 2$, zeros of Equation (67) are periodic. Therefore, we must have peaks of infinite current appearing periodically at the exit plane of this very long gap. This means that for a very long gap, this ballistic theory will predict velocities and currents beyond crossover and will converge fairly rapidly.

We have therefore found a region in which the series diverges but crossover has not yet occurred, and a region in which crossover has occurred but the series still converges rapidly. There are many intermediate steps between these two extremes. We have three parameters that determine crossover and series divergence: a , $a/2\phi_0$, and ωt_a . If these are fixed, then one can determine both series convergence and crossover at that point. Actually, only ωt_a and $a/2\phi_0$ are necessary to fix the series convergence. If the relation,

$$\frac{a}{2\phi_0} < \frac{1}{1 - \cos \omega t_a} , \quad (68)$$

is stipulated, then the series will converge, since ϵ will be less than unity. Then the a chosen will, together with the other two parameters, determine crossover. The most rapid way to check this is by graphic

or computer solutions of the zeros of Equation (65). If inequality (68) is satisfied, then the series expressions will hold even if crossover has occurred. However, in klystron gaps, the gap length is usually too short to allow crossover, and if crossover did occur, the space-charge forces in a bunch would cause a deviation from this ballistic theory.

Perhaps we should emphasize that there is a whole range of values of $a/2\phi_0 > 1/2$ for which the series converges for some ωt_a . The behavior of the beam for such large drive levels can be found by this convergent series only for $\pi - \delta > \omega t_a > \pi + \delta$, where δ is a small parameter, which is related to how much $a/2\phi_0$ exceeds 1/2. If $a/2\phi_0$ is less than 1/2, however, the series converges for all time.

We can conclude, therefore, that this series converges to a definite result for all values of time if $a < \phi_0$. If $a \geq \phi_0$, then the series will converge for all time except when ωt_a is in a neighborhood of π , the size of the neighborhood being determined implicitly by Equation (68). There seems to be no connection between crossover of electrons and divergence of the series. The series can, in many cases, give a convergent result for the region beyond crossover. Whether or not crossover also occurs in the region of series divergence is not known. We can now proceed to evaluate these equations with confidence within their region of convergence. The ultimate criterion for this theory, of course, is its actual numerical evaluation.

C. MEANING OF A VARIATION IN ENTRANCE VELOCITY

As we have indicated already, a possible application of this theory is to the output gap of a high-power klystron to determine the velocity and current at the exit plane of this gap. This information can

be used in the present problem of eliminating some of the harmful X-rays that are produced when high-velocity electrons strike the anode.

To apply this theory to an output gap, we must keep the most general initial conditions of arbitrary velocity and current at the entrance to the gap. In the ballistic theory, the current at the entrance plane enters into the calculation of the exit current only as a multiplying factor. The velocity at the entrance plane, however, significantly affects the transit time, exit velocity, and exit current. The time-varying part of this initial velocity, normalized against the d-c beam velocity, appears as the quantity $g(t_a)$ in the preceding analysis.

Perhaps a detailed explanation of the meaning of this term $g(t_a)$ should be made. In the preceding section, we considered the extension of the ballistic treatment for an electron with a single entrance time t_a and a single entrance velocity $v(t_a)$. We extended the theory to different electrons, each with its own different value of t_a , but each was assumed to have the same velocity, the d-c beam velocity of \dot{Z}_0 . There is no reason why each electron must have the same velocity, since the analysis was made for an arbitrary entrance velocity. If each electron had a different value of $v(t_a)$ for its own entrance time t_a , the analysis would still be valid. We therefore may assume a velocity function $v(t_a)$ that varies slightly about the d-c beam velocity. The term $g(t_a)$ is defined from this in Equation (30).

One may perhaps object that the initial conditions at the entrance plane of the gap are not the same with a velocity variation as well as an assumed entrance time variation. This is indeed true, in one respect. The number of electrons per unit time that enter the gap may be different

for each value of t_a . Furthermore, the velocity of these electrons may be different for each value of t_a . This means that the arbitrary phase θ of the applied gap voltage, which we could choose to be zero in the input gap case, can no longer be chosen as zero. Indeed, it makes a significant difference whether θ is chosen so as to make the applied voltage in phase or out of phase with respect to the entrance current. But the phase θ must be given as one of the known measurable parameters.

Insofar as the electrons themselves are concerned, it makes absolutely no difference, in the ballistic theory, whether a single electron or thousands of electrons are entering the output gap at a particular time t_a . The ballistic theory, as we have formulated it, does require, however, that all electrons entering at one particular time, t_a , have the same velocity. This neglects any fluctuations resulting from noise in the beam current.

With the extension of the analysis to the case of arbitrary entrance velocity and current one must still keep the general requirement that ϵ be less than unity. If this condition is satisfied, the series solutions will be convergent. This convergence requirement cannot be reduced easily to the simple form given for the input gap, but can be easily checked in the numerical computations of a particular case. In the next section, the explicit method of calculation will be shown for the general case of an output gap.

IV. APPLICATION TO X-RAY SUPPRESSION

A. INFORMATION REQUIRED FOR X-RAY SUPPRESSION

The simple small-signal klystron theory predicts that the electrons that are not in a bunch at the output gap will be out of phase with the voltage induced on the last gap and thus will be accelerated instead of retarded in this gap. Since the output gap voltage is usually of the order of the beam voltage, the out-of-phase electrons will have velocities roughly equivalent to twice the beam voltage. For beam voltages of the order of magnitude of tens and hundreds of kilovolts, very hard X-rays are produced, which are extremely dangerous for operating personnel. Current methods of solving this problem by shielding techniques using lead and other metals have resulted in very bulky equipment. The proposed method has been to limit the X-ray production by slowing down the fast electrons.

To apply this method, information is needed about the velocity and current distribution of the beam as it leaves the output gap. If the behavior of the beam is known one may be able to place a structure after the output gap to extract energy from the fast electrons. The velocity of the electrons is important, for if the electrons are of the same order of magnitude in velocity throughout a cycle, then the simplest solution would perhaps be a d-c retarding field. On the other hand, if the velocity and current distributions vary widely with time, then perhaps an r-f structure should be used, with the magnitude and phase of the applied voltage specified. To design such a structure, the current as well as the velocity must be known, so that the number of electrons in a particular cycle that possess the same velocity may be

calculated. In this way, one can obtain information about the intensity of the X-rays produced, as well as their wavelength.

B. LARGE SIGNAL SPACE-CHARGE WAVE THEORY IN DRIFT REGION

Very few large-signal analytical results for the drift region have been published to date. Some machine computation has been carried out, but the most prominent large-signal analytical efforts have been those of Paschke.^{4,5,6} In his first paper, Paschke⁴ derives the nonlinear space-charge wave equation. He solves this equation by the method of successive approximations, extending his results to the third harmonic in his most recent work.⁶ Rather than develop a similar approach to the problem or attempt a closed-form solution, we will, for purposes of computation, use Paschke's most recent results directly. His derivation of the nonlinear space-charge wave equation assumes one very important simplification; that the d-c beam velocity does not vary with distance. If Z is the distance variable in the drift tube, then his assumption is

$$\frac{\partial u_0}{\partial Z} = 0 \quad . \quad (63)$$

This assumption implies, from the equation of continuity, that

$$\frac{\partial \rho_0}{\partial Z} = 0 \quad . \quad (64)$$

There is no reason to suppose that this is the case for extremely large signals, for the portion of the total velocity that does not vary with time could conceivably change in magnitude with the distance Z . However, this assumption is necessary in order to put the nonlinear equation into a workable form. One should, however, remember that the solutions

are subject to this limitation, and therefore cannot give correct results if carried to higher orders indefinitely. Paschke's third-order result is probably the best nonlinear analysis yet published for the drift region.

For the general case of a finite diameter beam, Paschke⁶ gives the following results for the current and velocity:

1. Fundamental Current

$$\begin{aligned}
 \frac{i_\omega}{i_0} = & \frac{2\omega}{\omega_p p(\omega)} \frac{V_1}{4V_0} \cos(\omega t - \beta_e x) \left(\sin \alpha - \left[\frac{\omega}{\omega_p p(\omega)} \frac{V_1}{4V_0} \right]^2 \left\{ \frac{7\xi^2 - 1}{4(4\xi^2 - 1)} \sin^3 \alpha \right. \right. \\
 & + \frac{(1 - \xi^2)(2\xi^2 + 2\xi - 1)}{(2\xi + 1)(4\xi^2 - 1)} \left[\xi^2 \sin \alpha \left(\frac{1}{\xi} + 1 \right) - \xi(1 + \xi) \sin \alpha \right] \\
 & + \frac{(1 - \xi^2)(-2\xi^2 + 2\xi + 1)}{(2\xi - 1)(4\xi^2 - 1)} \left[-\xi^2 \sin \alpha \left(\frac{1}{\xi} - 1 \right) + \xi(1 - \xi) \sin \alpha \right] \\
 & \left. \left. + \frac{(1 - \xi^2)(8\xi^2 + 1)}{4(4\xi^2 - 1)} (-\alpha \cos \alpha + \sin \alpha) \right\} \right) \quad . \quad (65)
 \end{aligned}$$

2. Fundamental Velocity

$$\begin{aligned}
 \frac{v_\omega}{v_0} = & 2 \frac{V_1}{4V_0} \sin(\omega t - \beta_e x) \left(\cos \alpha - \left[\frac{\omega}{\omega_p p(\omega)} \frac{V_1}{4V_0} \right]^2 \left\{ \frac{29\xi^2 + 1}{16(4\xi^2 - 1)} (\cos \alpha - \cos 3\alpha) \right. \right. \\
 & + \frac{(1 - \xi^2)(1 - 2\xi - 2\xi^2)(1 + \xi)\xi}{(2\xi + 1)(4\xi^2 - 1)} \left[-\cos \alpha \left(\frac{1}{\xi} + 1 \right) + \cos \alpha \right] \\
 & \left. \left. + \frac{(1 - \xi^2)(1 + 2\xi - 2\xi^2)(1 - \xi)\xi}{(2\xi - 1)(4\xi^2 - 1)} \left[-\cos \alpha \left(\frac{1}{\xi} - 1 \right) + \cos \alpha \right] \right\} \right)
 \end{aligned}$$

$$\begin{aligned}
& + \frac{(1 - \xi^2)(8\xi^2 + 1)}{4(4\xi^2 - 1)} \alpha \sin \alpha + \frac{\xi(1 - \xi^2)}{4\xi^2 - 1} \left[\cos \alpha \left(\frac{1}{\xi} + 1 \right) - \cos \alpha \left(\frac{1}{\xi} - 1 \right) \right] \\
& - \xi^2 \cos \alpha + \frac{3\xi^2}{2(4\xi^2 - 1)} (\cos \alpha + \cos 3\alpha) \\
& - \frac{2\xi^2(1 - \xi^2)}{4\xi^2 - 1} \left[\cos \alpha \left(\frac{1}{\xi} + 1 \right) + \cos \alpha \left(\frac{1}{\xi} - 1 \right) \right] \} . \quad (66)
\end{aligned}$$

3. Second-Harmonic Current

$$\frac{i_{2\omega}}{i_0} = 2 \left[\frac{\omega}{\omega_p P(\omega)} \frac{V_1}{4V_0} \right]^2 \xi^2 \left[1 - \frac{3}{4\xi^2 - 1} \cos 2\alpha + \frac{4(1 - \xi^2)}{4\xi^2 - 1} \cos \frac{\alpha}{\xi} \right] \cos 2(\omega t - \beta_e x) , \quad (67)$$

4. Second-Harmonic Velocity

$$\frac{v_{2\omega}}{v_0} = \frac{\omega}{\omega_p P(\omega)} \left(\frac{V_1}{4V_0} \right)^2 \left[\frac{2\xi^2 + 1}{4\xi^2 - 1} \sin 2\alpha - \frac{4\xi(1 - \xi^2)}{4\xi^2 - 1} \sin \frac{\alpha}{\xi} \right] \sin 2(\omega t - \beta_e x) . \quad (68)$$

5. Third-Harmonic Current

$$\begin{aligned}
\frac{i_{3\omega}}{i_0} = & 6 \left[\frac{\omega}{\omega_p P(\omega)} \frac{V_1}{4V_0} \right]^3 \left\{ \frac{3(5\xi^2 + 1)}{2(4\xi^2 - 1)(9 - \frac{1}{\sigma^2})} \left(3\sigma \sin \frac{\alpha}{\sigma} - \sin 3\alpha \right) \right. \\
& + \frac{(1 - \xi^2)(8\xi^2 + 1)}{2(4\xi^2 - 1)(\frac{1}{\sigma^2} - 1)} (\sin \alpha - \sigma \sin \frac{\alpha}{\sigma}) \\
& + \left. \frac{(1 - \xi^2)(1 + 6\xi + 2\xi^2)}{(4\xi^2 - 1)[(1 + \xi)^2 - \frac{\xi^2}{\sigma^2}]} \left[\xi^2 \sin \alpha \left(\frac{1}{\xi} + 1 \right) - \xi(1 + \xi)\sigma \sin \frac{\alpha}{\sigma} \right] \right\}
\end{aligned}$$

$$+ \frac{(1 - \xi^2)(-1 + 6\xi - 2\xi^2)}{(4\xi^2 - 1)[(1 - \xi)^2 - \frac{\xi^2}{\sigma^2}]} \left\{ \xi^2 \sin \alpha \left(\frac{1}{\xi} - 1 \right) - \xi (1 - \xi) \sigma \sin \frac{\alpha}{\sigma} \right\} \cdot \cos 3(\omega t - \beta_e x) . \quad (69)$$

5. Third-Harmonic Velocity

$$\begin{aligned} \frac{v_{3\omega}}{v_0} = & \left[\frac{\omega}{\omega_p P(\omega)} \right]^2 \left(\frac{V_1}{4V_0} \right)^3 \left\{ \frac{(1 - \xi^2)(8\xi^2 + 1)}{(4\xi^2 - 1)(\frac{1}{\xi^2} - 1)} (\cos \alpha - \cos \frac{\alpha}{\sigma}) \right. \\ & - \frac{9(5\xi^2 + 1)}{(4\xi^2 - 1)(9 - \frac{1}{\sigma^2})} (\cos 3\alpha - \cos \frac{\alpha}{\sigma}) \\ & + \frac{2(1 - \xi^2)(1 + 6\xi + 2\xi^2)(\frac{1}{\xi} + 1)}{(4\xi^2 - 1)[(\frac{1}{\xi} + 1)^2 - \frac{1}{\sigma^2}]} \left[\cos \alpha \left(\frac{1}{\xi} + 1 \right) - \cos \frac{\alpha}{\sigma} \right] \\ & + \frac{2(1 - \xi^2)(-1 + 6\xi - 2\xi^2)(\frac{1}{\xi} - 1)}{(4\xi^2 - 1)[(\frac{1}{\xi} - 1)^2 - \frac{1}{\sigma^2}]} \left[\cos \alpha \left(\frac{1}{\xi} - 1 \right) - \cos \frac{\alpha}{\sigma} \right] \\ & + \frac{2\xi^2 + 1}{2(4\xi^2 - 1)} (\cos \alpha - \cos 3\alpha) + \frac{2\xi(1 - \xi^2)}{4\xi^2 - 1} \left[\cos \alpha \left(\frac{1}{\xi} - 1 \right) - \cos \alpha \left(\frac{1}{\xi} + 1 \right) \right] \\ & - 2\xi^2 \cos \alpha + \frac{3\xi^2}{4\xi^2 - 1} (\cos \alpha + \cos 3\alpha) - \frac{4\xi^2(1 - \xi^2)}{4\xi^2 - 1} \left[\cos \alpha \left(\frac{1}{\xi} + 1 \right) \right. \\ & \left. + \cos \alpha \left(\frac{1}{\xi} - 1 \right) \right] \left. \right\} \sin 3(\omega t - \beta_e x) . \quad (70) \end{aligned}$$

In these equations,

$$a = p(\omega) \beta_p x \quad , \quad (71)$$

$$\xi = \frac{p(\omega)}{p(2\omega)} \quad , \quad (72)$$

$$\sigma = \frac{p(\omega)}{p(3\omega)} \quad , \quad (73)$$

and $p(n\omega)$ is the plasma frequency reduction factor of the fundamental mode at the n^{th} harmonic frequency. Paschke's initial condition at $x = 0$ is

$$\frac{v}{v_0} = \frac{\eta V_1}{v_0} \sin \omega t \quad . \quad (74)$$

To adapt Paschke's results to the special case of an infinite beam, we set $\xi = \sigma = p(\omega) = 1$. Then his results simplify considerably. All of the terms containing the factor $(1 - \xi^2)$ in the numerator drop out. This drops the last three terms from the fundamental current, five terms from the fundamental velocity, a term from the second harmonic current and velocity, three terms from the third harmonic current, and four terms from the third harmonic velocity. In the final simplification we have the current as

$$\begin{aligned} \frac{i_c}{i_0} = & \left(\frac{a}{2} \right) \left(\frac{\omega}{\omega_p} \right) \left[\sin \beta_p x - \frac{1}{8} \left(\frac{a}{2} \right)^2 \left(\frac{\omega}{\omega_p} \right)^2 \sin^3 \beta_p x \right] \cdot \cos(\omega t - \beta_e x) \\ & + \frac{1}{2} \left(\frac{a}{2} \right)^2 \left(\frac{\omega}{\omega_p} \right)^2 [1 - \cos 2\beta_p x] \cos 2(\omega t - \beta_e x) \\ & + \frac{9}{32} \left(\frac{a}{2} \right)^3 \left(\frac{\omega}{\omega_p} \right)^3 (3 \sin \beta_p x - \sin 3\beta_p x) \cdot \cos 3(\omega t - \beta_e x) , \quad (75) \end{aligned}$$

and the velocity as

$$\begin{aligned}\frac{v}{v_0} = & \left(\frac{a}{2}\right) \left\{ \cos \beta_p x - \frac{1}{32} \left(\frac{a}{2}\right)^2 \left(\frac{\omega}{\omega_p}\right)^2 [\cos \beta_p x - \cos 3\beta_p x] \right\} \cdot \sin(\omega t - \beta_e x) \\ & + \frac{1}{4} \left(\frac{a}{2}\right)^2 \left(\frac{\omega}{\omega_p}\right) (\sin 2\beta_p x) \sin 2(\omega t - \beta_e x) \\ & + \frac{3}{32} \left(\frac{a}{2}\right)^3 \left(\frac{\omega}{\omega_p}\right)^2 (\cos \beta_p x - \cos 3\beta_p x) \sin 3(\omega t - \beta_e x) \quad . \end{aligned} \quad (76)$$

These results will be used to provide the initial conditions for the ballistic treatment of the output gap in the subsequent calculations.

C. LARGE-SIGNAL BALLISTIC THEORY IN THE OUTPUT GAP REGION

To apply the large-signal ballistic theory to the output gap, it is necessary to keep the most general form for the velocity and current, as is given in Equation (26) and (57). This results in a somewhat unwieldy expression for numerical calculation; therefore the results are obtained most easily from machine computation. The results, however, may be carried to any desired degree of accuracy in this way. Subject to the restrictions of the preceding section for convergence of the series, the general ballistic theory yields the current and velocity at any plane in the output gap.

One might inquire into the basic assumptions of the theory at this point; that is, just how valid is the ballistic theory for an output gap? The answer, of course, is that it is an approximation to the actual behavior, an approximation that neglects space-charge variations across the gap. This theory does allow for a variation in the quantity

of charge per unit time that enters the gap. It merely assumes that the potential depression at any instant across the gap is negligible compared to the potential caused by the alternating voltage applied to the grids. For short gaps, of the order of zero to two radians in length, there is no reason why these assumptions should not be a relatively valid approximation of the actual behavior.

These assumptions are further validated by the following consideration. Recall that in the mathematical statement of the problem, we assumed that there was a known voltage applied to the grids of the arbitrary gridded gap. All that was actually assumed was that the voltage existed there on the grids. This voltage, in the case of the input gap, was supplied from the outside and was assumed to be known, but for the output gap, the cavity is usually tuned to resonance at or near the fundamental frequency and extracts power from the beam. That is, the voltage appearing on the grids of the gap is not supplied from an external source, but is induced on the grids by the bunched beam. The beam, in so doing, gives up power to the external circuit and changes its values of current and velocity across the gap. Now, because of the induction of the voltage on the grids by the beam and because of the voltage producing a change in beam current and velocity, we can consider this behavior as a reciprocal relationship, and knowledge of the effect of the voltage on the beam is equivalent to knowledge of the effect of the changing beam upon the induced voltage. The reason for this equivalence is that there can be only one, unique voltage on the grids for a given beam behavior, and conversely, there can be only one, unique change in the beam configuration resulting from a given voltage

function. This change in the beam resulting from the known voltage function is determined by Newton's second law together with the boundary conditions. Therefore, if the magnitude and phase of the output voltage is measured, the ballistic theory using this information should give fairly reliable results when applied to the output gap.

D. CALCULATION PROCEDURE

The calculation proceeded in eight steps.

1. Input Current

$$\begin{aligned}
 I_c = \frac{i_c}{i_0} = 1 + \left(\frac{a}{2}\right) \left(\frac{\omega}{\omega_p}\right) & \left[\sin \beta_p x - \frac{1}{8} \left(\frac{a}{2}\right)^2 \left(\frac{\omega}{\omega_p}\right)^2 \sin^3 \beta_p x \right] \cdot \cos(\omega t - \beta_e x) \\
 & + \frac{1}{2} \left(\frac{a}{2}\right)^2 \left(\frac{\omega}{\omega_p}\right)^2 \left[1 - \cos 2 \beta_p x \right] \cos 2(\omega t - \beta_e x) \\
 & + \frac{9}{32} \left(\frac{a}{2}\right)^3 \left(\frac{\omega}{\omega_p}\right)^3 \left[3 \sin \beta_p x - \sin 3 \beta_p x \right] \cos 3(\omega t - \beta_e x) \tag{77}
 \end{aligned}$$

2. Input Velocity

$$\begin{aligned}
 v_c = 1 + g = 1 + \left(\frac{a}{2}\right) \left\{ \cos \beta_p x - \frac{1}{32} \left(\frac{a}{2}\right)^2 \left(\frac{\omega}{\omega_p}\right)^2 \left[\cos \beta_p x - \cos 3 \beta_p x \right] \right\} & \cdot \sin(\omega t - \beta_e x) \\
 & + \frac{1}{4} \left(\frac{a}{2}\right)^2 \left(\frac{\omega}{\omega_p}\right) \left[\sin 2 \beta_p x \right] \sin 2(\omega t - \beta_e x) \\
 & + \frac{3}{32} \left(\frac{a}{2}\right)^3 \left(\frac{\omega}{\omega_p}\right)^2 \left[\cos \beta_p x - \cos 3 \beta_p x \right] \sin 3(\omega t - \beta_e x) \tag{78}
 \end{aligned}$$

These two basic initial conditions were calculated from Paschke's results, Equations (75) and (76). The velocity is used in subsequent computations

of transit time.

3. Transit Time

$$\begin{aligned}
 \omega t_d = \omega t_c + \frac{\phi_1}{\left[1 + g + \frac{a_1}{2\phi_1} \cos(\omega t_c + \theta) \right]} - \frac{a_1 \sin(\omega t_c + \theta)}{2\phi_1 \left[1 + g + \frac{a_1}{2\phi_1} \cos(\omega t_c + \theta) \right]} \\
 + \sum_{l=1}^N \frac{2}{T} J_l \left\{ \frac{l a_1}{2\phi_1 \left[1 + g + \frac{a_1}{2\phi_1} \cos(\omega t_c + \theta) \right]} \right\} \\
 \cdot \sin l \left\{ \omega t_c + \theta + \frac{\phi_1}{\left[1 + g + \frac{a_1}{2\phi_1} \cos(\omega t_c + \theta) \right]} \right. \\
 \left. - \frac{a_1 \sin(\omega t_c + \theta)}{2\phi_1 \left[1 + g + \frac{a_1}{2\phi_1} \cos(\omega t_c + \theta) \right]} \right\} \tag{79}
 \end{aligned}$$

With the calculation of the transit time, the final velocity calculation is simplified.

4. Final Velocity

$$v_d = \frac{v_f}{v_o} = 1 + g + \frac{a_1}{2\phi_1} \left[\cos(\omega t_c + \theta) - \cos(\omega t_d + \theta) \right] \tag{80}$$

In order to calculate the final current at the exit plane of the output gap, one needs the derivative of Paschke's velocity.

5. Input Velocity Derivative

$$\begin{aligned}
 h = \frac{1}{\omega} \frac{dv_c}{dt} = \left(\frac{a}{2} \right) \left\{ \cos \beta_p x - \frac{1}{32} \left(\frac{a}{2} \right)^2 \left(\frac{\omega}{\omega_p} \right)^2 [\cos \beta_p x - \cos 3\beta_p x] \right\} \cdot \cos(\omega t - \beta_e x) \\
 + \frac{1}{2} \left(\frac{a}{2} \right)^2 \left(\frac{\omega}{\omega_p} \right) [\sin 2\beta_p x] \cos 2(\omega t - \beta_e x) \\
 + \frac{9}{32} \left(\frac{a}{2} \right)^3 \left(\frac{\omega}{\omega_p} \right)^2 [\cos \beta_p x - \cos 3\beta_p x] \cos 3(\omega t - \beta_e x) \quad (81)
 \end{aligned}$$

Now one can substitute steps 2 and 5 into the expression for the derivative of the transit time.

6. Transit Time Derivative

$$\begin{aligned}
 \frac{dt_d}{dt_c} = \frac{1}{\left[1 + g + \frac{a_1}{2\phi_1} \cos(\omega t_c + \theta) \right]^2} \cdot \left[1 + 2g + g^2 + \frac{a_1}{2\phi_1} \cos(\omega t_c + \theta) + \frac{a_1}{2\phi_1} g \cos(\omega t_c + \theta) \right. \\
 \left. + \frac{a_1}{2} \sin(\omega t_c + \theta) - \phi_1 h - \left(\frac{a_1}{2\phi_1} \right)^2 \sin^2(\omega t_c + \theta) + \frac{a_1}{2\phi_1} h \sin(\omega t_c + \theta) \right. \\
 \left. + \sum_{v=0}^M \left[\left(\frac{a_1}{2\phi_1} \right)^2 \sin(\omega t_c + \theta) - \left(\frac{a_1}{2\phi_1} \right) h \right] \cdot \left(J_v \left\{ \frac{(\nu + 1)a_1}{2\phi_1 [1 + g + \frac{a_1}{2\phi_1} \cos(\omega t_c + \theta)]} \right\} \right. \right. \\
 \left. \left. - J_{v+2} \left\{ \frac{(\nu + 1)a_1}{2\phi_1 [1 + g + \frac{a_1}{2\phi_1} \cos(\omega t_c + \theta)]} \right\} \right) \right]
 \end{aligned}$$

$$\begin{aligned}
& \cdot \sin(\nu + 1) \left\{ \omega t_c + \theta + \frac{\phi_1}{\left[1 + g + \frac{a_1}{2\phi_1} \cos(\omega t_c + \theta) \right]} \right. \\
& \left. - \frac{a_1 \sin(\omega t_c + \theta)}{2\phi_1 \left[1 + g + \frac{a_1}{2\phi_1} \cos(\omega t_c + \theta) \right]} \right\} \\
& + 2 \left[1 + 2g + g^2 + \frac{a_1}{2\phi_1} \cos(\omega t_c + \theta) + \frac{a_1}{2\phi_1} g \cos(\omega t_c + \theta) \right. \\
& \left. + \frac{a_1}{2} \sin(\omega t_c + \theta) - \phi_1 h - \left(\frac{a_1}{2\phi_1} \right)^2 \sin^2(\omega t_c + \theta) + \left(\frac{a_1}{2\phi_1} \right) h \sin(\omega t_c + \theta) \right] \\
& \cdot J_{\nu+1} \left\{ \frac{(\nu+1)a_1}{2\phi_1 \left[1 + g + \frac{a_1}{2\phi_1} \cos(\omega t_c + \theta) \right]} \right\} \\
& \cdot \cos(\nu+1) \left\{ \omega t_c + \theta + \frac{\phi_1}{\left[1 + g + \frac{a_1}{2\phi_1} \cos(\omega t_c + \theta) \right]} \right. \\
& \left. - \frac{a_1 \sin(\omega t_c + \theta)}{2\phi_1 \left[1 + g + \frac{a_1}{2\phi_1} \cos(\omega t_c + \theta) \right]} \right\} \quad (82)
\end{aligned}$$

The calculation of the final current is then easily performed.

7. Final Current

$$I_d = \frac{i_d}{i_o} = \frac{i_c}{i_o} \left[\frac{\frac{1}{dt_d}}{\frac{dt_d}{dt_c}} \right] \quad (83)$$

In order to find the average power added to the beam per period as the phase of the output voltage changes, we integrate Equation (60).

8. Average Kinetic Power Gain of the Beam per Period

$$P_{av} \approx \frac{1}{2\pi} \int_0^{2\pi} I_c (v_d^2 - v_c^2) d(\omega t_c) \quad . \quad (84)$$

The computation was done on a Burroughs 220 with punched-card input, and the program was designed so that any of the six parameters a , ω/ω_p , $\beta_p x$, a_1 , ϕ_1 , θ , could be given any values desired. Here, the subscripts 1 refer to the normalized voltage and drift length of the second cavity. Each step was printed out for 16 values of ωt_c between zero and 2π .

Several comments should be made about the calculations. In steps 1 and 2, the computation of the input current and input velocity from Paschke's theory, it is necessary to choose values of ω/ω_p and a so that the product $(a/2)(\omega/\omega_p)$ is always less than unity. If this condition is violated, then the magnitudes of the second and third harmonics could be greater than the fundamental for some values of $\beta_p x$. This implies that the assumed series solution that Paschke uses may diverge, and that the expression for current and velocity up to the third harmonic is an extremely poor approximation to the actual beam behavior. For our purposes, we used the values of $a = .3$ and $\omega/\omega_p = 5$. These values gave a product of .75, which was significantly less than one. We wished to choose the large value of ω/ω_p and the value of a to correspond more closely to the parameters used in modern high-power two-cavity klystron amplifiers, rather than to the parameters in

the domain of strict small-signal theory. The value of $\beta_e x$ was computed from the relation,

$$\beta_e x = \left(\frac{\omega}{\omega_p}\right) \beta_p x \quad . \quad (85)$$

Since most two-cavity klystrons are designed so that the drift length is a quarter of a plasma wavelength, the value of $\beta_p x = \pi/2$ was chosen. This makes the current have the maximum amplitude, and makes the velocity unity for all time; that is, the velocity at $\beta_p x = \pi/2$ is merely the d-c velocity. If the value of $(a/2)(\omega/\omega_p)$ is larger than unity, then the resulting current will be negative for some values of ωt and positive for other values of ωt . Since the velocity is always a constant positive unity, this corresponds to the physically impossible condition, that the charge density change sign as a function of time. The condition,

$$\left(\frac{a}{2}\right) \left(\frac{\omega}{\omega_p}\right) < 1 \quad , \quad (86)$$

must always hold.

In the computation, the steps 2 and 5 were included for generality, although they are one and zero respectively for all values of ωt_c for the $\beta_p x$ we have chosen.

In the evaluation of the series in steps 3 and 6, the criterion was included that the argument of the Bessel function must be less than the order. This is equivalent to condition (40), and insures convergence of the series. The further restriction was imposed that the number of terms in the series should not exceed 50. Neither of these restrictions were violated for the values of the parameters chosen.

The Bessel functions were computed from the power series expression for small arguments given in Equation (47). Accuracy was obtained to at least ten significant figures by this method. Accuracy of the total computation was compromised to five figures, since a graphic presentation of the results was to be given.

Paschke's expressions for the current and velocity use ωt , the time used to describe the voltage at the input gap, as an independent variable. There is a certain phase delay that enters into the expression for the current and voltage, if one wishes to express them as functions of time of arrival at the entrance plane of the output gap. Since Paschke assumes that the d-c beam velocity is constant in space and time, we can deduce that the difference between expressing the output gap entrance current and entrance velocity as a function of ωt or as a function of ωt_c is merely some phase constant. In the calculations, therefore, it was assumed that $\omega t = \omega t_c$, and this phase constant was implicitly contained in the phase θ . Strictly speaking, therefore, the meaning of the constant θ was slightly different in the calculation scheme than in its original derivation. However, θ was varied between zero and 2π , and results were therefore obtained to cover all possible cases. It still remained to find out what the relationship was between a particular θ and the tuning of the output cavity. Therefore, the change in kinetic power was computed for each value of ωt_c and was integrated over a period, giving the average power added to the beam. The phase θ which gives the most negative value for this average power was assumed to be the operating point of the klystron amplifier under normal conditions; that is, usually the output cavity is tuned to resonate at the

fundamental frequency and extract the maximum amount of power from the beam. It should be pointed out that the expression,

$$P_a \sim I_a \left(\frac{m}{2e} (v_b^2 - v_a^2) \right) \quad , \quad (87)$$

was used in the calculations, but this was merely a convenient choice.

We could have used, with the same validity, the expression,

$$P_b = I_b \frac{m}{2e} (v_b^2 - v_a^2) \quad . \quad (88)$$

These functions of course are different, but when integrated over a period, they are equivalent. This is easily shown as follows.

From Equation (59),

$$dE = I_a dt_a \frac{m}{2e} (v_b^2 - v_a^2) \quad , \quad (89)$$

for the kinetic energy change of the beam across two planes, a and b. But

$$I_a dt_a = I_b dt_b \quad ; \quad (90)$$

therefore

$$dE = I_b dt_b \frac{m}{2e} (v_b^2 - v_a^2) \quad , \quad (91)$$

where I_a and I_b represent the total current at planes a and b, respectively. Then we can define

$$P_b = \frac{dE}{dt_b} = I_b \frac{m}{2e} (v_b^2 - v_a^2) \quad (92)$$

as a function of wt_b . But

$$\frac{P_a}{P_b} = \frac{I_a}{I_b} = \frac{dt_b}{dt_a} \quad , \quad (93)$$

$$P_a dt_a = P_b dt_b \quad , \quad (94)$$

and, changing notation to the output planes c and d , we have

$$\frac{1}{2\pi} \int_0^{2\pi} P_c d(\omega t_c) = \frac{1}{2\pi} \int_0^{2\pi} P_d d(\omega t_d) \quad . \quad (95)$$

This equation is the result desired. Strictly speaking, the average power is equal to the value computed in step 8, multiplied by $I_o V_o$. The currents and velocities in the steps of calculation are all total currents and total velocities, normalized against the d-c beam current I_o and the d-c velocity Z_o . Therefore, the normalization is also implicitly included in the power calculation, as simple algebra will show.

In the actual integration to find average power, only approximate values were necessary for the integral, so the trapezoidal rule was used with 16 equally spaced intervals per period.

The following values of the six parameters and the time variable were used:

$$a = .3 \quad ,$$

$$\frac{\omega}{\omega_p} = 5 \quad ,$$

$$\beta_p x = \pi/2 \quad ,$$

$$\phi_1 = 1.8 \quad ,$$

$$a_1 = 0.6, 0.7, 0.8, 0.9, 1.0, 1.1 \quad ,$$

$$\theta = 0, \pi/8, 2\pi/8, 3\pi/8, \dots, 15\pi/8 \quad ,$$

$$\omega t_c = 0, \pi/8, 2\pi/8, 3\pi/8, \dots, 15\pi/8 \quad .$$

E. RESULTS

For each possible combination of the parameters used, all eight steps were evaluated and printed out. The most important results are the transit time, the final velocity and current, and the average power. Each set of parameter values yielded a unique value of arrival time at plane d, ωt_d^* . Since we are interested primarily in the current and velocity at plane d as a function of time, we must express most of the graphic results using ωt_d as a time variable. We must do this because we are eventually interested in the beam behavior beyond the output gap, at the collector. A structure will eventually be placed in the region between the output gap and the collector which will reduce the velocities of the fast electrons in the beam. In order to provide the entrance conditions to such a structure, we must express our current and velocity in terms of the entrance time to this structure, which is the same as the exit time of the output gap. The situation here is essentially analogous to that encountered in providing proper entrance conditions to the output gap. In that case, we expressed Paschke's current and velocity in terms of entrance time ωt_c and included the constant phase difference between ωt_c and ωt in the parameter θ . However, in this case, the phase difference between ωt_d and ωt_c is not constant, but is a function of entrance time ωt_c . It is contained in the transit time expression. Therefore we must include it explicitly by evaluating it numerically and then plotting current and velocity as functions of exit time ωt_d .

The values of exit current versus exit time for four different values of phase are plotted in Figure 6.

*From this point, "time" refers to normalized time; that is the angle ωt_c or ωt_d .

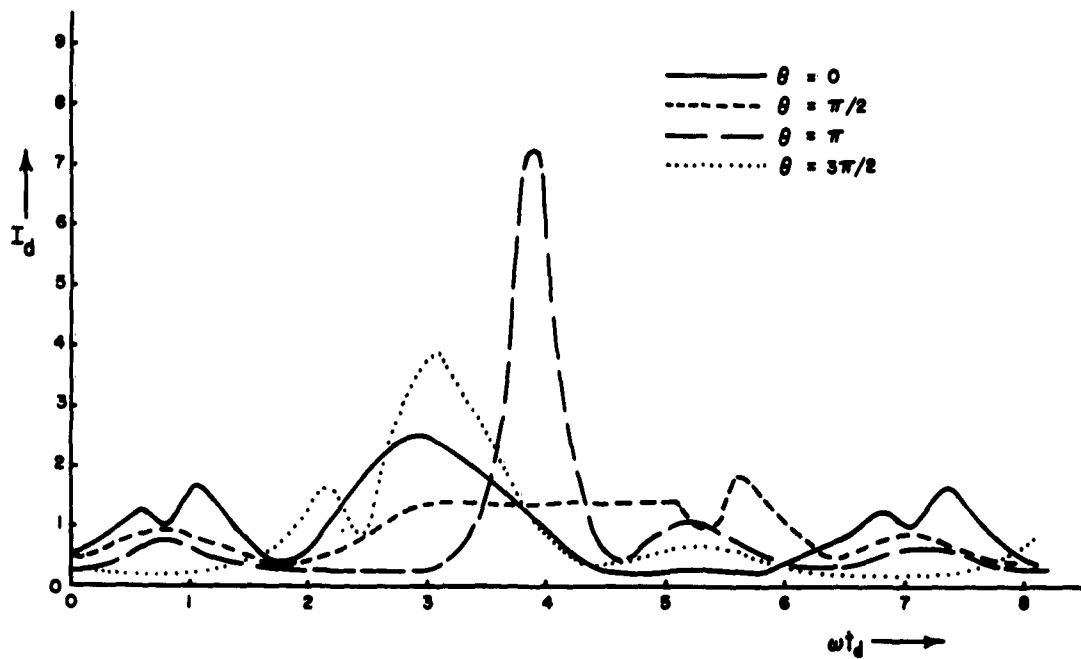


Figure 6. Output Gap Exit Current versus Exit Time for $a_1 = 1.1$.

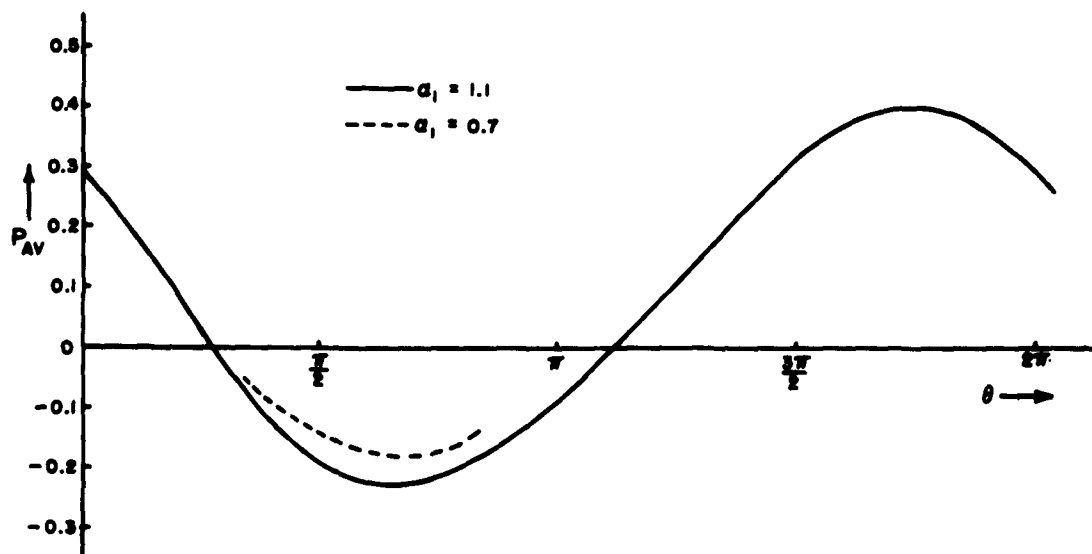


Figure 7. Average Normalized Kinetic Power per Period Added to Beam versus Phase of Output Voltage.

The single value of $a_1 = 1.1$ was used in this graph, and the effect of a change in phase upon the current was examined. As can be seen, the phase of the output gap voltage has a marked effect. For a phase of $\pi/2$, the current is very flat over a large portion of the curve. However, increasing the phase to π produces a very large current peak at $\omega t_d = 3.8$ radians with a relatively low value elsewhere. The other two values of phase given are intermediate between these two extremes. A more detailed graph for the phases between $\pi/2$ and π shows the flattened portion of the curve rising continuously from $\pi/2$ to the large peak observed at π . One would suspect that these two extremes correspond to maximum power extraction from the beam for the phase of $\pi/2$, and to maximum addition of power to the beam to produce the highly bunched condition for the phase of π . In order to check this, the average power per period versus the phase was calculated as outlined in the previous discussion. This is given in Figure 7.

The original curve for all values of θ was made with $a_1 = 1.1$. As was suspected, the beam loses the maximum amount of power in the vicinity of $\pi/2$; however, it gains the most power at $\theta = 7\pi/4$. This is far from the point of greatest bunching, π . Indeed, at $\theta = \pi$, the beam is still losing power to the gap. This would seem to indicate that a condition of maximum harmonic content of the beam current could be achieved while power is still being extracted from the beam.

The point of maximum power extraction is closer to $\theta = 5\pi/8$. A check of this point for a different value of a_1 ($a_1 = .7$) was made and is also presented on Figure 7. It seems that for a large change in a_1 , the minimum shifts slightly, being closer to $\pi/2$ for larger values of

a_1 . However, over the region of a_1 of interest, the change in the phase θ for maximum power extraction is very small. The maximum kinetic power extraction takes place when the phase θ is in the interval $(\pi/2, 3\pi/4)$. We therefore examine the exit current, exit velocity, and exit charge density as functions of time for these values of phase in Figures 8-16, since klystron amplifiers are normally operated under these conditions.

For a particular a_1 , all three velocity graphs are the same, but for each different θ they are displaced from each other. This is to be expected from the form of Equations (79) and (80), where the quantity $(\omega t_c + \theta)$ always appears, instead of ωt_c or θ separately. Therefore, a variation in phase merely causes a change in phase of the output velocity.

The current graphs show remarkable changes, but have some similarities. For $\theta = \pi/2$, the curve for $a_1 = 1.1$ is the same as is given in Figure 6. But, Figure 8 shows an increase in the current with decreasing a_1 , for electrons in the region $2.7 \leq \omega t_c \leq 5$. Figure 9 shows that these electrons have the lowest velocity. Therefore, it is very probable that the electrons with exit times in this region gave power to the external load and were slowed down. With less retarding field evidenced by a lower a_1 , the electron velocity would not be decreased as much, and the current would be greater, since it is the product of velocity and charge density. The charge density function does vary with time towards the end of this interval, as can be seen from Figure 10. This is evidence of a further bunching effect coming into play. It is interesting to note that the limiting case of smaller a_1 must be a value of one for the velocity at all time, and a current equal to the

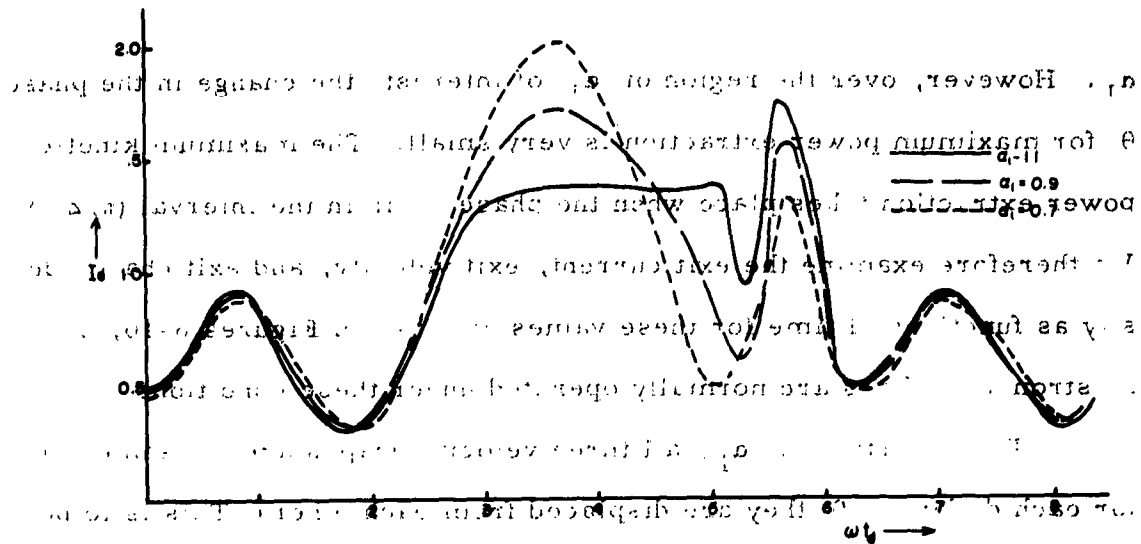


Figure 8.8. Output Gap Exit Current versus Exit Time; $\theta = \pi/2$.

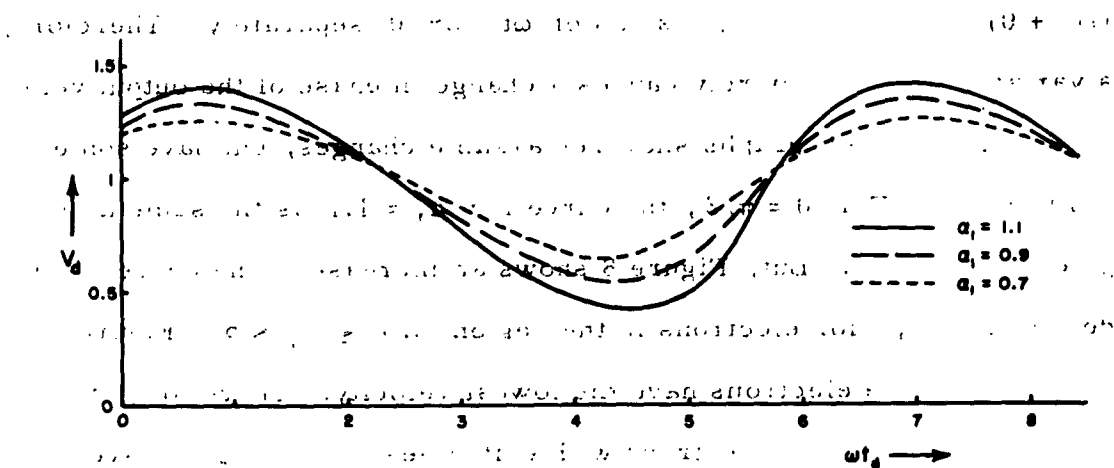


Figure 9. Output Gap Exit Velocity versus Exit Time; $\theta = \pi/2$.

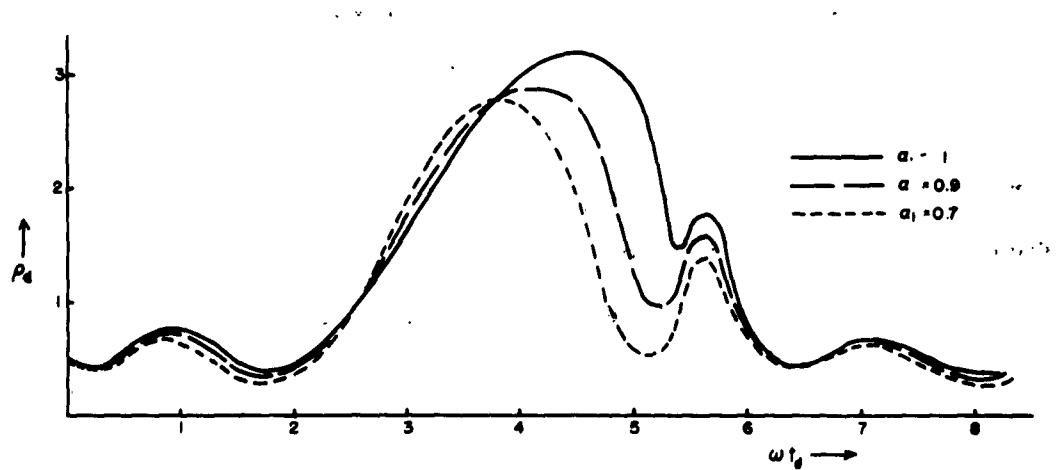


Figure 10. Output Gap Exit Charge Density versus Exit Time; $\theta = \pi/2$.

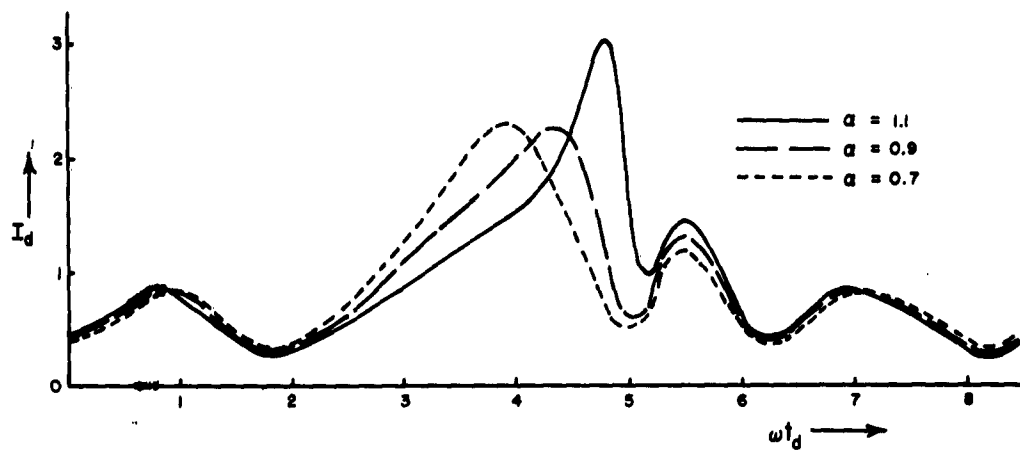


Figure 11. Output Gap Exit Current versus Exit Time; $\theta = 5\pi/8$.

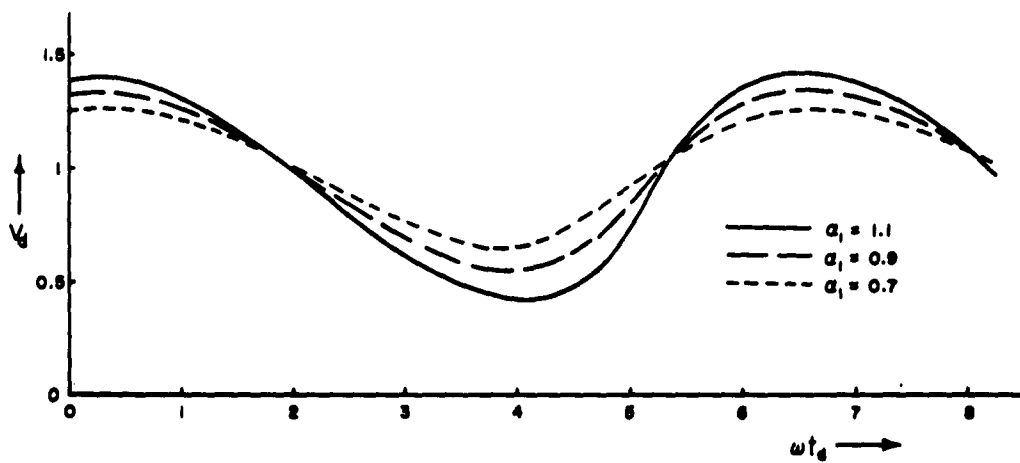


Figure 12. Output Gap Exit Velocity versus Exit Time; $\theta = 5\pi/8$.

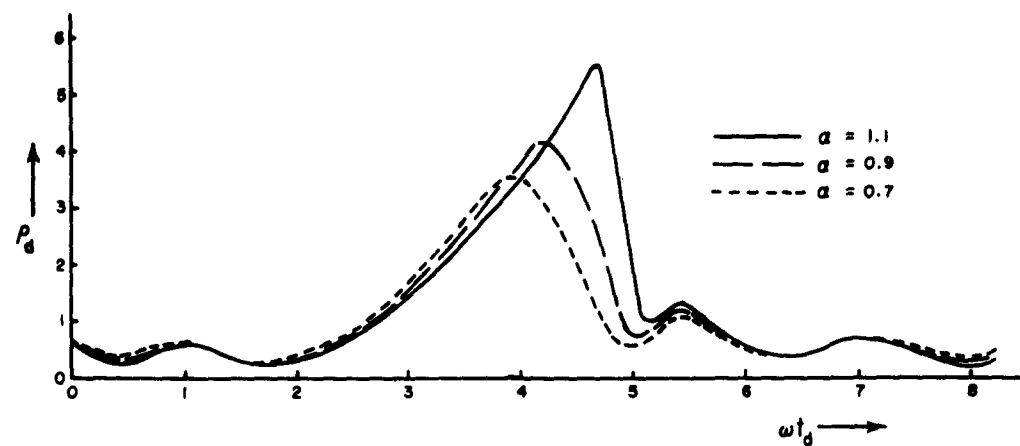


Figure 13. Output Gap Exit Charge Density versus Exit Time; $\theta = 5\pi/8$.

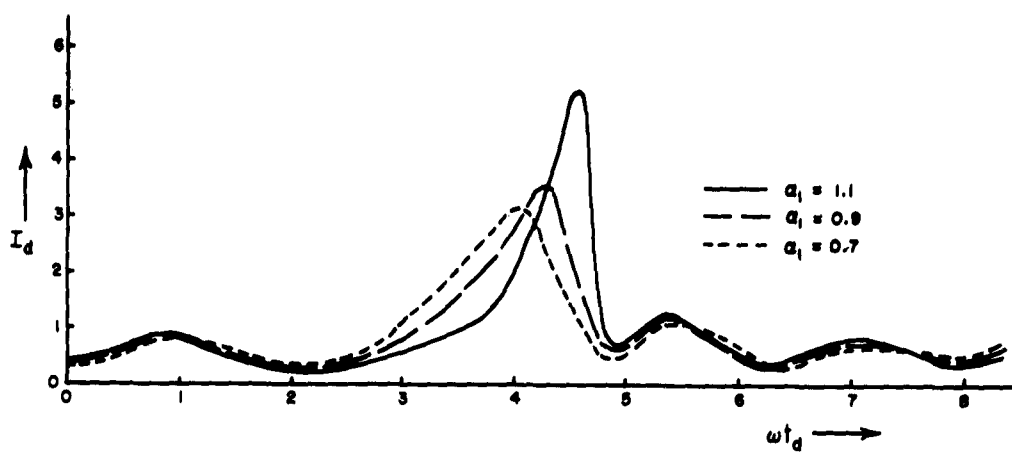


Figure 14. Output Gap Exit Current versus Exit Time; $\theta = 3\pi/4$.

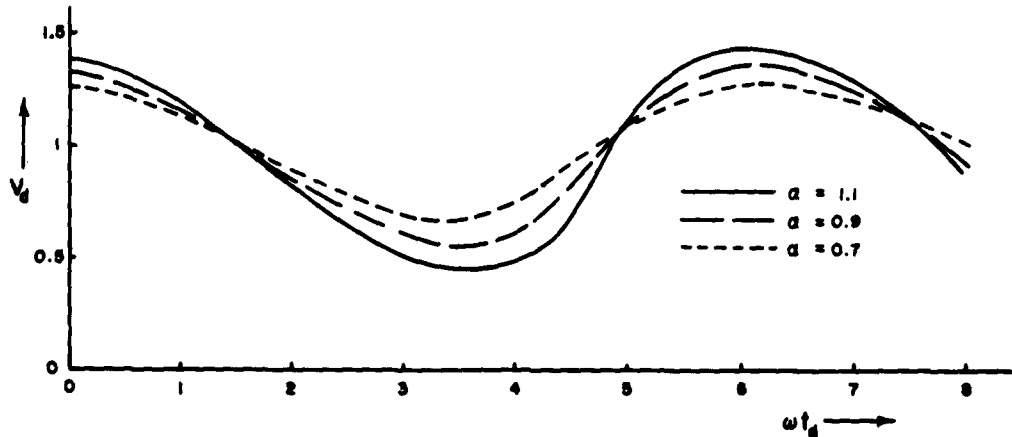


Figure 15. Output Gap Exit Velocity versus Exit Time; $\theta = 3\pi/4$.

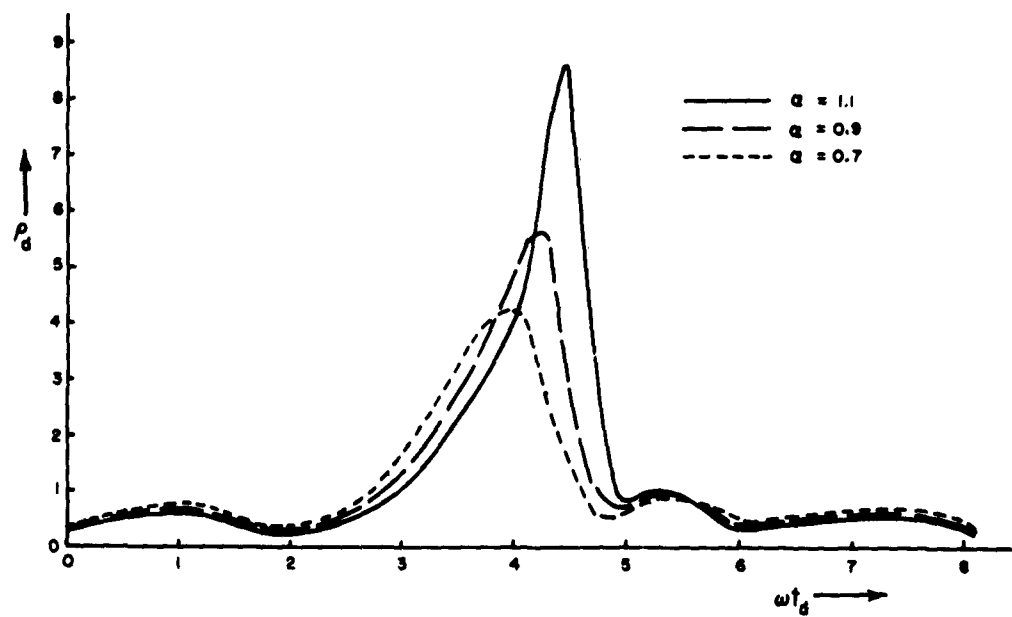


Figure 16. Output Gap Exit Charge Density versus Exit Time; $\theta = 3\pi/4$.

entrance current.

The mechanism just mentioned for power extraction at $\theta = \pi/2$ can also be observed at $\theta = 5\pi/8$ and $\theta = 3\pi/4$. In these cases, the region of minimum velocity is displaced, but the current variations are in general displaced in the same direction by approximately the same magnitude, so that the power extraction occurs during the interval of the large current bunch. It is worth noting that the charge-density functions show a huge peak during that interval, but since the velocity is larger outside the interval, we can conclude that the vast majority of the electrons give up their energy during that interval and that the current peaks outside that interval are caused by small numbers of relatively high-velocity electrons. The magnitude of the current in the region $5.2 \leq \omega t_d \leq 8.5$ seems to be relatively insensitive to changes in a_1 for a given θ . However, an increase in θ gives a slight decrease in the current in these two peaks, since the current in the largest peak increases, and the current must be conserved over a period in time.

The two smaller peaks in the current functions in the region $5.2 \leq \omega t_d \leq 8.5$ are caused by high-velocity electrons, as can be seen from the velocity curves. They have a relatively low charge density, indicating that the number of the high-velocity electrons is small. This is evident from the charge-density curves. The velocities of these high-velocity electrons are independent of phase but are directly proportional to voltage magnitude a_1 . The number of particles with the high velocities is not a function of voltage magnitude, but does decrease somewhat with increasing phase. The position in time of these high-velocity

bunches does not vary with magnitude or phase of the voltage.

As a side effect, one might point out that one would expect, for a value of $a_1 = 1.1$, a maximum value of velocity, which corresponds to approximately $\sqrt{2}$ times the d-c beam voltage, for the electrons that gained the most energy in passing through the gap. This is indeed the case, as can be seen on Figures 9, 12, and 15.

The results seem to indicate that the X-rays are produced by relatively few electrons at high velocity, which appear during the latter part of the period. Therefore a large d-c retarding field would not be practical, for if it were effective in slowing down the few fast electrons, it would cause the very large number of slow electrons to be repelled back into the gap, where they would interact with the later electrons. There is even the possibility of reflex oscillations under these conditions.

It seems very possible, however, that the often suggested r-f structure placed ahead of the collector could actually be used. It appears that it would have to be driven by an outside voltage source, possibly at twice the fundamental frequency ω in order to affect both fast bunches. Its effect on the slow large bunch would probably be only to speed up some electrons to the order of magnitude of the beam voltage, and would not necessarily cause any electrons to turn back, although there would be a tendency for some electrons entering in the large slow bunch to do so. Possibly a cavity tuned to twice the fundamental frequency could extract power from the fast electrons, but only a more detailed analysis could confirm this. At any rate, the coherent character of the beam current and velocity at the exit plane of the output gap leads one to believe that a r-f structure placed before the collector with

the proper voltage magnitude and phase maintained upon it could be singularly effective in slowing the two small bunches of fast electrons without seriously increasing the velocity of the rest of the beam.

V. CONCLUSIONS AND RECOMMENDATIONS

In the first half of the preceding analysis, the ballistic theory of an electron beam in a gridded gap was developed for large signals. The limits of validity of the expressions for velocity and current were established. With the neglect of space charge, this analysis provides a rigorous analysis of the electron beam in a gridded gap region. An experimental verification of this basic gap theory could be undertaken, using a set of parameters designed to realize more closely the assumption of an infinite beam and no space-charge effects.

This gap analysis was applied in the output gap, combined with the best available large-signal theory using space-charge waves for the drift region. The exit current and exit velocity of the beam at the end of the output gap was found for several values of the magnitude and phase of the output voltage. The change in average kinetic power of the beam across the gap was also calculated, and it was concluded that under conditions of normal operation of two-cavity klystron amplifiers, there are two small bunches of relatively high-velocity electrons in the beam. The positions of the bunches is constant for several voltages and phases, and the amplitude of the current bunches decreases with decreasing voltage.

As a logical continuation of this theoretical analysis, some experimental investigation of the possibility of slowing down the fast electrons with a r-f structure should be undertaken. It seems very

probable that such a structure could effectively slow the fast electrons
and prevent production of hard X-rays at the collector.

APPENDIX

A. DERIVATION OF POWER SERIES INVERSION

The derivation of Equation (41) has been quoted by many authors, but originated with Lagrange.¹⁴ We are following the method given by Tisserand¹⁵ (pp 262-269). Consider the equation

$$Z - a - af(Z) = 0 \quad , \quad (A. 1)$$

in which a , a , and Z designate real or imaginary quantities. Consider also a closed contour S such that one has, on all its points,

$$\text{mod} \frac{af(Z)}{Z - a} < 1 \quad . \quad (A. 2)$$

We further suppose the function $f(Z)$ to be holomorphic on the interior of S .

It has been shown that the Equation (A. 1) admits one and only one solution Z in the interior of S ; and, in designating by $\pi(Z)$ any holomorphic function of that root, we can develop $\pi(Z)$ in a converging series in powers of a :

$$\pi(Z) = \pi(a) + \sum_{n=0}^{n=\infty} \frac{a^{n+1}}{1:Z \dots (n+1)} \frac{d^n}{da^n} [\pi'(a) f^{n+1}(a)] \quad . \quad (A. 3)$$

We can take for Equation (A. 1) the Kepler equation,

$$u - \zeta - \epsilon \sin u = 0 \quad , \quad (A. 4)$$

in which we assume ζ and ϵ to be real. According to the preceding statement, if one can find a closed contour S on all points of which

$$\text{mod} \frac{\epsilon \sin u}{u - \zeta} = \epsilon \text{mod} \frac{\sin u}{u - \zeta} < 1 \quad , \quad (\text{A. 5})$$

then Equation (A. 4) admits one and only one root u in the interior of S , and one can develop the converging series,

$$\pi(u) = \pi(\zeta) + \sum_{n=0}^{n=\infty} \frac{\epsilon^{n+1}}{(n+1)!} \frac{d^n}{d\zeta^n} \left[\pi'(\zeta) \sin^{n+1} \zeta \right] \quad . \quad (\text{A. 6})$$

In making

$$\pi(u) = u \quad , \quad (\text{A. 7})$$

and

$$\pi(u) = \cos u \quad , \quad (\text{A. 8})$$

successively in Equation (A. 6), it follows that

$$u = \zeta + \epsilon \sin \zeta + \dots$$

$$+ \frac{\epsilon^m}{m!} \frac{d^{m-1}}{d\zeta^{m-1}} \sin^m \zeta + \dots \quad (\text{A. 9})$$

and

$$\begin{aligned} \cos u &= \cos \zeta - \epsilon \sin^2 \zeta - \dots \\ &- \frac{\epsilon^{m-1}}{(m-1)!} \frac{d^{m-2}}{d\zeta^{m-2}} \sin^m \zeta - \dots \end{aligned} \quad (\text{A. 10})$$

But, one also has these known formulas. For m even,

$$\sin^m \zeta = \frac{(-1)^{\frac{m}{2}}}{2^{\frac{m}{2}-1}} \left[\cos m\zeta - \frac{m}{1} \cos(m-2)\zeta + \frac{m(m-1)}{1 \cdot 3} \cos(m-4)\zeta - \dots \right] ; \quad (\text{A. 11})$$

and for m odd,

$$\sin^m \zeta = \frac{(-1)^{\frac{m-1}{2}}}{2^{m-1}} \left[\sin m\zeta - \frac{m}{1} \sin(m-2)\zeta + \frac{m(m-1)}{1 \cdot 2} \sin(m-4)\zeta - \dots \right]. \quad (A. 12)$$

From these formulas one can infer easily that

$$\begin{aligned} \frac{d^{m-1}}{d\zeta^{m-1}} \sin^m \zeta &= \frac{1}{2^{m-1}} \left[m^{m-1} \sin m\zeta - \frac{m}{1} (m-2)^{m-1} \sin(m-2)\zeta \right. \\ &\quad \left. + \frac{m(m-1)}{1 \cdot 2} (m-4)^{m-1} \sin(m-4)\zeta - \dots \right]. \quad (A. 13) \end{aligned}$$

This formula holds for the two cases of m even or odd. It is terminated at the term in $\sin 2\zeta$ if m is even, and at the term in $\sin \zeta$ if m is odd.

Using this relation in Equation (A. 9) and (A. 10), we have the final result:

$$\begin{aligned} u &= \zeta + \epsilon \sin \zeta + \frac{\epsilon^2}{2} \sin 2\zeta + \dots + \frac{\epsilon^m}{2^{m-1} m!} \left[m^{m-1} \sin m\zeta - \frac{m}{1} (m-2)^{m-1} \sin(m-2)\zeta \right. \\ &\quad \left. + \frac{m(m-1)}{1 \cdot 2} (m-4)^{m-1} \sin(m-4)\zeta - \dots \right], + \dots \quad (A. 14) \end{aligned}$$

B. CONVERGENCE OF POWER SERIES INVERSION

Laplace¹⁸ was the first to show the limit on the convergence of the power series. His method was very complicated, and so we shall give a simpler, shorter method ascribed to Rouché, that leads to the same result.

Let A be the point of the x axis where the abscissa is ζ , and m be the point where the abscissa is $\zeta + u$. We take for the contour S a circle of radius ρ drawn from A as center. Let us make the point M move on this circle, and designate the angle between the radius AM

and the x axis by ϕ . Let us adopt Tisserand's notation of $i = \sqrt{-1}$ and $E = \text{Naperian base} = 2.71828\dots$. Then we have, from these definitions,

$$u = \zeta + \rho E^{i\phi} \quad . \quad (\text{A. 15})$$

Condition (A. 5) becomes

$$\frac{\epsilon}{\rho} \text{ mod } \sin(\zeta + \rho E^{i\phi}) < 1 \quad . \quad (\text{A. 16})$$

Let $F(\rho)$ be the maximum value of the modulus of $\sin(\zeta + \rho E^{i\phi})$ when ϕ varies from zero to 2π and ζ takes on all possible real values. If the value for ϵ is such that

$$\epsilon < \frac{\rho}{F(\rho)} \quad , \quad (\text{A. 17})$$

the condition given in Equation (A. 16) will be satisfied and the series will converge for all values of ζ . If one could determine the value of ρ_1 of the radius ρ so that the expression $\rho/F(\rho)$ is as large as possible, and then one makes $\epsilon_1 = \rho_1/F(\rho_1)$, the series would converge for

$$\epsilon < \epsilon_1 \quad .$$

One must first find the form of $F(\rho)$. In order to do this, we compute the square of the modulus of $\sin(\zeta + \rho E^{i\phi})$. It is equal to

$$\begin{aligned} \sin(\zeta + \rho E^{i\phi}) \sin(\zeta + \rho E^{-i\phi}) &= \sin(\zeta + \rho \cos \phi + i\rho \sin \phi) \cdot \\ &\quad \sin(\zeta + \rho \cos \phi - i\rho \sin \phi) = \cos^2(i\rho \sin \phi) - \cos^2(\zeta + \rho \cos \phi) \quad . \quad (\text{A. 19}) \end{aligned}$$

One therefore has

$$\text{mod } \sin(\zeta + \rho e^{i\phi}) = \sqrt{\left(\frac{e^{\rho \sin \phi} + e^{-\rho \sin \phi}}{2}\right)^2 - \cos^2(\zeta + \rho \cos \phi)} . \quad (\text{A. 20})$$

The minimum of $\rho/F(\rho)$ occurs when Equation (A. 20) is at its maximum, for a given value of ρ . This takes place when

$$\left(\frac{e^{\rho \sin \phi} + e^{-\rho \sin \phi}}{2}\right)$$

is as large as possible, at $\sin \phi = 1$. Then, one will have at the same time

$$\cos^2(\zeta + \rho \cos \phi) = 0 , \quad (\text{A. 21})$$

$$\cos \zeta = 0 , \quad (\text{A. 22})$$

$$\zeta = \pm \frac{\pi}{2} . \quad (\text{A. 23})$$

For this case, it will happen that

$$F(\rho) = \frac{e^{\rho} + e^{-\rho}}{2} . \quad (\text{A. 24})$$

In order to find the maximum of the expression,

$$\frac{2\rho}{e^{\rho} + e^{-\rho}} , \quad (\text{A. 25})$$

we set its derivative equal to zero:

$$e^{\rho}(\rho - 1) - e^{-\rho}(\rho + 1) = 0 . \quad (\text{A. 26})$$

The first term in this equation takes values of opposite sign for $\rho = 1$ and $\rho = 2$; its derivative $\rho(e^{\rho} + e^{-\rho})$ is always positive. Therefore this equation has one and only one root ρ_1 , which is positive. One finds from numerical computations that

$$\rho_1 = 1.9967 \dots ; \quad (A.27)$$

so that the limit of convergence is

$$\epsilon_1 = \frac{2^2 \rho_1}{E^2 + E^{-\rho_1}} = 0.6627 \dots \quad (A.28)$$

This is the limit of convergence of the power series.

REFERENCES

1. D. L. Webster, "Cathode-Ray Bunching," J. App. Phys. 10 (1939), 501.
2. W. C. Hahn, "Small-Signal Theory of Velocity-Modulated Electron Beams," Gen. Elec. Rev. 42 (1939), 258.
3. S. Ramo, "Space Charge and Field Waves in an Electron Beam," Phys. Rev. 56 (1939), 276.
4. F. Paschke, "On the Nonlinear Behavior of Electron-Beam Devices," R. C. A. Rev. 18 (1957), 221.
5. F. Paschke, "Generation of Second Harmonic in a Velocity-Modulated Electron Beam of Finite Diameter," R. C. A. Rev. 19 (1958), 617.
6. F. Paschke, "Nonlinear Theory of a Velocity-Modulated Electron Beam with Finite Diameter," R. C. A. Rev. 21 (1960), 53.
7. T. G. Mihran, "Harmonic Current Growth in Velocity-Modulated Electron Beams," J. App. Phys. 30 (1959), 1346.
8. T. G. Mihran, "The Effect of Space Charge on Bunching in a Two-Cavity Klystron," Trans. I.R.E. P.G.E.D., 6, (1959).
9. A. H. W. Beck, Thermionic Valves, Cambridge: Cambridge University Press, 1953, p. 198, 353.
10. W. E. Blair, "Harmonic Analysis of Electron Beams in Klystrons," Res. Rept. EE 458, Cornell University, (January 1960), pp. 3-11.
11. R. Warnecke and P. Guénard, Les Tubes Electroniques à Commande Par Modulation de Vitesse, Paris: Gauthier - Villars, 1951, pp. 72-148.
12. W. J. Kleen, Electronics of Microwave Tubes, New York: Academic Press, 1958, pp. 54-57.

13. W. Sackinger, "A Note on Large-Signal Ballistic Klystron Theory," Res. Rept. EE 462, Cornell University, (February 1960), pp. 27-41.
14. J. L. Lagrange, Oeuvres de Lagrange, Vol. III, Paris: Gauthier-Villars, 1869, pp. 113-138.
15. F. Tisserand, Traité de Méchanique Céleste, Vol I, Paris: Gauthier-Villars et Fils, 1889, pp. 215-222, pp. 262-269.
16. E. T. Whittaker, A. Treatise on the Analytical Dynamics of Particles and Rigid Bodies, 4th ed., Cambridge: Cambridge University Press, 1937, p. 91.
17. Pierre Simon Marquis de Laplace, Méchanique Céleste, Vol I, transl. N. Bowditch, Boston: Hilliard, Gray, Little, and Wilkins, 1829, p. 356, et. seq.
18. Pierre Simon Marquis de Laplace, Oeuvres de Laplace, Vol. V, Paris: Imprimerie Royale, 1846, pp. 504-522.

FINAL REPORT

PART III:
CIRCUIT STUDIES

KLYSTRON CAVITIES FOR MINIMUM SPURIOUS OUTPUT POWER

L. A. MacKenzie

School of Electrical Engineering
CORNELL UNIVERSITY
Ithaca, New York

RESEARCH REPORT EE 418

KLYSTRON CAVITIES FOR MINIMUM SPURIOUS OUTPUT POWER

L. A. MacKenzie

**This report is based entirely upon a thesis submitted
by the author to the Faculty of the Graduate School
of Cornell University for the degree of Master of Science.**

**THEORETICAL AND EXPERIMENTAL INVESTIGATION
OF LINEAR-BEAM MICROWAVE TUBES**

Technical Report No. 1

31 January 1959

**Published under Contract No. AF 30(602)-1696
Rome Air Development Center
Griffiss Air Force Base, New York**

CONTENTS

| | Page |
|---|------|
| I. INTRODUCTION | 1 |
| II. RESONANT CAVITY THEORY | 4 |
| A. THEORETICAL ANALYSIS | 7 |
| 1. Cavity Admittance of Region 1 | 8 |
| 2. Cavity Admittance of Region 2 | 20 |
| 3. The Total Admittance Function | 23 |
| 4. Nonsymmetrical Higher-Order Modes | 35 |
| B. CONTROL EXPERIMENTS AT THE FUNDAMENTAL RESONANCE | 41 |
| C. SPECIFIC APPLICATION TO HIGHER-ORDER RESONANCES | 46 |
| D. OPTIMUM CAVITY DESIGN | 49 |
| III. PERTURBATION THEORY IN RESONANT CAVITIES | 62 |
| A. ORTHOGONAL ELECTROMAGNETIC FIELD FUNCTIONS | 62 |
| B. ILLUSTRATIVE EXPANSION OF CAVITY FIELDS | 71 |
| C. MAXWELL'S EQUATIONS WITH ORTHOGONAL FUNCTIONS | 73 |
| D. ILLUSTRATIVE PROBLEM | 77 |
| E. GENERAL PERTURBATION OF CAVITIES | 78 |
| 1. Class 1 Perturbation | 81 |
| 2. Class 2 Perturbation | 84 |
| 3. Practical Form of Perturbation Equations | 87 |
| F. CALIBRATION CONSTANTS | 87 |
| G. SPECIFIC EXPERIMENTS | 89 |
| 1. Calibration Constant | 89 |
| 2. Electric Field Measurements | 94 |

| | Page |
|--|-------------|
| IV. CONCLUSIONS AND RECOMMENDATIONS | 95 |
| APPENDIX | 97 |
| REFERENCES | 100 |

ILLUSTRATIONS

| Figure | Page |
|---|------|
| 1 Co-ordinate System for Cavities | 5 |
| 2 Cross-Section of Cylindrical Cavity Showing Dimensions | 11 |
| 3 Assumed and True Gap Field | 12 |
| 4 Average Gap Width for Rounded Edges | 23 |
| 5 Comparison of $b \cot_{\theta_0}(\alpha\theta - \theta)$ and $\cot\theta$ for $\alpha = 2.0$ | 25 |
| 6 Admittance of a Short-Circuited Radial Line | 26 |
| 7 Comparison of $b \coth(\alpha\theta - \theta)$ and $\coth\theta$ for $\alpha = 2$ | 28 |
| 8 Bessel Hyperbolic Cotangent Function $b \coth(\alpha\theta - \theta)$ | 29 |
| 9 Universal Curve Second Order Higher Mode Inductive Susceptance | 33 |
| 10 Inner Storage Admittance at the Gap of Two Hollow Cylinders | 36 |
| 11 Gap Electric Field at $r = r_a$ | 37 |
| 12 Sample Problem - Singly Re-Entrant Gridded-Gap Cavity | 43 |
| 13 Sample Problem - Singly Re-Entrant Gridded-Gap Cavity | 44 |
| 14 Cavity Used for Measurements | 45 |
| 15 Model of L-Band Klystron Cavity | 47 |
| 16 Total Admittance Function of L-Band Cavity Model | 50 |
| 17 Recommended Ranges of (βr_a) for Resonance for Different Values of $\alpha = r_b/r_a$ | 53 |
| 18 Cross-Section for Doubly Re-Entrant Cavities | 55 |
| 19 Recommended Ranges of Parameter x as Indicated by Shaded Areas | 56 |
| 20 Recommended Ranges of Parameter x as Indicated by Shaded Areas | 57 |
| 21 Recommended Ranges of Parameter x as Indicated by Shaded Areas | 58 |

| Figure | Page |
|--|------|
| 22 Electric Field Configuration for Typical Modes (Coaxial Line Mode Designation Shown in Parenthesis). | 61 |
| 23 Rectangular Cavity | 71 |
| 24 Perturbed Cavity | 82 |
| 25 Nomenclature Used for Ellipsoids | 90 |
| 26 Calibration Constants for Metal Prolate Spheroids (Direction of fields given either parallel or perpendicular to major axis of bead) | 92 |

ABSTRACT

In this report, the design of the coaxial cavities used by high-power klystrons is specified so as to minimize the spurious output power. A detailed theoretical analysis of a general doubly re-entrant grid-less gap coaxial cavity is made which enables one to calculate the fundamental and first three higher-order resonances. It is shown that the fundamental resonance may be held fixed while the first few higher-order resonances are adjusted in frequency so as to avoid the second and third harmonics of the signal frequency. In this way, the output cavity of a klystron may be optimized with respect to minimum spurious output power, which occurs largely at the harmonics. Experimental measurements made on a symmetrical cavity, i. e., no large output port or loop, indicate accuracies of a few per cent for the calculated resonances. Limited design curves are presented which have a universal application and equations are given so that additional curves may be calculated.

The second section of this report treats the general theory of the perturbation of resonant cavities from a physical viewpoint. The application of this theory can aid the large signal solution of the beam dynamics in a klystron, which would lead to the effects of the interaction phenomena on the spurious output. In particular, formulas are given for the calculation of absolute values of the fields from perturbation measurements. It is shown that the perturbing object must be on the order of two or three hundredths of a wavelength in size for these formulas to be accurate.

I. INTRODUCTION

Within the past few years, engineers have become increasingly aware of the serious problems presented by the spurious output of high-power microwave systems, and a recent paper by R. D. Campbell¹ has shown the severity of this problem as related to interference caused by radar. The paper cites experiments in which measurements were made on several radars to determine their power output spectrum. All of the radars showed "very substantial magnitudes" of power radiated at frequencies other than the signal frequency. The radars tested employed both magnetrons and klystrons as the microwave power source.

There are two broad methods of approaching this spurious output problem. The first is to suppress the unwanted output by some means external to the high-power microwave tubes, and the second is to improve the basic design of these tubes to prevent the generation of spurious signals. The first method can be used to improve existing installations while the second is desirable for future installations. This thesis is devoted to the second of these methods and deals with high-power klystrons.

As related to spurious outputs there are two approaches to klystron design:

- (1) active - the electron beam and interaction phenomena,
- (2) passive - the microwave circuitry of the tube.

These two subdivisions are by no means unrelated to each other. The large signal operation of klystrons produces nonlinearities which are the basis for the development of power at frequencies other than the signal frequency. Then for this power to become spurious output, the microwave circuit must couple to it. Part of the design of klystrons

is therefore associated with the optimum design of the output cavity, optimum in the sense that only the fundamental signal frequency is coupled out. This means that the pass bands, or essentially the resonant modes and frequencies, must be delineated, for it is only at or near these frequencies that the cavity can have any output.

The microwave circuitry of klystron design is undertaken in the first part of this thesis. The analysis is directed at calculating the resonances of the usual type of klystron cavity so that the results may be put into a form usable in design work. The general case of the doubly re-entrant, gridless-gap, coaxial-type cavity is treated. To date, no known solution of this type of cavity exists, although the singly re-entrant, gridded-gap cavity has been treated numerically at the fundamental resonance with very good results.^{2, 3}

After the analysis is completed and verified experimentally, design criteria are outlined that will permit the design of a cavity whose higher order resonances are removed from the harmonics of the signal frequency. The design has been developed to eliminate harmonics up to and including the fourth. This particular criterion based on the elimination of resonances at the signal harmonics has been used because a large part of the spurious output encountered in practice occurs at these harmonics.

The second part of this thesis is concerned with the general theory of the perturbation of resonant cavities. This theory is useful in that its application indirectly aids the large signal solution of the beam dynamics in a klystron, a solution that is a prerequisite to the study of the interaction phenomena as related to spurious outputs. In particular perturbation techniques can be used to determine relative

field distributions. This experimental fact is well known, but perhaps not so well known is precisely how various parameters affect the amount and type of perturbation. Some effort has been made here to clarify this and to show the limitations on absolute measurements.

II. RESONANT CAVITY THEORY

It is always a difficult problem to treat a high-frequency circuit by means of the lumped-circuit type of analog. Invariably several ways of defining the lumped-circuit parameters arise, the three usual ones being the following:

- (1) definitions based on geometry,
- (2) definitions based on stored energy,
- (3) definitions based on "equivalent" admittances.

The model used here to represent the microwave cavity is the one based on "equivalent" admittances. Essentially, this will involve finding the electromagnetic fields as a series summation for different regions of the cavity and then matching these solutions at the boundaries between the regions. Then as an aid in using these field expansions, admittance functions are defined so that the absolute value of the total admittance function is a minimum at a cavity resonance. This treatment idealizes the cavity structure to be lossless so that these minima correspond to true zeros of the total admittance function. This means that the model consists of a sequence of ideal, parallel, resonant, lumped circuits. In fact some of the properties of these two resonant devices are very similar.

The cavity geometry of particular interest is the doubly re-entrant gridless-gap type, which is the one usually associated with high-power klystrons. A typical cavity with its co-ordinate system is shown in Figure 1.

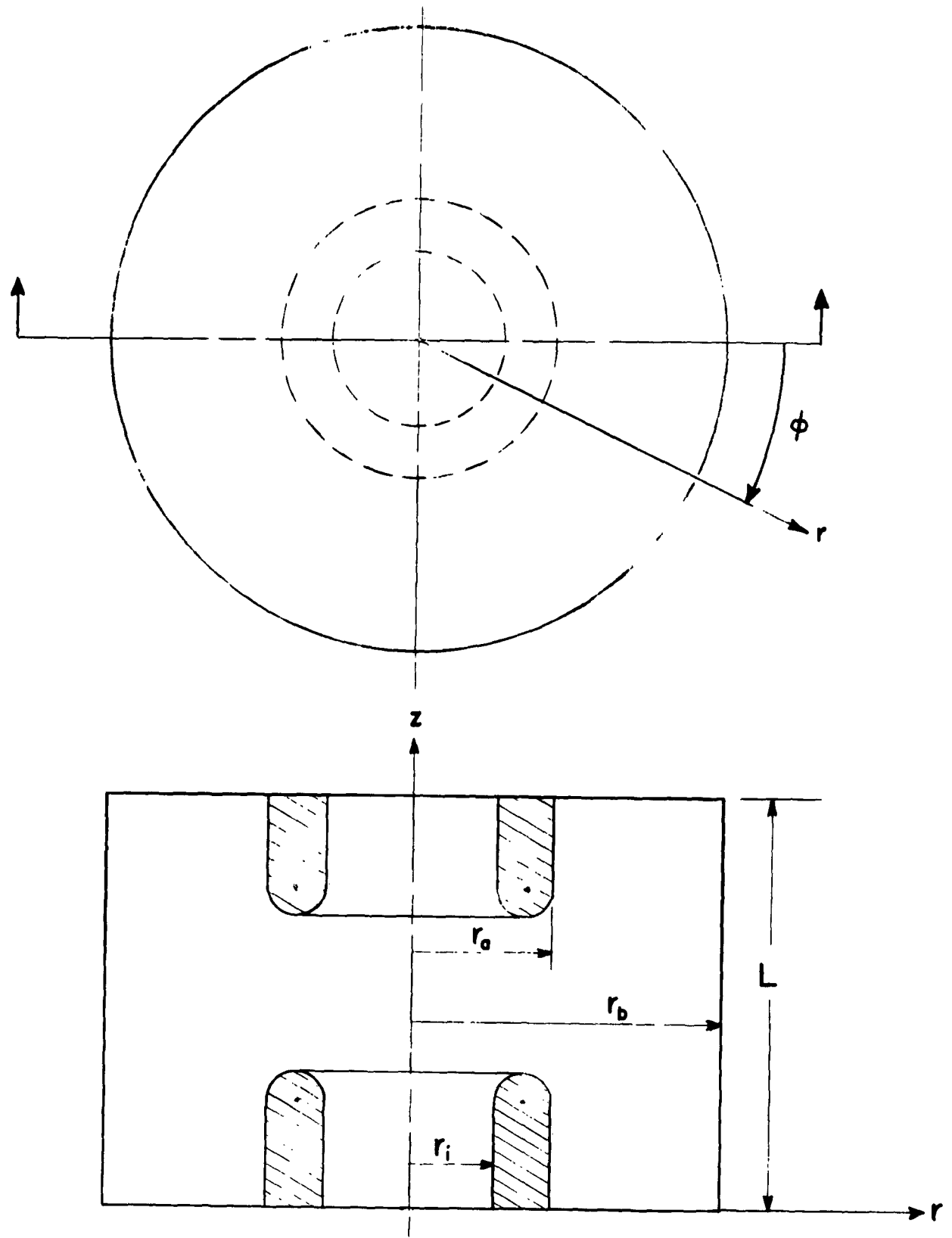


Figure 1. Co-ordinate System for Cavities.

For finding the field expansions, the cavity may be divided into two regions:

- 1) The region external to the drift tubes, henceforth called region 1. The range of r is $r_a \leq r \leq r_b$.
- 2) The region inside the outer radius of the drift tubes, henceforth called region 2. The range of r is $0 \leq r \leq r_a$.

The physical structure of the cavity lends itself well to a radial-line treatment, which is the reason for the two-part division above.

Region 1 corresponds to a radial line which is short-circuited at the outer radius, while region 2 involves the "capacitive" loading placed on this line.

The usual fundamental mode of oscillation of this cavity is the coaxial line TM_{010} mode, where the subscripts indicate the spatial variations (of the electromagnetic fields) in the ϕ , r , and z directions respectively and the TM refers to the transverse-magnetic type of mode, that is, one having no component of the magnetic field in the z direction. When used as an output device this type of cavity is excited by means of a z -directed electric field located in the gap region. This type of excitation can only couple to modes having a z component of electric field, so that the higher order resonant modes will also be of the TM type. Since the first region of this cavity is treated as a radial line, the above nomenclature may be confusing in that it applies to the transverse area dimensions r , ϕ while the radial line has transverse area dimensions ϕ , z . It would therefore be convenient to develop a nomenclature that would apply to the radial line. Since a nomenclature for the radial line has not been standarized yet, the following somewhat arbitrary definitions are adopted:

TEM mode — the mode which has electromagnetic field components only in the area transverse to the direction of propagation, i. e., only E_z and H_ϕ exist.

H_{mnp} mode — $H_z = 0$, subscripts refer to the spatial variations of the electromagnetic field in the z , ϕ , and r directions respectively.

E_{mnp} mode — $E_z = 0$, these correspond to the coaxial line TE modes and will not be used.

Thus it is apparent that the TEM mode corresponds to the coaxial line TM_{010} mode, while the H_{mnp} modes correspond to the coaxial line TM_{npl} modes. From this point on all mode designations are in terms of the radial-line nomenclature unless otherwise specified.

A. THEORETICAL ANALYSIS

Maxwell's equations may be solved in the cavity subject to the boundary conditions to give the electromagnetic field expansions in the form of series summations. From these field expansions, voltages and currents may be defined and the admittance function associated with the cavity resonances can then be obtained. One must, of course be consistent in these definitions; i. e., all voltages and currents must be defined at one particular reference "plane" or, as it turns out in this case, at one value of radius. The reference "plane" used here is the cylinder located at the outer radius of the drift tubes. For the principal part of this analysis symmetry in the ϕ direction is assumed, since this is how these cavities are theoretically designed to operate. However, it would also be of interest to include a treatment of nonsymmetrical

operation, since perturbations such as structural imperfections, and the tuners and antenna one invariably inserts in these cavities can easily excite nonsymmetrical modes. A first approximation to this nonsymmetrical operation is made in a later section, where a rather artificial technique is used to introduce the nonsymmetrical modes.

The assumptions made in the following derivation are quite usual, and are good approximations for the practical cavity which is either lightly loaded or symmetrically loaded. The conductivity of the metal walls of the cavity is assumed infinite and, most important, the gap edges are assumed to be square. The one further assumption (as mentioned above) is that perfect mechanical symmetry exists in the ϕ direction.

1. Cavity Admittance of Region 1

Since this region is to be treated as a short-circuited radial line, one need not begin with Maxwell's basic equations; instead a modal analysis can be used. These radial-line modes themselves have been derived from Maxwell's equations, so there is no loss of generality in applying them directly.*

The general expressions for the field components in a radial-line cavity for the H type modes are as follows:

*This derivation or its method may be found in any elementary textbook on electromagnetics.

$$E_z = [A_m J_n(\beta_t r) + B_m H_n^{(1)}(\beta_t r)] \cos n\phi \cos \beta_z z e^{j\omega t},$$

$$E_\phi = -\frac{n\beta_z}{r\gamma_t^2} [A_m J_n(\beta_t r) + B_m H_n^{(1)}(\beta_t r)] \sin n\phi \sin \beta_z z e^{j\omega t},$$

$$E_r = \frac{\beta_z}{\gamma_t^2} \left[A_m \left(\frac{n J_n(\beta_t r)}{r} - \beta_t J_{n+1}(\beta_t r) \right) \right.$$

$$\left. + B_m \left(\frac{n H_n^{(1)}(\beta_t r)}{r} - \beta_t H_{n+1}^{(1)}(\beta_t r) \right) \right] \cos n\phi \sin \beta_z z e^{j\omega t},$$

$$H_z = 0,$$

$$H_\phi = j \frac{\omega \epsilon}{\gamma_t^2} \left[A_m \left(\frac{n J_n(\beta_t r)}{r} - \beta_t J_{n+1}(\beta_t r) \right) \right.$$

$$\left. + B_m \left(\frac{n H_n^{(1)}(\beta_t r)}{r} - \beta_t H_{n+1}^{(1)}(\beta_t r) \right) \right] \cos n\phi \cos \beta_z z e^{j\omega t},$$

$$H_r = j \frac{\omega \epsilon n}{r \gamma_t^2} \left[A_m J_n(\beta_t r) + B_m H_n^{(1)}(\beta_t r) \right] \sin n\phi \cos \beta_z z e^{j\omega t},$$

where

$$\beta_z = \frac{m\pi}{L}; \quad \gamma_t^2 = -\beta_t^2, \quad (2)$$

and β_t is the radial phase constant (wave number),

$$\beta_t^2 = \omega^2 \mu \epsilon - \left(\frac{m\pi}{L} \right)^2. \quad (3)$$

Actually, in Equation (1) there is a choice of $\cos n\phi$ or $\sin n\phi$ for E_z .

The only time these occur simultaneously (termed mode splitting) is when the circular cavity is slightly out of round or some other perturbation in the ϕ direction is present.

For symmetrical modes, when $n = 0$, Equation (1) becomes

$$\left. \begin{aligned}
 E_z &= [A_m J_0(\beta_t r) + B_m H_0^{(1)}(\beta_t r)] \cos \beta_z z e^{j\omega t}, \\
 E_\phi &= 0, \\
 E_r &= \frac{\beta_z}{\beta_t} [A_m J_1(\beta_t r) + B_m H_1^{(1)}(\beta_t r)] \sin \beta_z z e^{j\omega t}, \\
 H_z &= 0, \\
 H_\phi &= j \frac{\omega \epsilon}{\beta_t} [A_m J_1(\beta_t r) + B_m H_1^{(1)}(\beta_t r)] \cos \beta_z z e^{j\omega t}, \\
 H_r &= 0.
 \end{aligned} \right\} \quad (4)$$

These equations now specify modes of the H_{m0p} type. The particular mode with $m = 0$ has $E_r = 0$ and is the TEM mode. At this point the meaning of "P variations in r " may not appear clear. This corresponds to having P variations in the standing wave pattern in the longitudinal direction of a rectangular cavity which is resonating.

Equation (4) can now be applied to the cavity. Figure 2 shows a section of the cavity and its dimensions. To find the coefficients A_m and B_m in Equation (4), a field may be assumed at the gap.

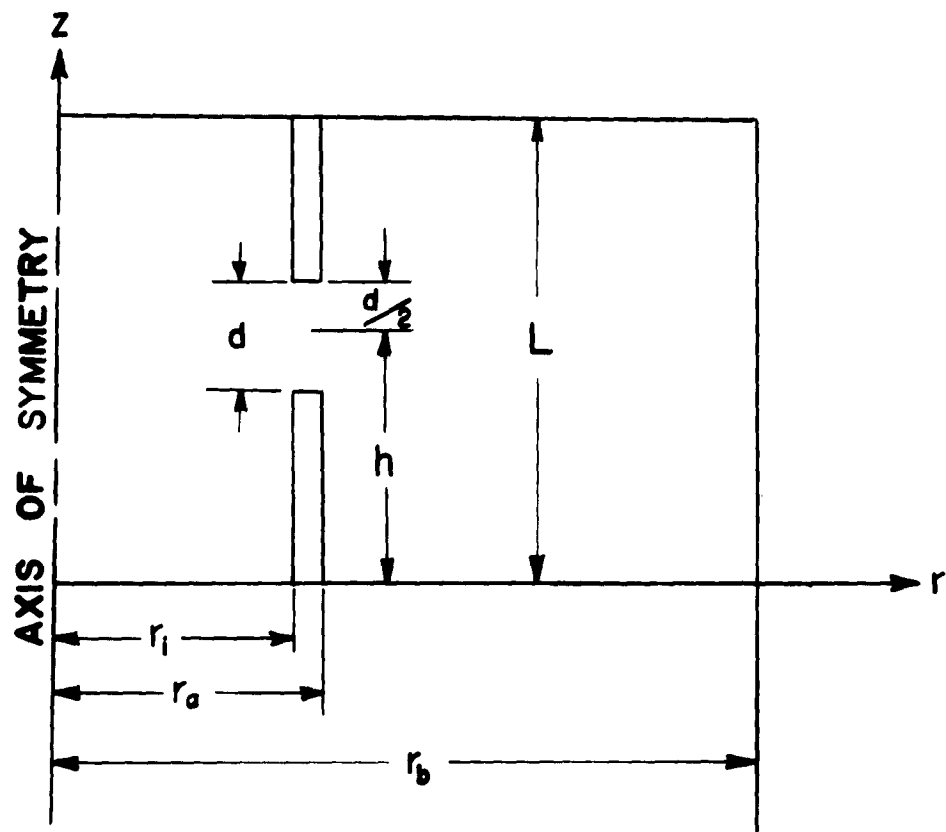


Figure 2. Cross-Section of Cylindrical Cavity Showing Dimensions.

From this same assumed field a voltage at the gap can be defined.

Then knowing H_ϕ , a current may be defined which can be used to give us the admittance associated with the short-circuited radial line.

For simplicity the actual field that will exist at the gap is approximated by a constant as follows:

$$E_z \Big|_{r_a} = E_0 e^{j\omega t} \quad . \quad (5)$$

Figure 3 shows the relationship between this assumed field and the true field.

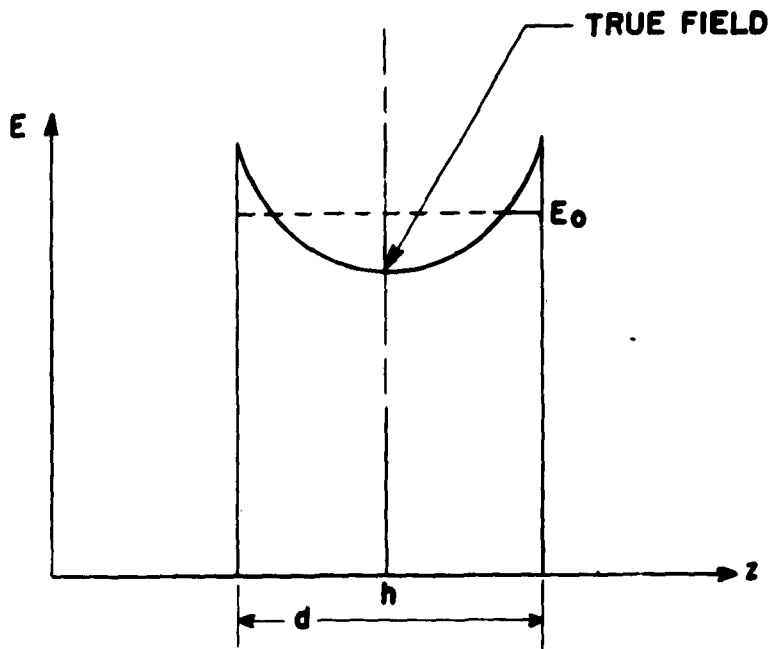


Figure 3. Assumed and True Gap Field.

For region 1 (in Figure 2, the region between r_a and r_b), the field coefficients can be found by knowing E and H at a particular value of radius, or by knowing one of these at two values of radius. Here the latter is chosen since E_z at r_a is known by Equation (5), and

since E_z at r_b is zero to match the boundary conditions. These conditions and Equation (4) give:

$$E_z \Big|_{r_a} = E_0 e^{j\omega t} = \sum_{m=0}^{\infty} [A_m J_0(\beta_t r_a) + B_m H_0^{(1)}(\beta_t r_a)] \cos\left(\frac{m\pi z}{L}\right) e^{j\omega t}, \quad (6)$$

and

$$E_z \Big|_{r_b} = 0 = \sum_{m=0}^{\infty} [A_m J_0(\beta_t r_b) + B_m H_0^{(1)}(\beta_t r_b)] \cos\left(\frac{m\pi z}{L}\right) e^{j\omega t}, \quad (7)$$

which now include a sum over all the possible modes allowed. Because of the orthogonal properties of $\cos\left(\frac{m\pi}{L} z\right)$, $m = 0, 1, 2, \dots$, over the transverse area both of these equations can be multiplied by a particular $\cos\left(\frac{m\pi}{L} z\right)$, integrated over the transverse area, and have one term left on the right hand side. Thus Equation (7) gives

$$A_m = \frac{-B_m H_0^{(1)}(\beta_t r_b)}{J_0(\beta_t r_b)} \quad (m = 0, 1, 2, \dots), \quad (8)$$

and Equation (6) becomes

$$\int_{h - \frac{d}{2}}^{h + \frac{d}{2}} E_0 \cos\left(\frac{m\pi}{L} z\right) dz = \int_0^L [A_m J_0(\beta_t r_a) + B_m H_0^{(1)}(\beta_t r_a)] \cos^2\left(\frac{m\pi}{L} z\right) dz,$$

$$\frac{2LE_0}{m\pi} \cos\left(\frac{m\pi h}{L}\right) \sin\left(\frac{m\pi d}{2L}\right) = [A_m J_0(\beta_t r_a) + B_m H_0^{(1)}(\beta_t r_a)] \frac{L}{2} ,$$

which holds for $m \neq 0$. The result is two equations with two unknowns

A_m and B_m . Solving for B_m gives the following:

$$B_m = \frac{J_0(\beta_t r_b) \frac{4E_0}{m\pi} \cos\left(\frac{m\pi h}{L}\right) \sin\left(\frac{m\pi d}{2L}\right)}{H_0^{(1)}(\beta_t r_a) J_0(\beta_t r_b) - H_0^{(1)}(\beta_t r_b) J_0(\beta_t r_a)} \quad (m \neq 0) , \quad (9)$$

$$B_0 = \frac{J_0(\beta r_b) \frac{E_0 d}{L}}{H_0^{(1)}(\beta r_a) J_0(\beta r_b) - H_0^{(1)}(\beta r_b) J_0(\beta r_a)} , \quad (10)$$

$$\text{where } \beta^2 = \beta_t^2 \Big|_{m=0} = \omega^2 \mu \epsilon$$

Equations (8), (9), and (10) give the coefficients of Equation (4) so that the complete fields in the cavity are now known. The voltage at the gap follows immediately from Equation (5) as follows:

$$V_{GAP} = -E_0 d e^{j\omega t} . \quad (11)$$

The current induced at the gap may be found from an integration of H_ϕ over the gap area as follows:

$$I_{GAP} = \int_A \frac{H_\phi}{d} dA = \frac{2\pi r_a}{d} \int_{h - \frac{d}{2}}^{h + \frac{d}{2}} H_\phi d_z . \quad (12)$$

Substituting for H_ϕ from Equation (4) and inserting the series coefficients just calculated, gives

$$I_{\text{GAP}} = j \frac{\omega \epsilon 2\pi r_a E_0 d}{\beta L} \left[\frac{-H_0^{(1)}(\beta r_b) J_1(\beta r_a) + H_1^{(1)}(\beta r_a) J_0(\beta r_b)}{H_0^{(1)}(\beta r_a) J_0(\beta r_b) - H_0^{(1)}(\beta r_b) J_0(\beta r_a)} \right] e^{j\omega t}$$

$$+ j \frac{\omega \epsilon E_0 16 r_a L}{\pi d} \sum_{m=1}^{\infty} \left[\frac{-H_0^{(1)}(\beta_{ta}) J_1(\beta_{tb}) + H_1^{(1)}(\beta_{tb}) J_0(\beta_{ta})}{H_0^{(1)}(\beta_{ta}) J_0(\beta_{tb}) - H_0^{(1)}(\beta_{tb}) J_0(\beta_{ta})} \right] \frac{\cos^2\left(\frac{m\pi h}{L}\right) \sin^2\left(\frac{m\pi d}{2L}\right)}{m^2 \beta_t} e^{j\omega t}$$
(13)

From Equation (3) β_t becomes

$$\beta_t = \omega \sqrt{\mu \epsilon} \sqrt{1 - \left(\frac{m\pi}{L \omega \sqrt{\mu \epsilon}} \right)^2} .$$

However, the cutoff frequency for the m th mode is

$$\omega_m = \frac{m\pi}{L \sqrt{\mu \epsilon}} , \quad (14)$$

so that β_t becomes

$$\beta_t = \beta \sqrt{1 - \left(\frac{\omega_m}{\omega} \right)^2} , \quad (15)$$

In calculating the admittance, it is convenient to normalize with respect to

$$Y_0 = \frac{2\pi r_a}{\sqrt{\frac{\mu}{\epsilon} L}} . \quad (16)$$

The admittance is found by using Equations (11), (13), (15) and (16) as follows:

$$y = \frac{I_{GAP}}{V_{GAP}} \quad \frac{1}{Y_0} = j \frac{B}{Y_0} \quad ,$$

$$y = -j \left[\frac{H_1^{(1)}(\beta_{r_a}) J_0(\beta_{r_b}) - H_0^{(1)}(\beta_{r_b}) J_1(\beta_{r_a})}{H_0^{(1)}(\beta_{r_a}) J_0(\beta_{r_b}) - H_0^{(1)}(\beta_{r_b}) J_0(\beta_{r_a})} \right]$$

$$-j \frac{8L^2}{\pi d^2} \sum_{m=1}^{\infty} \left[\frac{H_1^{(1)}(\beta_{t_a}) J_0(\beta_{t_b}) - H_0^{(1)}(\beta_{t_b}) J_1(\beta_{t_a})}{H_0^{(1)}(\beta_{t_a}) J_0(\beta_{t_b}) - H_0^{(1)}(\beta_{t_b}) J_0(\beta_{t_a})} \right] \frac{\cos^2\left(\frac{m\pi h}{L}\right) \sin^2\left(\frac{m\pi d}{2L}\right)}{m^2 \sqrt{1 - \left(\frac{\omega_m}{\omega}\right)^2}}$$

(17)

In the form given this equation applies strictly to the "propagating" modes, where a "propagating" mode is defined as having $\omega > \omega_m$. However, there will certainly be modes for which $\omega < \omega_m$ is true and these modes are called "cutoff." Equation (17) can be written to apply directly to all modes by using the proper value of the radial phase constant β_t for the cutoff modes. This value is

$$\beta_{\text{cutoff modes}} = -j \beta \sqrt{\left(\frac{\omega_m}{\omega}\right)^2 - 1} \quad . \quad (18)$$

Using the modified Bessel functions

$$I_n(x) = j^{-n} J_n(jx) \quad , \quad (19)$$

$$K_n(x) = \frac{\pi}{2} j^{n+1} H_n^{(1)}(jx) \quad ,$$

and making the substitution

$$\beta_t' = \beta \sqrt{\left(\frac{\omega_m}{\omega}\right)^2 - 1} \quad . \quad (20)$$

where the negative sign of Equation (18) is now taken into account by realizing that

$$\begin{aligned} J_0(-x) &= J_0(x) \quad , & H_0^{(1)}(-x) &= H_0^{(1)}(x) \quad , \\ J_1(-x) &= -J_1(x) \quad , & H_1^{(1)}(-x) &= -H_1^{(1)}(x) \quad , \end{aligned} \quad (21)$$

one can find the admittance function which accounts for all the modes in region 1:

$$\begin{aligned}
y = & -j \sqrt{\frac{H_1^{(1)}(\beta_{r_a}) J_0(\beta_{r_b}) - H_0^{(1)}(\beta_{r_b}) J_1(\beta_{r_a})}{H_0^{(1)}(\beta_{r_a}) J_0(\beta_{r_b}) - H_0^{(1)}(\beta_{r_b}) J_0(\beta_{r_a})}} \\
& - j \frac{8L^2}{\pi^2 d^2} \sum_{m=1}^K \left[\frac{H_1^{(1)}(\beta_{t' r_a}) J_0(\beta_{t' r_b}) - H_0^{(1)}(\beta_{t' r_b}) J_1(\beta_{t' r_a})}{H_0^{(1)}(\beta_{t' r_b}) J_0(\beta_{t' r_b}) - H_0^{(1)}(\beta_{t' r_b}) J_0(\beta_{t' r_a})} \right] \frac{\cos^2\left(\frac{m\pi h}{L}\right) \sin^2\left(\frac{m\pi d}{2L}\right)}{m^2 \sqrt{1 - \left(\frac{\omega_m}{\omega}\right)^2}} \\
& + j \frac{8L^2}{\pi^2 d^2} \sum_{m=K+1}^{\infty} \left[\frac{K_1(\beta_{t' r_a}) I_0(\beta_{t' r_b}) + K_0(\beta_{t' r_b}) I_1(\beta_{t' r_a})}{K_0(\beta_{t' r_a}) I_0(\beta_{t' r_b}) - K_0(\beta_{t' r_b}) I_0(\beta_{t' r_a})} \right] \frac{\cos^2\left(\frac{m\pi h}{L}\right) \sin^2\left(\frac{m\pi d}{2L}\right)}{m^2 \sqrt{\left(\frac{\omega_m}{\omega}\right)^2 - 1}}
\end{aligned} \tag{22}$$

In this equation the first K modes are "propagating" while all the higher modes are cutoff.

Before Equation (22) is actually used, it must converge. The only term that requires checking is the third, since this is the only infinite summation. From Equation (20),

$$\lim_{m \rightarrow \infty} \beta_t' = \lim_{m \rightarrow \infty} \beta \frac{m \omega_1}{\omega} , \quad (23)$$

where ω_1 is the first cutoff frequency and

$$\omega_m = m \omega_1 ,$$

which follows from Equation (14). It is also known that as the argument becomes large, the modified Bessel functions become

$$\begin{aligned} I_n(x) &\longrightarrow \sqrt{\frac{1}{2\pi x}} e^x & , \\ x \longrightarrow \infty & & \\ K_n(x) &\longrightarrow \frac{\pi}{2} \sqrt{\frac{2}{\pi x}} e^{-x} & . \\ x \longrightarrow \infty & & \end{aligned} \quad (24)$$

With the aid of Equations (23) and (24) it follows that:

$$\begin{aligned} \lim_{m \rightarrow \infty} & \left[\frac{K_1(\beta_t' r_a) I_0(\beta_t' r_b) + K_0(\beta_t' r_b) I_1(\beta_t' r_a)}{K_0(\beta_t' r_a) I_0(\beta_t' r_b) - K_0(\beta_t' r_b) I_0(\beta_t' r_a)} \right] \frac{\cos^2 \left(\frac{m\pi h}{L} \right) \sin^2 \left(\frac{m\pi d}{2L} \right)}{m^2 \sqrt{\frac{m\omega_1}{\omega}}^2 - 1} \\ & = \lim_{m \rightarrow \infty} \left[\frac{\frac{-2\beta \frac{m\omega_1}{\omega} (r_b - r_a)}{1+e}}{\frac{-2\beta \frac{m\omega_1}{\omega} (r_b - r_a)}{1-e}} \right] \frac{\cos^2 \left(\frac{m\pi h}{L} \right) \sin^2 \left(\frac{m\pi d}{2L} \right)}{\frac{m^3 \omega_1}{\omega}} \\ & = \lim_{m \rightarrow \infty} \left[\frac{\cos^2 \left(\frac{m\pi h}{L} \right) \sin^2 \left(\frac{m\pi d}{2L} \right)}{\frac{m^3 \omega_1}{\omega}} \right] . \end{aligned} \quad (25)$$

The term $\frac{\omega_1}{\omega}$ in the denominator is common to all the terms from here on and may be dropped. Then, since

$$\cos^2\left(\frac{m\pi h}{L}\right) \sin^2\left(\frac{m\pi d}{2L}\right) \leq 1 ,$$

and $\frac{1}{m^3}$ is known to converge, the series in Equation (22) also converges, provided $\omega \neq \omega_m$. Unfortunately Equation (22) is in a form such that the usual "convergence techniques" cannot be applied conveniently; that is, the method of separating a low frequency admittance from the infinite summation rather than adding contributions to this admittance from the various modes is not applicable in this case. This means that a calculation of the effect of the cutoff modes must certainly be delegated to a digital computer since experience has shown that twenty or thirty terms of this series are required for any reasonable accuracy.

2. Cavity Admittance of Region 2

Region 2, as Figure 2 shows, can be divided into two subregions. The first is the region directly between the ends of the drift tubes, for the drift tubes do have finite thickness and the second is inside the drift tubes. To be strictly correct, one should find the admittance of the inner region at the inside of the gap edge and, by the use of the general radial line equations transform this admittance from r_i to r_a . Also, the distributed admittance between the ends of the drift tubes should be accounted for by use of these same equations. However, for the cavity usually met in practice, these effects can be approximated by finding the admittance of the inner region at the inner edge of the gap and adding this directly to the radial line admittance in Equation (22). This admittance is called the inner storage admittance. The second

region, between the drift tubes, can be considered to have a lumped admittance, thus treating it essentially like a parallel-plate capacitor. This admittance is called the annular admittance.

The inner storage admittance has previously been calculated by C. C. Wang⁴ in a manner consistent with the definition of admittance used here. He also makes the assumption of square gap edges and infinite wall conductivity, and makes the same approximation to the field between the drift tube edges that is used here (see Figure 3). However, Wang does put the further restriction on his solution that $\beta r_i < 2.405$ in order to eliminate modes that can propagate down the drift tubes in the z direction. This is not a serious limitation since no klystron would be operated with its fundamental frequency in this region. Wang also points out that, to be perfectly safe, one ought to have $\beta r_i < 1.84$ so that the circular wave guide TE_{11} mode will not propagate, since a slight dissymmetry may excite this. This again gives no real difficulty. Wang's expression, normalized by the use of Equation (16) and written in terms of the quantities used here, is as follows:

$$j b_i = j \frac{r_i}{r_a} \frac{L}{d} \left[\frac{J_1(\beta r_i)}{J_0(\beta r_i)} - \frac{2r_i}{d} \sum_{n=1}^{\infty} \frac{(\beta r_i)}{\xi^3} \left(1 - e^{-\frac{d}{r_i} \xi} \right) \right], \quad (26)$$

where $\xi^2 = R_n^2 - (\beta r_i)^2$, and R_n is the n th root of J_0 .

Generally then, for consideration of modes having symmetry in the ϕ direction, the expression in Equation (26) will hold for $\beta r_i < 2.405$. To calculate resonances above this point some other means of approximating

the fields inside the drift tubes is needed, or else one must be content with the approximation the rest of the admittance function gives by itself. In most cases, resonances up to the fourth harmonic of the signal frequency can be included and still be within the range stated above; resonances beyond this point are not considered here.

As a first approximation for the annular admittance, the expression for the parallel plate capacitor can be used. This expression yields the following:

$$y = jb_a = j \frac{\omega \epsilon \pi (r_a^2 - r_i^2)}{Y_0 d} = j \beta r_a \frac{L}{2d} \left[1 - \left(\frac{r_i}{r_a} \right)^2 \right] \quad (27)$$

At this point, a better approximation for this particular admittance is possible if one admits that the gap edges of the drift tubes are not square. In the usual cavity the gap edge is rounded so that, in a cross-sectional view, the edge will approximate a semicircle. The varying distance between the gap edges can be accounted for by a straightforward averaging process. Let the corrected gap width be d' . From Figure 4,

$$d' = \frac{\text{Area}}{2t} = d + t(2 - \frac{\pi}{2}) \quad , \quad (28)$$

where $2t = r_a - r_i$. Now simply replace d in Equation (27) by d' as given above.

The annular admittance just calculated applies strictly only when the cavity is resonating in the TEM mode and does not apply directly for the higher-order resonances. However, this expression is used here when calculating the higher-order resonances since it does provide a reasonable approximation.

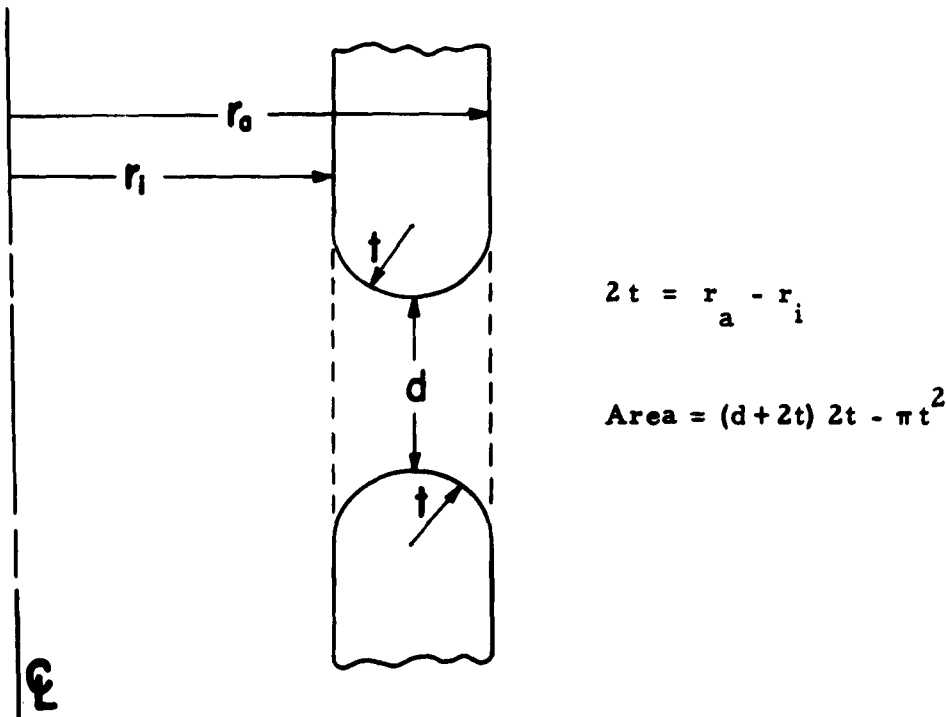


Figure 4. Average Gap Width for Rounded Edges.

3. The Total Admittance Function

All of the cavity admittances associated with the resonances have now been calculated. Each of the expressions can be combined to form a total admittance function or a "resonance equation", so called since the fundamental cavity resonance occurs at the first zero of this function. Before combining the admittance terms, shorthand techniques can be employed to simplify some of the expressions. In particular, the cavity admittance of region 1 is especially cumbersome to write, to say nothing of calculating this in the form given. Examining the expression for the TEM mode admittance in Equation (22), one can substitute for the Hankel functions as follows:

$$H_n^{(1)}(x) = J_n(x) + j N_n(x) \quad , \quad (29)$$

and obtain

$$\frac{H_1^{(1)}(\beta r_a) J_0(\beta r_b) - H_0^{(1)}(\beta r_b) J_1(\beta r_a)}{H_0^{(1)}(\beta r_a) J_0(\beta r_b) - H_0^{(1)}(\beta r_b) J_0(\beta r_a)} = \frac{N_1(\beta r_a) J_0(\beta r_b) - N_0(\beta r_b) J_1(\beta r_a)}{N_0(\beta r_a) J_0(\beta r_b) - N_0(\beta r_b) J_0(\beta r_a)} . \quad (30)$$

If a plot of this quantity is made as a function of $\beta(r_b - r_a)$, it is very similar to the circular cotangent function with $\beta(r_b - r_a)$ as an argument.

In fact at large values of this argument, the expression in Equation (30) approaches the value of the cotangent as an "asymptote." Because of the similarity of these two quantities, we shall venture to call the expression in Equation (30) the Bessel cotangent function of zeroth order, and define it as follows:

$$b \cot_0 \beta(r_b - r_a) = \frac{N_1(\beta r_a) J_0(\beta r_b) - N_0(\beta r_b) J_1(\beta r_a)}{N_0(\beta r_a) J_0(\beta r_b) - N_0(\beta r_b) J_0(\beta r_a)} . \quad (31)$$

In addition, for aid in computation one may write this as

$$b \cot_0 \beta(r_b - r_a) = b \cot_0 \beta r_a (a - 1) , \quad (32)$$

where $a = \frac{r_b}{r_a}$.

Figure 5 shows a comparison between the Bessel cotangent function and the circular cotangent function for $a = 2$. The similarity mentioned earlier is very apparent in this plot. Figure 6 shows the absolute value

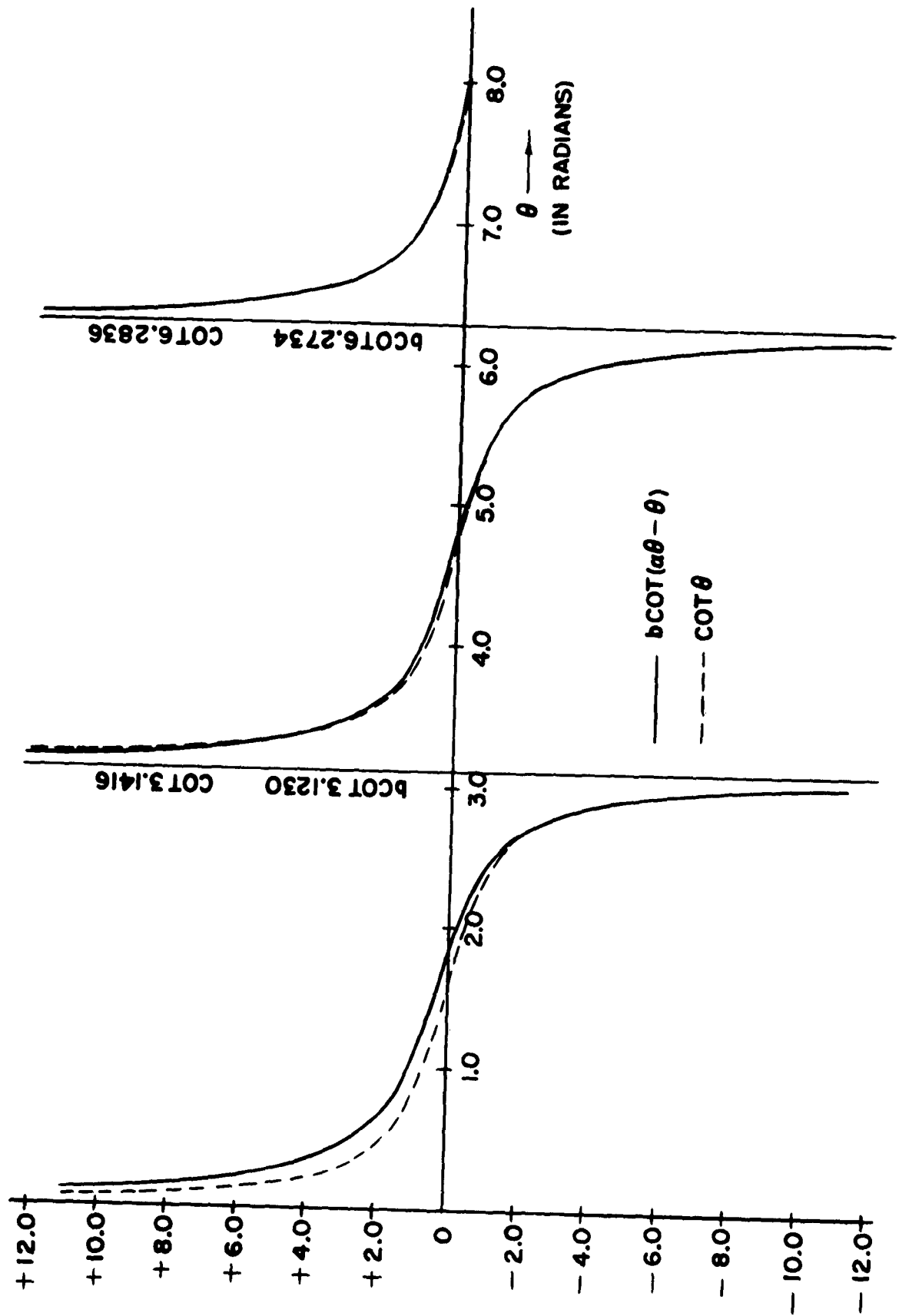


Figure 5. Comparison of $b \cot_0 (\alpha \theta - \theta)$ and $\cot \theta$ for $\alpha = 2.0$.

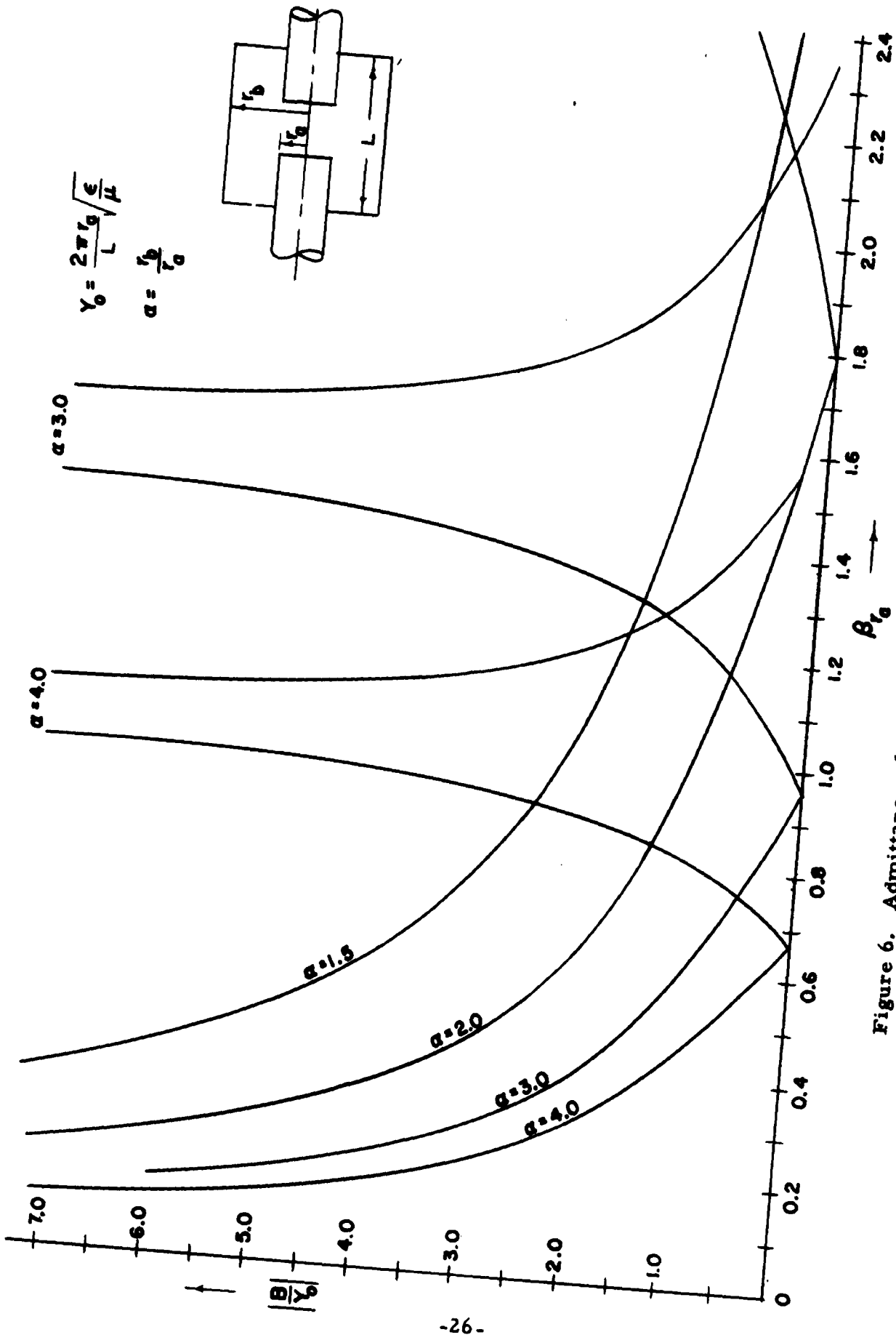


Figure 6. Admittance of a Short-Circuited Radial Line.

of $b \cot_{0 a} \beta r (a - 1)$ plotted as a function of βr_a for several values of a . This also represents the absolute value of the TEM mode admittance for a short-circuited radial line, hence Figure 6 is so labeled.

As it turns out, there are more combinations of Bessel functions which are similar to other trigonometric functions, such as the Bessel sine and cosine functions. These two sets of functions also have many similar properties; for example, the following is true for the Bessel cotangent function:

$$b \cot(b - a) = \frac{b \cos(b - a)}{b \sin(b - a)} .$$

In addition, Bessel hyperbolic trigonometric functions can be derived from the Bessel circular trigonometric functions as follows:

$$b \coth(b - a) = j \frac{b \cos j(b - a)}{b \sin j(b - a)} = j b \cot j(b - a) ,$$

where $b \coth$ is the Bessel hyperbolic cotangent function. Substituting the quantities in the equation above in terms of modified Bessel functions gives

$$b \coth(b - a) = \left[\frac{K_1(a) I_0(b) + K_0(b) I_1(a)}{K_0(a) I_0(b) - K_0(b) I_0(a)} \right] . \quad (33)$$

This is just the form of the part of Equation (22) dealing with the cutoff modes. At large values of argument this function asymptotically approaches the value of one just as the hyperbolic cotangent function does. A comparison between the $b \coth$ and \coth functions is shown in Figure 7. Figure 8 shows the $b \coth$ function for several values of a .

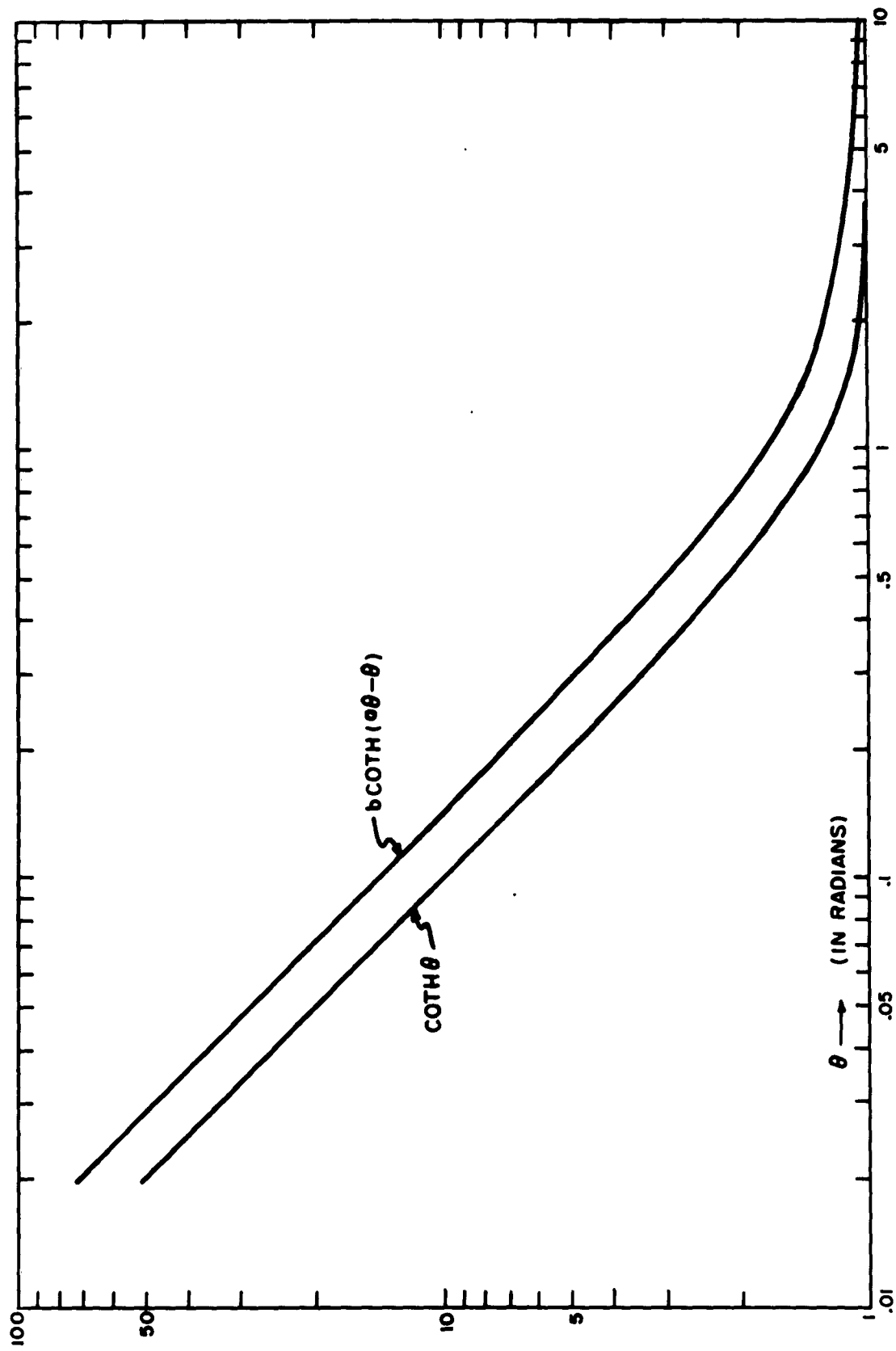


Figure 7. Comparison of $b \cot(\alpha \theta - \theta)$ and $\cot \theta$ for $\alpha = 2$.

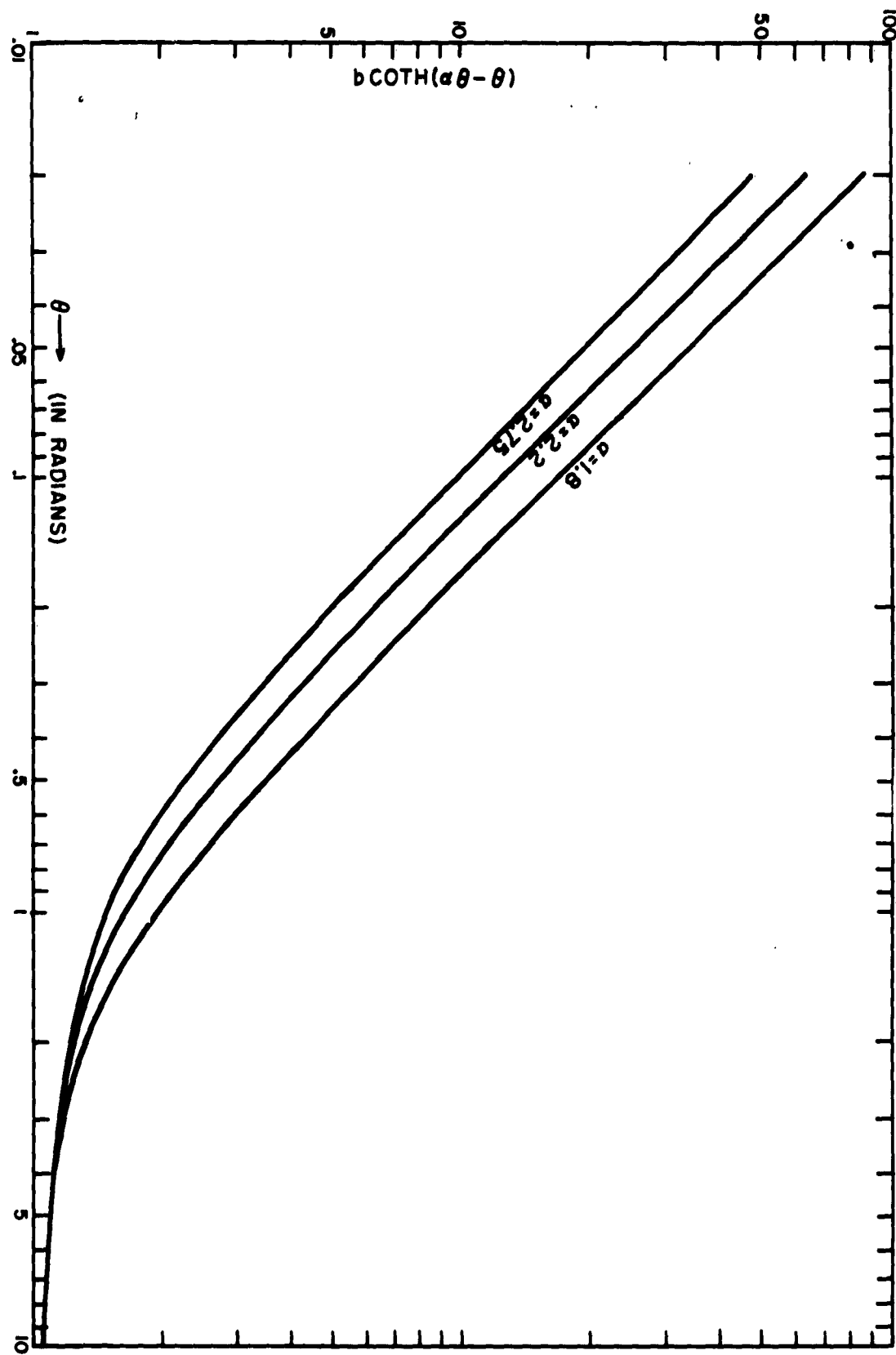


Figure 8. Bessel Hyperbolic Cotangent Function $b \coth(\alpha\theta - \theta)$.

Now by combining all the admittance terms and making the substitutions for the Bessel functions just discussed, the so-called "resonance equation" is obtained:

$$\begin{aligned}
 y = & -j b \cot_0 [\beta r_a (\alpha - 1)] - j \frac{8L^2}{\pi^2 d^2} \sum_{m=1}^K \frac{b \cot_0 [\beta_t r_a (\alpha - 1)] \cos^2 \left(\frac{m\pi h}{L} \right) \sin^2 \left(\frac{m\pi d}{2L} \right)}{m^2 \sqrt{1 - (\omega_m/\omega)^2}} \\
 & + j \frac{8L^2}{\pi^2 d^2} \sum_{m=K+1}^{\infty} \frac{b \coth [\beta_t r_a (\alpha - 1)] \cos^2 \left(\frac{m\pi h}{L} \right) \sin^2 \left(\frac{m\pi d}{2L} \right)}{m^2 \sqrt{(\omega_m/\omega)^2 - 1}} \\
 & + j \frac{r_i}{r_a} \frac{L}{d} \left[\frac{J_1(\beta r_i)}{J_0(\beta r_i)} - \frac{2r_i}{d} \sum_{n=1}^{\infty} \frac{(\beta r_i)}{\xi^3} \left(\frac{d\xi}{r_i} \right)^2 \right] \\
 & + j \frac{\beta r_a L}{2d} \left[1 - \left(\frac{r_i}{r_a} \right)^2 \right] \quad . \tag{34}
 \end{aligned}$$

Finally, the resonances may be found by determining the values of frequency and the conditions on the parameters which give the zeros of this total admittance function. The simplest way to find the values of the parameters that meet this condition is to solve the resonance equation graphically.

The procedure adopted for this graphic solution is to plot the absolute value of each of the admittance terms as a function of βr_a . Then the intersection of the total inductive and capacitive curves indicates a resonance. This procedure is used in lieu of a chart or nomograph type of presentation because of the large number of parameters involved and consequently the extensive calculation that would

be necessary. This graphic procedure does not seriously limit the accuracy in finding resonances, for once one is familiar with the type of curves, all that need be plotted is a small section of each curve in the region of resonance. This of course may be on an expanded scale so that graphic errors can be on the same order of magnitude as any error inherent in the resonance equation.

As an aid in using Equation (34), several parts of it have been calculated and are included here. The TEM admittance function is shown in Figure 6. In addition, the Appendix includes a short table for noninteger values of a , and integer values of a are given by Marcuvitz.^{5*} Figure 6 shows that the short-circuited radial line behaves just like any other short-circuited wave guide; that is, if one looks at the short circuit in the plane of the short circuit, the admittance is infinite. Then as one proceeds away from the short circuit, first the short circuit appears inductive and finally the admittance goes to zero; then the admittance becomes capacitive and goes to infinity again. Then the cycle repeats itself. The same behavior can be observed at a fixed position in the line by increasing the frequency from zero. The important difference between the radial line and an ordinary guide (rectangular or coaxial) is that the admittance discontinuities do not appear at an integer number of half-guide wavelengths from the short circuit. The expression guide wavelength is meaningless in a radial line due to the ever-changing transverse area. Also in Figure 6 it should be pointed out that since the absolute value of the admittance function is plotted, the inductive parts have a negative slope while the capacitive parts

⁵ Marcuvitz calls the " $b \cot_0$ " function the "ct" function.

have a positive slope. In the actual use of these curves, it is convenient to remember this.

The second term of Equation (34) deals with the "propagating" higher-order mode admittance. These modes behave essentially as the TEM admittance does, except that the modes do not appear until the frequency is above the cutoff frequency for any particular mode. These modes add another set of discontinuities to the admittance plot at $\omega = \omega_m$ for $m = 1, 2, 3, \dots$. Note that if the gap is exactly centered, $\frac{h}{L} = \frac{1}{2}$, then only the even-numbered modes are excited. However it has been standard practice in such a case to include the discontinuities of the odd modes on the admittance plot, for the physical cavity will never have the gap exactly centered and a resonance is possible no matter how weak. This admittance term should be calculated for each particular cavity; although an attempt has been made to produce a universal type of curve for this which may be used as an initial approximation. This curve is shown in Figure 9. This has been calculated for a centrally located gap in a doubly re-entrant cavity and is the inductive part of the second higher-order mode for which $m = 2$. The type of nomenclature involving R and x will be discussed in the section on optimum cavity design (II-D). The value

$$2\pi R = \frac{2\pi r_a}{\frac{L}{R}}$$

is merely the value of βr_a for the $m = 2$ cutoff. From Equation (14),

$$\omega_2 = \frac{2\pi}{L\sqrt{\mu\epsilon}},$$

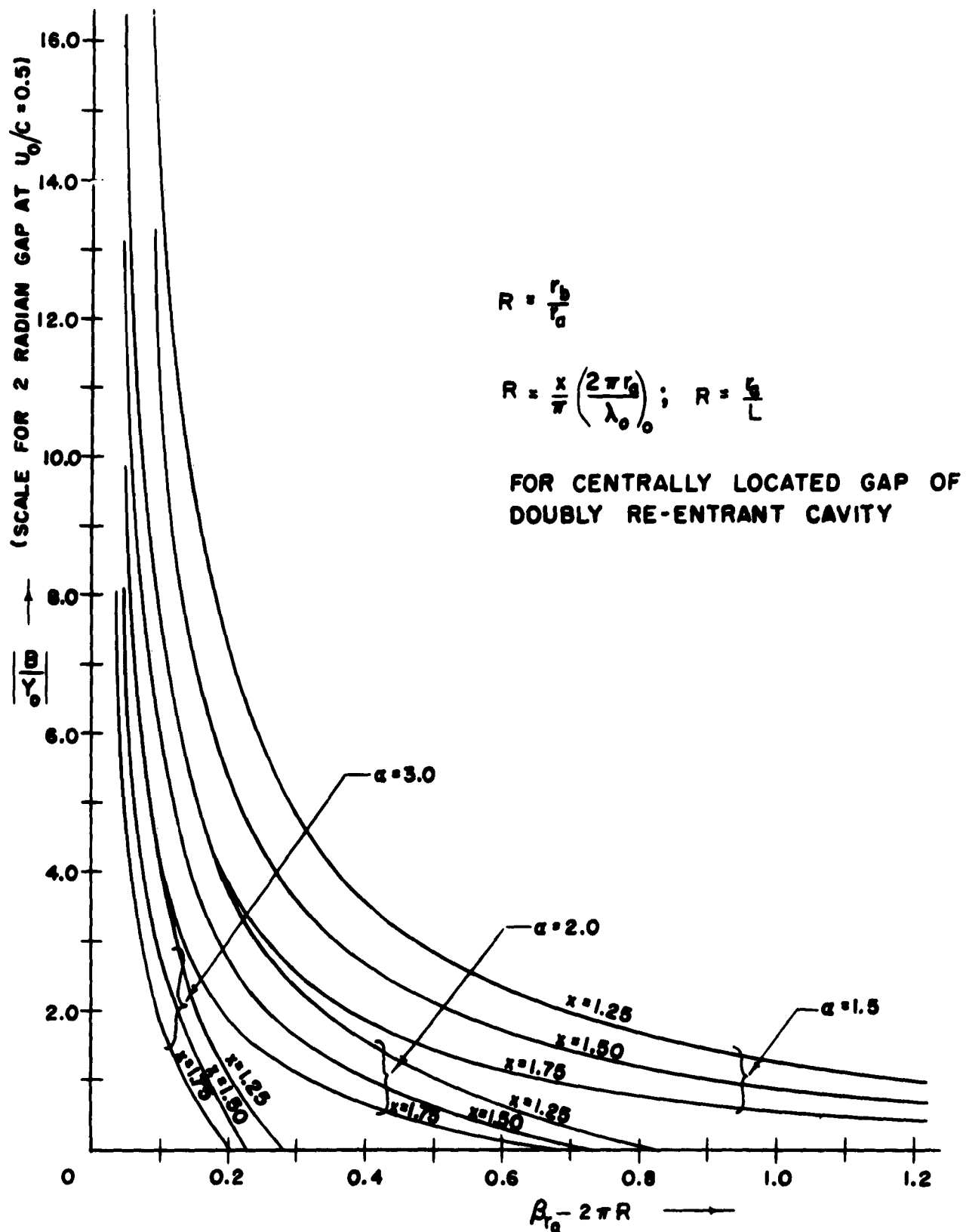


Figure 9. Universal Curve Second-Order Higher Mode Inductive Susceptance.

or

$$\omega_2 \sqrt{\mu\epsilon} r_a = \beta r_a = \frac{2\pi r_a}{L} \quad . \quad (35)$$

Since the graphs presented here cannot be used with any accuracy, a table of this higher-mode admittance is included in the Appendix as Table A-2. The table has been calculated on the basis of a two-radian gap at $u_0/c = 0.5$ (u_0 is the d-c beam velocity). A method for adjusting the values in this table for other gap lengths is also shown in the Appendix.

The third term of Equation (34) involves the admittance due to the energy storage in the fields of the cutoff modes about the gap. This term has discontinuities in it, for as the frequency increases, each successive mode will "pop" into "propagation" and will no longer contribute to this term. Little can be done in presenting curves of this admittance term because of the large numbers of parameters and because it is particularly sensitive to the value of cutoff frequency, or to the ratio r_a/L which is related to this frequency. Because of the large number of terms needed in this series a computer solution is almost a necessity. No known tables of the Bessel hyperbolic cotangent function exist, so this part is probably best calculated separately then approximated by curve-fitting techniques for use in a digital computer. The data for the different values of a used so far, as well as the range of errors involved in the curve fittings, are presented in Table A-3 in the Appendix. As previously mentioned, twenty to thirty terms of the series are required to keep the error in the series summation on the same order of magnitude as that in the approximations for the $b \coth$ function, which is less than one per cent.

The fourth term in Equation (34) is the inner storage admittance discussed previously. This has been calculated for all cases and is shown in Figure 10. The admittance multiplied by r_a/L is plotted as a function of βr_i with $\frac{d}{2r_i}$ as a parameter. For actual use a table with this same information, Table A-4, is given in the Appendix. When using this admittance on a plot of the "resonance equation" the abscissa must be changed from βr_i to βr_a , which is a trivial conversion.

The final term in Equation (34) is the annular admittance term. As is easily seen, this is a straight line and no difficulties are presented in using it.

Besides the value of frequency at the different resonances, Equation (34) can give the value of R_{sh}/Q_0 at the fundamental resonance. At the resonant frequency ω_0

$$\omega_0 L = \frac{R_{sh}}{Q_0} \quad . \quad (36)$$

Then the point of intersection indicating the fundamental resonance on the plot of the absolute value of the "resonance equation" is b_0 ,

$$b_0 = \frac{1}{\omega_0 L Y_0} \quad . \quad (37)$$

Combining Equation (36) and (37) gives

$$\frac{R_{sh}}{Q_0} = \frac{1}{b_0 Y_0} \quad , \quad (38)$$

where Y_0 is the normalizing admittance given in Equation (16).

4. Nonsymmetrical Higher-Order Modes

The assumption of symmetry in the ϕ direction of a klystron

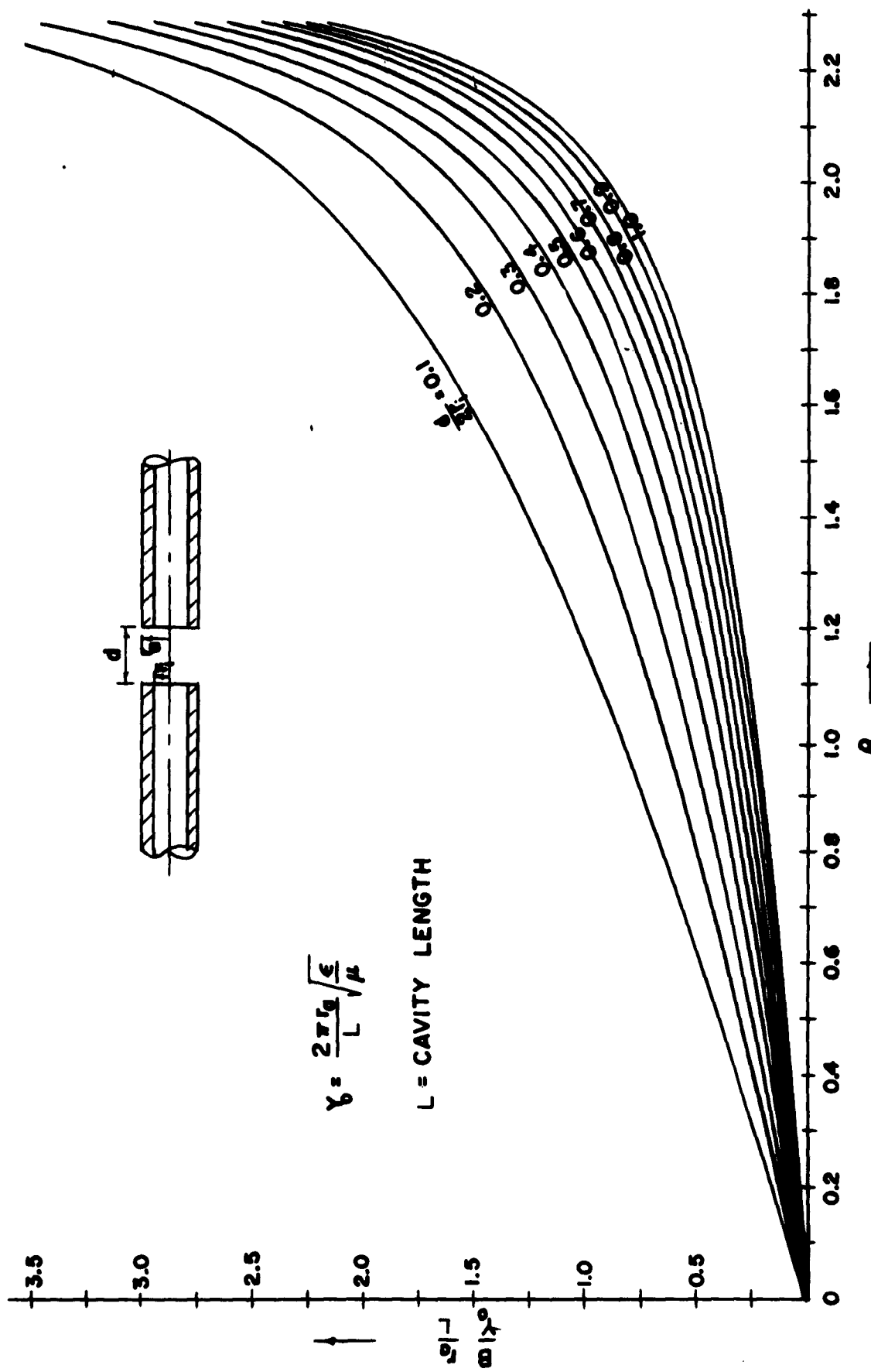


Figure 10. Inner Storage Admittance at the Gap of Two Hollow Cylinders.

cavity is rarely adhered to, especially in the output cavity of a high power klystron. In present-day klystrons some sort of iris or antenna that is large compared with the cavity is usually used as a means of removing the output power from the tube. The heavy, nonsymmetrical loading caused by this coupling will certainly cause nonuniformities either in the gap electric field or in the cavity fields or both. A first approximation of the effects of any of the resulting modes that have variations in the ϕ direction is made by an analysis similar to the one just performed. In a distortion of the electric field at the gap caused by a large coupling loop, the resulting gap field can be approximated as shown in Figure 11.

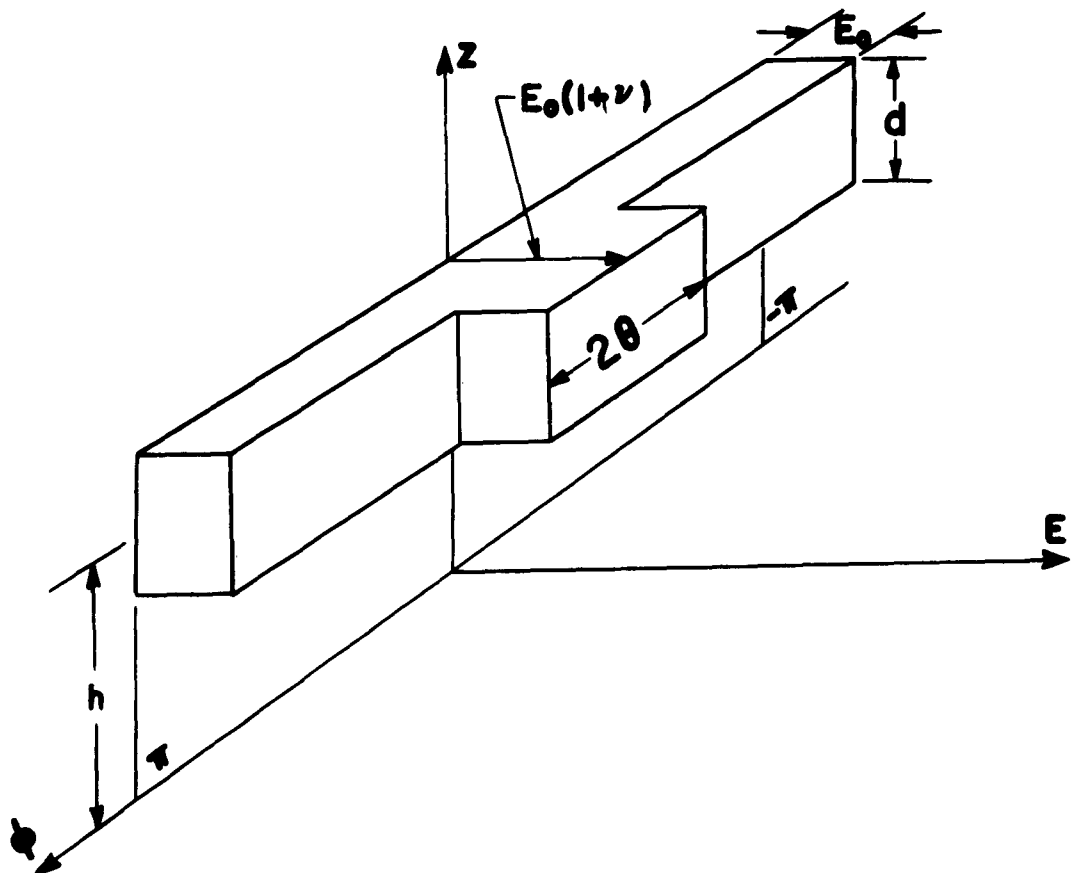


Figure 11. Gap Electric Field at $r = r_a$.

One can now proceed to find the fields given in Equation (1) and the respective series coefficients in the same manner as for no ϕ variations. However if one carried this out, it would be difficult to define a current at the gap since H_ϕ now depends on ϕ . This difficulty can be overcome by defining an admittance Y at the input gap as follows:

$$\frac{Y^* V^2}{2} = \frac{1}{2} \int_A \left(E_z \times H_\phi^* \right) dA , \quad (39)$$

A
 $r=r_a$

where the integral is over the transverse area of the gap. Then to find the voltage,

$$V = -\frac{1}{2\pi} \int_A E_z dA , \quad (40)$$

A
 $r=r_a$

which essentially is an approximation of the voltage based on the "average" of the electric field at the gap.

The detailed steps are not shown here since they are involved and lengthy. If the definition of the Bessel cotangent function as given in Equation (31) is extended to include higher-order Bessel functions,

$$b \cot_n (b-a) = \frac{N_{n+1}(a) J_n(b) - N_n(b) J_{n+1}(a)}{N_n(a) J_n(b) - N_n(b) J_n(a)} . \quad (41)$$

A similar extension can be made of the Bessel hyperbolic functions. Using Equations (39) and (40) and these new combinations of Bessel functions, the normalized admittance for the short-circuited radial line is as follows:

$$\begin{aligned}
y = & -j b \cot_0 [\beta r_a (\alpha-1)] - j \frac{8L^2}{\pi^2 d^2} \sum_{m=1}^K \frac{b \cot_0 [\beta r_a (\alpha-1)] \cos^2 \left(\frac{m\pi h}{L} \right) \sin^2 \left(\frac{m\pi d}{2L} \right)}{m^2 \sqrt{1 - \left(\frac{\omega_m}{\omega} \right)^2}} \\
& + j \frac{8L^2}{\pi^2 d^2} \sum_{m=K+1}^{\infty} \frac{b \coth_0 [\beta r_a (\alpha-1)] \cos^2 \left(\frac{m\pi h}{L} \right) \sin^2 \left(\frac{m\pi d}{2L} \right)}{m^2 \sqrt{\left(\frac{\omega_m}{\omega} \right)^2 - 1}} \\
& - j \frac{2\nu^2}{\pi^2} \left[1 - \frac{\nu\theta}{\pi} \right] \sum_{n=1}^{\infty} \left[\frac{1}{n\beta r_a} + \frac{1}{nZ} b \cot_n [\beta r_a (\alpha-1)] \right] \sin^2 \left(\frac{n\theta}{Z} \right) \\
& - j \frac{16\nu^2 L^2}{\pi^2 d^2} \left[1 - \frac{\nu\theta}{\pi} \right] \sum_{m=1}^K \frac{\frac{1}{n\beta r_a} + \frac{1}{nZ} b \cot_n [\beta r_a (\alpha-1)]}{m^2 \sqrt{1 - \left(\frac{\omega_m}{\omega} \right)^2}} \cos^2 \left(\frac{m\pi h}{L} \right) \sin^2 \left(\frac{m\pi d}{2L} \right) \sin^2 \left(\frac{n\theta}{Z} \right) \\
& + j \frac{16\nu^2 L^2}{\pi^2 d^2} \left[1 - \frac{\nu\theta}{\pi} \right] \sum_{m=K+1}^{\infty} \frac{\frac{1}{n\beta r_a} + \frac{1}{nZ} b \coth_n [\beta r_a (\alpha-1)]}{m^2 \sqrt{\left(\frac{\omega_m}{\omega} \right)^2 - 1}} \cos^2 \left(\frac{m\pi h}{L} \right) \sin^2 \left(\frac{m\pi d}{2L} \right) \sin^2 \left(\frac{n\theta}{Z} \right)
\end{aligned}$$

(42)

In this equation, the last three terms are introduced by the modes with ϕ variations. Of course, these terms go to zero if either v or θ is zero, which is as it should be, since this gives the symmetric case originally calculated.

As it turns out the magnitude of these last terms is small compared with the admittance terms which do not depend on ϕ variations except at the discontinuities. In the fifth and sixth terms of Equation (42), the discontinuities are caused by the denominator and they occur at the same values of βr_a as do the discontinuities of the admittance function for the symmetric case. The fourth term has discontinuities which depend on the roots of terms like

$$N_n(\beta r_a) J_n(\beta r_a) - N_n(\beta r_a') J_n(\beta r_a') = 0 \quad . \quad (43)$$

However for a fixed value of a , this equation is satisfied at values of βr_a , which are nearly independent of the order n .

The next few sections show that the higher-order resonances of the cavity occur largely in the region of some of the discontinuities. Thus the fact that the nonsymmetrical modes only contribute a significant admittance near these discontinuities means that, to the first approximation, these modes and their admittance terms can be neglected when compared with the whole admittance function. At the best, they can shift only slightly the higher-order resonances which occur near the discontinuities.

It should again be emphasized that this treatment of the non-symmetrical modes of a klystron cavity is only a first approximation. It is not meant to brush aside these modes with only a cursory glance as it might at first appear. Certainly a careful treatment of them would prove worthwhile since any practical output cavity of a present-day

high-power klystron will have these nonsymmetric modes present. It is just that the first consideration of this whole problem has been to treat those first few higher-order resonances which are known to exist experimentally and which involve primarily the symmetrical type of mode.

B. CONTROL EXPERIMENTS AT THE FUNDAMENTAL RESONANCE

Several experiments were performed as a check on the results that Equation (34) predicts. The first of these was the comparison of the fundamental resonance of a gridded-gap, singly re-entrant cavity calculated by curves* similar to the ones in Moreno³ and calculated by Equation (34). This equation may be revised to apply to this type of cavity by letting $r_i \rightarrow 0$. This essentially approximates the total capacity inside the gap as the d-c parallel plate capacity. Table 1 shows the results of these calculations. Agreement is very good if

Table 1. Calculated Fundamental Resonance for a Singly Re-entrant Cavity.

| Cavity Parameters | | | | Calculated Resonant Frequencies | | |
|-------------------|-----------------|-------------------|---------------|---------------------------------|-----------|--------------------------|
| $\frac{L}{r_a}$ | $\frac{d}{r_a}$ | $\frac{r_b}{r_a}$ | r_a (cm) | Hansen's Curves | Eq. 34 | Percent of Difference |
| 1.0 | 0.61 | 2.0 | 1.59 | 3000 Mc/s | 3060 Mc/s | 1.9 |
| 1.0 | 0.122 | 2.0 | 2.50 | 955 Mc/s | 959 Mc/s | 0.4 |

one considers that for the first example, the d-c approximation to the gap capacity is applied to a very large gap. Hansen's curves have been used

* An enlarged set of the curves appearing in Moreno³ were used. Although not so named in this reference, these curves are called Hansen's.

here for a comparison since these are known to be an accurate means of computing resonances for this type of cavity. In addition Figures 12 and 13 show the plot of each term of Equation (34) for these cavities. About seventeen terms of the infinite series for the admittance of the "nonpropagating" modes were necessary for these cavities. In Figures 12 and 13 the quantity $(\beta r_a)_0$ is the value of βr_a at resonance.

The second experiment performed was the measurement of the fundamental resonant frequency and Rsh/Q_0 of an existing cavity. This is a doubly re-entrant cavity with solid posts, which represent a gridded gap. One of the posts was threaded so that it could be moved to adjust the width of the gap. Since only one of these posts moved, this meant that the gap was off center except at one position, which occurred when the gap was as wide as possible (corresponded to the highest resonant frequency). Equation (34) was used to predict resonances for several gap widths and the value of Rsh/Q_0 at one of these.

Hansen's curves were used to predict two resonances, one with the gap centered and the other with the gap slightly off-center. Hansen's curves apply strictly to a singly re-entrant gridded-gap cavity, but a symmetrical doubly re-entrant cavity may be treated by considering one-half of this cavity. The nonsymmetrical cavity was divided in the middle of the gap and the predicted resonance for each half was averaged.

Two other means of calculating Rsh/Q_0 were used to see how well these compared with the experimental value. The first of these was from the same data used for Hansen's curves,² while the second was from an expression often used for this type of cavity; that is:

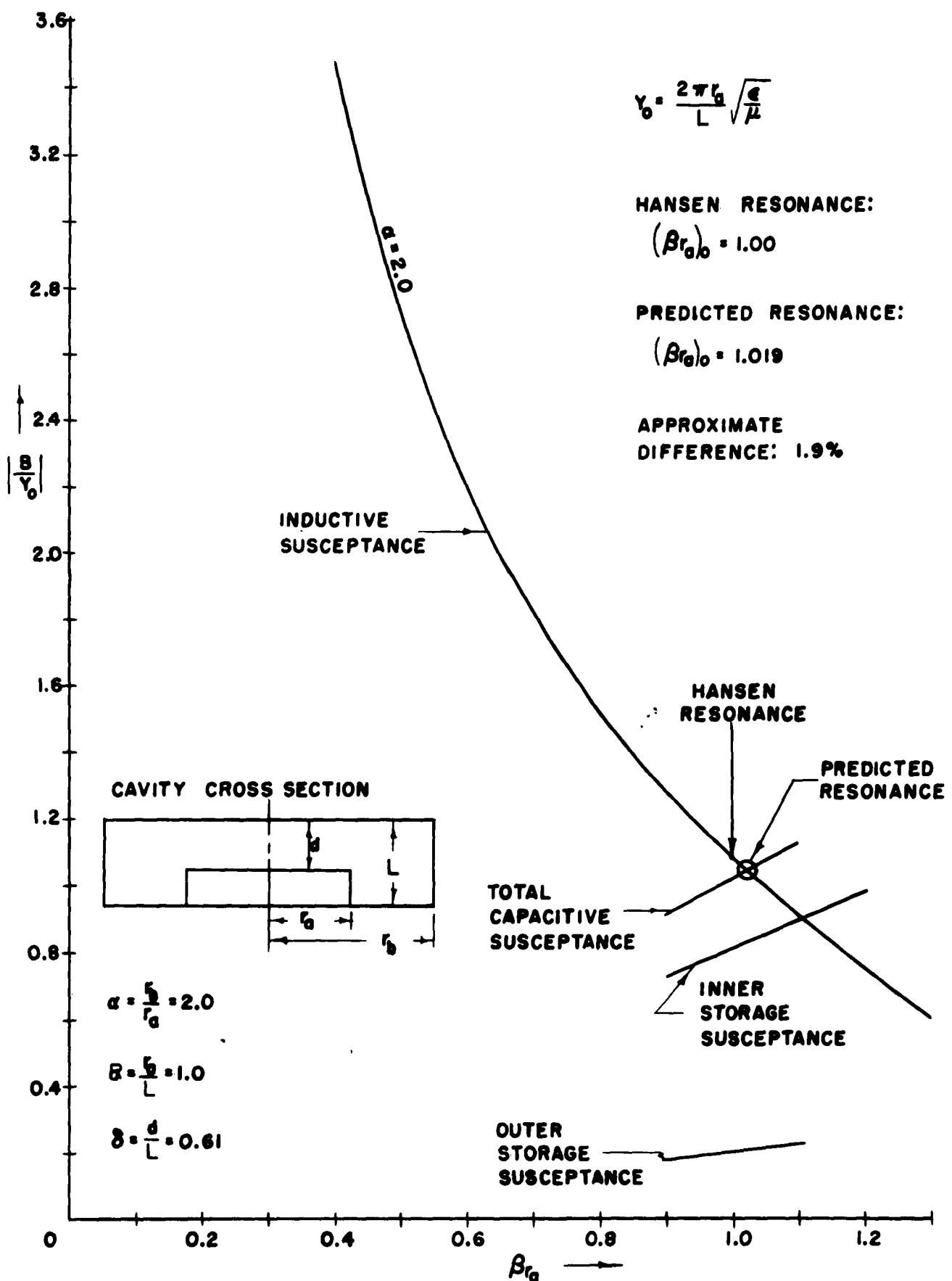


Figure 12. Sample Problem - Singly Re-entrant Gridded-Gap Cavity.

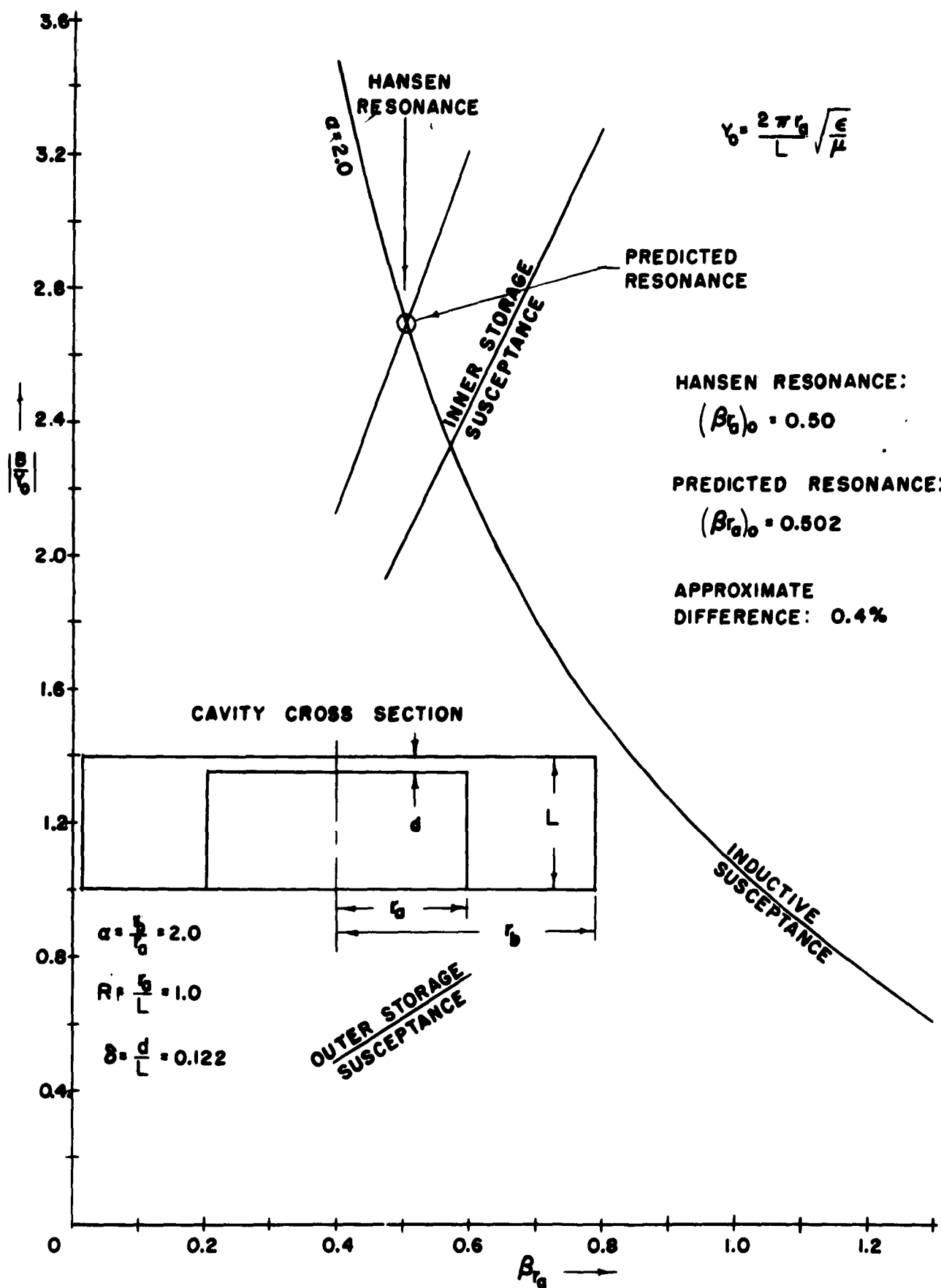


Figure 13. Sample Problem - Singly Re-entrant Gridded-Gap Cavity.

SAMPLE PROBLEM

Doubly Re-entrant Gridded Gap Cavity Gap Distance is Mechanically Variable

Table 2. Resonances of S-Band Cavity

| Measured | | Hansen's Curves | | | Predicted Values | | |
|---------------------|-----------------|-----------------|---------------------|------------------------|------------------|---------------------|------------------------|
| λ_0 (cm) | $(\beta r_a)_0$ | $(\beta r_a)_0$ | λ_0 (cm) | % Diff. to Measured | $(\beta r_a)_0$ | λ_0 (cm) | % Diff. to Measured |
| 9.60 | 0.3125 | 0.3182 | 9.43 | 1.77 | 0.3170 | 9.46 | 1.46 |
| 10.10 | 0.2971 | — | — | — | 0.3000 | 10.00 | 1.00 |
| 10.50 | 0.2857 | *0.2906 | 10.32 | 1.71 | 0.2895 | 10.36 | 1.33 |
| 11.10 | 0.2703 | — | — | — | 0.2730 | 10.99 | 0.99 |

* Approximate Due to Asymmetrical Cavity

Table 3. R_{sh}/Q_0 at $\lambda_0 = 10.50$ cm

| Method Used | R_{sh}/Q_0 - ohms | % Diff. to Measured |
|----------------|---------------------|------------------------|
| Measured | 65.3 | — |
| Hansen | 56.8 | 13.0 |
| Simple Formula | 54.1 | 17.2 |
| Predicted | 60.5 | 7.4 |

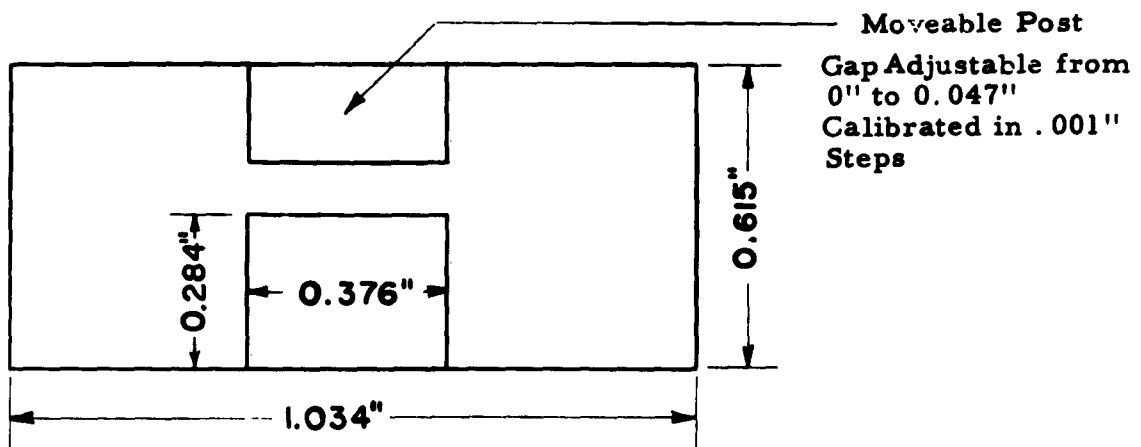


Figure 14. Cavity Used for Measurements.

$$\frac{R_{sh}}{Q_0} = 60\pi \left(\frac{2L}{\lambda_0}\right) \ln \left(\frac{r_b}{r_a}\right) \quad (44)$$

The experimental and calculated data for this cavity are listed in Tables 2 and 3. The values marked "predicted" are from Equation (34). The cavity dimensions are shown in Figure 14.

These simple control experiments indicate that good accuracy may be obtained from calculations using Equation (34). The experiment including R_{sh}/Q_0 in particular indicates that this equation gives better accuracy for this quantity than the other methods used here.

C. SPECIFIC APPLICATION TO HIGHER-ORDER RESONANCES

The utility of the admittance function as applied to fundamental resonances has now been demonstrated by experiment. It remains to be shown that this function predicts the higher-order resonant frequencies with a reasonable accuracy. For this purpose a model of an L-band klystron cavity was constructed. This cavity was doubly re-entrant and had a gridless gap with rounded gap edges. The drift tubes of this model were extended far enough in the z direction so that the discontinuity at the ends of the tubes would not be reflected back into the cavity. Figure 15 shows the approximate sizes involved in this model. The gap was very nearly centrally located in the z direction.

Two rectangular loops were made so that the cavity could be tested as a transmission-type cavity. The loops were approximately $3/4" \times 1 1/4"$, although for the resultant tests these were only projected $1/4$ in. into the cavity since this position gave the best match. When the cavity was tested for resonances through the third harmonic of the

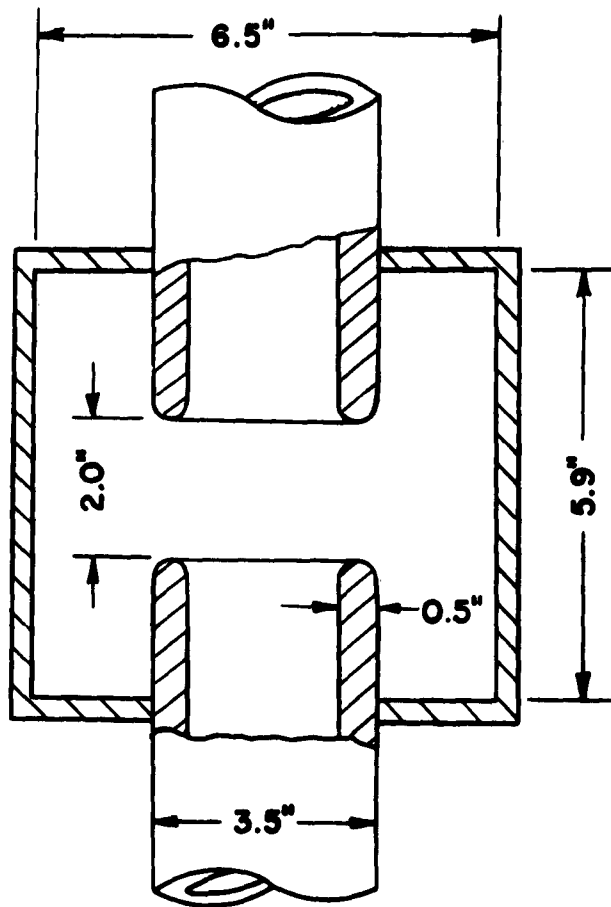


Figure 15. Model of L-Band Klystron Cavity.

fundamental, six resonances other than the ones predicted were observed. It turned out that these were resonances of ϕ -directed (nonsymmetrical) modes excited by the presence of the two coupling loops in the cavity. Because of the method of exciting these modes, a simple approximation to the expected resonant frequencies can be made.

For this consider Equation (1) with $m = 0$. An admittance for region 1 of the cavity may be defined as

$$y = - \frac{2\pi r_a}{Y_L} \frac{H_\phi}{E_z} . \quad (45)$$

The series coefficients of the field expansions can be found using the boundary conditions at the outer radius of the cavity, since only the relationship between A_0 and B_0 in Equation (45) is needed. Making this substitution and using the definitions of the Bessel trigonometric functions, the admittance for the n th mode follows:

$$y_n = j \left[\frac{n}{a} + b \cot_n \left[\beta r_a (a-1) \right] \right] . \quad (46)$$

This expression may be combined with the inner storage admittance given in Equation (26) and the annular admittance given in Equation (27) to give the resultant admittance function for the H_{0n1} modes. Of course this is only approximate since the other susceptances will not apply precisely to these ϕ -directed modes.

The computation of these resonances was performed and showed that the first eight ϕ -directed modes had a resonance within the frequency test range of the cavity. A comparison of the model lobes in ϕ and the positions of the two coupling loops showed that extremely weak coupling was present for just two modes, precisely the two that had not been measured. Agreement between the measured and calculated values of resonance for the other six ϕ -directed modes was reasonable. Differences ranged from less than 3 per cent to about 19 per cent (this large difference was for the H_{041} mode, which occurred close to the cutoff frequency of the H_{201} mode).

The resonances of the symmetrical modes of this cavity were calculated by Equation (34). For this case approximately 25 terms of

the infinite series representing the cutoff modes were required. To give an idea of what these terms look like graphically, a complete plot for this cavity is given in Figure 16. The experimental results and the calculated predictions for the symmetrical modes are shown in Table 4.

Table 4. Resonances of L-Band Cavity.

| Radial Line Mode | Coaxial Mode | Calculated Resonance (Mc/s) | Measured Resonance (Mc/s) | Error in Calculation |
|------------------|-------------------|-----------------------------|---------------------------|----------------------|
| TEM ₁ | TM ₀₁₀ | 819.7 | 823.0 | -0.40% |
| H ₁₀₁ | TM ₀₁₁ | 1004.2 | 1048.0 | -4.18% |
| H ₂₀₁ | TM ₀₁₂ | 2301.8 | 2538.9 | -9.34% |

As can be seen from the results, the admittance function is excellent for the fundamental resonance and is a good approximation at the first few higher-order resonances. The error is expected to increase as one considers these higher-order resonances, since the admittance terms connected with the "gap capacity" are not precise, as explained in the section on theoretical analysis.

D. OPTIMUM CAVITY DESIGN

All of the data and equations given up to this point are quite convenient for analyzing an existing cavity. However, to design a cavity by using this theory, the problem of where to begin presents itself. For this reason it is desirable to present a design technique and the general limits for certain of the cavity parameters. In the interest of serving the most usual cavity, the following type of doubly

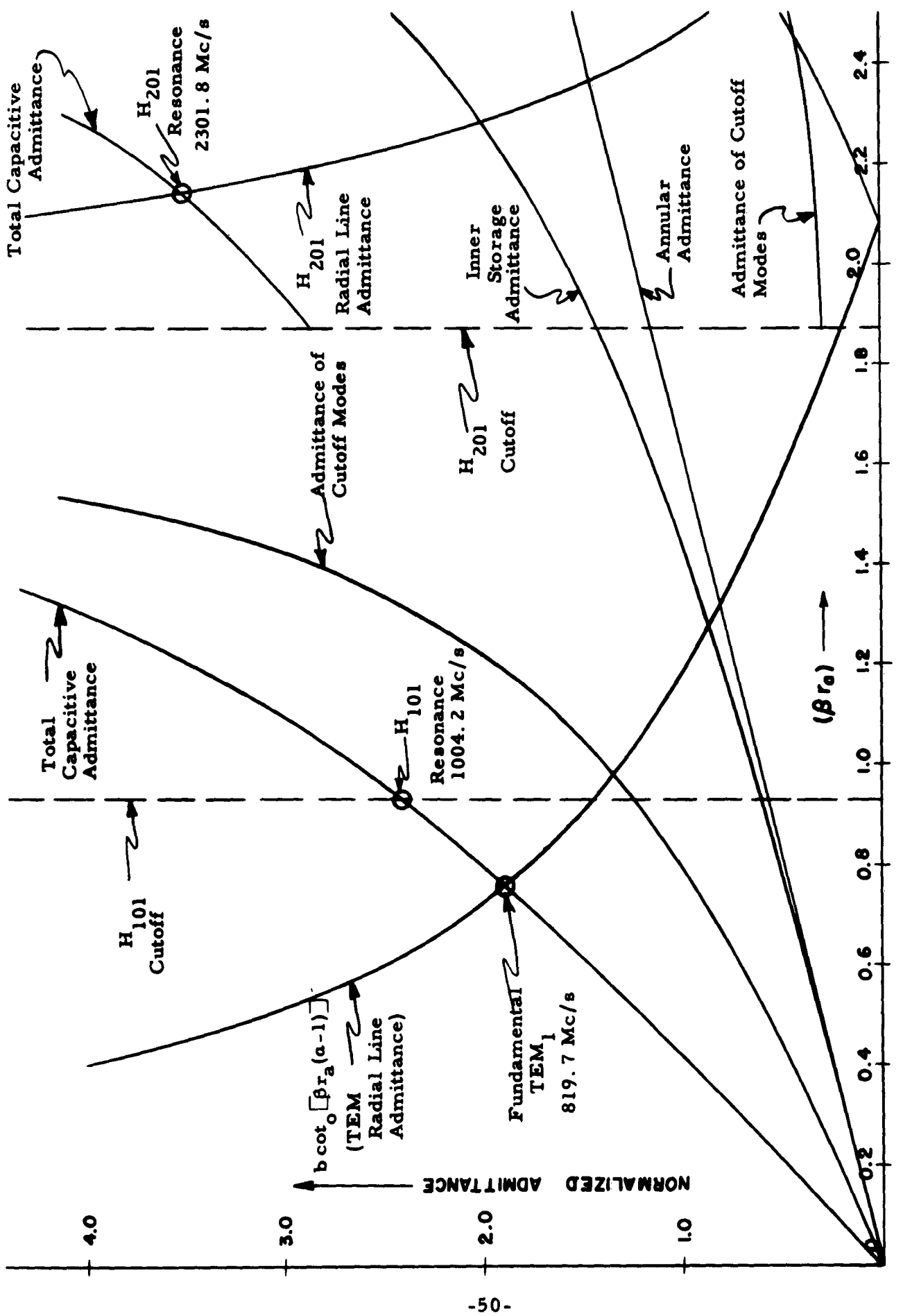


Figure 16. Total Admittance Function of the L-Band Cavity Model ($r_a = 1.750$ in., $\alpha = 1.85$).

re-entrant gridless-gap cavity is considered:

(1) the gap is centrally located $\left(\frac{h}{L} = \frac{1}{2}\right)$,

(2) the gap is one or two radians long,

(3) the d-c electron beam velocity is one-half the speed of light,

$$\left(\frac{u_0}{c} = \frac{1}{2}\right)$$

The first of these restrictions means that the modes having an odd number of variations in the z direction are only weakly excited. The second and third restriction give a measure of the gap length or strength of excitation of the higher-order modes. The cavity is to be designed so that harmonics of the signal frequency up to and including the fourth wil' not occur at or near any higher-order resonances of the cavity.

If one examines the curves of the TEM inductive susceptance, one can see that on the basis of the discontinuity points of these curves and the type of cavity cross-sections represented, the usual range of a where $a = \frac{r_b}{r_a}$ would be from 1.5 to 3.0. A lower value of a would give an extremely "thin" cavity which would be unsuitable for high-power applications. A larger value of a would necessitate a very low value of $(\beta r_a)_0$ in order to avoid trouble with the harmonics at the discontinuities of the inductive curves. Before qualifying the selection of a particular value of a , one should know something about the effects of the other parameters. The length of the cavity L controls the higher-order cutoff frequencies, as shown in Equation (14). From this equation, one can find the value of the first higher mode cutoff by

$$\beta r_a = \frac{\pi r_a}{L} = \pi R \quad . \quad (47)$$

This can be rewritten to apply to the value of βr_a at the fundamental resonance $(\beta r_a)_0$ by introducing the parameter x as follows:

$$R = \frac{r_a}{L} = \frac{x}{\pi} (\beta r_a)_0 . \quad (48)$$

This equation now makes it possible to find a value for $\frac{d}{L}$, or the gap length to cavity length ratio. For a one-radian gap,

$$\beta_e d = \frac{\omega}{u_0} d = 1 .$$

Substituting from Equation (48) gives

$$\delta = \frac{d}{L} = \left(\frac{u_0}{c} \right) \frac{x}{\pi} , \quad (49)$$

which is for a one-radian gap. For a two-radian gap it is obvious that

$$\delta = \frac{d}{L} = \left(\frac{u_0}{c} \right) \frac{2x}{\pi} . \quad (50)$$

Now returning to the TEM admittance curves, one can see that the likely range of $(\beta r_a)_0$ for $1.5 \leq a \leq 3.0$ is from 0.3 to 1.0 (perhaps even a bit higher for $a = 1.5$). Specifically, one can now recommend the range of $(\beta r_a)_0$ for a particular a . Figure 17 shows these recommended values for $a = 1.5, 2.0$ and 3.0 .

From Equation (48), since the first higher-mode cutoff frequency is normally between the fundamental and second harmonic of the signal frequency, a condition on the parameter x is obtained as follows:

$$1.0 < x < 2.0 \quad (51)$$

One is now in a position to make calculations for some specific

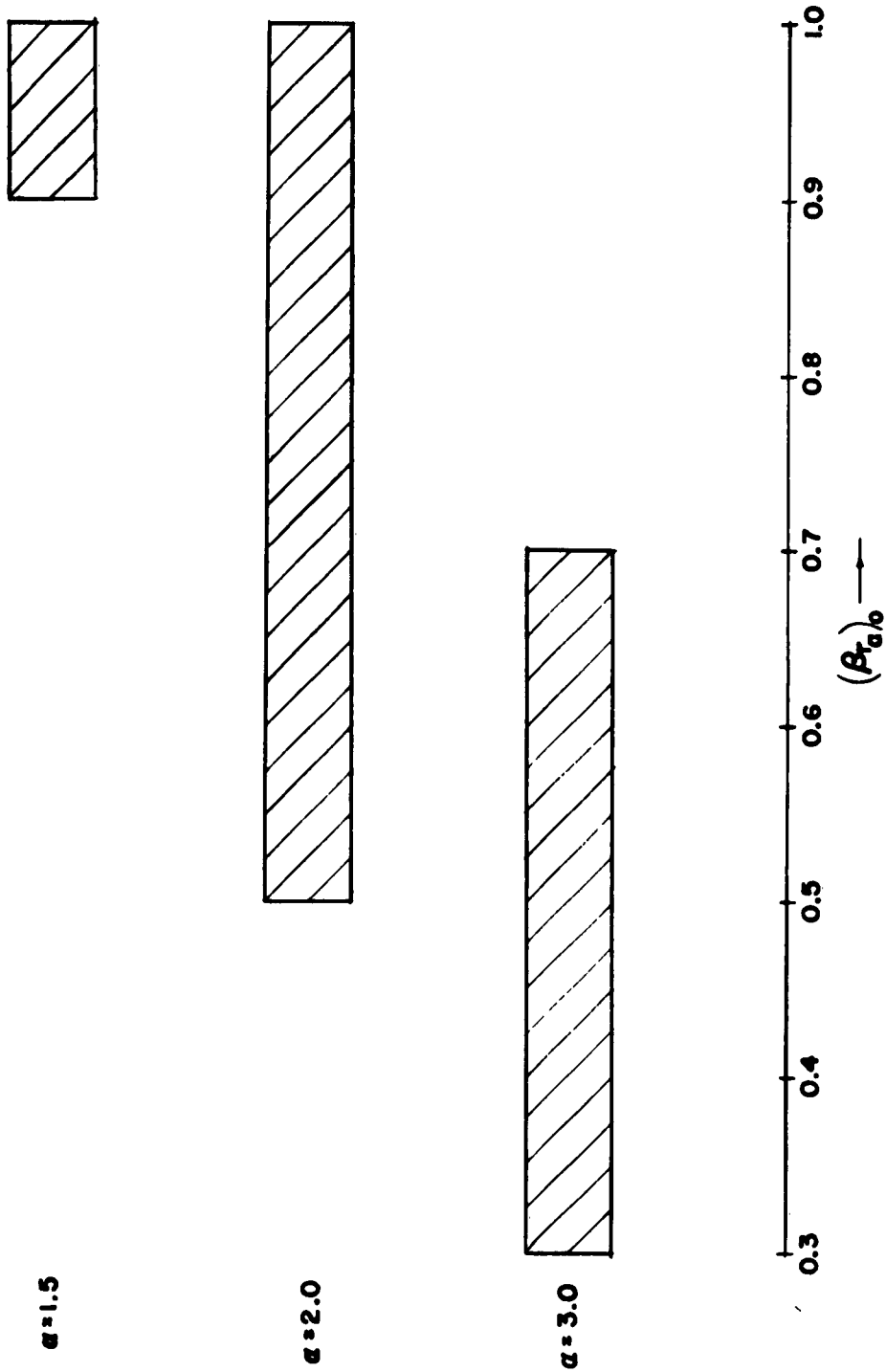


Figure 17. Recommended Ranges of $\{\beta_{r_a}\}$ for Resonance for Different Values of $\alpha = r_b/r_a$.

cases, then interpolate between these so as to cover all the values of the parameters mentioned here. Cavities with the following properties are considered:

$$a : 1.5, 2.0, 3.0$$

$$x : 1.25, 1.50, 1.75$$

$$(\beta r_a)_0 : 0.2, 0.6, 0.9$$

$$\beta_e d : 1, 2$$

Figure 18 shows the cross-sectional views of the cavities these values represent so that the physical effect of varying one of these parameters can be observed.

The effects of these parameters on the higher-order resonances of a cavity can be observed by marking the values of $(\beta r_a)_0$ on a scale of βr_a , and indicating the harmonics of these values of $(\beta r_a)_0$. Then the cutoff values of βr_a for the particular values of x chosen can be marked. Once this is done, the inductive susceptance of the second higher-order mode $m = 2$ in z is calculated and plotted as a function of βr_a . This susceptance is added to the inductive susceptance produced by the TEM mode which gives the total inductive susceptance of the cavity. From past experience one knows that the first few higher-order resonances occur in the region of the large values of the higher-order mode inductive susceptances and can stipulate the "safe" range of the parameter x . The conceptual process is not obtruse but the actual solution is involved since one must also be careful to keep the cavity resonances away from the harmonics at values of $(\beta r_a)_0$ other than the three chosen here for the sample calculations.

The results of these calculations are shown in Figures 19, 20, and 21.

(FOR $\alpha = 3.0, 2.0, 1.5$ AND WITH ONE AND TWO RADIAN GAPS AT $U_0/c = 0.5$)

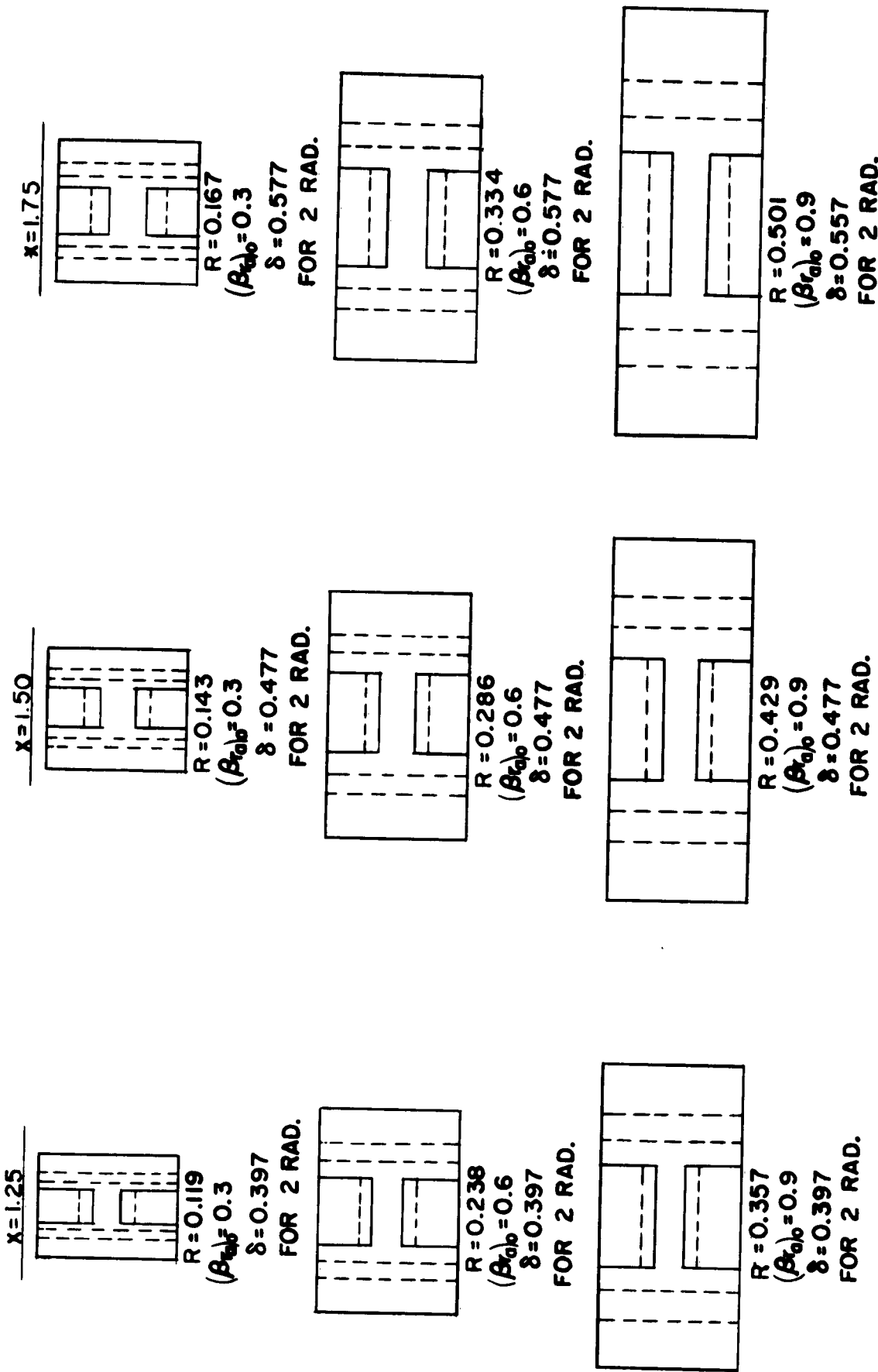


Figure 18. Cross-Section for Doubly Re-entrant Cavities.

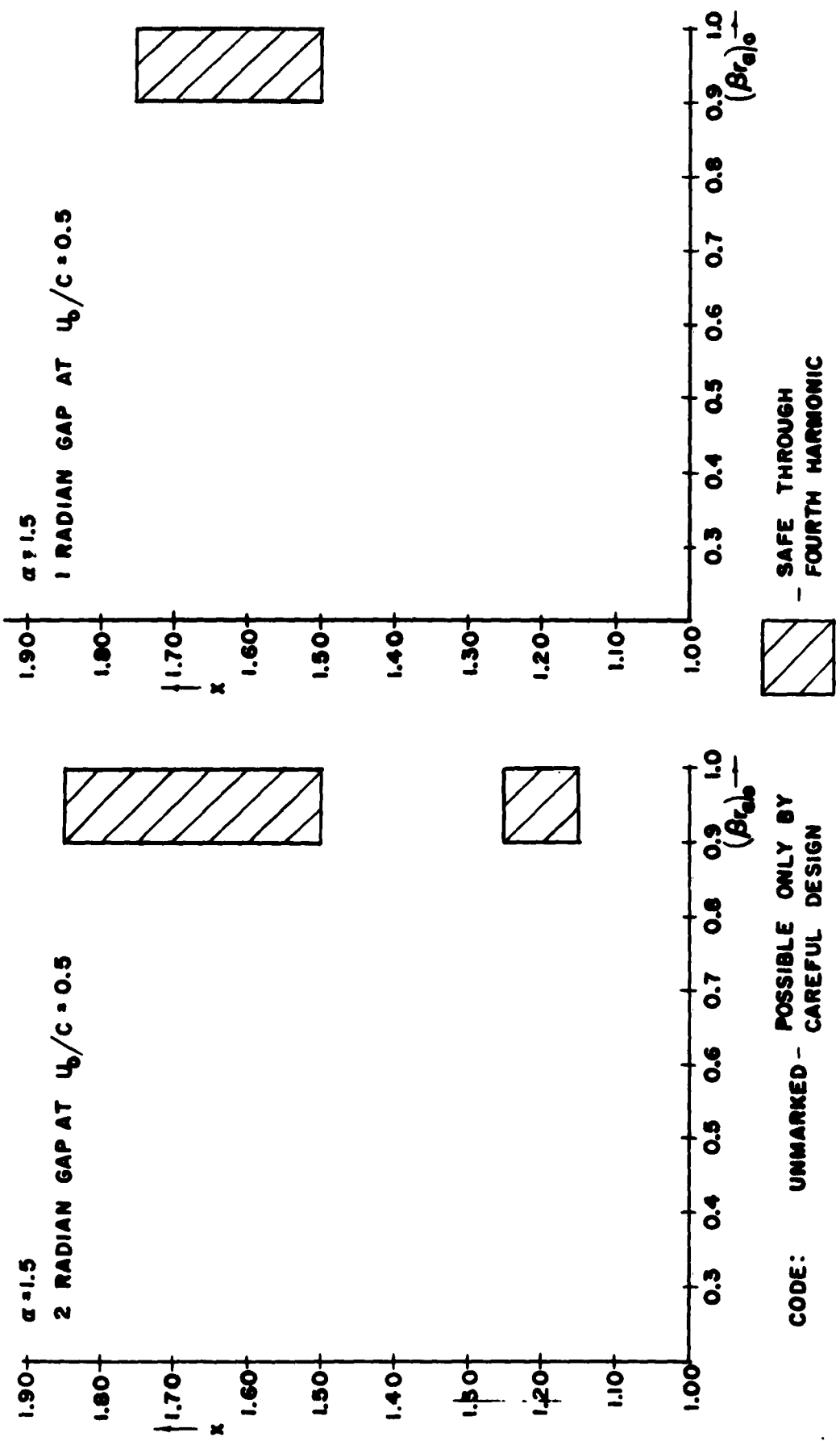


Figure 19. Recommended Ranges of Parameter x as Indicated by Shaded Areas.

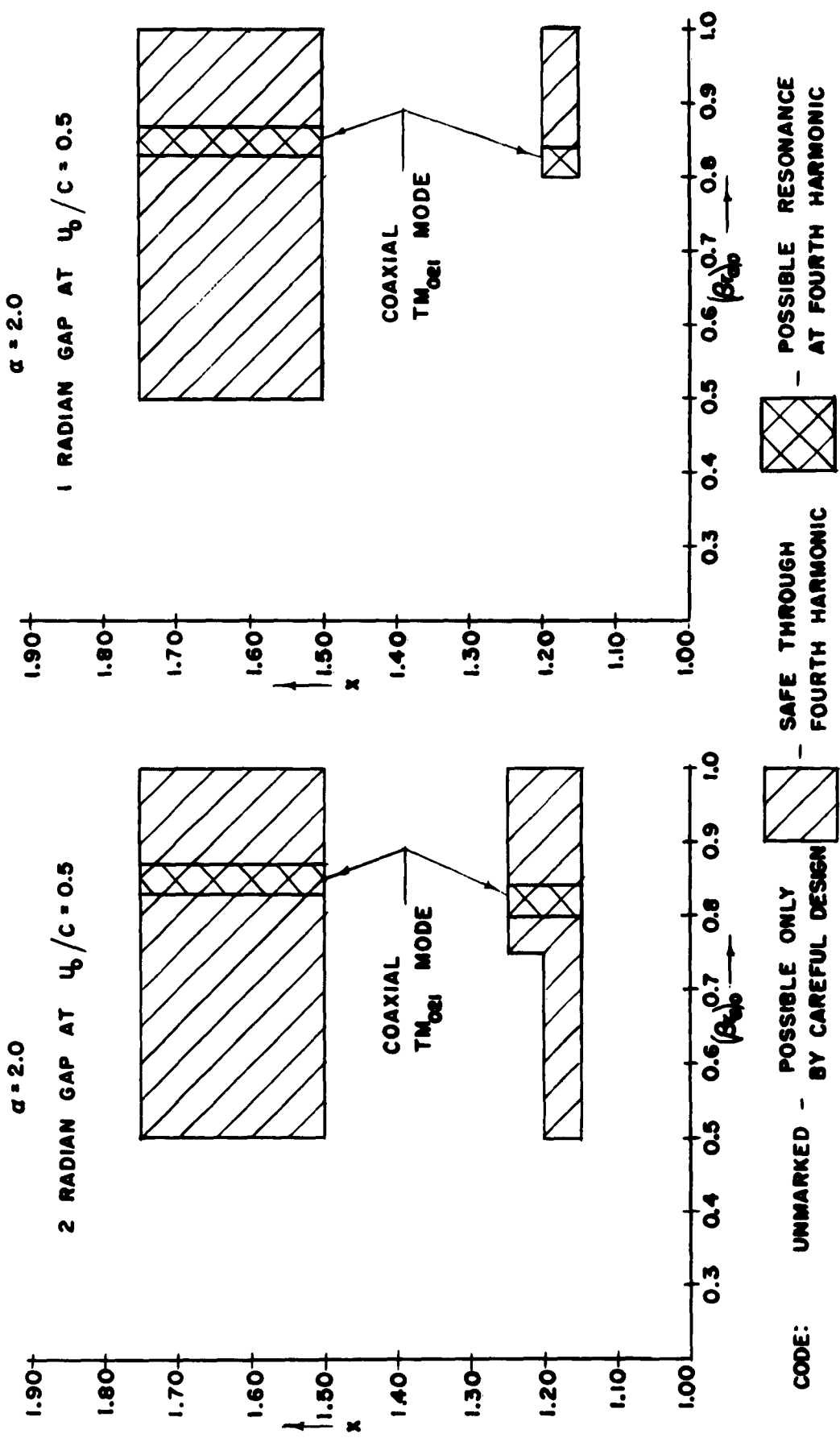


Figure 20. Recommended Ranges of Parameter x as Indicated by Shaded Areas.

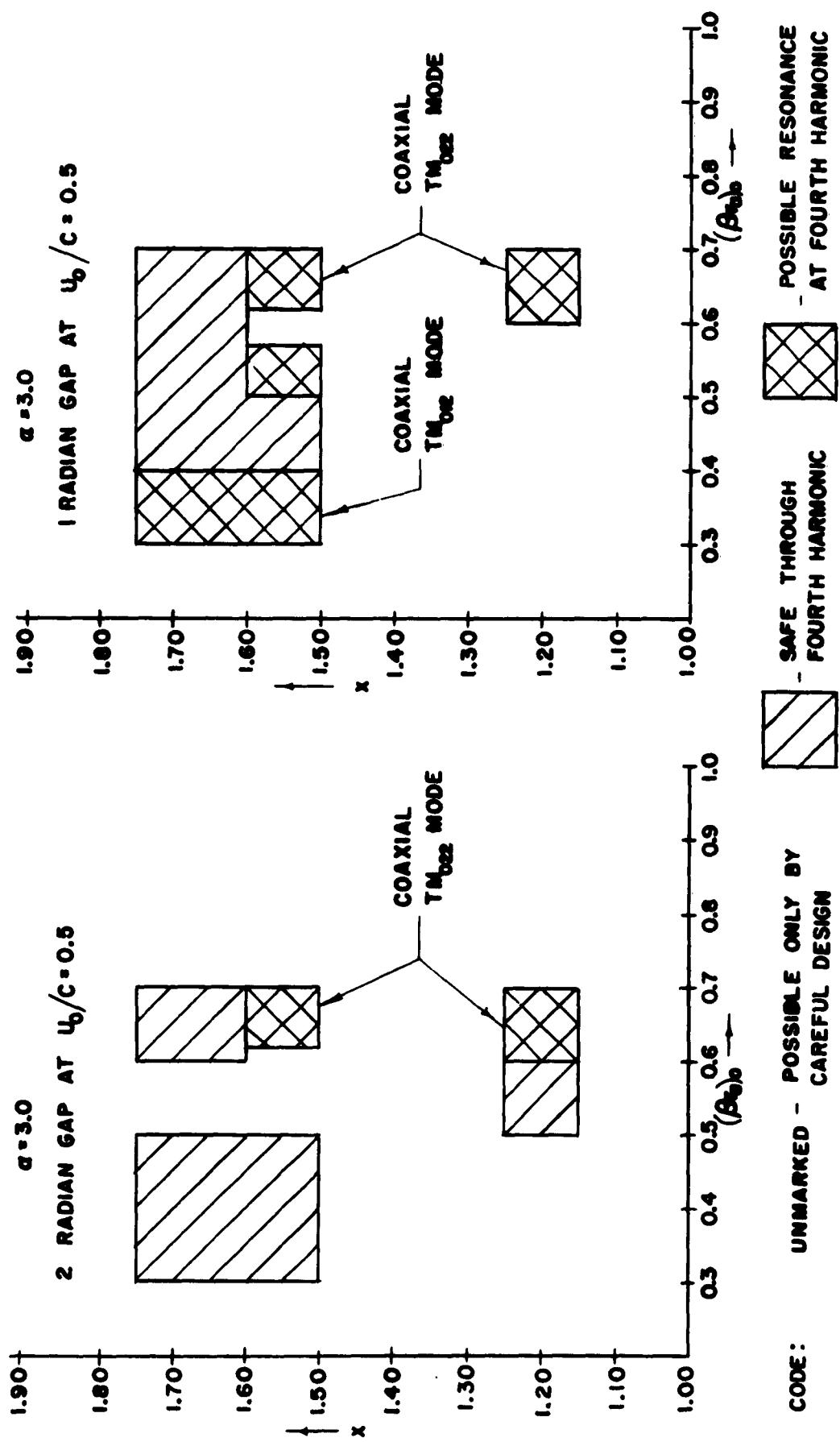


Figure 21. Recommended ranges of Parameter x as indicated by shaded areas.

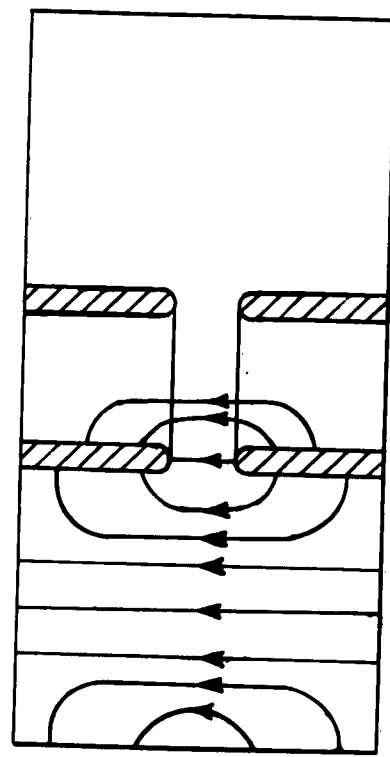
Each of these figures is for a specific value of a (1.5, 2.0, and 3.0) and shows the recommended range of x for any $(\beta r_a)_0$. Each of these figures has been subdivided into curves for a one- and a two-radian gap so that a rough interpolation may be made for any other expected gap length.

The cavity has not been completely specified yet, for there is the ratio r_i/r_a to be specified. This can actually be chosen last, since it affords a minor adjustment on the resonant frequencies of the cavity. Now the ratios of all the physical measurements of the cavity are completely specified, although a "scaling factor" must still be determined. This may actually be found from the value of $(\beta r_a)_0$. The operating frequency, or value of β , will be known when the tube design is begun and from the resulting electron beam characteristics a value of r_a may be estimated. Once this particular physical parameter is known, the rest of the cavity parameters can be found from the information given above, and in the figures following.

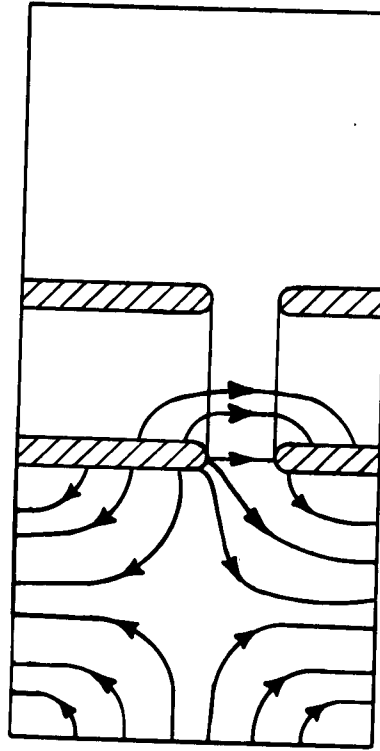
Perhaps it should be pointed out that this design does not consider the effect of only a few higher-order modes; rather it accounts for all the symmetric higher-order modes which are of the H_{mop} type. Table 5 lists the important ones that were considered in specifying the design technique outlined here. Each mode is identified in both the radial and coaxial nomenclature. In addition, Figure 22 shows the electric field configurations on cavity cross sections of several typical modes. This field structure for the other modes may be easily obtained by extension.

Table 5. Modes Considered in Design

| Mode Description | Radial Line Designation | Coaxial Line Designation |
|---|-------------------------|--------------------------|
| Fundamental | TEM_1 | TM_{010} |
| 1 st Cutoff Mode | H_{101} | TM_{011} |
| 2 nd Cutoff Mode | H_{201} | TM_{012} |
| 3 rd Cutoff Mode | H_{301} | TM_{013} |
| 2 nd Order Fundamental | TEM_2 | TM_{020} |
| 2 nd Order of 1 st Cutoff | H_{102} | TM_{021} |
| 2 nd Order of 2 nd Cutoff | H_{202} | TM_{022} |

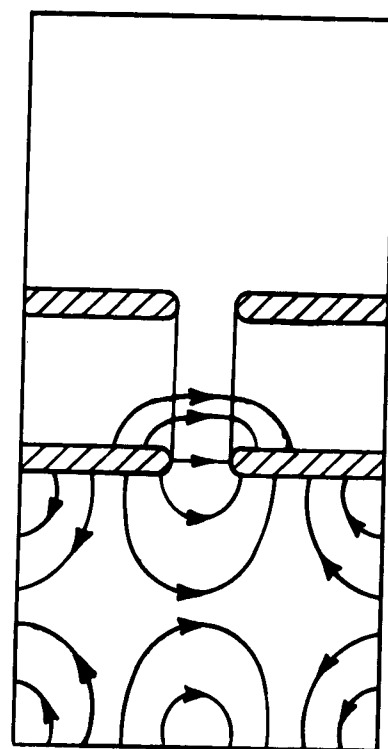


$\text{TEM}_1 \text{ (TM}_{010}\text{)}$

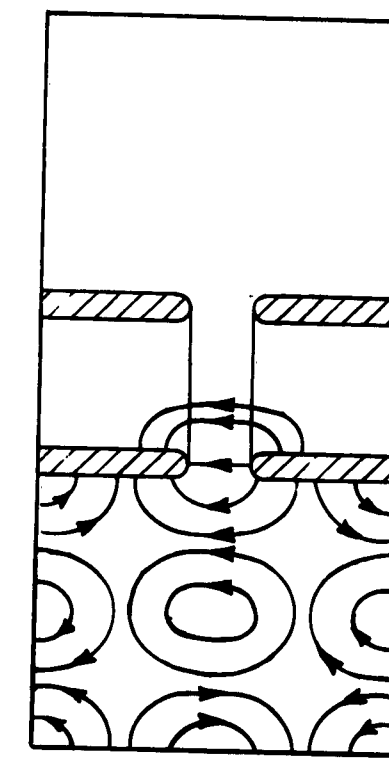


$\text{H}_{101} \text{ (TM}_{011}\text{)}$

Gap off center to show coupling



$\text{H}_{201} \text{ (TM}_{012}\text{)}$



$\text{H}_{202} \text{ (TM}_{022}\text{)}$

Figure 22. Electric Field Configuration for Typical Modes (Coaxial Line Mode Designation Shown in Parenthesis.)

III. PERTURBATION THEORY IN RESONANT CAVITIES

The general case of perturbation of cavities by the insertion of some object has not been treated. Slater⁶ treated the general case of boundary perturbation but did not consider an object apart from the boundary. Over the past few years several articles^{7, 10, 11} have treated cavity perturbation, but largely from the experimental point of view. A few articles calculate the calibration constant mentioned later in this section for several types of beads, but most use an assumed form of perturbation equation. Casimer⁷ does give a brief derivation for certain types of perturbation in terms of total magnetic and electric moments which will depend on field strength and the size of the perturbing object. Here perturbation theory is developed in general, with the approximations and assumptions clearly shown. Rather than deal with moments, the equations are developed so that they are true in general, with only a calibration constant to differentiate between types of beads. This calibration constant is independent of field strength and size of the perturbing bead. It depends only on the geometry and orientations of the bead.

A convenient way to handle perturbation is to use normalized orthogonal functions for the fields in a cavity. A short development of these is shown in the next sections. For those who are unfamiliar with this type of treatment, an illustrative problem which shows how these functions might be used has been included.

A. ORTHOGONAL ELECTROMAGNETIC FIELD FUNCTIONS

In dealing with cavities, it is often convenient to expand the

fields in terms of a series of orthogonal functions. This reduces the solutions of Maxwell's equations in the cavity to the problem of finding the coefficients of expansion. The form of this expansion is immediately suggested by Helmholtz's theorem,⁸ which states that any vector field \underline{F} , that is finite, uniform, and continuous, may be expressed as the sum of a gradient of a scalar ϕ and a curl of a zero-divergence vector \underline{A} , as:

$$\underline{F} = \text{grad } \phi + \text{curl } \underline{A} \quad (51)$$

The vectors $\text{grad } \phi$ and $\text{curl } \underline{A}$ are often termed "irrotational" and "solenoidal" respectively, since one has zero curl while the other has zero divergence.

This expansion for the cavity fields was performed by Slater⁶ several years ago. However, Kurokawa⁹ recently pointed out a fundamental error in Slater's derivation. Since Slater's expansion has not been entirely corrected, it is worthwhile to indicate this expansion here. For purposes of reference the nomenclature used here will in large measure agree with that used by Slater.

In general a cavity is considered of volume V bounded by short-circuited surfaces s and open-circuited surfaces s' , which are so named because of the type of boundary conditions at the surfaces. For the expansions of the scalar fields in the volume there are two sets of orthogonal functions which satisfy the following relationships and boundary conditions:

$$\nabla^2 \psi_a + k_a^2 \psi_a = 0 \quad ,$$

$$\psi_a = 0 \quad (\text{on } s) \quad , \quad \frac{\partial \psi_a}{\partial n} = 0 \quad (\text{on } s') \quad (52)$$

$$\nabla^2 \phi_\lambda + k_\lambda^2 \phi_\lambda = 0 ,$$

$$\phi_\lambda = 0 \quad (\text{on } s') , \quad \frac{\partial \phi_\lambda}{\partial n} = 0 \quad (\text{on } s) \quad (53)$$

Similarly for the expansions of the vector fields in the volume, two sets of orthogonal functions may be used:

$$\nabla^2 \underline{\psi}_p + k_p^2 \underline{\psi}_p = 0$$

$$\left. \begin{array}{l} \underline{n} \times \underline{\psi}_p = 0 \\ \nabla \cdot \underline{\psi}_p = 0 \end{array} \right\} \quad (\text{on } s) \quad \left. \begin{array}{l} \underline{n} \times \nabla \times \underline{\psi}_p = 0 \\ \underline{n} \cdot \underline{\psi}_p = 0 \end{array} \right\} \quad (\text{on } s')$$

$$(54)$$

$$\nabla^2 \underline{\xi}_q + k_q^2 \underline{\xi}_q = 0$$

$$\left. \begin{array}{l} \underline{n} \times \underline{\xi}_q = 0 \\ \nabla \cdot \underline{\xi}_q = 0 \end{array} \right\} \quad (\text{on } s') \quad \left. \begin{array}{l} \underline{n} \times \nabla \times \underline{\xi}_q = 0 \\ \underline{n} \cdot \underline{\xi}_q = 0 \end{array} \right\} \quad (\text{on } s)$$

$$(55)$$

Some of the functions of Equations (54) and (55) have the common eigenvalues k_a ($a = 1, 2, 3, \dots$) and are related by the expressions

$$k_a \underline{\psi}_p = \nabla \times \underline{\xi}_q , \quad k_a \underline{\xi}_q = \nabla \times \underline{\psi}_p . \quad (56)$$

These particular $\underline{\psi}_p$ and $\underline{\xi}_q$ will be denoted as \underline{E}_a and \underline{H}_a respectively, so that Equation (56) becomes

$$k_a \underline{E}_a = \nabla \times \underline{H}_a , \quad k_a \underline{H}_a = \nabla \times \underline{E}_a ; \quad (57)$$

\underline{E}_a and \underline{H}_a will now satisfy the boundary conditions:

$$\left. \begin{array}{l} \underline{n} \times \underline{E}_a = 0 \\ \underline{n} \cdot \underline{H}_a = 0 \end{array} \right\} \quad \text{(on } s\text{)} \quad \left. \begin{array}{l} \underline{n} \cdot \underline{E}_a = 0 \\ \underline{n} \times \underline{H}_a = 0 \end{array} \right\} \quad \text{(on } s'\text{)} \quad (58)$$

All the other $\underline{\psi}_p$'s and $\underline{\phi}_q$'s which do not satisfy Equation (56) are denoted as \underline{F}_a ($a = 0, 1, 2, \dots$) and \underline{G}_λ ($\lambda = 0, 1, 2, \dots$). Since these functions have zero curl, they satisfy the relations:

$$\begin{aligned} k_a \underline{F}_a &= \nabla \underline{\psi}_a \quad (a \neq 0) \\ k_\lambda \underline{G}_\lambda &= \nabla \underline{\phi}_\lambda \quad (\lambda \neq 0) \end{aligned} \quad , \quad (59)$$

where the $\underline{\psi}_a$ and $\underline{\phi}_\lambda$ are from Equations (52) and (53). The particular solutions \underline{F}_a ($a = 0$) and \underline{G}_λ ($\lambda = 0$) correspond to the electrostatic and magnetostatic fields under certain conditions; however these are neglected here since they are not important in the development of perturbation theory.

By examining Equation (57) and (59), it is apparent that $\text{grad } \phi$ in Equation (51) corresponds to the \underline{F}_a and \underline{G}_λ functions (the "irrotational" functions) while $\text{curl } \underline{A}$ corresponds to the \underline{E}_a and \underline{H}_a functions (the "solenoidal" functions). Thus one can now expand the electromagnetic fields by using Equation (51) as a guide. The general form can be seen by considering the electric field which can be expressed in terms of \underline{F}_a and \underline{E}_a (since these have boundary conditions similar to the actual field \underline{E} in a cavity):

$$\underline{E} = \sum_a e_a \underline{E}_a + \sum_a f_a \underline{F}_a . \quad (60)$$

Here e_a and f_a are the series coefficients of the expansion. These

coefficients can in general be found by using the orthogonal properties of the functions \underline{E}_a , \underline{H}_a , \underline{F}_a , and \underline{G}_a and by considering them normalized over the cavity volume so that

$$\int_V (\underline{E}_n \cdot \underline{E}_m) dv = \int_V (\underline{H}_n \cdot \underline{H}_m) dv = \int_V (\underline{F}_n \cdot \underline{F}_m) dv = \int_V (\underline{G}_n \cdot \underline{G}_m) dv = \delta_{nm}$$

$$\delta_{nm} = 0 \quad , \quad n \neq m$$

$$\delta_{nm} = 1 \quad , \quad n = m \quad . \quad (61)$$

Of course, the "cross products" of different functions integrated over the volume are always zero, that is, equations of the form

$$\int_V (\underline{E}_n \cdot \underline{F}_m) dv = 0 \quad \left. \begin{array}{l} n = m \\ n \neq m \end{array} \right\} \quad . \quad (62)$$

Thus to find the series coefficient e_a in Equation (60), multiply through by \underline{E}_b and integrate over the volume to obtain

$$\int_V (\underline{E} \cdot \underline{E}_b) dv = \sum_a e_a \int_V (\underline{E}_a \cdot \underline{E}_b) dv + \sum_a f_a \int_V (\underline{F}_a \cdot \underline{E}_b) dv \quad .$$

By virtue of Equations (61) and (62) the only term remaining on the right side occurs when $b = a$ which gives

$$\int_V (\underline{E} \cdot \underline{E}_a) dv = e_a \quad . \quad (63)$$

The coefficients f_a may be found in a similar way and are as follows:

$$\int_V (\underline{E} \cdot \underline{F}_a) dv = f_a \quad . \quad (64)$$

It is easily seen that all further series coefficients of expansion will have the form of Equations (63) and (64).

Now in considering the expansion of the magnetic field, since the divergence of this field is always zero, it is a temptation to expand this in terms of a solenoidal function only, for this also has zero divergence. One must remember, however, that the magnetic field being considered does not exist in infinite space, but in a bounded space, that is, inside a cavity. Because of this an irrotational function is also required to expand the magnetic field. Mathematically this may be seen by examining the general solution for ϕ and \underline{A} in Equation (51) which is as follows:⁸

$$\underline{F}(r) = \text{grad} \left\{ \int \frac{\underline{F}(r') \cdot d\underline{A}}{4\pi R} - \int_V \frac{\underline{v}' \cdot \underline{F}(r')}{4\pi R} dv' \right\} + \text{curl} \left\{ \int \frac{\underline{F}(r') \times d\underline{A}'}{4\pi R} + \int_V \frac{\underline{v}' \times \underline{F}(r')}{4\pi R} dv' \right\}, \quad (65)$$

where $R = r - r'$ and \underline{v}' is a differential operator on r' . Even though $\underline{v} \cdot \underline{F} = 0$ there is no assurance that $\underline{F} = \underline{v} \times \underline{A}$ only. Hence, the magnetic field must be expanded in terms of the \underline{H}_a (solenoidal) and \underline{G}_λ (irrotational) functions.

Also because of similar boundary conditions, \underline{J} (electron current) is expanded in terms of \underline{E}_a and \underline{F}_a , and ρ (electron charge density) is expanded in terms of ψ_a . This gives the following field expansions:

$$\underline{E} = \sum_a \underline{E}_a \int_V (\underline{E} \cdot \underline{E}_a) dv + \sum_a \underline{F}_a \int_V (\underline{E} \cdot \underline{F}_a) dv ,$$

$$\begin{aligned}
 \underline{H} &= \sum_a \underline{H}_a \int_V (\underline{H} \cdot \underline{H}_a) dv + \sum_\lambda \underline{G}_\lambda \int_V (\underline{H} \cdot \underline{G}_\lambda) dv , \\
 \underline{J} &= \sum_a \underline{E}_a \int_V (\underline{J} \cdot \underline{E}_a) dv + \sum_a \underline{F}_a \int_V (\underline{J} \cdot \underline{F}_a) dv , \\
 \rho &= \sum_a \psi_a \int_V (\rho \psi_a) dv . \tag{66}
 \end{aligned}$$

In order to use Maxwell's equations, expansions are needed for the curl and divergence of the electric and magnetic fields. Since $\underline{\nabla} \times \underline{E}$ behaves like \underline{H} this can be expanded in terms of \underline{H}_a and \underline{G}_λ as follows:

$$\underline{\nabla} \times \underline{E} = \sum_a \underline{H}_a \int_V (\underline{\nabla} \times \underline{E} \cdot \underline{H}_a) dv + \sum_\lambda \underline{G}_\lambda \int_V (\underline{\nabla} \times \underline{E} \cdot \underline{G}_\lambda) dv . \tag{67}$$

This can be put into a more tractable form by making use of the vector identity

$$\underline{\nabla} \cdot (\underline{A} \times \underline{B}) = \underline{B} \cdot \underline{\nabla} \times \underline{A} - \underline{A} \cdot \underline{\nabla} \times \underline{B} , \tag{68}$$

so that

$$\underline{\nabla} \cdot [\underline{E} \times (\underline{\nabla} \times \underline{E}_a)] = \underline{\nabla} \times \underline{E} \cdot \underline{\nabla} \times \underline{E}_a - \underline{E} \cdot \underline{\nabla} \times \underline{\nabla} \times \underline{E}_a$$

or

$$\underline{\nabla} \cdot (\underline{E} \times k_a \underline{H}_a) = \underline{\nabla} \times \underline{E} \cdot k_a \underline{H}_a - \underline{E} \cdot k_a^2 \underline{E}_a .$$

Integrating this over the cavity volume and using Gauss' theorem gives

$$\int_V (\underline{\nabla} \times \underline{E} \cdot \underline{H}_a) dv = k_a \int_V (\underline{E} \cdot \underline{E}_a) dv + \int_{S, S'} (\underline{E} \times \underline{H}_a) \cdot \underline{n} dA ,$$

where \underline{n} is the outer normal to the surface. The order of the vectors can be permuted in the surface integral and with $\underline{n} \times \underline{H}_a = 0$ on s' ,

$$\int_V (\underline{\nabla} \times \underline{E} \cdot \underline{H}_a) dv = k_a \int_V (\underline{E} \cdot \underline{E}_a) dv + \int_s \underline{H}_a \cdot (\underline{n} \times \underline{E}) dA . \quad (69)$$

An expression for the second term of Equation (67) can be obtained by using

$$\begin{aligned} \underline{\nabla} \cdot (\underline{E} \times \underline{G}_\lambda) &= \underline{G}_\lambda \cdot \underline{\nabla} \times \underline{E} - \underline{E} \cdot \underline{\nabla} \times \underline{G}_\lambda , \\ &= \underline{G}_\lambda \cdot \underline{\nabla} \times \underline{E} , \end{aligned}$$

since the curl of an irrotational function is zero. Again, integrating over the cavity volume, and using Gauss' theorem gives

$$\int_{s, s'} (\underline{n} \cdot \underline{E} \times \underline{G}_\lambda) dA = \int_V (\underline{\nabla} \times \underline{E} \cdot \underline{G}_\lambda) dv .$$

One can permute the order of the vectors in the surface integral and with $\underline{n} \times \underline{G}_\lambda = 0$ on s' , obtain

$$\int_V (\underline{\nabla} \times \underline{E} \cdot \underline{G}_\lambda) dv = \int_s \underline{G}_\lambda \cdot (\underline{n} \times \underline{E}) dA . \quad (70)$$

Equations (69) and (70) may be inserted into Equation (67) to give for the expansion of $\underline{\nabla} \times \underline{E}$

$$\begin{aligned} \underline{\nabla} \times \underline{E} &= \sum_a \underline{H}_a \left[k_a \int_V (\underline{E} \cdot \underline{E}_a) dv + \int_s \underline{H}_a \cdot (\underline{n} \times \underline{E}) dA \right] \\ &+ \sum_\lambda \underline{G}_\lambda \int_s \underline{G}_\lambda \cdot (\underline{n} \times \underline{E}) dA . \end{aligned} \quad (71)$$

In a corresponding manner $\underline{\nabla} \times \underline{H}$ behaves like \underline{E} so that

$$\begin{aligned}
 \underline{\mathbf{v}} \times \underline{\mathbf{H}} = & \sum_a \underline{\mathbf{E}}_a \left[k_a \int_V (\underline{\mathbf{H}} \cdot \underline{\mathbf{H}}_a) dv + \int_{S'} \underline{\mathbf{E}}_a \cdot (\underline{\mathbf{n}} \times \underline{\mathbf{H}}) dA \right] \\
 & + \sum_a \underline{\mathbf{F}}_a \int_{S'} \underline{\mathbf{F}}_a \cdot (\underline{\mathbf{n}} \times \underline{\mathbf{H}}) dA
 \end{aligned} \quad (72)$$

Since $\underline{\mathbf{G}}_\lambda$ is related to $\underline{\mathbf{H}}$, expand $\underline{\mathbf{v}} \cdot \underline{\mathbf{B}}$ in terms of the ϕ_λ as follows:

$$\underline{\mathbf{v}} \cdot \underline{\mathbf{B}} = \sum_\lambda \phi_\lambda \int_V (\underline{\mathbf{v}} \cdot \underline{\mathbf{B}} \phi_\lambda) dv$$

However, by using the vector relation

$$\begin{aligned}
 \underline{\mathbf{v}} \cdot (\phi_\lambda \underline{\mathbf{B}}) &= \underline{\mathbf{B}} \cdot \underline{\mathbf{v}} \phi_\lambda + \phi_\lambda \underline{\mathbf{v}} \cdot \underline{\mathbf{B}} \\
 &= \underline{\mathbf{B}} \cdot k_\lambda \underline{\mathbf{G}}_\lambda + \phi_\lambda \underline{\mathbf{v}} \cdot \underline{\mathbf{B}}
 \end{aligned}$$

integrating over the cavity volume, and using Gauss' theorem, one obtains

$$\int_V (\phi_\lambda \underline{\mathbf{v}} \cdot \underline{\mathbf{B}}) dv = -k_\lambda \int_V (\underline{\mathbf{B}} \cdot \underline{\mathbf{G}}_\lambda) dv + \int_{S', S} (\phi_\lambda \underline{\mathbf{B}} \cdot \underline{\mathbf{n}}) dA$$

Since $\phi_\lambda = 0$ on S' the surface integral over this part of the area of zero. Now Equation (73) becomes

$$\underline{\mathbf{v}} \cdot \underline{\mathbf{B}} = \sum_\lambda \phi_\lambda \left[-k_\lambda \int_V (\underline{\mathbf{B}} \cdot \underline{\mathbf{G}}_\lambda) dv + \int_S (\phi_\lambda \underline{\mathbf{B}} \cdot \underline{\mathbf{n}}) dA \right]$$

In a corresponding manner one can obtain for $\underline{\mathbf{v}} \cdot \underline{\mathbf{D}}$

$$\underline{\mathbf{v}} \cdot \underline{\mathbf{D}} = \sum_a \psi_a \left[-k_a \int_V (\underline{\mathbf{D}} \cdot \underline{\mathbf{F}}_a) dv + \int_{S'} (\psi_a \underline{\mathbf{D}} \cdot \underline{\mathbf{n}}) dA \right]$$

Equations (66), (71), (72), (74) and (75) give the expansions for the various electromagnetic field quantities which can now be used in Maxwell's equations.

B. ILLUSTRATIVE EXPANSION OF CAVITY FIELDS

If one lacks experience in handling cavity fields with the type of expansions made here, it might prove helpful to make a specific expansion at this time. Consider a rectangular cavity with ideal metal walls as shown in Figure 23, which is operating in the TE_{mnp} mode.

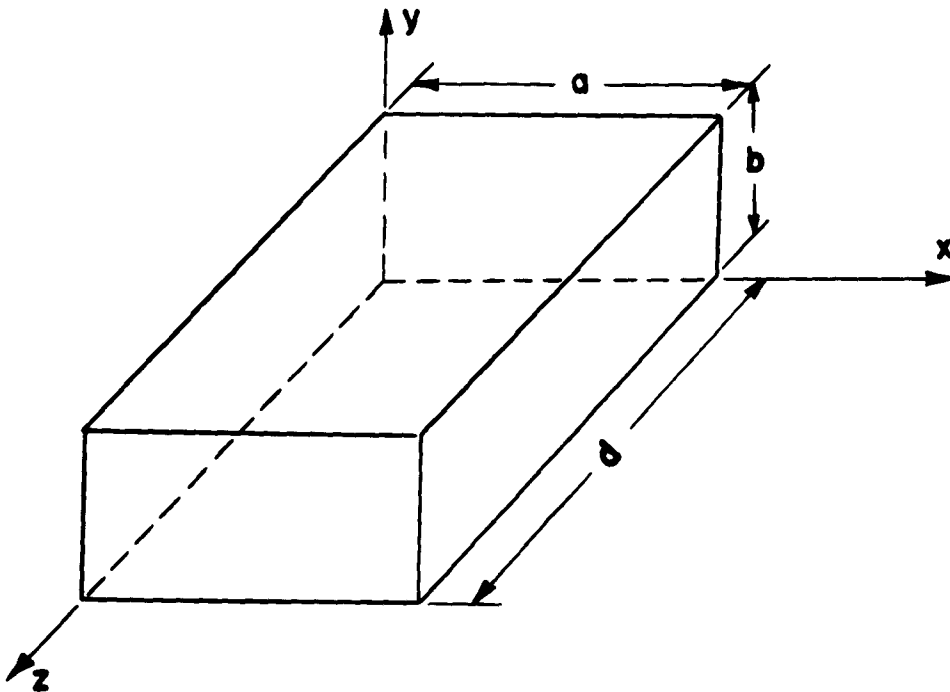


Figure 23. Rectangular Cavity.

The fields in this cavity may be expressed as follows:

$$\begin{aligned}
 H_z &= H_0 \cos \beta_x x \cos \beta_y y \sin \beta_z z e^{j\omega t}, \\
 H_x &= -H_0 \frac{\beta_z \beta_x}{\beta_c^2} \sin \beta_x x \cos \beta_y y \cos \beta_z z e^{j\omega t}, \\
 H_y &= -H_0 \frac{\beta_z \beta_y}{\beta_c^2} \cos \beta_x x \sin \beta_y y \cos \beta_z z e^{j\omega t}, \\
 E_x &= j \frac{\omega \mu H_0 \beta_y}{\beta_c^2} \cos \beta_x x \sin \beta_y y \sin \beta_z z e^{j\omega t}, \\
 E_y &= -j \frac{\omega \mu H_0 \beta_x}{\beta_c^2} \sin \beta_x x \cos \beta_y y \sin \beta_z z e^{j\omega t}
 \end{aligned} \quad (76)$$

where

$$\begin{aligned}
 \beta_x &= \frac{n\pi}{a}; \quad \beta_y = \frac{m\pi}{b}; \quad \beta_z = \frac{p\pi}{d}, \\
 \beta_c^2 &= \beta_x^2 + \beta_y^2
 \end{aligned} \quad (77)$$

The particular cavity chosen needs only the solenoidal parts of the expansion for \underline{E} and \underline{H} to describe these fields. One can find

$$\begin{aligned}
 \int_V (\underline{E} \cdot \underline{E}_a) dv \text{ by taking } \int_V (\underline{E} \cdot \underline{E}^*) dv \text{ and realizing that the residue} \\
 \text{is } \left[\int_V (\underline{E} \cdot \underline{E}_a) dv \right] \left[\int_V (\underline{E} \cdot \underline{E}_a) dv \right]^*. \text{ Then } \underline{E}_a \text{ may be found by} \\
 \text{comparing the coefficient } \int_V (\underline{E} \cdot \underline{E}_a) dv \text{ with } \underline{E}. \text{ These operations give} \\
 \int_V (\underline{E} \cdot \underline{E}_a) dv = j \frac{\omega \mu H_0}{\beta_c} \sqrt{\frac{abd}{8}} e^{j\omega t}, \quad (78)
 \end{aligned}$$

$$\underline{E}_a = \sqrt{\frac{8}{abd}} \left[i \frac{\beta_y}{\beta_c} \cos \beta_x x \sin \beta_y y \sin \beta_z z - j \frac{\beta_x}{\beta_c} \sin \beta_x x \cos \beta_y y \sin \beta_z z \right].$$

A similar operation on \underline{H} gives

$$\int_V (\underline{H} \cdot \underline{H}_a) dv = - \frac{H_0 k_a}{\beta_c} \sqrt{\frac{abd}{8}} e^{j\omega t} ,$$

$$\underline{H}_a = \sqrt{\frac{8}{abd}} \left[\begin{aligned} & i \frac{\beta_z \beta_x}{\beta_c k_a} \sin \beta_x x \cos \beta_y y \cos \beta_z z + j \frac{\beta_z \beta_y}{\beta_c k_a} \cos \beta_x x \sin \beta_y y \cos \beta_z z \\ & - k \frac{\beta_c}{k_a} \cos \beta_x x \cos \beta_y y \sin \beta_z z \end{aligned} \right] ,$$

$$k_a^2 = \beta_x^2 + \beta_y^2 + \beta_z^2 .$$

C. MAXWELL'S EQUATIONS WITH ORTHOGONAL FUNCTIONS

It is now possible to substitute the series obtained in section A into Maxwell's equations (assuming μ and ϵ are constant throughout the cavity volume). Of course, the resulting equations will be a summation of series involving various combinations of the basic functions \underline{E}_a , \underline{H}_a , \underline{G}_λ , and \underline{F}_a . Actually the primary interest of these equations are the coefficients of these functions, as expressed by the various volume and surface integrations [see for example Equations (63) and (64)]. A particular "set" of coefficients may be examined by using the orthogonal properties of the basic functions. This process is illustrated in the next few paragraphs.

From

$$\underline{\nabla} \times \underline{E} = - \frac{\partial \underline{B}}{\partial t} ,$$

is obtained

$$\begin{aligned} \sum_a \underline{H}_a \left[k_a \int_V (\underline{E} \cdot \underline{E}_a) dv + \int_S \underline{H}_a \cdot (\underline{n} \times \underline{E}) dA \right] + \sum_\lambda \underline{G}_\lambda \int_S \underline{G}_\lambda \cdot (\underline{n} \times \underline{E}) dA \\ = -\mu \frac{d}{dt} \left[\sum_a \underline{H}_a \int_V (\underline{H} \cdot \underline{H}_a) dv + \sum_\lambda \underline{G}_\lambda \int_V (\underline{H} \cdot \underline{G}_\lambda) dv \right] . \end{aligned}$$

Multiply through this equation by \underline{H}_a , integrate over the volume, and obtain an equation in terms of the coefficients for this particular \underline{H}_a .

The same technique can be used with \underline{G}_λ so that for the \underline{H}_a coefficients,

$$k_a \int_V (\underline{E} \cdot \underline{E}_a) dv + \int_S \underline{H}_a \cdot (\underline{n} \times \underline{E}) dA = -\mu \frac{d}{dt} \int_V (\underline{H} \cdot \underline{H}_a) dv ; \quad (80)$$

and for the \underline{G}_λ coefficients,

$$\int_S \underline{G}_\lambda \cdot (\underline{n} \times \underline{E}) dA = -\mu \frac{d}{dt} \int_V (\underline{H} \cdot \underline{G}_\lambda) dv . \quad (81)$$

Similarly $\underline{v} \times \underline{H} - \frac{\partial \underline{D}}{\partial t} = \underline{J}$ becomes

$$k_a \int_V (\underline{H} \cdot \underline{H}_a) dv - \epsilon \frac{d}{dt} \int_V (\underline{E} \cdot \underline{E}_a) dv = \int_V (\underline{J} \cdot \underline{E}_a) dv - \int_S \underline{E}_a \cdot (\underline{n} \times \underline{H}) dA ,$$

$$\int_S \underline{F}_a \cdot (\underline{n} \times \underline{H}) dA - \epsilon \frac{d}{dt} \int_V (\underline{E} \cdot \underline{F}_a) dv = \int_V (\underline{J} \cdot \underline{F}_a) dv . \quad (83)$$

The equation $\underline{v} \cdot \underline{D} = \rho$ gives

$$-k_a \int_V (\underline{D} \cdot \underline{F}_a) dv + \int_S (\Psi_a \underline{D} \cdot \underline{n}) dA = \int_V (\rho \Psi_a) dv . \quad (84)$$

The equation $\underline{v} \cdot \underline{B} = 0$ gives

$$k_\lambda \int_V (\underline{B} \cdot \underline{G}_\lambda) dv = \int_S (\Phi_\lambda \underline{B} \cdot \underline{n}) dA . \quad (85)$$

Now from Equations (80) to (85) the expansion coefficients

$$\int_V (\underline{E} \cdot \underline{E}_a) dv , \int_V (\underline{H} \cdot \underline{H}_a) dv , \int_V (\underline{E} \cdot \underline{F}_a) dv , \text{ and } \int_V (\underline{H} \cdot \underline{G}_\lambda) dv$$

may be found and then substituted into Equation (66) to give the electric and magnetic fields in the cavity. Slater⁶ has shown that Equations (83) and (84) lead to the continuity of electric charge,

$$\underline{\nabla} \cdot \underline{J} + \frac{\partial}{\partial t} \rho = 0 \quad (86)$$

Equations (81) and (85) may be combined by taking the time derivative of (85) and substituting into (81) to obtain

$$-\frac{\partial}{\partial t} \int_s (\phi_\lambda \underline{B} \cdot \underline{n}) dA = k_\lambda \int_s \underline{G}_\lambda \cdot (\underline{n} \times \underline{E}) dA = \int_s \underline{\nabla} \phi_\lambda \cdot (\underline{n} \times \underline{E}) dA. \quad (87)$$

To simplify the second term introduce the differential operator $\underline{\nabla}_A$ on the surface, which is equivalent to $\underline{\nabla} - \underline{n} \frac{\partial}{\partial \underline{n}}$. By vector identity,

$$\underline{\nabla}_A \cdot (\phi_\lambda \underline{n} \times \underline{E}) = \underline{\nabla}_A \phi_\lambda \cdot (\underline{n} \times \underline{E}) + \phi_\lambda \underline{\nabla}_A \cdot (\underline{n} \times \underline{E}) .$$

By integrating this over the surface and realizing that $\underline{\nabla}_A \phi_\lambda = \underline{\nabla} \phi_\lambda$ (since $\frac{\partial}{\partial \underline{n}} \phi_\lambda = 0$ on s and $\phi_\lambda = 0$ on s'),

$$\int_{s, s'} \underline{\nabla}_A \cdot (\phi_\lambda \underline{n} \times \underline{E}) dA = \int_s \underline{\nabla} \phi_\lambda \cdot (\underline{n} \times \underline{E}) dA + \int_s \phi_\lambda \underline{\nabla}_A \cdot (\underline{n} \times \underline{E}) dA .$$

The operator $\underline{\nabla}_A$ treats the surface as an equivalent "volume" so that

$$\int_{s, s'} \underline{\nabla}_A \phi_\lambda \cdot (\underline{n} \times \underline{E}) dA = - \int_{s, s'} (\phi_\lambda \underline{n} \times \underline{E}) dl ,$$

where dl is on the perimeter of the cavity surface. However, the line integral about the surface surrounding the cavity volume is zero since its perimeter vanishes; therefore

$$\int_s \underline{\nabla} \phi_\lambda \cdot (\underline{n} \times \underline{E}) dA = - \int_s \phi_\lambda \underline{\nabla}_A \cdot (\underline{n} \times \underline{E}) dA ,$$

and Equation (87) becomes

$$\frac{d}{dt} \int_S (\phi_\lambda \underline{B} \cdot \underline{n}) dA = \int_S \phi_\lambda \underline{v}_A \cdot (\underline{n} \times \underline{E}) dA ,$$

or

$$\frac{d}{dt} (\underline{B} \cdot \underline{n}) = \underline{v}_A \cdot (\underline{n} \times \underline{E}) . \quad (88)$$

Equation (88) expresses the conservation of the fictitious surface magnetic charge just as Equation (86) expresses the conservation of electric charge.

This leaves Equations (70) and (82), which may be combined and

solved for $\int_V (\underline{E} \cdot \underline{E}_a) dv$ and $\int_V (\underline{H} \cdot \underline{H}_a) dv$. This solution is straightforward since these equations are of the form

$$ax + by = c ,$$

$$dx + cy = f ,$$

Their solution gives

$$\begin{aligned} & \left(\mu \epsilon \frac{d^2}{dt^2} + k_a^2 \right) \int_V (\underline{E} \cdot \underline{E}_a) dv \\ &= -\mu \frac{d}{dt} \left[\int_V (\underline{J} \cdot \underline{E}_a) dv - \int_S \underline{E}_a \cdot (\underline{n} \times \underline{H}) dA \right] - k_a \int_S \underline{H}_a \cdot (\underline{n} \times \underline{E}) dA \end{aligned} \quad (89)$$

$$\begin{aligned} & \left(\mu \epsilon \frac{d^2}{dt^2} + k_a^2 \right) \int_V (\underline{H} \cdot \underline{H}_a) dv \\ &= k_a \left[\int_V (\underline{J} \cdot \underline{E}_a) dv - \int_S \underline{E}_a \cdot (\underline{n} \times \underline{H}) dA \right] - \epsilon \frac{d}{dt} \int_S \underline{H}_a \cdot (\underline{n} \times \underline{E}) dA . \end{aligned} \quad (90)$$

These two equations, (89) and (90), form the basis for the rest of this development. In fact, these two equations will usually be the most important in any type of analysis using this orthogonal expansion for the cavity fields. The series coefficients $\int_V (\underline{E} \cdot \underline{E}_a) dv$ and $\int_V (\underline{H} \cdot \underline{H}_a) dv$ determine the solenoidal parts of \underline{E} and \underline{H} , which is the part showing properties of wave propagation. This part of the field is usually regarded as the "radiation" field. The other coefficients $\int_V (\underline{E} \cdot \underline{F}_a) dv$ and $\int_V (\underline{H} \cdot \underline{G}_a) dv$ which determine the irrotational parts of \underline{E} and \underline{H} may be found from Equations (81), (83), (84), and (85). This part of \underline{E} and \underline{H} of course has zero curl, and hence is derivable from a scalar potential as shown by Equation (51). Except for the $a = 0$ and $\lambda = 0$ functions, the problem of finding these parts of \underline{E} and \underline{H} is similar to the electrostatic or magnetostatic problem but with time-varying charge distributions. Note that no account has been taken here of time retardation or of finite velocities of propagation of a disturbance.

D. ILLUSTRATIVE PROBLEM

It would be of value at this point to see just how the material derived may be used. Consider a cavity with ideal metal walls (no s' surfaces) filled with a lossy dielectric. Thus in the cavity $\sigma \neq 0$, therefore $\underline{J} = \sigma \underline{E}$; also $(\underline{n} \times \underline{E}_s) = 0$, since the walls are ideal. With this information Equation (89) becomes

$$\left[\mu \epsilon \frac{d^2}{dt^2} + \mu \sigma \frac{d}{dt} + k_a^2 \right] \int_V (\underline{E} \cdot \underline{E}_a) dv = 0 . \quad (91)$$

Assume a solution of the form

$$\int_V (\underline{E} \cdot \underline{E}_a) dv = C e^{j\omega t} ,$$

where ω is the complex frequency,

$$\omega = \omega_1 + j\omega_2 .$$

Now Equation (91) may be solved by realizing that

$$\omega_a^2 = \frac{k_a^2}{\mu \epsilon} \quad (\text{ideal resonant frequency}) ,$$

and

$$Q_d = \frac{\epsilon \omega_a}{\sigma} \quad (\text{dielectric Q}) .$$

This solution yields

$$\omega_a^2 = \omega_1^2 + \omega_2^2 ,$$

and

$$\omega = \pm \omega_a \sqrt{1 - \left(\frac{1}{2Q_d}\right)^2} + j \frac{\omega_a}{2Q_d} ;$$

so that the oscillation frequency ω_1 becomes

$$\omega_1^2 = \omega_a^2 \left[1 - \left(\frac{1}{2Q_d}\right)^2 \right] .$$

E. GENERAL PERTURBATION OF CAVITIES

The general case of perturbation by the insertion of any substance in a cavity can be divided into these three classes:

- (1) fields do not penetrate;
- (2) fields totally penetrate the substance; and
- (3) fields partially penetrate the substance.

These correspond approximately to the respective conditions $\frac{\sigma}{j\omega} \gg \epsilon$, $\frac{\sigma}{j\omega} \ll \epsilon$, and $\frac{\sigma}{j\omega} \approx \epsilon$. Since the first and second classes most nearly match the usual physical situation when a substance is

intentionally inserted, only these will be treated here.

The general method of attack in both these cases will be to assume a given ideal cavity in which the fields \underline{E}_a and \underline{H}_a are known. Then if the object inserted in the cavity is small so that the perturbation is also small, the original fields will be only slightly altered. This slight change can be accounted for by applying a correction term to the original fields. In this manner the frequency shift caused by the perturbing object can be calculated.

Perhaps some insight may be gained into the problem of correcting the original fields by considering Poynting's power-flow theorem,

$$-\int_A \underline{n} \cdot (\underline{E} \times \underline{H}) dA = \int_V (\mu \underline{H} \cdot \frac{\partial \underline{H}}{\partial t} + \epsilon \underline{E} \cdot \frac{\partial \underline{E}}{\partial t} + \underline{J} \cdot \underline{E}) dv , \quad (92)$$

where the left side is the closed integral on the area surrounding the volume and represents the power flow into the volume. Suppose only the a^{th} mode is present so that the following may be substituted for \underline{E} and \underline{H} :

$$\begin{aligned} \underline{E} &= \underline{E}_a \int_V (\underline{E} \cdot \underline{E}_a) dv , \\ \underline{H} &= \underline{H}_a \int_V (\underline{H} \cdot \underline{H}_a) dv , \end{aligned} \quad (93)$$

where only the solenoidal functions is now considered since this is the important one in determining the "radiation" field mentioned earlier. Equation (92) becomes

$$\begin{aligned}
& - \int_A \underline{n} \cdot (\underline{E}_a \times \underline{H}_a) dA \int_V (\underline{E} \cdot \underline{E}_a) dv \int_V (\underline{H} \cdot \underline{H}_a) dv \\
& = \int_V \left[j \omega_a \mu H_a^2 \left(\int_V (\underline{H} \cdot \underline{H}_a) dv \right)^2 + j \omega_a \epsilon E_a^2 \left(\int_V (\underline{E} \cdot \underline{E}_a) dv \right)^2 \right] dv . \tag{94}
\end{aligned}$$

Equation (92) has now been applied to an ideal cavity, hence $\sigma = 0$ inside the cavity. In Equation (94) H_a^2 is understood to mean $\underline{H}_a \cdot \underline{H}_a^*$ and E_a^2 means $\underline{E}_a \cdot \underline{E}_a^*$. The same is true for the square of the series coefficients,

$$\int_V (\underline{E} \cdot \underline{E}_a) dv \quad \text{and} \quad \int_V (\underline{H} \cdot \underline{H}_a) dv .$$

These two coefficients may be related by using Equation (80) and the fact that

$$\omega_a^2 = \frac{k_a^2}{\mu \epsilon}$$

for an ideal cavity. Equation (80) becomes

$$\begin{aligned}
k_a \int_V (\underline{E} \cdot \underline{E}_a) dv &= -j \mu \omega_a \int_V (\underline{H} \cdot \underline{H}_a) dv , \\
\frac{\int_V (\underline{E} \cdot \underline{E}_a) dv}{\int_V (\underline{H} \cdot \underline{H}_a) dv} &= -j \sqrt{\frac{\mu}{\epsilon}} . \tag{95}
\end{aligned}$$

Of course, this 90° time relationship between the electric and magnetic fields is just what is expected in an ideal cavity. Substituting Equation (95) into Equation (94) gives

$$-\int_A \underline{n} \cdot (\underline{E}_a \times \underline{H}_a) dA = -k_a \int_V (\underline{H}_a^2 - \underline{E}_a^2) dv . \quad (96)$$

This is the result sought. It shows the form of the expression for the energy flow into and out of a given volume. If one approaches the problem of perturbation from the energy viewpoint; that is, by considering the change in energy over the volume of the perturbing object caused by the different electrical properties of this object, then one should be using terms of the form of Equation (96).

In the derivations following the approach suggested above is used directly for the first part, and indirectly for the second. In reality, the small perturbations, on the whole, affect the cavity fields only slightly; however, immediately in the vicinity of the perturbing object the fields are often grossly changed. In the first analysis this effect on the "near fields" is neglected and is included later in a term called the calibration constant. This method is used to give a clear physical picture at first, before giving a more precise final result.

1. Class 1 Perturbation ($\frac{\sigma}{j\omega} \gg \epsilon$, or metal beads)

Assume a cavity with perfect metal walls and operating in the a^{th} mode for which the fields \underline{E}_a and \underline{H}_a and their respective coefficients are known. Now suppose a small metal bead of volume τ is placed in this cavity such that the perturbation is small. Figure 24 shows the original and perturbed states with the associated volumes and surface normals involved.

First examine Equation (89) with the current integral dropped (since $\underline{J} = 0$) and the surface integral over s' dropped (no s' surfaces).

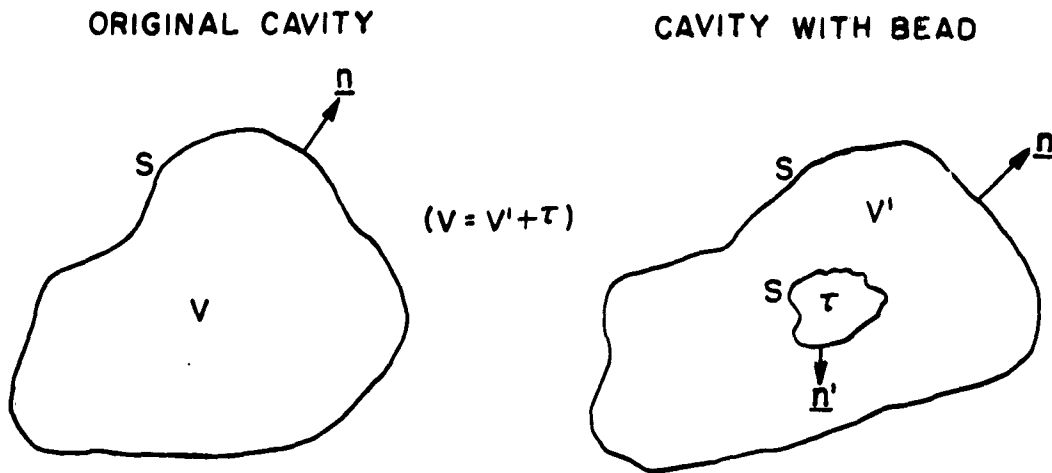


Figure 24. Perturbed Cavity.

This becomes:

$$\mu \epsilon \frac{d^2}{dt^2} + k_a^2 \int_V (\underline{E} \cdot \underline{E}_a) dv = -k_a \int_S \underline{H}_a \cdot (\underline{n} \times \underline{E}) dA .$$

Since the cavity is assumed ideal, the right side should be zero (no tangential component of \underline{E} at the metal walls). Permute the order of the vectors, and substitute Equation (93), since only the a^{th} mode is present.

$$\left(\mu \frac{d^2}{dt^2} + k_a^2 \right) \int_V (\underline{E} \cdot \underline{E}_a) dv = -k_a \int_S \underline{n} \cdot (\underline{E}_a \times \underline{H}_a) dA \int_V (\underline{E} \cdot \underline{E}_a) dv .$$

The right side of this equation is now recognized from Equation (96). This term acts as a "driving force" and represents energy being fed into the cavity. In an ideal cavity, as was just pointed out, this term is zero. If the cavity has wall losses, then the term is not zero (there will now exist a small tangential component of \underline{E} at the walls) since energy must be fed into the cavity if it is to continue to operate.

Now to return to the metal bead inside the cavity shown in Figure 24, it is apparent that the bead removes a small portion of the cavity fields or of the internal energy since no fields can exist inside the metal bead. Of course this alters the original fields slightly. However,

the original fields may still be considered to be present if the region of the bead is considered as an energy "sink." That is in Equation (97) the right side of the equation can be adjusted to represent energy removed from the cavity by the bead. The surface integral is then over the surface of the bead and the algebraic sign is changed to indicate energy fed out of the cavity with respect to the normal \underline{n} . Equation (97) becomes

$$\left(\mu \epsilon \frac{d^2}{dt^2} + k_a^2 \right) \int_V (\underline{E} \cdot \underline{E}_a) dv = k_a \int_S \underline{n} \cdot (\underline{E}_a \times \underline{H}_a) dA \int_V (\underline{E} \cdot \underline{E}_a) dv .$$

(over bead)

In terms of \underline{n}' ,

$$\underline{n} = -\underline{n}'$$

Substituting this and Equation (96) into the above equation gives

$$\left[\mu \epsilon \frac{d^2}{dt^2} + k_a^2 \left(1 + \int_{\tau} (\underline{H}_a^2 - \underline{E}_a^2) dv \right) \right] \int_V (\underline{E} \cdot \underline{E}_a) dv = 0 . \quad (98)$$

Now the integral over τ represents the energy removed by the bead.

Assuming a solution of the form

$$\int_V (\underline{E} \cdot \underline{E}_a) dv = C e^{j\omega t} ,$$

gives

$$-\omega^2 \mu \epsilon + k_a^2 \left[1 + \int_{\tau} (\underline{H}_a^2 - \underline{E}_a^2) dv \right] = 0 ,$$

or

$$\omega^2 = \omega_a^2 \left[1 + \int_{\tau} (\underline{H}_a^2 - \underline{E}_a^2) dv \right] . \quad (99)$$

Equation (99) now relates the new resonant frequency ω to the original resonant frequency ω_a . If δ is defined as

$$\delta = \frac{\omega - \omega_a}{\omega_a} \quad , \quad (100)$$

and a small perturbation is assumed, Equation (99) becomes

$$\delta = \frac{(H_a^2 - E_a^2)}{2} \tau \quad (101)$$

The calibration constants mentioned earlier can now be included so that Equation (101) becomes:

$$\delta = (K_{1h} H_a^2 - K_{1e} E_a^2) \frac{\tau}{2} \quad (102)$$

where K_{1e} refers to class 1 electric field perturbation and K_{1h} to class 1 magnetic field perturbation. These quantities are calculated in a later section.

2. Class 2 Perturbation $\frac{\sigma}{j\omega} \ll \epsilon$ (or dielectrics and ferrites)

This case is quite different from the one just calculated since the fields in the cavity will also exist inside this type of bead. Figure 24 still applies, only now the cavity has the properties μ_0 and ϵ_0 while the bead has the properties μ and ϵ . Equation (92) suggests the use of the displacement current $\partial D / \partial t$ and the fictitious magnetic current $\partial B / \partial t$ in accounting for the bead effects. In this way it may be possible to calculate an equivalent μ' and ϵ' of the combination of bead and cavity. With the bead inserted in the cavity, the total displacement current is given by

$$i_D = \epsilon_0 \frac{d}{dt} \underline{E} + \underbrace{(\epsilon - \epsilon_0) \frac{d}{dt} \underline{E}}_{\text{over } \tau} \quad . \quad (103)$$

Equation (93) can be substituted for \underline{E} , and the resulting expression used in Maxwell's $\underline{v} \times \underline{H}$ equation to integrate over the volumes concerned to find the relative contributions of displacement current:

$$k_a \int_V (\underline{E}_a \int_V (\underline{H} \cdot \underline{H}_a) dv) dv$$

$$= \epsilon_0 \frac{d}{dt} \int_V \left(\underline{E}_a \int_V \underline{E} \cdot \underline{E}_a dv \right) dv + (\epsilon - \epsilon_0) \frac{d}{dt} \int_V \left(\underline{E}_a \int_V \underline{E} \cdot \underline{E}_a dv \right) dv$$

Now one can differentiate with respect to the volume V ,

$$k_a \underline{E}_a \int_V (\underline{H} \cdot \underline{H}_a) dv = \epsilon_0 \frac{d}{dt} \underline{E}_a \int_V (\underline{E} \cdot \underline{E}_a) dv + (\epsilon - \epsilon_0) \frac{d}{dt} \int_V \underline{E}_a (\underline{E} \cdot \underline{E}_a) dv .$$

Substituting for \underline{E} in the last term, dividing through by \underline{E}_a , and collecting terms gives

$$k_a \int_V (\underline{H} \cdot \underline{H}_a) dv = \epsilon_0 \left[1 + (K_d - 1) \int_V \underline{E}_a^2 dv \right] \frac{d}{dt} \int_V (\underline{E} \cdot \underline{E}_a) dv , \quad (104)$$

where

$$K_d = \frac{\epsilon}{\epsilon_0}$$

A similar solution of Maxwell's $\underline{v} \times \underline{E}$ equation can be obtained using the fictitious magnetic current which gives

$$k_a \int_V (\underline{E} \cdot \underline{E}_a) dv + \mu_0 \left[1 + (K_m - 1) \int_V \underline{H}_a^2 dv \right] \frac{d}{dt} \int_V (\underline{H} \cdot \underline{H}_a) dv = 0 , \quad (105)$$

where

$$K_m = \frac{\mu}{\mu_0}$$

Combining Equations (104) and (105) to solve for $\int_V (\mathbf{E} \cdot \underline{\mathbf{E}}_a) dv$ and $\int_V (\mathbf{H} \cdot \underline{\mathbf{H}}_a) dv$ separately results in

$$\left\{ \mu_0 \epsilon_0 \left[1 + (K_d - 1) \int_T \mathbf{E}_a^2 dv \right] \left[1 + (K_m - 1) \int_T \mathbf{H}_a^2 dv \right] \frac{d^2}{dt^2} + k_a^2 \right\} \left\{ \begin{array}{l} \int_V (\mathbf{E} \cdot \underline{\mathbf{E}}_a) dv \\ \int_V (\mathbf{H} \cdot \underline{\mathbf{H}}_a) dv \end{array} \right\} = 0 . \quad (106)$$

In comparing this equation to Equations (89) and (90), it is seen that the equivalent μ' and ϵ' are as follows:

$$\epsilon' = \epsilon_0 \left[1 + (K_d - 1) \int_T \mathbf{E}_a^2 dv \right] , \quad (107)$$

$$\mu' = \mu_0 \left[1 + (K_m - 1) \int_T \mathbf{H}_a^2 dv \right] .$$

As is customary a solution of form $e^{j\omega t}$ is assumed for Equation (106); then

$$\omega^2 = \frac{\omega_a^2}{\left[1 + (K_d - 1) \int_T \mathbf{E}_a^2 dv \right] \left[1 + (K_m - 1) \int_T \mathbf{H}_a^2 dv \right]} . \quad (108)$$

Since the perturbation is assumed small, second order terms can be neglected and Equation (100) can be used to obtain

$$\delta = - (K_d - 1) \frac{\mathbf{E}_a^2 \tau}{2} - (K_m - 1) \frac{\mathbf{H}_a^2 \tau}{2} . \quad (109)$$

Upon insertion of the calibration constants Equation (109) becomes

$$\delta = -K_{2e} (K_d - 1) \frac{E_a^2 \tau}{2} - K_{2h} (K_m - 1) \frac{H_a^2 \tau}{2} \quad (110)$$

where K_{2e} refers to class 2 electric field perturbation and K_{2h} to class 2 magnetic field perturbation.

3. Practical Form of Perturbation Equations

If one is unaccustomed to using the normalized fields \underline{E}_a and \underline{H}_a , then Equations (102) and (110) may be written in terms of the conventional \underline{E} and \underline{H} fields as follows:

$$\delta = \frac{(K_{1h} \mu_0 H^2 - K_{1e} \epsilon_0 E^2) \tau}{4U} \quad (\text{Class 1}) , \quad (111)$$

$$\delta = \frac{-K_{2e} (K_d - 1) \epsilon_0 E^2 \tau}{4U} - \frac{K_{2h} (K_m - 1) \mu_0 H^2 \tau}{4U} \quad (\text{Class 2}) , \quad (112)$$

where U equals the total stored energy in the cavity.

F. CALIBRATION CONSTANTS

It was mentioned earlier that the reason for introducing the calibration constants is the effect the bead has on its near fields in the cavity, even though, on the whole, the fields are only slightly altered. This calibration constant may be calculated if we impose the conditions that the bead is small compared to a wavelength both inside and outside the bead so that the bead in the cavity is in a region of nearly uniform fields, and also that the bead is kept several diameters away from the cavity boundaries so as to avoid image effects. This calculation may then be made by considering the effects of placing the particular bead in question in a uniform electrostatic or magnetostatic field. Thus the problem may be reduced to approximately the static solution of

Laplace's equation.

As it turns out the calibration constant depends on four factors:

- 1) material of the bead,
- 2) shape of the bead,
- 3) orientation of the bead in the field,
- 4) type of field the bead is perturbing (E or H).

Once this "constant" is determined for a particular set of these conditions it will remain constant, independent of field strength, provided the assumptions made concerning size and nearness to boundaries are adhered to.

Since the static solution to Laplace's equation involves matching boundary conditions, only beads whose boundaries may be expressed simply are considered here. This includes spheres by the use of spherical co-ordinates and ellipsoids of revolution by the use of elliptical co-ordinates. The general ellipsoid with three unequal axes is not considered here since elliptic integrals of the second kind result. As an example the calibration constant for a metal sphere perturbing an electric field is calculated.

The insertion of this bead into a uniform electric field E_0 may be shown easily by the use of Legendre polynomials to cause a field

$E_r = 3E_0 \cos \theta$, $E_\theta = 0$, $E_\psi = 0$ to exist at the surface of the metal sphere. Here r , θ , and ψ are the spherical co-ordinates. When this metal bead is placed in the cavity it acts as though it is placed in a region where the electric field has the same value as that at the surface of the bead. Thus E^2 over the volume of the bead is taken as

$$E^2 = 9E_0^2 \cos^2 \theta$$

and K_{le} is defined as follows:

$$K_{le} = \frac{\int_{\tau} E^2 dv}{\int_{\tau} E^2 dv} . \quad (113)$$

Substituting into Equation (113) gives

$$K_{le} = \frac{2 \int_0^a \int_0^{\pi/2} 9 E_0^2 \cos^2 \theta 2\pi r^2 \sin \theta d\theta dr}{E_0^2 \frac{4}{3} \pi a^3} = 3 \quad (114)$$

where a is the radius of the metal sphere.

Figure 25 shows the nomenclature used for the ellipsoids, while Tables 6, 7, and 8 show the calibration constants for different conditions. Figure 26 gives a pictorial representation for metal prolate spheroids as a function of the slenderness ratio. In the tables $E//$ and $H//$ mean that E and H are parallel to the semimajor axis while $E\perp$ and $H\perp$ mean that E and H are perpendicular to the semimajor axis.

G. SPECIFIC EXPERIMENTS

1. Calibration Constant

A small number of experimental measurements were made using metal spheres to check the calculated calibration constant for this type of bead in an electric field. A rectangular cavity was made from L-band wave guide so that the internal fields could be calculated accurately. The cavity size was 12.4 cm x 24.8 cm x 105.5 cm and the resonant frequency was approximately 624 megacycles. A simple arrangement was used to measure the frequency shift directly. Two oscillators were used, one to supply the cavity and the other as a standard. The output signals of these oscillators were mixed and then fed to a receiver. The

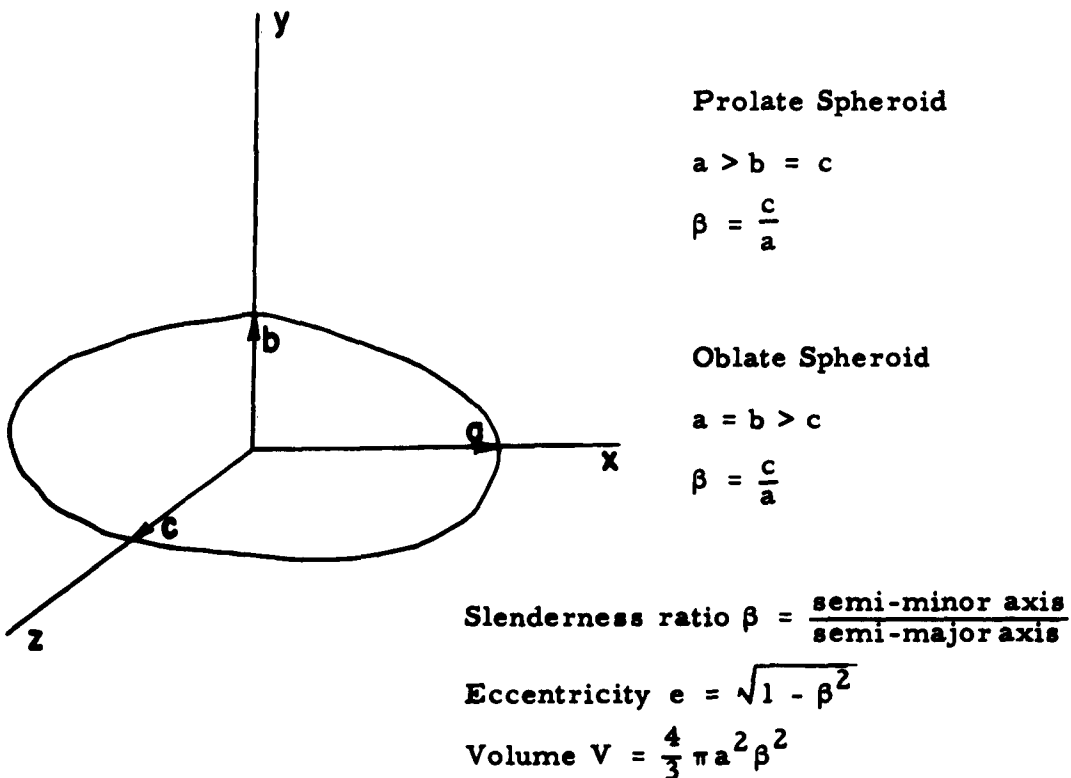


Figure 25. Nomenclature Used for Ellipsoids.

Table 6. Calibration Constants for Spheres.

| Type of Sphere | H-Field | E-Field |
|--------------------------|---------------------|---------------------|
| Metal | $\frac{3}{2}$ | 3 |
| Dielectric ($K_m = 1$) | No perturbation | $\frac{3}{K_d + 2}$ |
| Ferrite ($K_d = 1$) | $\frac{3}{K_m + 2}$ | No perturbation |

Table 7. Calibration Constants for Ellipsoids of Revolution

| Type of Bead | Material | E 1 | H 1 |
|-------------------|--------------------------|--|--|
| Prolate Spheroids | Metals | $\frac{2e^3}{e - \frac{\beta^2}{2} \ln \left(\frac{1+e}{1-e} \right)}$ | $\frac{2e^3}{(1 - 2\beta^2)e + \frac{\beta^2}{2} \ln \left(\frac{1+e}{1-e} \right)}$ |
| | Dielectrics and Ferrites | $\frac{2e^3}{(K_d - 1)\beta^2 \left[\frac{e}{\beta^2} - \frac{1}{2} \ln \frac{1+e}{1-e} \right] + 2e^3\beta^2}$ | $\frac{2e^3}{(K_m - 1)\beta^2 \left[\frac{e}{\beta^2} - \frac{1}{2} \ln \frac{1+e}{1-e} \right] + 2e^3\beta^2}$ |
| Oblate Spheroids | Metals | $\frac{e^3}{\beta^2 \left[\frac{e}{\beta} + \tan^{-1} \frac{\beta}{e} - \frac{\pi}{2} \right]}$ | $\frac{e^3}{\beta^2 \left[\frac{\pi}{2} - \tan^{-1} \frac{\beta}{e} - \beta e \right]}$ |

Table 8. Calibration Constants for Ellipsoids of Revolution

| Type of Bead | Material | E // | H // |
|-------------------|--------------------------|---|---|
| Prolate Spheroids | Metals | $\frac{e^3}{\beta^2 \left[\frac{1}{2} \ln \left(\frac{1+e}{1-e} \right) - e \right]}$ | $\frac{e^3}{e - \frac{\beta^2}{2} \ln \left(\frac{1+e}{1-e} \right)}$ |
| | Dielectrics and Ferrites | $\frac{e^3}{(K_d - 1)\beta^2 \left[\frac{1}{2} \ln \frac{1+e}{1-e} - e \right] + \beta^2 e^3}$ | $\frac{e^3}{(K_m - 1)\beta^2 \left[\frac{1}{2} \ln \frac{1+e}{1-e} - e \right] + \beta^2 e^3}$ |
| Oblate Spheroids | Metals | $\frac{2e^3}{\beta^2 \left[\frac{\pi}{2} - \tan^{-1} \frac{\beta}{e} - \beta e \right]}$ | $\frac{2e^3}{\beta^2 \left[\tan^{-1} \frac{\beta}{e} + \frac{2 - \beta^2}{\beta} e - \frac{\pi}{2} \right]}$ |

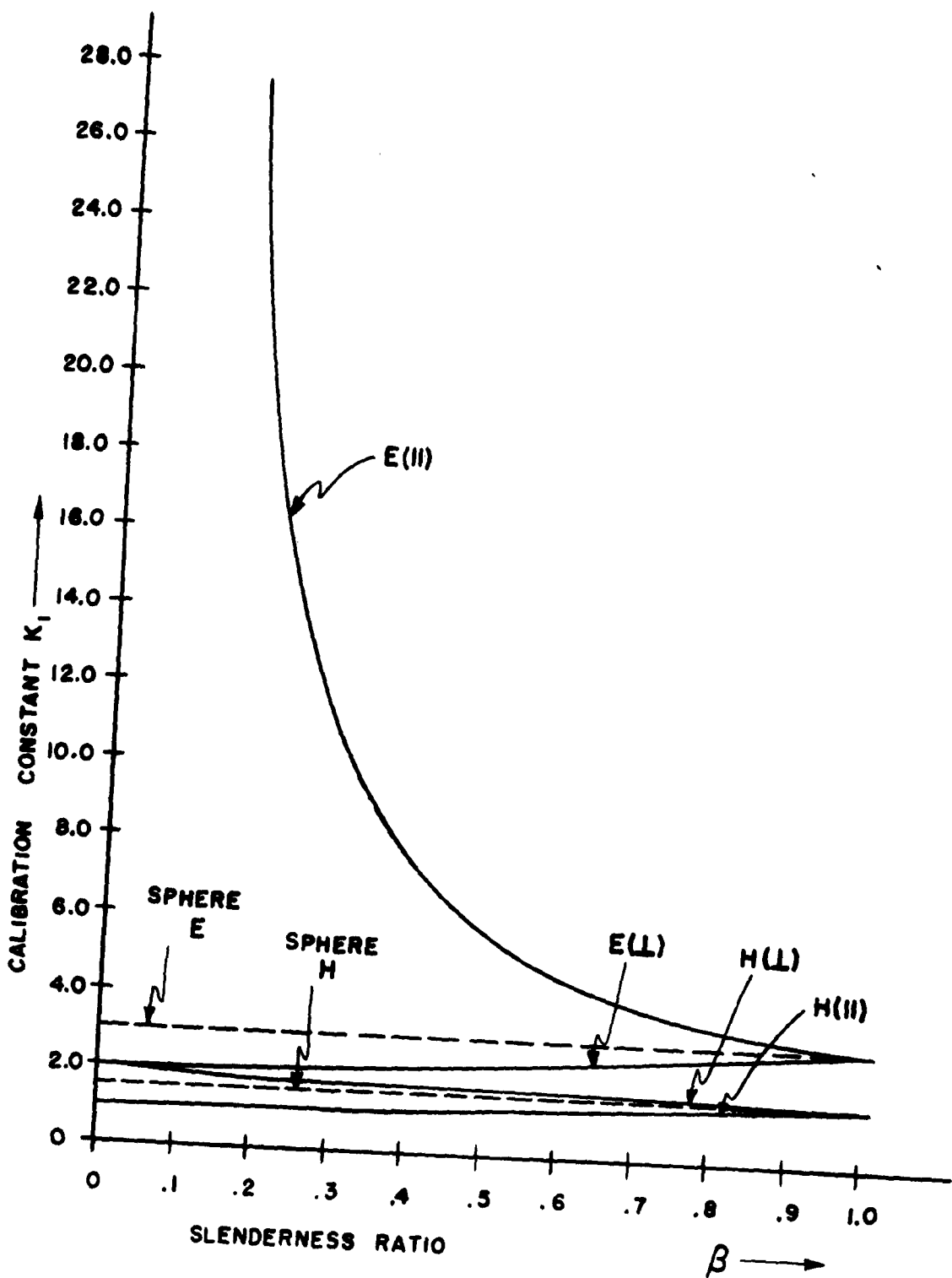


Figure 26. Calibration Constants for Metal Prolate Spheroids.
(Direction of fields given either parallel or perpendicular to major axis of bead.)

cavity oscillator was adjusted for resonance, then the bead was inserted and the oscillator readjusted for resonance. The change in the receiver reading was the frequency shift caused by the bead. The receiver had been previously calibrated against a 100 kc crystal frequency standard. For measurements of this type the suspension used for the bead is always a problem, since this can also perturb the cavity. Silk and nylon threads were finally used. The beads were inserted through the side of the cavity so that the volume of the thread was a least an order or two of magnitude smaller than the volume of the bead. The results are shown in Table 9.

Table 9. Calibration Constant Measurements for Electric Field Perturbation by Metal Spheres

| Bead Diameter | Diameter in Wavelengths | Measured K_{le} | Percent of Error | Suspension Thread |
|---------------|-------------------------|-------------------|------------------|-------------------|
| 0.177 in. | .0094 | 3.2404 | 8.0 | .002 in. silk |
| 0.500 in. | .0266 | 3.0148 | 0.5 | .003 in. nylon |
| 1.00 in. | .0532 | 5.2760 | 75.9 | .005 in. nylon |

Since the frequency shift for the smallest bead was on the order of six kilocycles and the order of error in setting the cavity on resonance was ± 2 kilocycles, this measurement is not too meaningful. Of course this data is inadequate for making any predictions but the results do indicate that the largest bead is too large compared with a wavelength for the theoretical value of the calibration constant to be valid. The measured frequency shift of this bead was 1.75 megacycles.

Other measurements of this type have been described in the literature.^{10, 11}

2. Electric Field Measurements*

The perturbation technique has been used to measure the electric field along the axis of a gridless-gap coaxial type cavity. A sensitive scheme for measuring the frequency shift was used that consisted essentially of a low-frequency sweep generator which modulated the signal generator. The cavity was used as a transmission cavity so that the dynamic resonance curve could be viewed on an oscilloscope. A calibrated signal generator used in conjunction with the sweep generator provided a frequency marker which was placed on the "z" axis of the oscilloscope. This marker was moved to line up with the resonance curve and was used to measure the frequency shift directly. The accuracy of the equipment alone was estimated as being less than one per cent. Over-all accuracy for the final measurements was estimated as being a few per cent.

* W. E. Blair, graduate student, now studying at Cornell, set up the equipment and made these measurements. A detailed account of this may be found in Research Report EE 377, Cornell University, May 1958, p. 35.

IV. CONCLUSIONS AND RECOMMENDATIONS

The design of the general doubly re-entrant gridless-gap coaxial cavity has been completely specified. This type of cavity can now be designed in such a manner that at least the first three higher-order resonances do not occur at harmonics of the signal frequency. The accuracy of this method at the fundamental resonance is within several per cent and at the higher-order resonances the error is somewhat greater. The design techniques given should cover most applications, but if not, one need only use the formulas given to set the design criteria for any special case. The general formulas developed will of course also apply to any cavity that is derived from the type considered here; i. e., singly re-entrant cavities and gridded-gap cavities. A by-product of this theory is the ability to obtain the value of R_{sh}/Q_0 at the fundamental resonance with an accuracy that appears equal to and perhaps even better than existing methods. No general calculations of either shunt resistance (R_{sh}) or cavity Q_0 are attempted here because of the strong dependence of these separate quantities on surface conductivity and incalculable losses. Accuracies better than twenty to thirty per cent would be difficult to realize.

Nonsymmetrical modes have been considered, but only on a small signal basis; i. e., these were only considered to be weakly excited (see section II-A). However, any present-day high-power klystron cavity is bound to excite these modes strongly because of the large nonsymmetrical devices for coupling out the power. The relatively small coupling loops used in the cavity model described in

section II-C excited the nonsymmetrical modes strongly enough so that these resonances were easily measured. One can imagine, then, what must occur in an output cavity with a large coupling loop or even an iris. Any meaningful analysis of a cavity under these conditions would be exceedingly difficult to make. One answer to the analysis difficulties and to the practical difficulties presented by present-day output coupling systems would be to consider a symmetrical output system for the cavity. It would certainly be worth while both analytically and experimentally to study such a possibility.

The perturbation of resonant cavities has been treated for the types of materials one is likely to use. In addition, methods for obtaining the formulas for the calculation of absolute values from perturbation measurements have been developed. It has been shown that the perturbing object or bead must be on the order of two or three hundredths of a wavelength in size for these formulas to be accurate. For larger beads, one can usually obtain only relative values of the fields. In many cases however, this is all that is required.

APPENDIX

Table A-1

$$b \cot_0 \beta r_a (a - 1)$$

Absolute Value of the Short-Circuited Radial Line Admittance

| βr_a | $a = 1.5$ | $a = 1.8$ | $a = 2.2$ |
|-------------|-----------|-----------|-----------|
| 0.10 | 24.6920 | 17.0042 | 12.6626 |
| 0.15 | — | 11.2736 | 8.3753 |
| 0.20 | 12.2905 | 8.4640 | 6.2644 |
| 0.25 | — | 6.7221 | 4.9668 |
| 0.30 | 8.1653 | 5.5994 | 4.1058 |
| 0.35 | — | 4.7601 | 3.4818 |
| 0.40 | 6.1104 | 4.1463 | 3.0042 |
| 0.50 | 4.8361 | 3.2616 | 2.3237 |
| 0.60 | 4.0021 | 2.6676 | 1.8567 |
| 0.70 | — | 2.2355 | 1.5091 |
| 0.80 | 2.9466 | 1.9039 | 1.2344 |
| 0.90 | — | 1.6380 | 1.0068 |
| 1.00 | 2.2961 | 1.4188 | 0.9114 |
| 1.20 | 1.8493 | 1.0714 | 0.4774 |
| 1.40 | 1.5185 | 0.8002 | 0.1784 |
| 1.60 | 1.2609 | 0.5816 | 0.1234 |
| 1.70 | — | 0.4715 | 0.2883 |
| 1.80 | 1.0507 | 0.3734 | 0.4721 |
| 1.90 | — | 0.2787 | 0.6861 |
| 2.00 | 0.8728 | 0.1856 | 0.9469 |
| 2.20 | 0.7183 | 0.0050 | 1.7706 |
| 2.40 | 0.5801 | 0.1926 | 4.0304 |
| 2.60 | 0.4537 | 0.4056 | 449.00 |
| 2.80 | 0.3350 | 0.6581 | 4.3027 |
| 3.00 | 0.2219 | 0.9804 | 2.1101 |

Table A-2*. UNIVERSAL CURVE

Second Order Higher Mode Inductive Susceptance
(Absolute Value Tabulated)

| | $a = 1.5$ | | | | $a = 2.0$ | | | | $a = 3.0$ | |
|-----------------------------|-----------|----------|----------|----------|-----------|----------|----------|----------|-----------|--|
| $(\beta r_a - 2\pi R)^{**}$ | $x=1.25$ | $x=1.50$ | $x=1.75$ | $x=1.25$ | $x=1.50$ | $x=1.75$ | $x=1.25$ | $x=1.50$ | $x=1.75$ | |
| .05 | 28.75 | 23.05 | 15.40 | 16.32 | 13.05 | 8.65 | 9.38 | 7.35 | 4.77 | |
| .10 | 14.30 | 11.07 | 7.84 | 7.90 | 6.01 | 4.22 | 3.98 | 2.86 | 1.83 | |
| .15 | 9.62 | — | — | 5.11 | — | — | 2.07 | — | — | |
| .20 | 7.22 | 5.40 | 3.84 | 3.72 | 2.73 | 1.90 | 1.08 | 0.47 | 0.09 | |
| .30 | 4.83 | 3.63 | 2.53 | 2.30 | 1.64 | 1.07 | < 0 | < 0 | < 0 | |
| .40 | 3.61 | 2.64 | 1.85 | 1.52 | 1.00 | 0.62 | | | | |
| .50 | 2.85 | 2.17 | 1.44 | 1.01 | 0.66 | 0.33 | | | | |
| .60 | 2.36 | 1.77 | 1.16 | 0.63 | 0.36 | 0.11 | | | | |
| .70 | 1.96 | 1.41 | 0.96 | 0.35 | 0.09 | < 0 | | | | |
| .80 | 1.69 | 1.19 | 0.79 | 0.09 | < 0 | | | | | |
| .90 | 1.45 | 1.01 | 0.66 | < 0 | | | | | | |
| 1.00 | 1.25 | — | 0.56 | | | | | | | |
| 1.10 | 1.07 | — | — | | | | | | | |
| 1.20 | 0.94 | 0.64 | 0.41 | | | | | | | |
| 1.30 | 0.82 | — | — | | | | | | | |
| 1.40 | 0.74 | — | — | | | | | | | |

* This table has been calculated by assuming a two-radian gap at

$u_0/c = 0.5$. The scale may be changed by multiplying the values by

$$\left[\frac{\sin \left(p x \frac{u_0}{c} \right)}{p \frac{u_0}{c} \sin (x)} \right]^2$$

where p is the gap length in radians. The table is approximate and is meant to be used only as a guide.

** Note: $2\pi R = \frac{2\pi r_a}{L}$ is the second higher mode cutoff.

Table A-3. Approximations for $b \coth(a\theta - \theta)$ for Computer Use.

$$b \coth(a\theta - \theta) = \frac{a_1 + a_2 \theta + a_3 \theta^2 + a_4 \theta^3}{\theta + a_5 \theta^2 + a_6 \theta^3}$$

| a | a_1 | a_2 | a_3 | a_4 | a_5 | a_6 | Range of Errors |
|------|---------|---------|---------|---------|---------|---------|------------------|
| 1.80 | 1.70129 | 0.77400 | 0.61093 | 0.35363 | 0.40705 | 0.35563 | ± 0.50 |
| 2.00 | 1.44110 | 0.77684 | 0.72857 | 0.35854 | 0.51525 | 0.35854 | + 0.25 to - 0.65 |
| 2.20 | 1.26830 | 0.87775 | 1.08918 | 0.87559 | 0.62598 | 0.87559 | ± 0.50 |
| 2.75 | 0.98853 | 0.75202 | 1.49002 | 1.61887 | 0.61812 | 1.61887 | + 0.65 to - 0.20 |

Table A-4. Calculated Data for Inner Storage Admittance.

(Table has values of $\frac{B}{y_o} \frac{r_a}{L}$ shown)

| $\frac{d}{2r_i}$ | 0.1 | 0.2 | 0.3 | 0.4 | 0.5 | 0.6 | 0.7 | 0.8 | 0.9 | 1.0 |
|------------------|--------|--------|--------|--------|--------|--------|--------|--------|--------|--------|
| 0.2857 | 0.2285 | 0.1700 | 0.1378 | 0.1165 | 0.1011 | 0.0892 | 0.0798 | 0.0721 | 0.0658 | 0.0604 |
| 0.5714 | 0.4625 | 0.3452 | 0.2810 | 0.2380 | 0.2067 | 0.1827 | 0.1636 | 0.1480 | 0.1351 | 0.1242 |
| 0.8571 | 0.7095 | 0.5330 | 0.4357 | 0.3704 | 0.3225 | 0.2857 | 0.2563 | 0.2323 | 0.2124 | 0.1954 |
| 1.1429 | 0.9805 | 0.7432 | 0.6115 | 0.5228 | 0.4573 | 0.4065 | 0.3658 | 0.3324 | 0.3044 | 0.2806 |
| 1.4286 | 1.2930 | 0.9938 | 0.8262 | 0.7120 | 0.6270 | 0.5605 | 0.5067 | 0.4621 | 0.4246 | 0.3926 |
| 1.7143 | 1.6865 | 1.3238 | 1.1179 | 0.9754 | 0.8678 | 0.7824 | 0.7125 | 0.6539 | 0.6042 | 0.5611 |
| 2.0000 | 2.2860 | 1.8565 | 1.6077 | 1.4316 | 1.2958 | 1.1855 | 1.0934 | 1.0146 | 0.9464 | 0.864 |
| 2.1429 | 2.8200 | 2.3510 | 2.0762 | 1.8790 | 1.7243 | 1.5965 | 1.4880 | 1.3936 | 1.3110 | 1.2372 |
| 2.2857 | 3.9415 | 3.4512 | 3.1532 | 2.9325 | 2.7539 | 2.6023 | 2.4700 | 2.3519 | 2.2455 | 2.1481 |

REFERENCES

1. R. D. Campbell, "Radar Interference to Microwave Communication Services," Electrical Engineering, 77, (October 1958), p. 916.
2. L. Denichel, "Net Point Calculations for Fields in Re-entrant Cavities," Master's Thesis, Stanford University (1948).
3. T. Moreno, Microwave Transmission Design Data, New York: Doyer Publications Inc., 1958.
4. C. C. Wang, "Electromagnetic Field Inside a Cylinder with a Gap," J. Ap. Physics, 16, (June 1945), p. 351.
5. N. Marcuvitz, Waveguide Handbook, New York: McGraw-Hill, 1951, p. 40.
6. J. C. Slater, Microwave Electronics, New York: D. Van Nostrand Co., Inc., 1950.
7. H. B. G. Casimer, "On the Theory of EM Waves in Resonant Cavities," Philips Res. Rep. No. 6, (1951).
8. P. M. Morse and H. Feshback, Methods of Theoretical Physics, New York: McGraw-Hill, 1953, p. 52.
9. K. Kurokawa, "The Expansions of Electromagnetic Fields in Cavities," Proc. I. R. E. PGM TT, 6, (April 1958), p. 178.
10. L. C. Maire, Jr. and J. C. Slater, "Field Strength Measurements in Resonant Cavities," J. Ap. Physics, 23, (Jan. 1952), p. 68.
11. S. W. Kitchen and A. D. Schelberg, "Resonant Cavity Field Measurements," J. Ap. Physics, 26, (May 1955), p. 618.

NOTE ON THE PRELIMINARY RESULTS
OF SPURIOUS OUTPUT POWER MEASUREMENTS

A. Ray Howland, Jr.

NOTE ON THE PRELIMINARY RESULTS OF SPURIOUS
OUTPUT POWER MEASUREMENTS

A. Ray Howland, Jr.

The output spectrum of a large klystron was measured up to the fifth harmonic. Specific measurements were made on the fundamental, second harmonic, third harmonic, fourth harmonic, and fifth harmonic. The fundamental power output of the klystron was measured in the output wave guide. The harmonic measurements were made in the output cavity of the klystron by means of a small coupling loop (sampling loop) placed in the output cavity. The sampling loop was not calibrated so that all the harmonic power measurements show the relative change in a particular harmonic as a function of r-f drive power and as a function of the beam voltage. All of the spurious output measurements made to date have used the SAL-36 klystron.

Two earlier reports^{1, 2} have described the measurement technique and the reasons for using the sampling loop rather than attempting to make model power measurements in the output wave guide of the tube under test

The measurement circuit used to measure the fundamental output power as a function of r-f drive power and as a function of beam voltage is shown in Figure 1. The measurement circuit used to measure the second, third, fourth, and fifth harmonic outputs is shown in Figures 1 and 2. Briefly the fundamental power was measured by means of a pair of cross-guide couplers in the output wave guide. The harmonic measurements were made by sampling the harmonic power of the output cavity by means of the small coupling loop. The sampling loop output was fed through the appropriate filters as shown in Figure 2. The harmonic output was

then fed to a mixer where it was combined with the local-oscillator signal to produce a 30-Mc/s signal that was first amplified by an i-f amplifier and then further amplified and detected by a receiver for display on an oscilloscope. In making the measurements the vertical displacement of the signal on the oscilloscope was kept constant. The relative change of a signal was measured by a calibrated attenuator in the harmonic signal output line and by a calibrated attenuator in the receiver. The relative change of a harmonic signal in decibels is the amount that the attenuators had to be changed to keep the display on the oscilloscope constant. The r-f input drive power was measured by means of a pair of coaxial directional couplers.

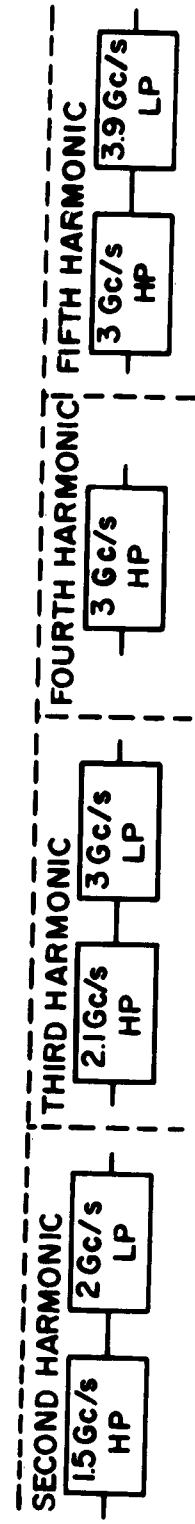
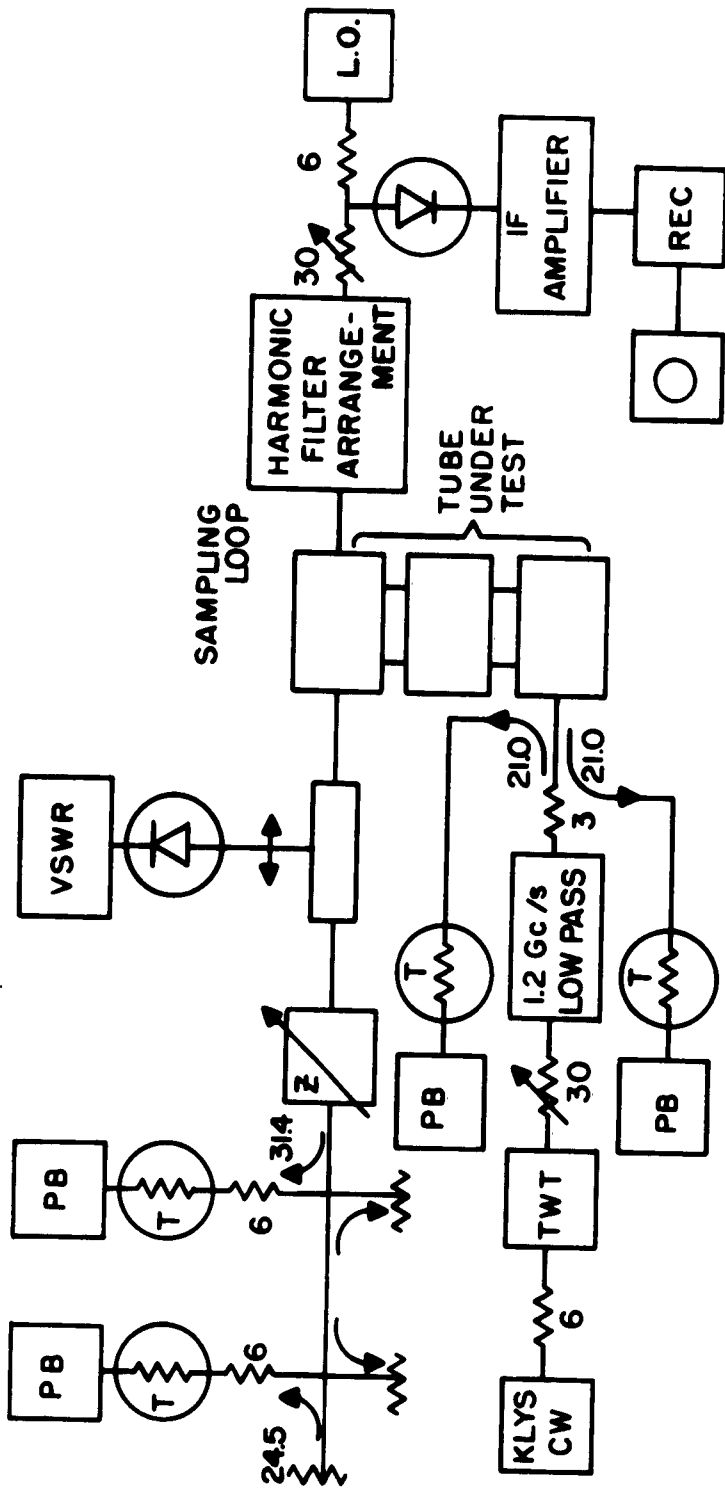
In making the harmonic power measurements, it was necessary to use a high-pass filter with a large attenuation in the stop band. The only type of high-pass filter presently available that is capable of removing the fundamental and all harmonics of lower frequency than the harmonic being measured sufficiently well is a wave guide operated beyond cutoff. The high-pass filters for the second, fourth, and fifth harmonics were constructed for these measurements. The third harmonic filter was made from standard S-band wave guide.

Measurements of the relative change in second through fifth harmonics of the SAL-36 are shown in Figures 3 and 4. Figure 3 shows the changes in the harmonics for a beam voltage of approximately 65 kv; Figure 4 shows the changes for a beam voltage of approximately 80 kv. The nominal operating beam voltage of the SAL-36 is 120. It is seen from both Figures 3 and 4 that in the small-signal case the rate of change in the fundamental or in the harmonics with respect to r-f drive power

is at the rate predicted by small-signal theory.³ The drive level for which this small-signal analysis is valid is a function of the beam voltage of the tube under test. This is demonstrated by making a comparison of Figures 3 and 4, where the beam voltage is the only parameter changed for the two sets of data. It is noted that as the beam voltage is increased, the harmonics saturate at a lower drive level.

REFERENCES

1. A. S. Gilmour, Jr., "Measurements of Beam Harmonics in a Three-Cavity Klystron," in Research Report EE 462, Cornell University, February 1960.
2. L. F. Eastman, "Note on the Preliminary Results of Experiments on Spurious Output Powers," in Research Report EE 431, Cornell University, February 1959.
3. W. E. Blair, "Harmonic Analysis of Electron Beams in Klystrons," Research Report EE 458, Cornell University, 30 January 1960.



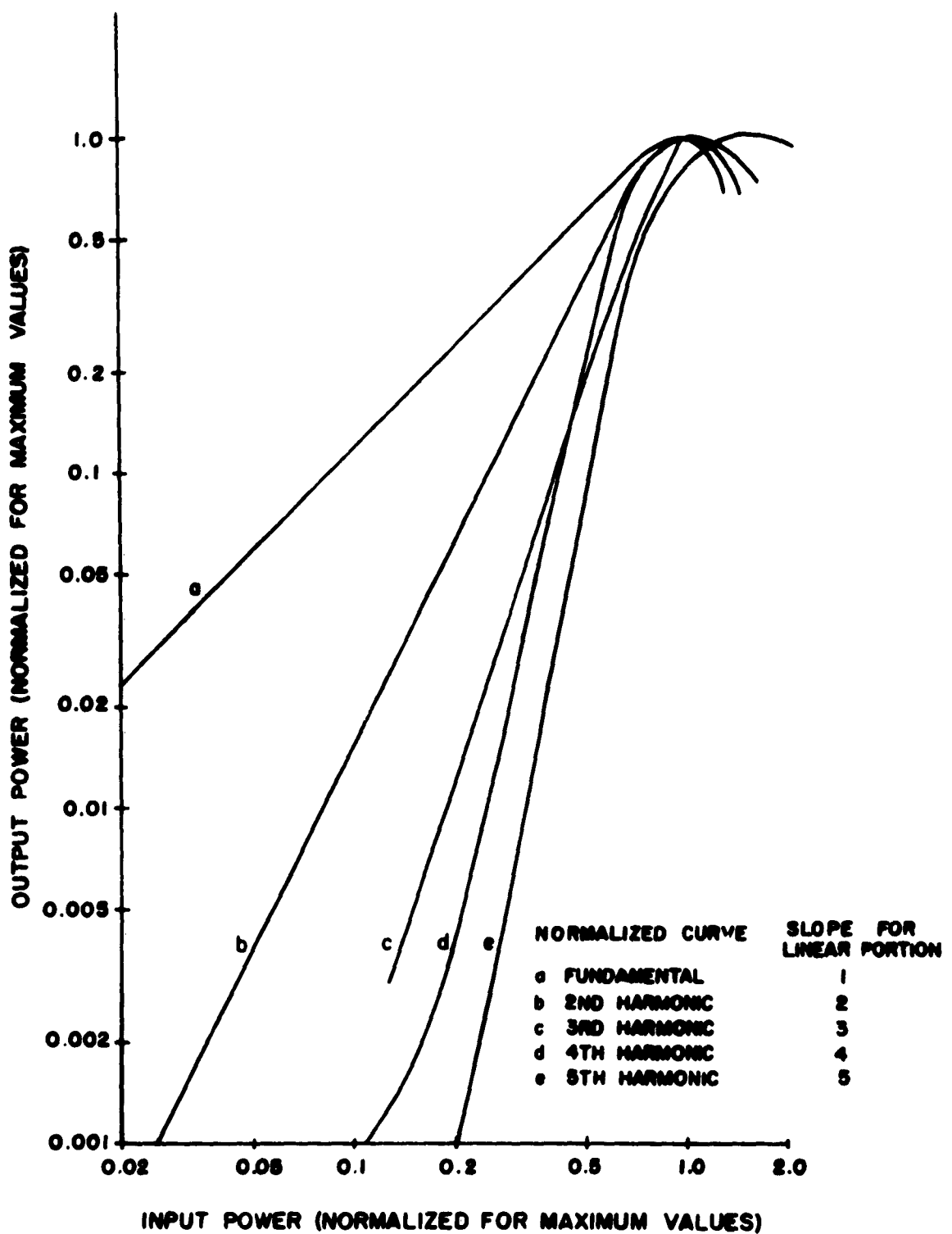


Figure 3. Variations of Fundamental and Harmonic Powers as a Function of Input Power for a Beam Voltage of 65 kv.

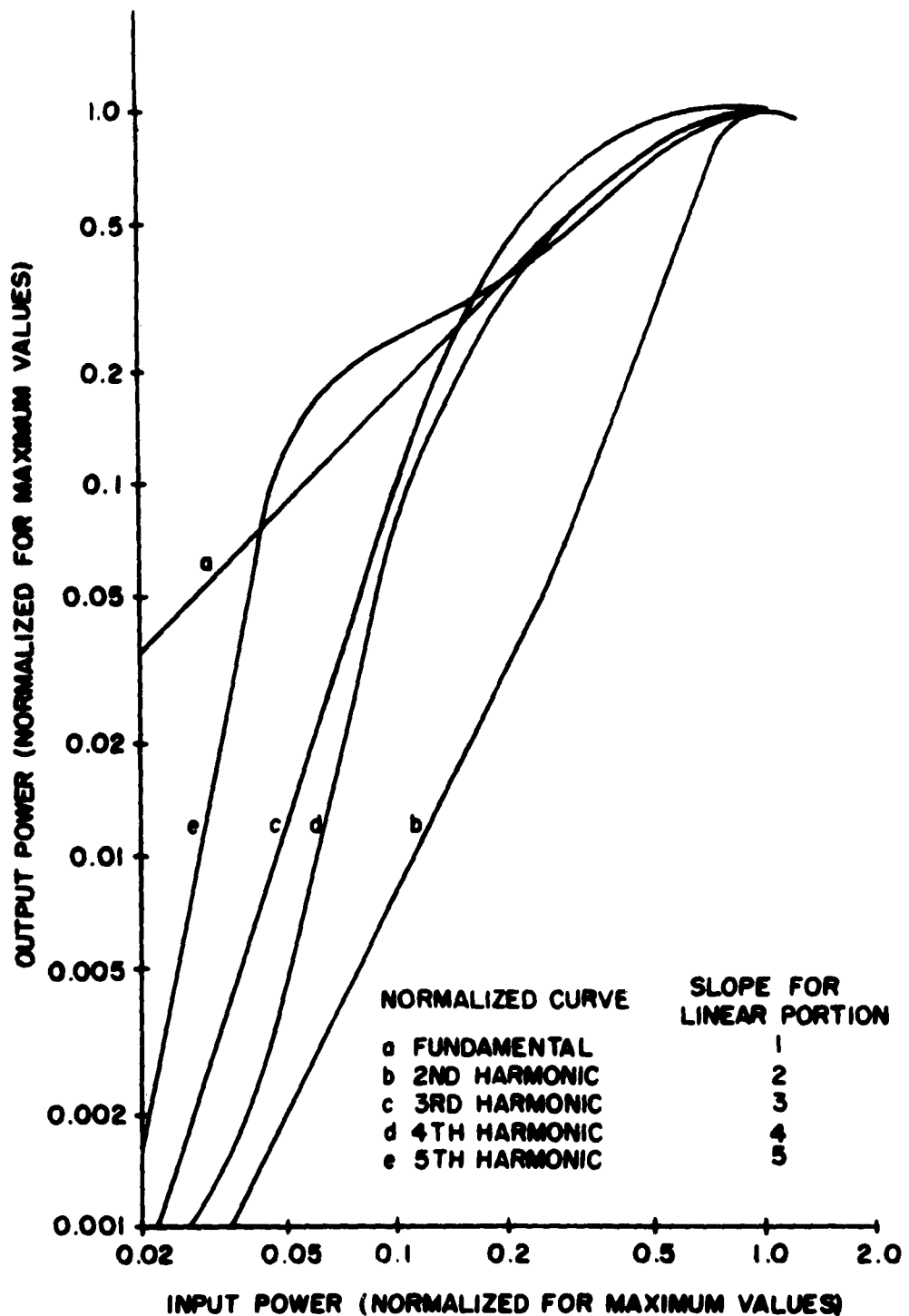


Figure 4. Variations of Fundamental and Harmonic Powers as a Function of Input Power for a Beam Voltage of 80 kv.

PERTURBATION TECHNIQUE

W. E. Blair

School of Electrical Engineering
CORNELL UNIVERSITY
Ithaca, New York

RESEARCH REPORT EE 429

PERTURBATION TECHNIQUE

W. E. Blair

THEORETICAL AND EXPERIMENTAL INVESTIGATION
OF LINEAR-BEAM MICROWAVE TUBES

Technical Report No. 3

29 May 1959

Published under Contract No. AF 30(602)-1696
Rome Air Development Center
Griffiss Air Force Base, New York

ABSTRACT

The perturbation technique described is a method by which the electric and magnetic field intensities can be measured at any point inside a resonant microwave structure. Small magnetic or dielectric objects, generally spheres, are used to distort the electric or magnetic fields. In the electric case, this field distortion causes a slight decrease in the resonant frequency of the cavity, which is proportional to the field strength. Data can be obtained very precisely to within 0.3 per cent and the accuracy within 1 per cent. A finite bead causes slight errors in resolution, but a decrease in bead size causes too great a loss in sensitivity.

A. DESCRIPTION

This technique provides a method of accurately measuring electric and magnetic field intensities at any position in a resonant microwave structure. The method by which this is done, is to use a perturbing object which disturbs the natural field pattern of the structure and changes its resonant frequency.

The perturbing object can be made of any substance and have any geometry; but a small, spherical bead, made of metal or dielectric, is the simplest to analyze. The apparatus is somewhat complex to set up, but once initial calibrating and balancing procedures are complete, data can be taken quickly and accurately with less than one per cent error.

B. PERTURBATION THEORY AS APPLIED TO THIS TECHNIQUE

The general perturbation equations¹ are used as the basis of the theory; for metals,

$$\delta = \frac{df}{f_a} = \frac{K_{1h} \mu_0 H^2 - K_{1e} \epsilon_0 E^2}{4U} \tau ; \quad (1)$$

and for dielectrics and ferrites,

$$\delta = \frac{df}{f_a} = \frac{-K_{2h} (K_m - 1) \mu_0 H^2 - K_{2e} (K_d - 1) \epsilon_0 E^2}{4U} \tau ; \quad (2)$$

where

E = electric field intensity;

¹ L. A. MacKenzie, "Klystron Cavities for Minimum Spurious Output Power," Research Report EE 418, Equations (111) and (112).

H = magnetic field intensity;

K_m = relative permeability μ/μ_0 for dielectric;

K_d = dielectric constant ϵ/ϵ_0 for dielectric,

τ = volume of the perturbing bead;

U = total stored energy in cavity;

K_{lh} } = correction constants that are functions of bead shape,
 K_{le} } = size, and material; of type of field; and to some extent
 K_{2h} } of the position of bead in the cavity;

K_{2e}

$$\delta = \frac{f - f_0}{f_0} = \frac{df}{f_0}$$

df = incremental change in the resonant frequency caused by
bead, frequency deviation, and

f_0 = natural resonant frequency in a th mode.

Because of the simplicity of analysis and results, metallic and dielectric spherical beads will be the only types considered in calculating the correction constants.

Consequently if the E and H field strengths are desired at a particular point in a microwave cavity, both a metallic bead and a dielectric bead can be placed at this point and the frequency deviation, df , can be measured for both beads. Substituting the values of df into Equation (1) and (2), and knowing the other variables, E and H can be obtained by simultaneous solutions of these equations.

For convenience of experimentation, these equations may be simplified by making the proper choice of:

- (1) the geometry of the microwave structure,
- (2) the position at which the bead is placed.

In a cylindrical microwave cavity of a general geometry of Figure 1, assume that the bead is moved along the z-axis of cavity. This simply means that with small enough beads, the H field and the radial E field are theoretically zero. Then E becomes E_{cza} , the electric field along the z-axis;

$$\delta = \frac{df}{f_a} = - \frac{K_{1e} \epsilon_0 E_{cza}^2}{4U} , \quad (3)$$

and

$$\delta = \frac{df}{f_a} = - \frac{K_{2e} (K_d - 1) \epsilon_0 E_{cza}^2}{4U} \tau . \quad (4)$$

For Equation (2) the H-term is also zero because K_m for most dielectrics is approximately one.

Equations (3) and (4) can be written in the form

$$\frac{E_{cza}^2}{U} \propto \frac{df}{f_a} , \quad (5)$$

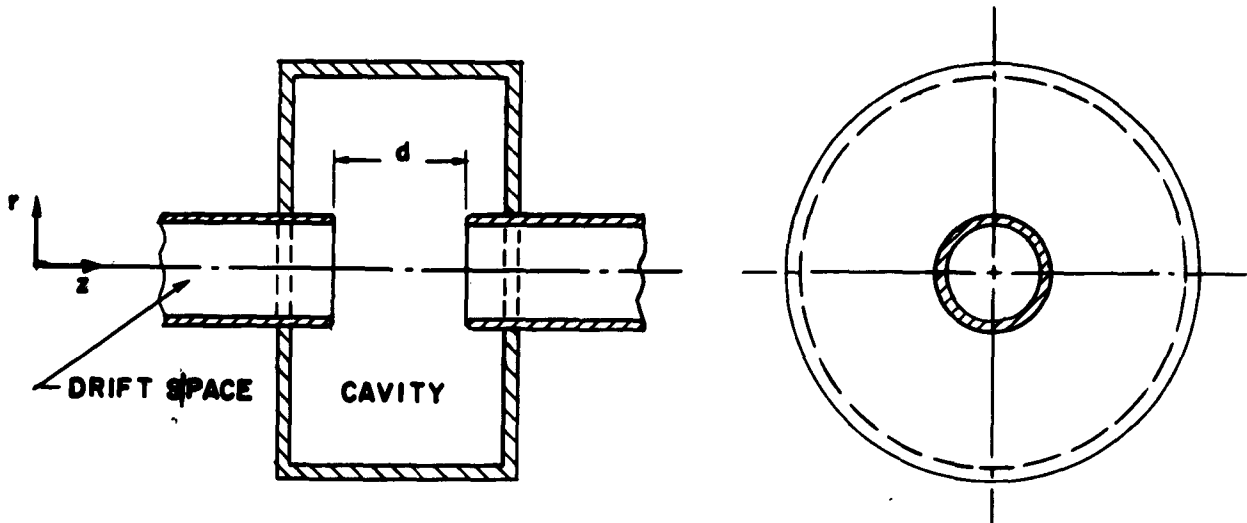


Figure 1. Cylindrical Microwave Klystron Cavity.

or

$$\frac{E_{cza}}{\sqrt{U}} \propto \sqrt{\frac{df}{r_a}} \quad . \quad (6)$$

This form is maintained for a more general presentation of results, as shown later. Essentially, E_{cza} varies as \sqrt{df} for either a metal or dielectric bead.

For cavities of this geometry, E_{cza} can be obtained from an electrolytic tank. Its general form is shown in Figure 2.

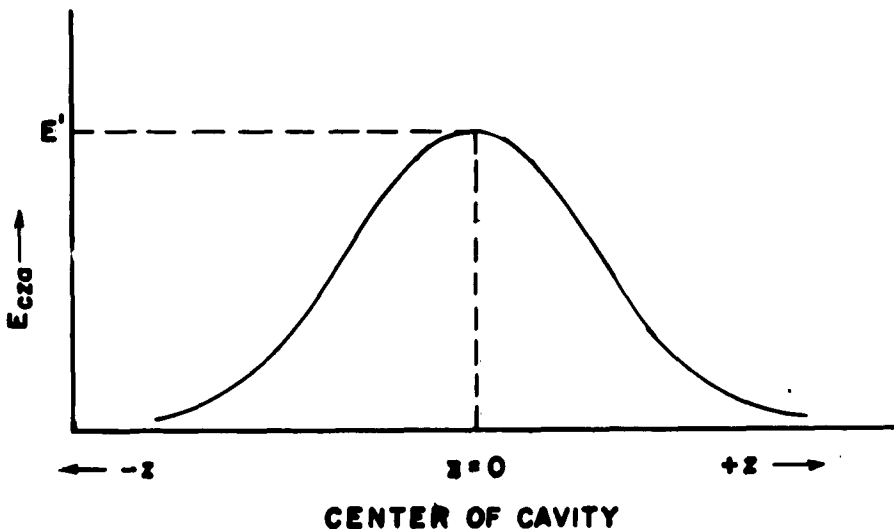


Figure 2. E_{cza} versus z for Klystron Cylindrical Cavity

Let the maximum value of $E_{cza} = E'$ so $E' \propto df$ maximum. The vertical axis can be normalized to E' and df maximum. This allows Equation (6) to become

$$\frac{E_{cza}/\sqrt{U}}{E'/\sqrt{U}} = \frac{E_{cza}}{E'} = \sqrt{\frac{df}{df_{\text{max.}}}} \quad . \quad (7)$$

The horizontal axis can be normalized by d , the separation of the ends of the drift spaces. This normalized is shown in Figure 3.

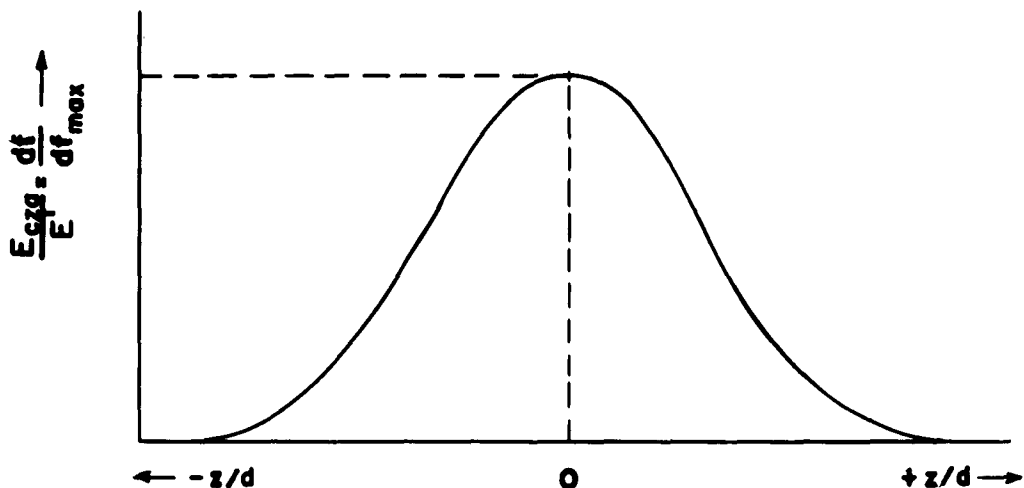


Figure 3. E_{cza} , Normalized by E' , versus z/d

The most general plot E_{cza} can be obtained by normalizing E by E_{czo} ; E_{czo} is the uniform equivalent field of two parallel plates as in the equivalent gridded klystron gap with a voltage V , separated by the distance d , such that $E_{czo} = V/d$. However, for normalized E_{cza} in Figure 3, $V = \text{area under the curve of Figure 2} = \int E \cdot dl$. Since E_{cza} has a tendency to spread out, it is logical to assume E' to be less than E_{czo} .

Letting the ratio $\frac{E_{cza}}{E_{czo}} = \frac{E_{cza}/\sqrt{U}}{E_{czo}/\sqrt{U}}$ and normalizing Equation 6 by E_{czo} . Equation 8 is obtained:

$$\frac{E_{cza}/\sqrt{U}}{E_{czo}/\sqrt{U}} = \frac{E'}{E_{czo}} \sqrt{\frac{df}{df_{max}}} \quad (8)$$

Plotting Equation(8) with the gridded gap produces a curve similar to that in Figure 4, where the two areas are equal.

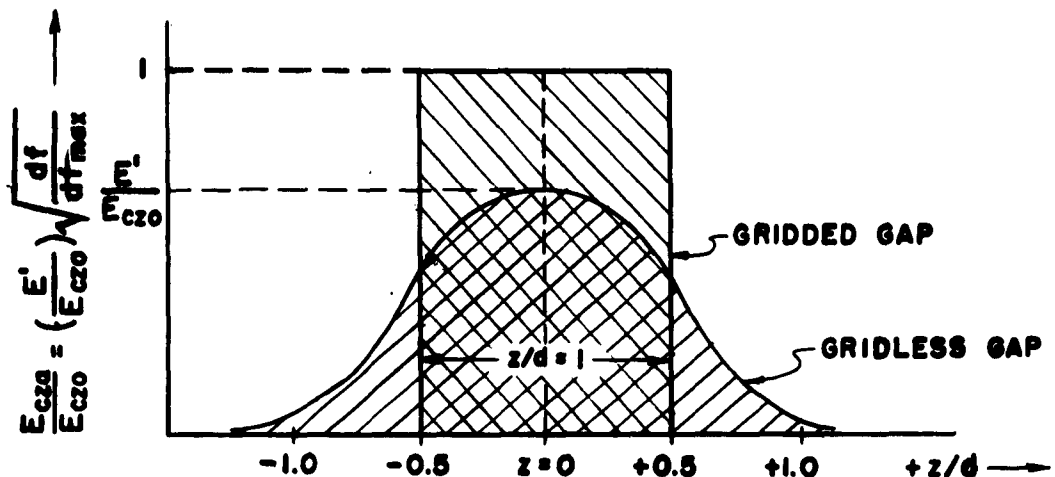


Figure 4. E_{cza} Normalized by E_{czo} versus z Normalized by d

The equations are often written in the form of E_{cza}/\sqrt{U} rather than merely E_{cza} . This is used because the value of U in Equation 3 and 4 is often not known. Since all data are normalized, it is not needed unless the values for E_{cza} in volts/meter are desired. This can be obtained by knowing U and merely scaling Figure 4, U can be obtained in various ways, for example, by measuring power input and Q from the basic definition of Q :

$$Q = \frac{\omega_0 \text{ (stored energy)}}{\text{(power input)}} = \frac{\omega_0 U}{W} \quad . \quad (9)$$

C. METHOD OF PERTURBATION MEASUREMENT

Figure 5 is a general block diagram of the circuit for making perturbation measurements. The nucleus of the setup is the balanced modulator. It mixes a main signal generator output f_0 with a Marka Sweep output Δf . The main signal f_0 is for example 1 Mc/s above the natural resonance of the cavity f_a . The Marka Sweep generates a constant voltage, but a varying frequency output that

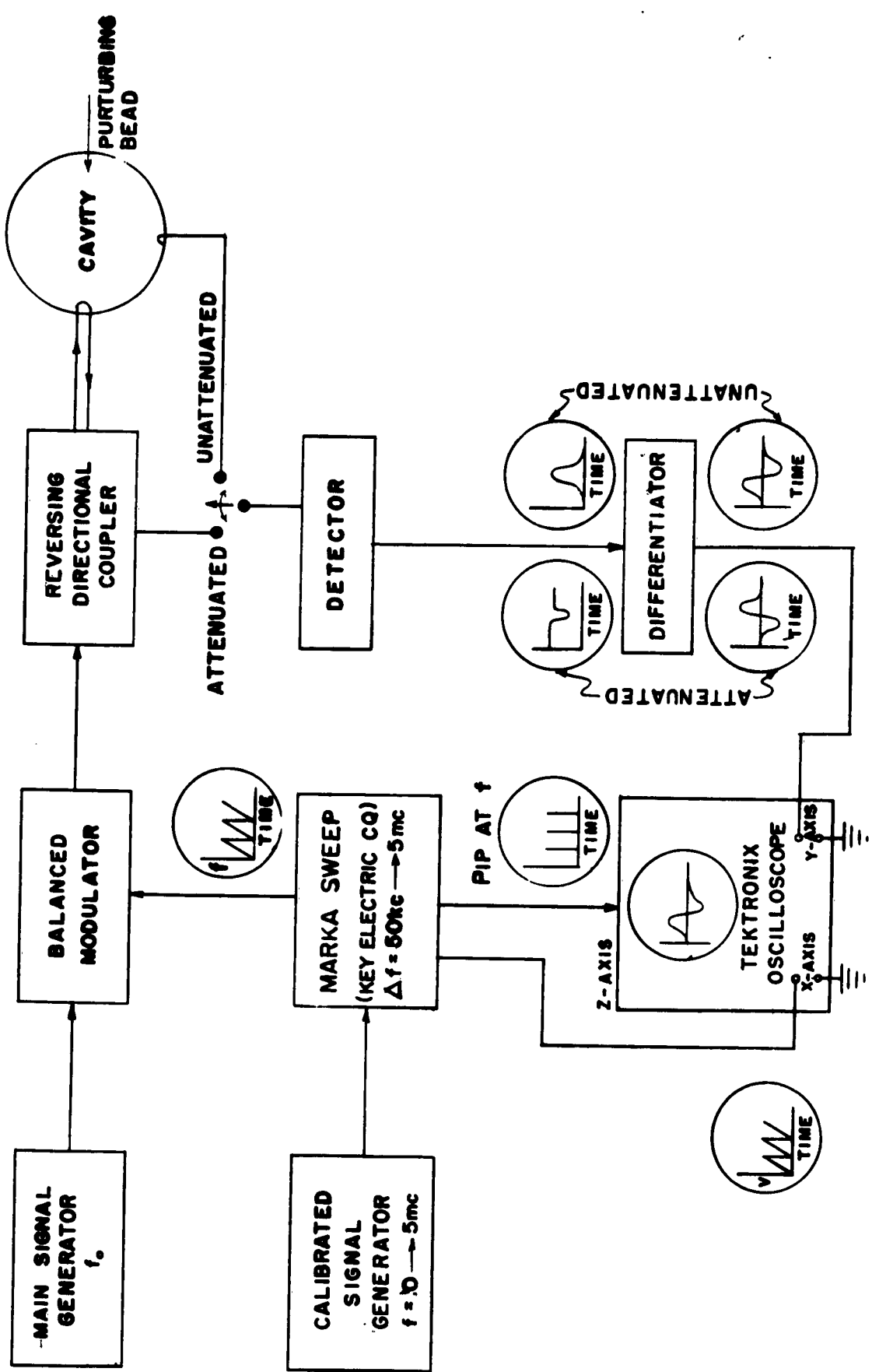


Figure 5. Diagram for Perturbation Measurement

modulates the carrier f_o . This Δf varies in frequency linearly and periodically in time from 50 kc to 5 Mc/s; that is, it is a sawtooth-varying frequency with sweep rate of 60 cps.

The balanced modulator, which suppresses f_o , passes the sidebands $f_o \pm \Delta f$ into the cavity. The lower sideband will pass through the cavity resonance since $f_o > f_a$. Consequently, energy of the upper sideband and the lower sideband (other than at resonance) will be reflected; so the cavity output will be a superposition of the two sidebands. (Figure 6a) The sharpness of the dip depends on the Q of the cavity.

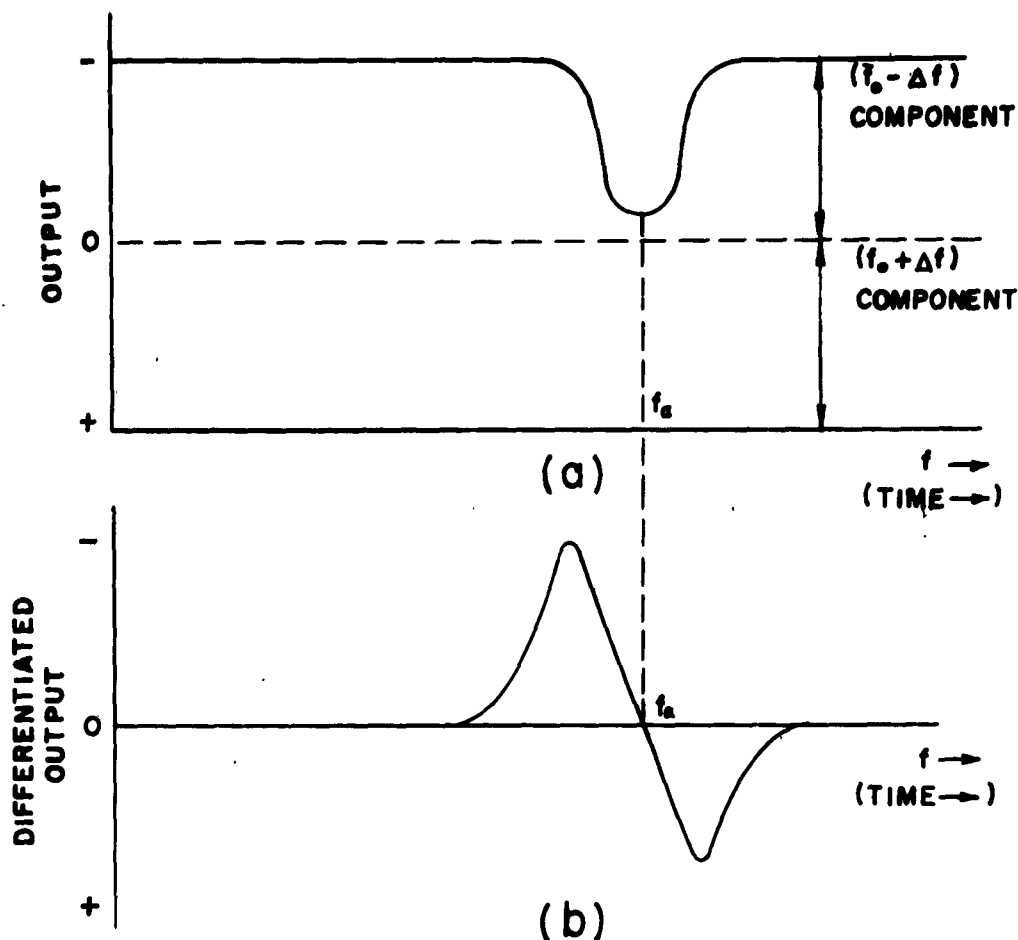


Figure 6. Cavity Output versus Frequency

The output for high-powered signals may be taken off at the directional coupler; low-powered signals may be coupled directly out of the cavity, with little attenuation. This cavity output is detected, differentiated, and finally becomes the Y-axis input to the Tektronix oscilloscope (Figure 6b). The wave form is differentiated because the interaction of the curve and the reference line is more easily distinguishable in Figure 6b than in Figure 6a.

In order that the wave form of Figure 6b be viewed by an oscilloscope, it is necessary that the X-axis be swept with a 60 cps sawtooth. In addition, it is necessary that the X-axis voltage-varying sawtooth be exactly proportional to the frequency-varying sawtooth. The Marka Sweep provides such a sweep; this is the X-axis input.

Finally, a calibrated signal generator is used as an external source to trigger a marker pulse in the Marka Sweep. This pulse is triggered at the exact instant the Marka Sweep modulating output passes through the frequency at which the calibrated signal generator is set. This pulse is used to Z-axis (intensity) modulate the oscilloscope. Thus a pip is produced at the instant the output signal (Y-axis) passes through frequency $f_o + f$, where f is the frequency of the calibrated signal generator.

With $f_o > f_a$ by 1 Mc/s, f can be set at 1 Mc/s. This would position the pip exactly at the cavity resonance (Figure 7a). If the perturbing bead is positioned in the cavity at some point z' , on the z-axis, the resonant frequency will be reduced by a small amount, df' . This causes the resonant curve to shift to

the right by df' (Figure 7b). Then by decreasing the frequency of the calibrated signal generator, the pip can be adjusted back to the zero point of the wave form (Figure 7c). The amount the frequency changed is recorded as df' at the point z' .

Next, move the bead to the next point, z'' , and find the frequency change df'' . This procedure is continued until point by point, data has been obtained for frequency deviation df versus bead position z . This data is used to obtain the normalized plots from Equation (8) and Figure 4.

D. EXPERIMENTAL RESULTS AND CONCLUSIONS

Figure 8 shows the experimental setup as it was used to obtain data of df versus z for several beads. Beads of various geometries, sizes, and materials were used to perturb the cavity; they were suspended in the cavity by nylon thread. The cavity, middle cavity of SAL-36 klystron, and the bead support arrangement can be seen at the right side of the figure.

Some beads were used to verify the theoretical values for correction constants (K_{1h} , K_{1e} , K_{2h} , K_{2e}). Typical data for one, a spherical brass bead, was plotted in Figure 9; this can be compared to Figure 4. By any of the standard methods of approximating a curve by a polynomial (e.g., the least-square method), Figure 9 can be represented by a polynomial in z , and since the bead was positioned along the z -axis, the polynomial² will be $A(z)$. That is, $\mu_z(r, z)|_{r=0} = A(z)$.

²L. A. MacKenzie, "Electrolytic Tank," Research Report EE 377, Equation 5.

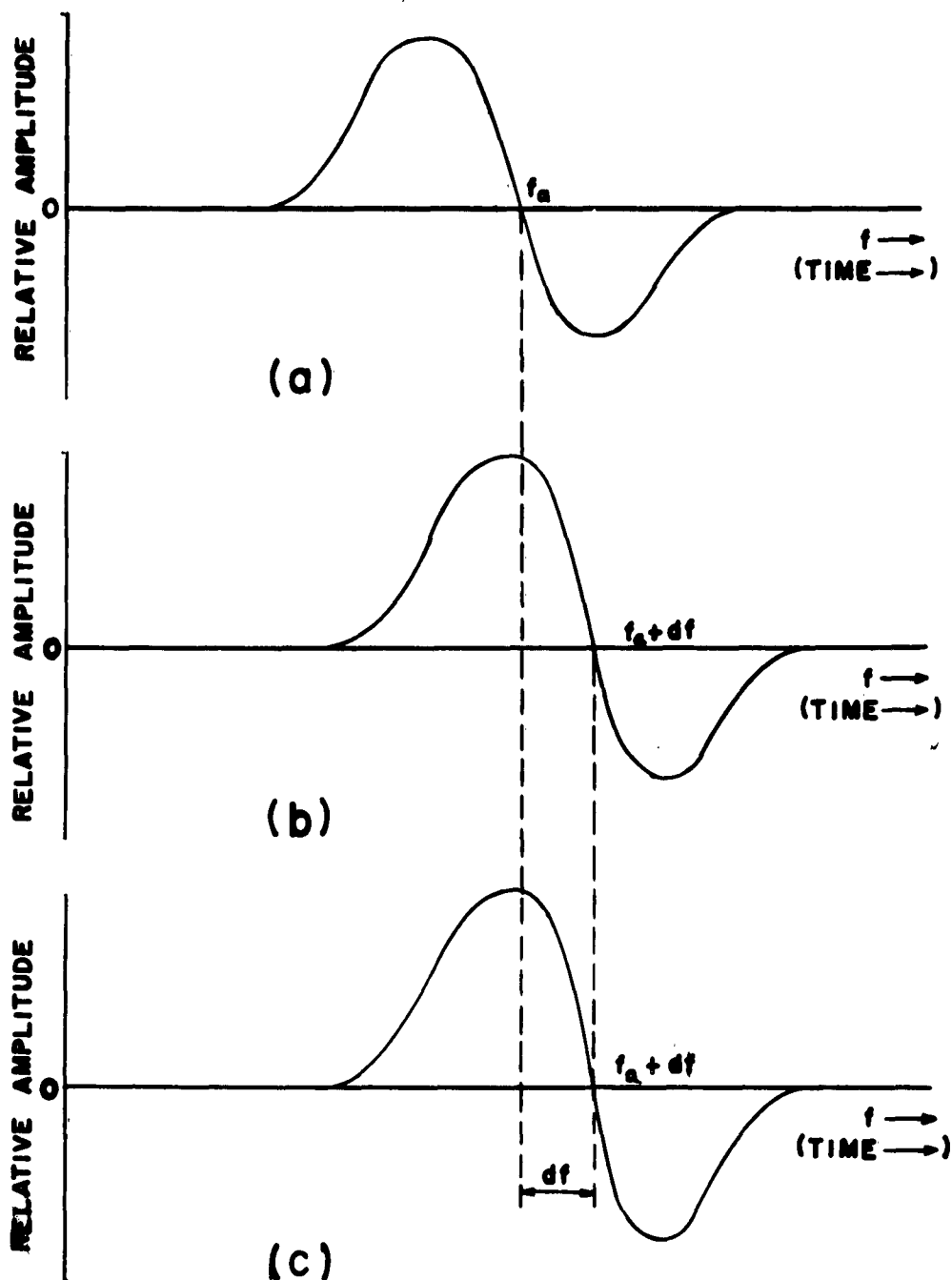


Figure 7. Three Steps in Obtaining Frequency Shift

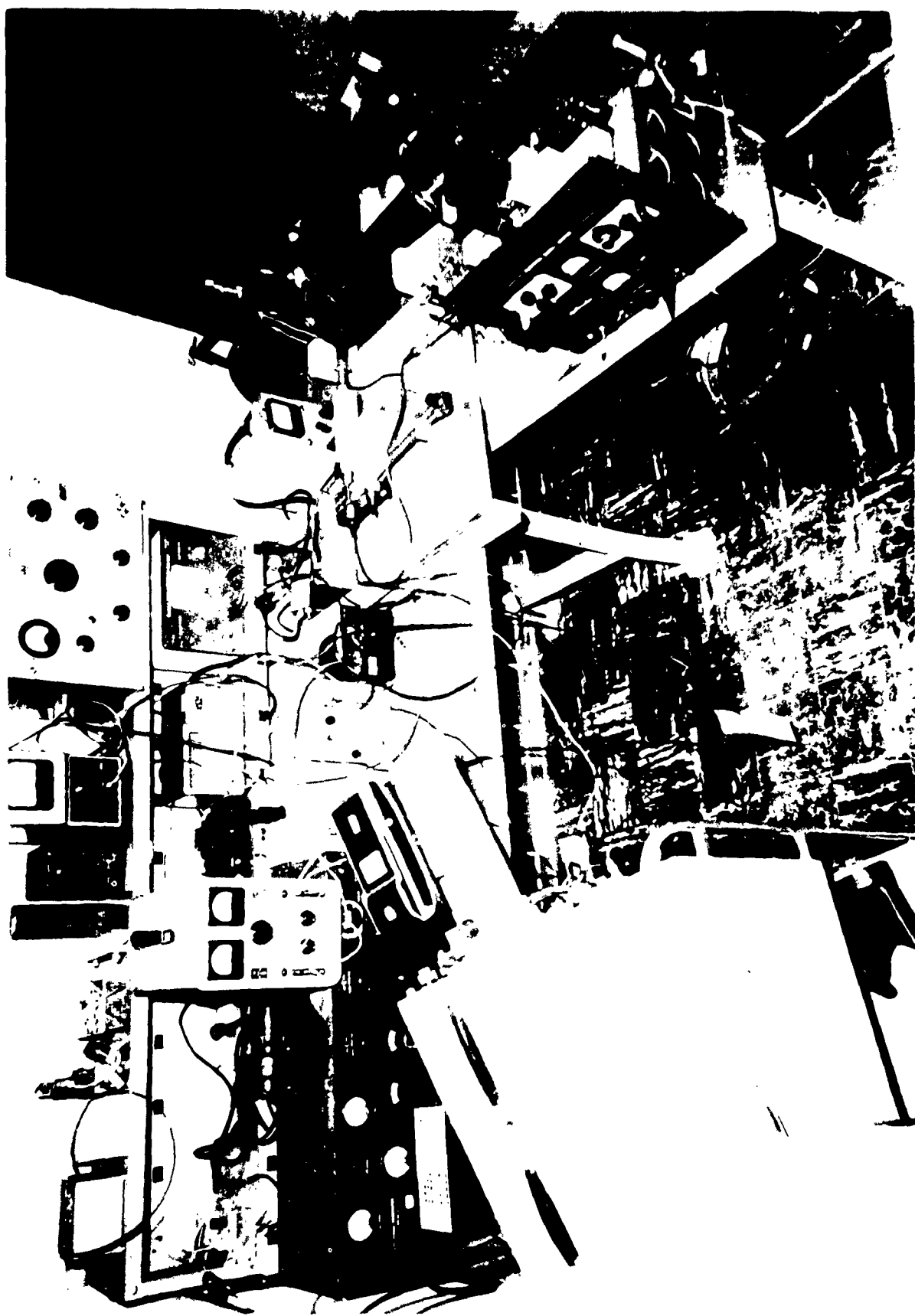


Figure 8 Experimental Setup for Perturbation Measurements.

The experimental value of $\frac{E'}{E_{czo}}$ = 0.758 and the general shape of Figure 2 compares well with that obtained in the electrolytic tank.³

Although data was obtained precisely, with error less than 0.3 per cent, there are possible sources of error. The largest source is probably resolution. In order to obtain perfect resolution, the bead size must be small enough to insure a uniform field across its cross-section and must distort the field only at the "point" of measurement. This, however, decreases the sensitivity so only strong fields can be measured. Consequently, a compromise between sensitivity and resolution must be made.

³ Op. cit., Figure 14.

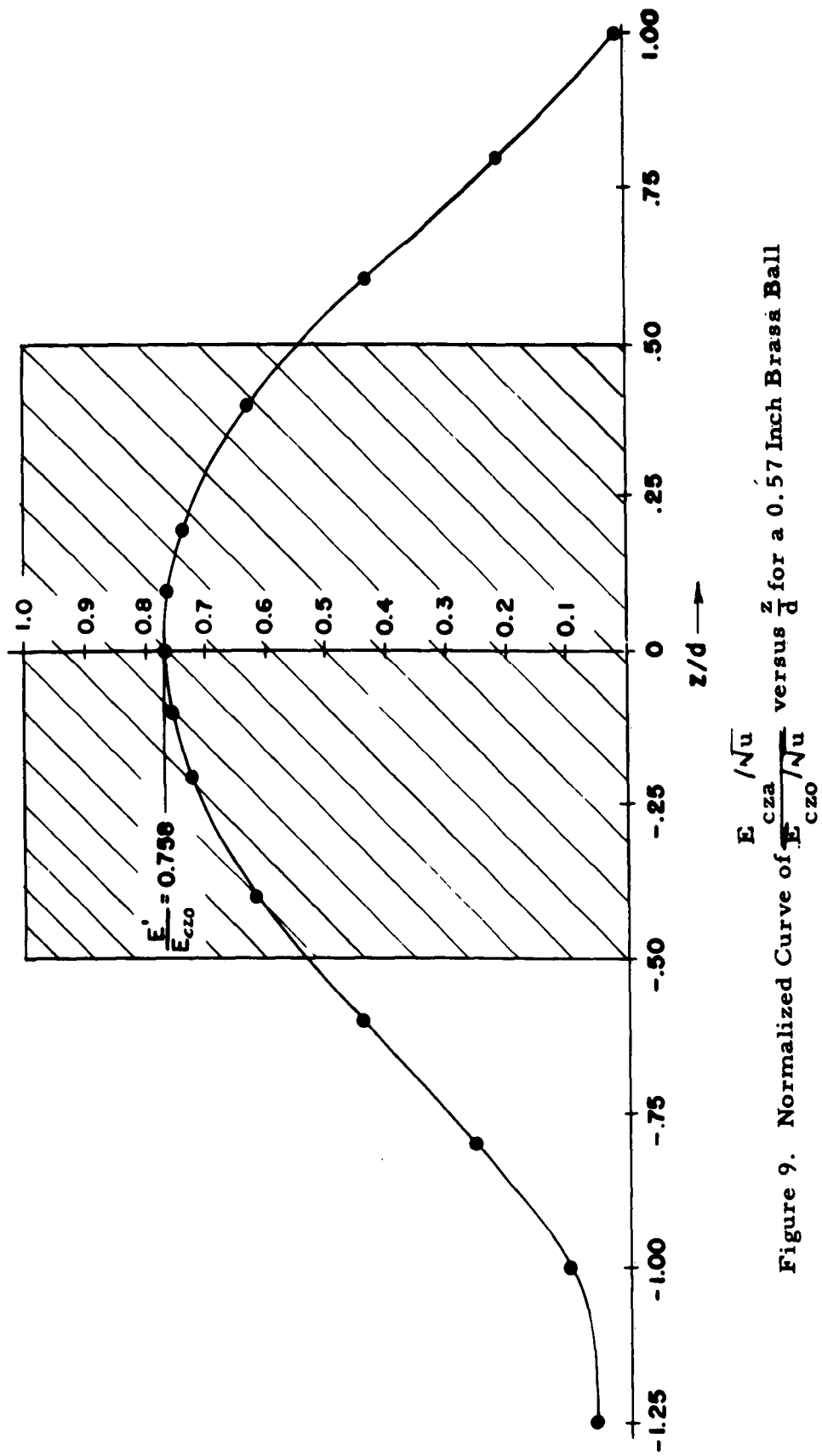


Figure 9. Normalized Curve of $\frac{E_{cza}}{\sqrt{u}}$ versus $\frac{z}{d}$ for a 0.57 Inch Brass Ball